



Combustion Diagnostics in Homogeneous Charge Compression Ignition Optical and Thermal Single Cylinder Engines

Pawel Mirosław Luszcz

School of Mechanical Engineering

The University of Birmingham

*A thesis submitted to The University of Birmingham
for the degree of Doctor of Philosophy*

School of Mechanical Engineering

The University of Birmingham

August 2009

UNIVERSITY OF
BIRMINGHAM

University of Birmingham Research Archive

e-theses repository

This unpublished thesis/dissertation is copyright of the author and/or third parties. The intellectual property rights of the author or third parties in respect of this work are as defined by The Copyright Designs and Patents Act 1988 or as modified by any successor legislation.

Any use made of information contained in this thesis/dissertation must be in accordance with that legislation and must be properly acknowledged. Further distribution or reproduction in any format is prohibited without the permission of the copyright holder.

Abstract

The work presented in this thesis is intended to investigate the effects of fuel properties, injection strategy and timing on autoignition and combustion characteristics of a Homogeneous Charge Compression Ignition (HCCI) engine with a negative valve overlap (NVO) strategy. Conventional (pressure-transducer based) measurements and passive optical research have contributed to understanding of the chemical-physical sites of HCCI autoignition and combustion. This experimental work was undertaken on matching thermal and optical single cylinder research engines in configurations derived from a production Jaguar V8 engine.

A thermal engine study using a range of fuels including conventional gasoline and primary reference fuels has been performed to gain insight into autoignition and combustion characteristics of various chemically dissimilar blends or components. This was done at different operating conditions by varying the engine speed and the proportion of residuals trapped. These measurements have shown that the autoignition and combustion characteristic of an HCCI operated engine are highly dependent on fuel blend composition and are also affected by engine operating conditions. It was found that the autoignition process type which the mixture undergoes, whether it is one- or two-step, depends very strongly both on fuel blend composition and on engine operating conditions. More specifically the presence and also proportion of particular chemical compounds in a blend could significantly contribute to the alteration of the process type. Similar experiments using the chosen engine operating points were repeated on the optical engine using passive optical diagnostics such as imaging and spectroscopy. Thereby it was possible to gain insight into the chemistry of one-step and two- step ignition processes.

The image analysis of the port fuel injected (PFI) HCCI operation have been carried out for stoichiometric and lean conditions. A crank-angle resolved high-speed imaging technique was employed a piston crown window for optical access to the combustion chamber. The spatial repeatability nature of autoignition occurrence and the directions of combustion

progress were evaluated using especially developed image processing technique. The insight into the expansion rates of burned areas and of the spreading velocities of reacting structures fronts was also gained by introducing two new image processing techniques.

Various direct injection strategies (single and split injection) and timings, including fuel injection prior to and during the negative valve overlap period were optically investigated. The comprehensive study included the application of three diagnostic instruments: the Complementary Metal-Oxide Semiconductor (CMOS) high-speed colour imager, the intensified Charge Couple Device (CCD) and the imaging spectrograph. Among the other observations the applied passive techniques, the imaging and the spectroscopy in conjunction with adequate image processing techniques have shown that the combustion behaviour and also the colour of the burning mixture are dependent on the fuel injection scheme. With the investigated split (double) injection, when some of fuel is injected prior to TDC NVO the combustion behaviour is significantly different than when it is injected during even at TDC (NVO). There is a strong indication that a form of incandescence occurs during the NVO, which probably comes from the glowing soot. This is further supported by a quantification of the emitted luminescence and spectroscopic measurements during this phase.

Dedication

I would like to dedicate this thesis to my parents for their encouragement and endless support given to me not only during the period of the DPhil but also throughout my entire life.

Acknowledgements

During work on this PhD, a number of persons to deserve thanks for the help and support that they gave to me.

Firstly, I would like to thank my main supervisor Prof Hongming Xu and my associate supervisor Dr Athanosios Tsolakis for their guidance and encouragement of my studies throughout the period of my PhD course. Furthermore I would like to express my gratitude to Professor Mirosław Wyszynski for his supervision and help.

I would like to thank the School of Mechanical Engineering at the University of Birmingham and Jaguar Cars Ltd. for funding my studentship as well as the financial and technical support during the project. Help from Mr Thomas Gardiner, Dr Jun Qiao, Dr Trevor Wilson and Dr Robert Stevens is greatly acknowledged. I am also grateful to Mr Dave Banner from the instrumentation department of Jaguar Cars Ltd for his extremely supportive help in engine instrumentation commission. Help from the engine technicians Mr. Peter Thornton and Mr Carl Hingley of the University of Birmingham is also gratefully acknowledged. Also special thanks to EPSRC Engineering Instrument Loan Pool Scheme for Phantom v7.1 CMOS imager loan that was granted. Shell Global Solutions U.K. is also greatly acknowledged for providing number of fuels necessary to conduct experiments covered in this thesis.

Finally, I would like to thank to all the dear friends I have met during my stay in Birmingham for their help or contribution to my life: in particular to Adam P., Alana T., Aleksandra Pawlik, Dale Turner, Emila Cieslak, George Constantinides, Kampanart Theinnoi, Jacek Misztal, Marek Kopicki, Paulina Pianko-Oprych, Paul Rounce, Rizalman Mammat, Usama Elghawi, Sathaporn Chuepeng and Simbarashe Sitshebo.

Contents

List of Figures	ix
List of Tables	xvi
Nomenclature	xviii
List of Publications and Conferences Attended	xxi
Chapter 1 Introduction	1
1.1 Overview.....	1
1.2 Concept of Homogenous Charge Compression Ignition.....	2
1.2.1 Developmental history.....	2
1.2.2 Characteristic of the HCCI concept.....	4
1.3 Diagnostic techniques for combustion study.....	14
1.3.1 Passive measurement techniques.....	15
1.4 Research objectives, scope and outline.....	17
Chapter 2 Literature Review	23
2.1 Physicochemical nature of an HCCI autoignition and combustion.....	24
2.2 The influence of fuel molecule type and engine operating variables on the character of HCCI autoignition and combustion.....	28
2.3 Current fuel autoignition quality designators and their role and relevance in the HCCI autoignition process.....	30
2.4 Injection strategy and timing as a means of controlling the combustion onset and optimising the process.....	34
2.5 Solid carbonaceous particles and HCCI operation.....	38
2.6 Summary.....	39

Chapter 3 Experimental Systems	40
3.1 Introduction.....	40
3.2 Engine facilities.....	40
3.2.1 Thermal engine.....	42
3.2.2 Optical engine.....	43
3.3 Engine control systems.....	53
3.3.1 Engine timing control system.....	55
3.3.2 Variable cam timing control system.....	59
3.4 Summary.....	65
 Chapter 4 Diagnostic Instrumentation	 66
4.1 Introduction.....	66
4.2 Fundamentals of scientific cameras.....	66
4.2.1 Imager attributes.....	67
4.2.2 Working principles of CCD, iCCD and CMOS imagers.....	69
4.3 Andor iStar iCCD imager and UV-Nikkor lens.....	73
4.3.1 Andor iStar iCCD camera.....	73
4.3.2 UV-Nikkor 105 mm f/4.5 lens.....	76
4.4 Phantom CMOS imager and Nikon 24-85 mm lens.....	77
4.4.1 Phantom CMOS camera.....	77
4.4.2 Nikon 24 – 85 mm f/2.8 – 4 lens.....	79
4.5 Oriel MS260i imaging spectrograph.....	81
4.6 Potential noise sources of imager and image noise content analysis.....	82
4.6.1 Potential noise sources of camera.....	82
4.6.2 Image noise content analysis.....	84
4.7 Summary.....	88
 Chapter 5 Data Acquisition and Processing	 89
5.1 Introduction.....	89

5.2	Engine conventional data acquisition and processing.....	90
5.2.1	Data acquisition systems – codes and instrumentation.....	90
5.2.2	Data analysis.....	96
5.3	Optical data/image acquisition.....	100
5.4	Optical data/image processing.....	101
5.4.1	Image normalised histogram and its statistics.....	105
5.4.2	Image object area determination.....	109
5.4.3	Image objects distance determination.....	111
5.4.4	Image processing techniques for autoignition and combustion analysis.....	113
5.4.4.1	Autoignition occurrence and combustion development pattern likelihood of repeatability technique.....	113
5.4.4.2	Expansion rate of burned areas.....	118
5.4.4.3	Reacting structure front spreading velocity.....	119
5.5	Summary.....	121
Chapter 6	Characteristic of HCCI Autoignition and Combustion Phases	122
6.1	Introduction.....	122
6.2	Fundamentals of HCCI autoignition and combustion.....	123
6.3	Effects of engine operational variables	127
6.3.1	Experimental aspects.....	127
6.3.2	Engine speed influence.....	129
6.3.3	Residuals rate influence.....	134
6.4	Physicochemical characteristics of one- and two-step ignition processes.....	141
6.4.1	Experimental aspects.....	141
6.4.2	Physicochemical analysis of one- and two-step ignition process.....	145
6.5	Correlation of ignition process type with fuel octane quality.....	152
6.5.1	Experimental aspects.....	152
6.5.2	Fuel octane number and ignition process.....	154
6.5.3	Fuel octane sensitivity and ignition process.....	155
6.6	Summary.....	157

Chapter 7 Autoignition and Combustion Analysis of Port Fuel Injected HCCI	159
7.1 Introduction.....	159
7.2 Experimental aspects.....	160
7.3 Insight into autoignition occurrence and combustion progress patterns.....	163
7.4 Analysis of the combustion growth rate	177
7.5 Analysis of the front spreading velocities of reacting structures.....	182
7.6 Summary.....	188
 Chapter 8 Characteristic of HCCI Operation with Direct Injection Strategies	 190
8.1 Introduction.....	190
8.2 Experimental aspects.....	191
8.3 Analysis of gasoline HCCI operation with various injection strategies and timings	196
8.4 Analysis of PRF40 HCCI operation with various injection strategies and timings	228
8.5 Spectra of NVO of PRF40 HCCI operation with split injection strategies	233
8.6 Summary	239
 Chapter 9 Conclusions and Future Work	 242
9.1 Conclusions.....	242
9.1.1 The development of image processing techniques for an HCCI autoignition- combustion analysis.....	242
9.1.2 Analysis of the nature of HCCI autoignition and combustion.....	244
9.1.3 Analysis of the premixed HCCI based on high-speed imaging.....	246
9.1.4 A characterisation of HCCI operation with different direct injection strategies and timings	247
9.2 Suggestions for future work.....	248
 Appendix A Fuel Data	 251
Appendix B Image Thresholding Techniques	252
References	258

List of Figures

1.1	Illustrative form of classical CI and SI engines' combustions versus HCCI combustion. (NAFT, www.naftc.wvu.edu)	3
1.2.	Different arrangements of valve lift control; Audi's two-stage valve lifts control (www.audi.com) and BWM's Valvetronic – continuous valve lift management (www.bmw.com).	6
1.3.	Today's representative Homogeneous Charge Compression Ignition engine operational envelope (Qiao <i>et al</i> 2005).	13
1.4.	Today's European driving cycle and Homogeneous Charge Compression Ignition engine operational envelope (Koopmans <i>et al</i> 2007).	14
3.1.	Thermal single cylinder engine.	42
3.2.	Optical single cylinder engine.	44
3.3.	Cross section (schematic) of optical research engine. Two constructed optical paths (bottom and view) are illustrated.	46
3.4.	Flat-topped optical piston with quartz piston-crown insert (window).	46
3.5.	Radiation transmittance characteristics of several optical materials for UV, VIS and IR spectral regions (Skoog <i>et al</i> 2004).	50
3.6.	Transmittances radiations for ultraviolet grade synthetic fused silica, optical grade fused quartz and full spectrum synthetic fused silica (Alkor).	51
3.7.	Complete engine control system. ETCS and VCTCS components, their arrangements and signals flow. Interface box inputs (IN); Interface box outputs (OUT).	54
3.8.	Cutaway of incremental encoder.	56
3.9.	Front panel of ETCS.	58
3.10.	Components of VCTCS and their locations.	60
3.11.	Cam phaser (Reproduced from Steinberg <i>et al</i> 1998); A – Cross section; B – Cutaway view.	61
3.12.	Arrangement of camshaft's trigger wheel and position sensor.	62
3.13.	Front panel of VCTCS.	64

4.1.	Non-uniformity patterns under various illumination conditions for three imager array elements (pixels).	68
4.2.	Schematic representation of full frame CCD camera architecture.	70
4.3.	Cutaway of iCCD imager (Andor Product Overview) and intensifier cross section.	71
4.4.	Schematic representation of CMOS imager architecture.	73
4.5.	Andor iStar iCCD camera (model DH734I – 18 F – 04).	74
4.6.	The spectral responsivity curves versus wavelength for Andor iStar imagers. The model Andor iCCD DH734I – 18 F – 04 is represented by a blue line curve. (Reproduced from Andor iCCD DH734I Camera Technical Guide).	74
4.7.	UV-Nikkor 105 mm f/4.5 lens.	76
4.8.	Spectral responsivity (quantum efficiency) curves for Phantom v7.1 CMOS color camera: A) General spectral responsivity curve; B) Spectral responsivity curves for each individual color – red, green, blue (Reproduced from Phantom v7.1 CMOS Color Camera Technical Guide).	78
4.9.	Phantom v7.1 color CMOS camera.	78
4.10.	Nikon 24 – 85 mm f/2.8 – 4 IF lens.	80
4.11.	Oriel MS260i™ 1/4m Imaging Spectrograph 74050 inside. The dashed line shows the radiation (light) pathway.	82
4.12.	Individual (A) and ensemble-average dark frames (B) pixels intensities distributions of iCCD camera.	86
4.13.	Individual (A,B,C) and ensemble-average dark frames (D,E,F) pixels intensities distributions of CMOS camera.	86
5.1.	Front panel of high-speed data acquisition system.	92
5.2.	Front panel of low-speed data acquisition system.	93
5.3.	Complete arrangement of data acquisition systems and signals flow.	95
5.4.	Front panel of Labview™ combustion analysis code.	97
5.5.	Test image (A & C), and its histogram (B) and thresholded images (D & E). Thresholded image (D) represents image appearance of test image (C) segmented with threshold level (TL = 8) indicated by Image Histogram based Triangle Algorithm Procedure. The thresholded image (E) corresponds to test image appearance (C) segmented with consistent indication of TL=4 delivered by three other methods utilized: Otsu, Gray Level Gradient and Iterative Techniques. As a test image is featured by dark grey level characteristics, what is seen on its histogram (B), image array elements of all images included here (A,C,D & E) were multiplied by a factor of 19, obviously after image thresholding techniques application.	104
5.6.	Illustrations of asymmetrical distributions - a positively and negatively skewed distribution of the identical skewness degree of opposing signs. σ_L^2 – left-hand side (below mean) data distribution variance; σ_R^2 – right-hand side (above mean) data distribution variance.	107

5.7.	Illustrations of various distribution characteristics with different kurtosis indications.	108
5.8.	Comparison illustrating area size determination upon function used and image object shape.	110
5.9.	Review of image distance measurement metrics (methods).	111
5.10.	Representative illustration of <i>bwdist function</i> operation – its difference in distance evaluation and distribution for single object and double objects images contents. The distance was determined using <i>euclidean distance</i> metric.	112
6.1.	Representation of one- versus two-step ignition process.	124
6.2.	Influence of hydrocarbon fuel type on low temperature heat release.	125
6.3.	Engine speed effect on autoignition and combustion proceeding at constant fuelling rate; Total heat release profiles (A) and low temperature heat release profiles (B).	130
6.4.	Mass of fresh charge inducted, entrapped residuals and their ratios as a function of engine speeds investigated.	131
6.5.	Cylinder pressure histories (A) and estimated cylinder charge average temperatures (B).	132
6.6.	The influence of internal exhaust gases on autoignition and combustion proceeding at constant fuelling rate; Total heat release profiles (A) and low temperature heat release profiles (B).	135
6.7.	Cylinder pressure histories (A) and estimated cylinder charge average temperatures (B) prior to HTHR activities for constant fuelling rate tests.	135
6.8.	Influence of internal exhaust gases on autoignition and combustion proceeding at constant fuel-air equivalence ratio; Total heat release profiles (A) and low temperature heat release profiles (B).	136
6.9.	Cylinder pressures histories (A) and estimated cylinder charge average temperatures (B) prior to HTHR activities for constant fuel-air equivalence ratio tests.	136
6.10	Induction stroke BDC temperature and iEGR mass fraction as a function of exhaust valve closing point for constant fuelling rate and fuel-air ratios.	137
6.11.	Effect of fuelling rate on autoignition and combustion proceeding at nearly identical residuals fraction; Total heat release profiles (A) and low temperature heat release profiles (B).	140
6.12.	Access through triangular vertical head window in reference to combustion chamber artifacts locations.	142
6.13.	Profiles of heat release rates for two different valve timing events activities.	146
6.14.	Single images of various crank angles, illustrating different phases of autoignition and combustion process proceeding at investigated VTE#1.	147

6.15.	Light emission intensity as a function of crank angle for autoignition and combustion activities at investigated VTE#1.	147
6.16.	Single images of various crank angles, illustrating different phases of autoignition and combustion process proceeding at investigated VTE#2.	148
6.17.	Light emission intensity as a function of crank angle for autoignition and combustion activities at investigated VTE#2.	148
6.18.	Spectrum of potential low temperature heat release activities (A) and heat release activities (B) at corresponding crank angle degrees – VTE#1.	151
6.19.	Spectrum of potential low temperature heat release activities (A) and heat release activities (B) at corresponding crank angle degrees – VTE#2.	151
6.20	Magnitudes of cool flame activities of PRF40 and PRF80 blends for a range of various engine speeds and residuals fractions conditions.	154
6.21	Magnitudes of cool flame activities of PRF75.6 and TSF75.6 blends for a range of intake air temperatures at constant valve timing event, engine speed and stoichiometric fuel-air ratio.	156
7.1.	Imaged combustion chamber part with reference to its artifacts.	162
7.2.	Sequence of ensemble images showing autoignition and combustion at $\Phi=1$.	165
7.3.	Heat release rate profiles of individual imaged cycle at $\Phi=1$.	166
7.4.	Traditional cylinder pressure traces mass fraction burned derived (MFB), area fraction enflamed (AFE) profiles and enflamed areas ratios. The total area enflamed (fraction) is entire autoignition/combustion area occupied in ensemble image regardless of ensemble image pixels intensities within the interval [1, 12]. The so called 'Brightest Object(s) Area' corresponds to grey-level pixel intensity (random variable) of 12 indicated area of the entire autoignition/combustion area in the ensemble image. The enflamed area ratio was computed as 'Brightest Object(s) Area' and total enflamed area indications.	170
7.5.	Sequence of ensemble images showing autoignition and combustion at $\Phi\approx 0.83$.	172
7.6.	Heat release rate profiles of individual imaged cycle at $\Phi\approx 0.83$.	174
7.7.	Expansion rate of burned areas distribution for each individual imaged engine cycle at $\Phi=1$.	178
7.8.	Expansion rate of burned areas distribution for each individual imaged engine cycle at $\Phi\approx 0.83$.	178
7.9.	Reactions fronts spreading velocities distribution along the reactions contours for individual cycle at $\Phi=1$ operating conditions. The left column shows the reacting structures (their contours) of image pair taken into analysis and right column illustrates the velocities distribution along the reacting structure contour(s). Numerated are single reactions structures development, which were computed separately.	183/184
7.10.	Reactions fronts spreading velocities distribution along the reactions contours for individual cycle at $\Phi\approx 0.83$ operating conditions. The left column shows the reacting structures (their contours) of image pair taken into analysis and right column illustrates the velocities distribution along the reacting structure	185/186

contour(s). Numerated are single reactions structures development, which were computed separately.

- | | | |
|------|--|---------|
| 8.1. | A representative presentation of injection strategies investigated in reference to engine cycle cylinder pressure. EVC and IVO plotted designate exhaust valves closing and intake valve opening points respectively. | 193 |
| 8.2. | Single cycle image sequence of <i>negative valve overlap</i> and <i>main autoignition-combustion</i> periods of split gasoline injection with timing of 680/140° CA at $\Phi=1$. Images were acquired throughout the piston-crown window with Phantom v7.1 camera. Symbols in quotations refer to heat release rate burn point. | 198 |
| 8.3. | Ensemble-average image sequence of <i>negative valve overlap</i> and <i>main autoignition-combustion</i> periods of split gasoline injection with timing of 680/140° CA at $\Phi=1$. An ensemble image sequence of <i>main autoignition-combustion</i> period is also included. Symbols in quotations refer to average heat release rate burn points. Standard deviations of these corresponding burn points are 1.2, 1.1 and 1 for CA5, CA10 and CA50 respectively. | 199 |
| 8.4. | Single cycle image sequence of <i>negative valve overlap</i> and <i>main autoignition-combustion</i> periods of split gasoline injection with timing of 0/140° CA at $\Phi=1$. Images were acquired throughout the piston-crown window with Phantom v7.1 camera. Symbols in quotations refer to heat release rate burn points. In order to enhance visuality of the presented <i>main autoignition-combustion</i> period images, the intensities of all pixels at any RGB image location were multiplied by factor five. | 200 |
| 8.5. | Ensemble-average image sequence of <i>negative valve overlap</i> and <i>main autoignition-combustion</i> periods of split gasoline injection with timing of 0/140° CA at $\Phi=1$. An ensemble image sequence of <i>main autoignition-combustion</i> period is also included. Symbols in quotations refer to average heat release rate burn points. Standard deviations of these corresponding burn points are 2.3, 2.3, 2.5 and 2.6 for CA5, CA10, CA50 and CA90 respectively. In order to enhance visuality of the presented <i>main autoignition-combustion</i> period images, the intensities of all pixels at any RGB image location were multiplied by factor five. | 201/202 |
| 8.6. | Single cycle image sequence of <i>negative valve overlap</i> and <i>main autoignition-combustion</i> periods of split gasoline injection with timing of 40/140° CA at $\Phi=1$. Images were acquired throughout the piston-crown window with Phantom v7.1 camera. Symbols in quotations refer to heat release rate burn points. In order to enhance visuality of the presented <i>main autoignition-combustion</i> period images, the intensities of all pixels at any RGB image location were multiplied by factor five. | 203 |
| 8.7. | Ensemble-average image sequence of <i>negative valve overlap</i> and <i>main autoignition-combustion</i> periods of split gasoline injection with timing of 0/140° CA at $\Phi=1$. An ensemble image sequence of <i>main autoignition-combustion</i> period is also included. Symbols in quotations refer to average heat release rate burn points. Standard deviations of these corresponding burn points are 2.3, 2.3, 2.5 and 2.6 for CA5, CA10, CA50 and CA90 respectively. In order to enhance visuality of the presented <i>main autoignition-combustion</i> period images, the intensities of all pixels at any RGB image location were multiplied by factor five. | 205/206 |

8.8.	Single cycle image sequence of <i>negative valve overlap</i> and <i>main autoignition-combustion</i> periods of single gasoline injection with timing of 140° CA at $\Phi=1$. Images were acquired throughout the piston-crown window with Phantom v7.1 camera. Symbols in quotations refer to heat release rate burn points. In order to enhance visuality of the presented <i>main autoignition-combustion</i> period images, the intensities of all pixels at any RGB image location were multiplied by factor five.	207
8.9.	Ensemble-average image sequence of <i>negative valve overlap</i> and <i>main autoignition-combustion</i> periods of single gasoline injection with timing of 140° CA at $\Phi=1$. An ensemble image sequence of <i>main autoignition-combustion</i> period is also included. Symbols in quotations refer to average heat release rate burn points. Standard deviations of these corresponding burn points are 3.2, 3.4, 4.8 and 6.1 for CA5, CA10, CA50 and CA90 respectively. In order to enhance visuality of the presented <i>main autoignition-combustion</i> period images, the intensities of all pixels at any RGB image location were multiplied by factor five.	208/209
8.10.	Light intensity distribution for three individual planes of RGB ensemble-average image at 369°CA of split gasoline injection with timing of 680/140° CA. Means estimated for each plane equal to 98.7, 82.9 and 69.3 with their standard deviations of 30.7, 28.9 and 21.3 for red, green and blue plane respectively, calculated within the distinguished combustion chamber area.	210
8.11.	Light intensity distribution for three individual planes of RGB ensemble-average image at 372°CA of split gasoline injection with timing of 0/140° CA. Means estimated for each plane equal to 5.7, 5.8 and 12.5 with their standard deviations of 2.1, 2.2 and 4.3 for red, green and blue plane respectively, calculated within the distinguished combustion chamber area.	211
8.12.	Light intensity distribution for three individual planes of RGB ensemble-average image at 374°CA of split gasoline injection with timing of 40/140° CA. Means estimated for each plane equal to 7, 7.9 and 18.4 with their standard deviations of 2.5, 2.4 and 4.2 for red, green and blue plane respectively, calculated within the distinguished combustion chamber area.	212
8.13.	Light intensity distribution for three individual planes of RGB ensemble-average image at 374°CA of single gasoline injection with timing of 140° CA. Means estimated for each plane equal to 6.8, 6.5 and 14.2 with their standard deviations of 2.1, 1.8 and 3 for red, green and blue plane respectively, calculated within the distinguished combustion chamber area.	213
8.14.	Responses of three camera channels as a from of corresponding channels signals ratios during the NVO activities of investigated split gasoline injection with timing of 680/140° CA at $\Phi=1$. Presented ratios abbreviated to R/B, R/G and G/B designate ratios between signals of respective channels - red-to-blue, red-to-green and green-to-blue.	215
8.15.	Distribution of expansion rates of burned areas in a relation to burned points of CA5, CA10, CA50 and CA90 for an imaged cycles of split gasoline injection with timing of 680/140° CA at $\Phi=1$.	226
8.16.	Distribution of expansion rates of burned areas in a relation to burned points of CA5, CA10, CA50 and CA90 for an imaged cycles of split gasoline injection with timing of 0/140° CA at $\Phi=1$.	226
8.17.	Distribution of expansion rates of burned areas in a relation to burned points of CA5, CA10, CA50 and CA90 for an imaged cycles of split gasoline injection with timing of 40/140° CA at $\Phi=1$.	227

8.18.	Distribution of expansion rates of burned areas in a relation to burned points of CA5, CA10, CA50 and CA90 for an imaged cycles of single gasoline injection with timing of 140° CA at $\Phi=1$.	227
8.19.	Monochromatic ensemble-average images of NVO with different injection timing and strategies. The individual images composing ensemble-average image were taken through the side view using iCCD camera.	229
8.20.	Quantification of natural light (radiation) emission intensity during the period of recompression stroke for split injections with pilot pulses at 680°CA and 0°CA.	231
8.21.	Quantification of natural light (radiation) emission intensity during the period of combustion within CA10-CA90 points region for split injections with pilot pulses at 680°CA and 0°CA.	232
8.22.	Spectra sequences for NVO period with split injection of pilot pulse at 680°CA for PRF40. Spectra sequences demonstrate activities at corresponding crank angles 710-712°CA (A), 0-2°CA (B) and 10-12°CA (C).	234
8.23.	Spectra sequences for NVO period with split injection of pilot pulse at 0°CA for PRF40. Spectra sequences demonstrate activities at corresponding crank angles 0-2°CA (top) and 10-12°CA (bottom).	236

List of Tables

1.1. Gasoline fuel characteristics regulations – past (Category I) and future (Category IV) (Worldwide Fuel Charter 2006).	11
1.2. Diesel fuel characteristics regulations – past (Category I) and future (Category IV) (Worldwide Fuel Charter 2006).	12
3.1. Specification of thermal single cylinder engine.	43
3.2. Specification of optical single cylinder engine.	44
3.3. Properties of several TORLON grades (Solvay Advanced Polymers).	48
3.4. Properties of full spectrum grade synthetic fused silica (Alkor).	52
3.5. Shaft encoders specifications (Baumer).	56
3.6. NI PCI-6602 technical data (NI).	57
3.7. Technical specifications of variable cam timing control system.	60
4.1. Specification of Andor iStar iCCD camera (DH734I – 18 F – 04).	75
4.2. Technical specifications of UV-Nikkor 105 mm f/4.5 lens.	77
4.3. Specification of Phantom v7.1 CMOS color camera.	79
4.4. Technical specifications of Nikon 24-85mm f/2.8-4D IF lens.	80
4.5. Technical data of Oriel MS260i [™] 1/4 m 74050 imaging spectrograph.	81
4.6. Cameras settings of dark frames acquisitions.	85
4.7. Individual and ensemble-average dark frames characteristics of iCCD camera.	87
4.8. Individual and ensemble-average dark frames characteristics of CMOS camera.	87
5.1. Technical specifications of Kistler [®] 6051A and 6041 pressure transducers.	91
5.2. Technical specifications of Druck PMP 1400 pressure transducer.	91
5.3. Technical specifications of NI PCI-6023E interface card.	94

6.1.	Reactions pathway leading to an autoignition process.	125
6.2.	Engine operating conditions for test of engine speed and residual rates influence.	128
6.3.	Engine valve timing events matrix.	129
6.4.	Characteristic of LTHR phases for engine speeds instances of 800 - 1400 rpm.	130
6.5.	Optical engine operating conditions.	142
6.6.	Settings of iCCD Andor iStar monochromatic imager.	144
6.7.	Settings of Oriel MS260i [™] spectrograph and iCCD imager.	144
6.8.	Engine operating conditions for PRF40 and PRF80 tests.	153
6.9.	Engine operating conditions for PRF75.6 and TSF75.6 tests.	153
7.1.	Optical engine operational conditions.	160
7.2.	Settings of Phantom v7.1.	162
7.3.	Statistical descriptors of ensemble images of stoichiometric ($\Phi=1$) conditions.	166
7.4.	Statistical descriptors of ensemble images of lean ($\Phi\approx 0.83$) conditions.	173
8.1.	Engine operational conditions.	192
8.2.	Statistical descriptors of ensemble images of split injection 680 and 140°CA combustion.	221
8.3.	Statistical descriptors of ensemble images of split injection 0 and 140°CA combustion.	222
8.4.	Statistical descriptors of ensemble images of split injection 40 and 140°CA combustion.	222
8.5.	Statistical descriptors of ensemble images of single injection 140°CA combustion.	223

Nomenclature

Abbreviations

ARC	Active Radical Combustion
ATAC	Active Thermo-Atmospheric Combustion
BDC	Bottom Dead Centre
BMEP	Brake Mean Effective Pressure
CA	Crank Angle
CAI	Controlled Autoignition
CA5	5% Heat Release (Cumulative) Burned Point
CA10	10% Heat Release (Cumulative) Burned Point
CA50	50% Heat Release (Cumulative) Burned Point
CA90	90% Heat Release (Cumulative) Burned Point
CCD	Charge Couple Device
CFPP	Cold Filter Plugging Point
CFR	Cooperative Fuel Research
CHASE	Controlled Homogeneous Autoignition Supercharged Engine
CHARGE	Control Homogenous Autoignition Reformed Gas Engine
CI	Compression Ignition
CMOS	Complementary Metal-Oxide Semiconductor
CMY	Cyan Magenta Yellow
CMYK	Cyan Magenta Black
CO	Carbon Monoxide
COV	Coefficient of Variation
CPS	Combustion Stoichiometric Products
CR	Compression Ratio
CVCTS	Continuous Variable Cam Timing System
DAQ	Data Acquisition
DDG	Digital Delay Generator
DI	Direct Injection
DOHC	Double Overhead Camshafts
EBCCD	Electron Bombardment Charge Couple Device
EMCCD	Electron Multiplying Charge Couple Device
EPS	Exhaust Phasing System
ETCS	Engine Timing Control System
EVC	Exhaust Valve Closing
EP	End Point Temperature
E70	Percentage Evaporated at 70°C
E100	Percentage Evaporated at 100°C
FPN	Fix Pattern Noise
GDI	Gasoline Direct Injection
HC	Hydrocarbons
HCCI	Homogenous Charge Compression Ignition
HiMICS	Homogenous Charge Intelligent Multiple Injection Combustion
HHV	Higher Heating Value
HRR	Heat Release Rate
HSDAQ	High Speed Data Acquisition
HSV	Hue Saturation Value
iCCD	Intensified Charge Couple Device

iEGR	Internal Exhaust Gas Recirculation
IF	Internal Focusing
IMEP	Indicated Mean Effective Pressure
IPS	Intake Phasing System
IPW	Injection Pulse Width
IR	Infrared
ITHR	Intermediate Temperature Heat Release
IVO	Intake Valve Opening
LHV	Lower Heating Value
LPDC	Lean Premixed Diesel Combustion
LSDAQ	Low Speed Data Acquisition
LTHR	Low Temperature Heat Release
MCP	Micro Channel Plate
MFB	Mass Fraction Burnt
MON	Motor Octane Number
NI	National Instruments
NIR	Near Infrared
NO _x	Nitrogen Oxides
NTC	Negative Temperature Coefficient
NVO	Negative Valve Overlap
PAI	Polyamid-imide
PCCI	Premixed Charge Compression Ignition
PFI	Port Fuel Injected
PID	Proportional Integral Derivative
PIV	Particle Image Velocimetry
PLIF	Planar Laser induced Fluorescence
PM	Particulate Matters
QE	Quantum Efficiency
PM	Particulate Matter
PPR	Pulses per Revolution
PRF40	Primary Reference Fuel 40
PRF80	Primary Reference Fuel 80
PRF 75	Primary Reference Fuel 75
PRF75.6	Primary Reference Fuel 75.6
PWM	Pulse Width Modulation
R&D	Research and Development
RN	Random Noise
ROI	Region of Interest
RON	Research Octane Number
SCCI	Stratified Charge Compression Ignition
SI	Spark Ignition
SNR	Signal to Noise Ratio
std	Standard Deviation
TDC	Top Dead Centre
TS	Toyota-Soken (Combustion Type)
TSF75.6	Toluene Standardization Fuel 75.6
T10	Recovery Temperature at 10% Evaporated
T50	Recovery Temperature at 50% Evaporated
T90	Recovery Temperature at 90% Evaporated
UEGO	Universal Exhaust Gas Oxygen
ULG 95	Unleaded Gasoline of RON 95
UNIBUS	Uniform Bulky Combustion System
UV	Ultraviolet
VCR	Variable Compression Ratio
VCT	Variable Cam Timing

VCTCS	Variable Cam Timing Control System
VIS	Visible Light
VTEC	Variable Valve Timing and Lift Electronic Control
VVEL	Variable Valve Event and Lift

Symbols

c_p	Heat Capacity at Constant Pressure
c_v	Heat Capacity at Constant Volume
i	Intensity Level
K	Kurtosis
L	Possible Number of Intensities Levels
p_i	Pressure at Given Crank Angle
Δp	Pressure Rise
Δp_c	Pressure Rise Due to Combustion
Δp_v	Pressure Rise Due to Volume Changes
M	Mode
M_3	Third Statistical Central Moment
M_4	Fourth Statistical Central Moment
n	Polytropic Index
n	Number of Measurements
n	Total Number of Pixels in an Analysed Image
n_i	Number of Pixels Having the Same Intensity
$P.O.O_{max}$	The Greatest Occurrence Probability Magnitude
R	Range
R	Gas Constant
S	Skewness
T	Temperature
V_C	Cylinder Clearance Volume
u	Internal Energy
V_i	Volume at Given Crank Angle
V_{i+1}	Volume at Subsequent Crank Angle
V_S	Cylinder Swept Volume
W	Work
x_i	Single Measurement
\bar{x}	Average Measurement
μ_T	Mean
γ	Gamma – specific heats ratio (c_p/c_v)
σ	Standard Deviation
σ^2	Variance

List of Publications and Conferences Attended

Publications:

- 1) P.Luszcz, H.Xu, M.Wyszynski, A.Tsolakis, M.Frackowiak, T.Wilson, J.Qiao. **An Investigation of the Presence of Uncontrolled Combustion Phenomenon in Spark Ignition Single Cylinder Engine.** Journal of KONES Powertrain and Transport, Vol.13, No.2, 2006.
- 2) A.F.M.Mahrous, A.Potrzebowski, M.Wyszynski, H.Xu, A.Tsolakis, P.Luszcz. **A 1D Analysis into the Effect of Variable Valve Timing on HCCI Engine Parameters.** SAE Technical Paper 2008-01-2459, 2008.
- 3) A.M.F.Mahrous, A.Potrzebowski, M.Wyszynski, H.Xu, A.Tsolakis, and P.Luszcz, **Modeling Study into the Effects of Variable Valve Timing on the Gas Exchange Process and Performance of a 4-Valve DI Homogeneous Charge Compression Ignition (HCCI) Engine.** Energy Conversion and Management 50 (2009), p. 393-398.
- 4) P.Luszcz, H.Xu, M.Wyszynski, A.Tsolakis, R.Stevens, J.Qiao. **Image Processing Techniques for HCCI Autoignition and Combustion Analysis Using Matlab® and An Insight into Port Fuel Injected HCCI Autoignition and Combustion Process based on High-Speed Imaging.** Submitted to Combustion and Flame, Jun 2009, (Ref. CNF-D-09-00176).
- 5) P.Luszcz, H.Xu, M.Wyszynski, A.Tsolakis, R.Stevens. **An Influence of Direct Injection Strategy and Timing on Recompression Stroke, Autoignition and Combustion Activities in NVO Operated HCCI Optical Engine.** Submitted to Combustion and Flame, September 2009, (Ref. CNF-D-09-00312).

Contribution to Conferences:

- 1) **32nd International Scientific Congress on Powertrain and Transport Means, European KONES 10-13 September 2006, Naleczow, Poland.** *Presentation Title:* An Investigation of the Presence of Uncontrolled Combustion Phenomenon in Spark Ignition Single Cylinder Engine.
- 2) **XX International Symposium on Combustion Processes, 2-5 September, 2007, Pultusk, Poland.** *Presentation Title:* A characterization of a single and a double stage auto ignition process in Homogenous Charge Compression Ignition (HCCI) engine, in XX International Combustion Symposium, Combustion Institute.
- 3) **II International Congress on Combustion Engines, 7-9 May, 2007, Krakow, Poland.** *Poster Title:* Relevance of Research and Motor Octane Number on Controlling Autoignition Process in HCCI Operated Engine.

Chapter 1

Introduction

The implementations of gradually stringent tail pipe emissions requirements in conjunction with worldwide demands for fuel consumption reductions has forced engine manufacturers either to advance current types of internal combustion engines or develop new propulsion technology. One such instance is a Homogenous Charge Compression Ignition (HCCI) engine concept which combines aspects of the conventional Diesel and Gasoline engines. As this technology claims potential benefits with regards to emissions, lowering especially nitrogen oxides (NO_x) and particulate matter (PM), and fuel consumption reductions this combustion system has recently become of great interest to the worldwide engine research and development community – both academic and industrial.

1.1 Overview

This chapter is dedicated to introducing the concept of Homogenous Charge Compression Ignition by presenting an overview of the developmental history as well as the key parameters and strategies in HCCI operation such as dilution, valve timing, compression ratios, injection strategies and the suitability of potential fuels. As these parameters have a great influence on engine operation and in fact implement restrictions to the operational envelope they are addressed in greater depth in relation to the autoignition and combustion characteristics of HCCI mode. The new fuel legislations are also discussed, as a production-scale HCCI engine will have to be fuelled with one of the commercially available fuel blends. Finally, the research objectives and scope of this thesis are presented.

1.2 Concept of Homogenous Charge Compression Ignition

1.2.1 Developmental history

The first successful attempt of Homogenous Charge Compression Ignition engine operation was reported in open literature in 1979 by Onishi *et al* (1979). This discovery came from two-stroke engine combustion studies. Over the past thirty years of HCCI development, this combustion process was assigned various names in the open literature. These different names most likely derive or are related to corresponding investigated or observed process characteristics. Originally this process was termed as Active Thermo-Atmospheric Combustion (ATAC) (Onishi *et al* 1979), then probably owing to R&D facility name, where the development was conducted it was named as a Toyota-Soken Combustion (TS) (Noguchi *et al* 1979) and finally as Active Radical Combustion (ARC) (Ishibashi *et al* 1996). These aforementioned names are related to two-stroke engine combustion investigations. The latest worldwide four-stroke engine combustion R&D activities using HCCI produced other names such as Premixed Charge Compression Ignition (PCCI), Lean Premixed Diesel Combustion (LPDC), Uniform Bulky Combustion System (UNIBUS), Homogenous Charge Intelligent Multiple Injection Combustion (HiMICS), Controlled Auto-Ignition (CAI) or alternatively Stratified Charge Compression Ignition (SCCI).

The Homogenous Charge Compression Ignition mode is a process in which combustion is accomplished throughout charge auto-ignition. In accordance with HCCI technological assumptions the charge (air-fuel mixture) should be premixed (homogenous) or nearly premixed and the whole charge which traverses identical in-cylinder pressure-temperature history regardless of unavoidable temperature inhomogeneities should autoignite concurrently at multiple points in the cylinder volume once temperature conditions are favoured. As it stands there is no direct combustion timing control and the process (combustion onset) is purely chemically kinetically controlled.

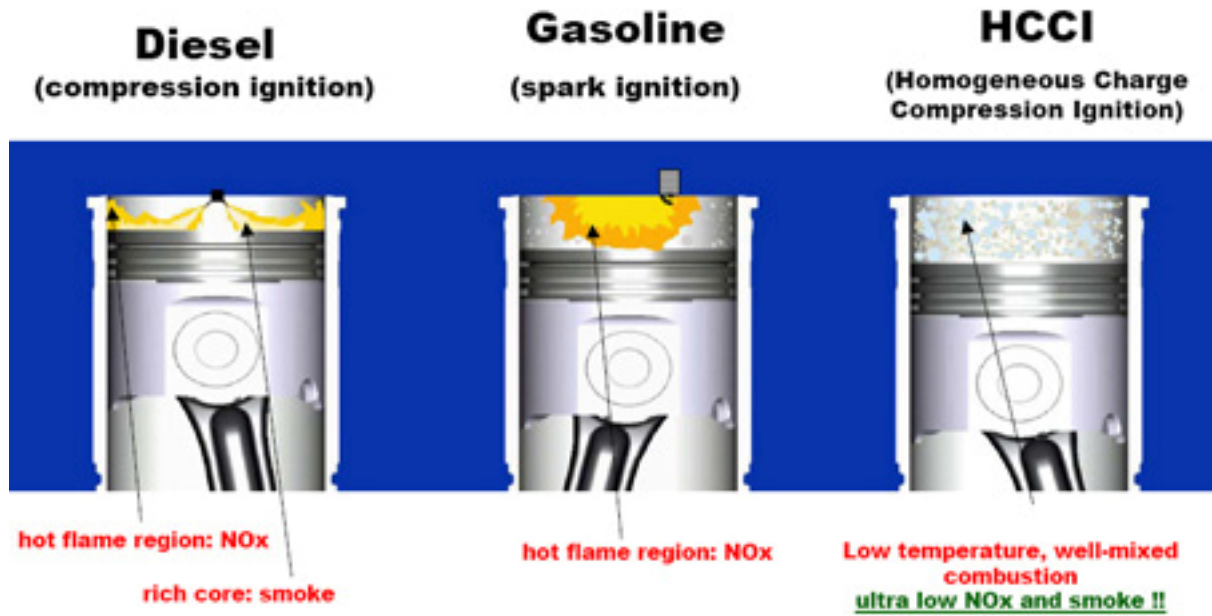


Figure 1.1. Illustrative form of classical CI and SI engines' combustions versus HCCI combustion. (NAFTC, www.naftc.wvu.edu).

This novel engine combustion mode attracted the worldwide engine research and development community (both academic and industrial) because of the potential benefits it offers; there are significant reductions in fuel consumption and emission, more specifically emissions of nitrogen oxides (NO_x) and particulate matters (PM). The promising low NO_x emissions are essentially owing to lower combustion temperatures. Unfortunately these low combustion temperatures consequently contribute to elevated carbon monoxide (CO) and hydrocarbons (HC) emissions, which constitutes one of the crucial drawbacks of HCCI. The other key shortcomings associated with HCCI operation are restricted operational envelope and a lack of direct means for controlling combustion timing as mentioned above.

Although nearly a thirty year period of HCCI research and development activities has passed overlapping with the advent of advanced electronics and their application to engine, there are unresolved issues in HCCI operation like those stated above. In fact these shortcomings prevent the application of HCCI engines, particularly to automobiles. The production scale (scenario) of Homogenous Charge Compression Ignition engines is also uncertain.

1.2.2 Characteristic of the HCCI concept

Dilution strategies

In order to provide successful operation of HCCI the foremost issue is to supply sufficient energy for an autoignition to occur on the one hand and to limit the heat release rates once they become excessive on the other. In particular this first becomes more relevant for low compression ratio engines or light load conditions but especially if there is a combination of both. The second is related more to higher compression ratio engines or higher loads or finally as a consequence of the two. So far two dilution strategies have been proposed. Firstly trapping a significant amount of residuals is commonly used, especially for low compression ratio engines with ones equivalent to spark ignited engines. The trapping of residuals is realized with early exhaust valve closing (EVC) and late intake valve opening (IVO); a negative valve overlap (NVO) strategy. The method is also frequently referred to as internal exhaust gas recirculation (iEGR). A second dilution strategy is based on the lean air-fuel mixture creation and mostly is applicable in HCCI engines of higher compression ratios corresponding to diesel ones. This is primarily utilized to avoid excessive pressure rise rates. Also trapped or recirculated exhaust gases, besides their relevance to autoignition promotion, serve as a means of decelerating reactions rates, especially important at high load conditions. The open literature has shown successful HCCI operation with any of both aforementioned dilution strategies (Aroonsrisopon *et al* 2002; Koopmans *et al* 2004; Wilson *et al* 2005 and Shibata *et al* 2007); however the iEGR seems to be more practical for implementation into commercial applications.

The dilution strategy considerably determines the characteristics of the HCCI autoignition and combustion process. Shibata *et al* (2007) undertook research to correlate the low temperature heat release (LTHR) with fuel autoignition propensities as a potential HCCI index development. This study yielded promising results. This was achieved with high

compression ratio engine and positive valve overlap strategy. Then the suppressive effect of artificial and external exhaust gases on LTHR activities was presented by Sjoberg *et al* (2007). The evidence of one- to two-step ignition process transition as an effect of recirculating more EGR has been demonstrated in their study. They also determined the potential suppressive effect of each individual component of stoichiometric combustion products (CPS) in a quantitative and qualitative way. The brief example given above outlines the significance of selecting a particular dilution strategy and its impact on overall HCCI combustion philosophy.

Valve timing strategies

The recent advent of advanced electronics and their application to internal combustion engines enabled optimization of engine operation, that were not feasible before. One such example is the implementation of variable opening/closing timings of valves and the management of their lifts. This system also plays a significant role in research and development of HCCI engines. By adjusting appropriate valve positions and/or lifts to actual engine operating conditions, successful HCCI operation with its greatest benefits could be accomplished.

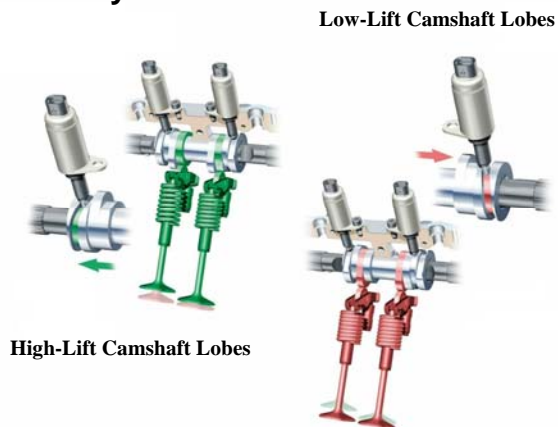
Generally the valve control system could be realized as continuous variable valve timing but without lift control, a continuous variable camshafts phasing positions with two different valve lifts (camshafts lobes – high lift and low lift), or as continuous variable valve timing and lift control. The last in fact constitutes the best option from an engine operation optimization standpoint.

The first *automated* camshaft system was introduced by Honda in its DOHC engine in 1990 and was named VTEC (Variable Valve Timing and Lift Electronic Control). Even though Honda is recognized as an originator in the automotive field for these kinds of systems other companies rapidly started advancing this idea with their own technical solutions proposed. Audi developed an indefinitely (within shifting range) variable valve phasing system with two

different valve lifts control. In 2000 BMW put into its engines a Valvetronic system, which manages continuous control of valves timing and their lifts, varying from 0 to 9.7 mm. Other automotive makers offer similar systems under various commercial names for instance VVEL, Valvematic or VCT of Nissan, Toyota and Ford (Jaguar) respectively.

There are instances in open literature showing HCCI research conducted with a fixed valve timing events (Richter *et al* 1999), with variable operation of valve opening and closing positions and lift control (Zhao *et al* 2002) and investigations conducted with electromagnetic valve train allowing flexible control of valves opening, closing, lift and as importantly opening duration (Koopmans *et al* 2001). The HCCI operation and its envelop are highly dictated by an allowable valve timing control because this defines the engine effective compression ratio value. It has been well documented over the last few years of HCCI research that flexible valves control could significantly expand the operational window as compared to a fixed valve timing strategy.

Audi's System



BMW's System

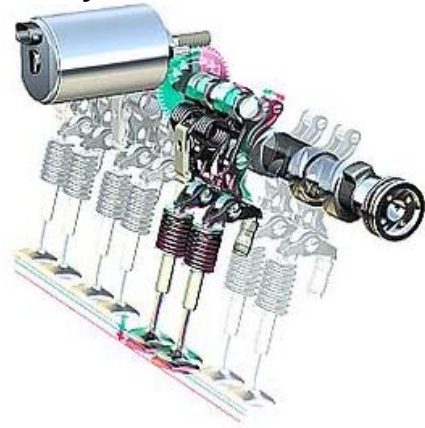


Figure 1.2. Different arrangements of valve lift control; Audi's two-stage valve lifts control (www.audi.com) and BMW's Valvetronic – continuous valve lift management (www.bmw.com).

Compression ratio

The selection of a compression ratio for an HCCI engine is neither an obvious issue or a straightforward task. Nowadays there is evidence showing successful Homogenous Charge Compression Ignition engine operation with a high compression ratio (diesel like) (Dec *et al* 2003) on the one hand and with low compression ratio values (gasoline like) (Koopmans *et al* 2004) on the other hand. The appropriate choice of CR is highly dependent on the dilution strategy and utilized fuel reactivities among other parameters such as engine operating variables. Indeed the compression ratio belongs to a group of parameters determining the boundaries of operational window. With an increasing compression ratio the lower boundary (low loads conditions) is extended, however, simultaneously it shifts down the upper border of the operation once the same fuel is used. Also it was reported that CR has a crucial effect on governing the combustion process type (single step or two step ignition) as the LTHR activities of two step ignition process are highly in-cylinder pressure-temperature dependent (Christensen *et al* 1998).

For HCCI engine operation the ideal scenario would be the implementation of a Variable Compression Ratio (VCR) engine enabling continuous shifting of CR values while matching actual engine operating conditions and requirements. Such an attempt was made by Hyvonen *et al* (2005). They demonstrated HCCI operation under various geometrical compression ratio magnitudes using a Saab VCR engine concept. As a result of geometric CR value alterations this study showed further potential ways to expand the operating window.

Engine Boosting

Engine boosting for HCCI operation stands as another way of controlling the combustion process and as an alternative way for an operational envelope expansion. Nevertheless the

boosting application is limited to some extent because of the pressure increases - air mass drawn for engine cycles and thus higher combustion cylinder pressure values are expected when the engine is running under a fixed air-fuel equivalence ratio. Engine air-boosting has been demonstrated in open literature as a key parameter (among others) governing and affecting the HCCI combustion process (combustions process type). Christensen *et al* (Christensen *et al* 1998) observed LTHR activities with the intake boosted, while with the same fuel (potentially single-step ignition fuel) the cool flame activities were not observed under unboosted conditions. Hence the combustion process type transition was identified as a consequence of engine boosting application. Furthermore their study has shown the dependency of LTHR magnitude exhibited with intake boost pressure value. It also emphasizes the importance of operational envelope expansion at boosted conditions.

Fuel injection strategies

Principally the homogenous or nearly homogenous air-fuel mixture is accomplished by injecting fuel into the engine intake manifold using a conventional port fuel injection (PFI) system. Until now successful HCCI operation by inserting fuel into intake manifold (Sjoberg *et al* 2003) or in close vicinity to the intake valves (Luszcz *et al* 2009) has been demonstrated by many researchers. Although this type of fuel injection provides good air-fuel mixing process, it does not provide a means of combustion phasing control. This is the direct fuel injection (DI) system injecting fuel into the engine cylinder, which enables benefiting of combustion onset management. Dec *et al* (2004) has shown that efficient control of combustion onset could be gained with different injection timings. Besides different fuel distribution, injection timing changes the residence time of the mixture, either by shortening or prolonging the time which favours or disfavours the reactions to occur according to the requirements. Even more significantly combustion phasing control may be gained when some of fuel is injected into NVO, indeed for those engines operated with NVO strategies

(Koopmans *et al* 2003). Because as the injection in recompression stroke under the lean operating conditions promotes pre-reactions, this is essentially the matter of two parameters; how much fuel is injected and in what crank angle degree it is injected in NVO to obtain demanded effect (combustion phasing).

Potential fuels

As the Homogeneous Charge Compression Ignition combustion is achieved via autoignition the process is chemically kinetically controlled and the combustion initiation point is highly conditioned by fuel reactivity (chemical kinetics) one the other hand and actual operating conditions – in-cylinder temperature, pressure, fuel-air ratio etc. on the other. The HCCI operation is quite fuel flexible, which is also emphasised by the flexible choices of dilution and valve timing event strategies or compression ratios for example. A lot of investigations have been conducted in order to define the relevant fuel autoignition characteristics, and to provide new indexing for HCCI operation (Kalghatgi *et al* 2003,2004; Koopmans *et al* 2004; Risberg *et al* 2003,2004,2005; Bradley *et al* 2004 or Shibata *et al* 2004,2005,2006,2007). Obviously these aforementioned attempts reported were carried out under different operating conditions with range of various fuels either those commercially available or those available only in laboratories, spanning from a single component via binary mixtures to multi-component blends of various reactivities. This was extensively researched with conventional (pressure-transducer based) measurements as stated above literature instances as well as with the application of optical diagnostics e.g. Hildingsson *et al* 2004 or Hwang *et al* 2008. Also frequently to gain a supplementary understanding of an observed experimental trend, the modeling part conducted was employed (Naik *et al* 2005, Hwang *et al* 2008 or Sjoberg *et al* 2007).

The main thought obtained from the above brief literature overview is that fuels for HCCI like autoignition and combustion operation can be broadly classified as one- or two-step ignition fuels. Their characteristics are highly dependent upon the fuel composition, not only

the two-step (LTHR activities) ignition process contributors (e.g. n-paraffinic hydrocarbons) but also other constituents when the fuel blend is a multi-components fuel. As importantly there is an indication that instantaneous operating conditions contribute significantly to autoignition and combustion characteristics.

This is because the Homogenous Charge Compression Ignition operation is still fuel flexible, successful operation has been achieved with gasoline as well as diesel-like blends, therefore it is profitable to review the past and future fuel characteristics legislations. Firstly these regulations determine fuel characteristics such as blend composition with the permissible content of each common hydrocarbon family or even specified chemical component(s) levels. Secondly as this is the case the fuels legislations influence the directions taken in propulsion technologies advancements. Finally once the HCCI engine reaches production scale it will have to run with one of the commercial fuels, or with a new fuel of the specification that has been restricted by fuels legislation. Also the quick review of the future fuels legislations serves as a good reference of outcomes of fuel investigations conducted in this thesis to the realistic scenario blend with a specified composition.

Fuel technology develops in collaboration with engine development to provide the greatest benefits from engine performance and emission. Besides the major gasoline characteristic restrictions phasing out lead alkyl and manganese as additives of octane enhancers several years ago, nowadays the overall trend for both types of fuels, gasoline and diesel, was to enhance volatility characteristics (having a crucial effect on engine emission and performance) by lowering allowable final boiling points. A drastic reduction of permissible sulphur content (gasoline from 1000 mg/kg to 10 mg/kg and diesel from 2000 mg/kg to 10 mg/kg) is noticeable as seen in Table 1.1. As importantly the permitted aromatics content has been reduced for gasoline, and specified for diesel blends. Other features are increased reactivities (autoignition propensities) of diesel fuel for instance.

Properties		Gasoline Fuel	
		Category I	Category IV
91 RON	RON (Min)	91	91
	MON (Min)	82	82.5
95 RON	RON (Min)	95	95
	MON (Min)	85	85
98 RON	RON (Min)	98	98
	MON (Min)	88	88
Oxidation stability		360 minutes	480 minutes
Sulphur Content (Max)		1000 mg/kg	10 mg/kg
Oxygen Content ¹ (Max)		2.7 % m/m	2.7 % m/m
Olefins Content (Max)		not determined	10 % v/v
Aromatics Content (Max)		50 % v/v	35 % v/v
Benzene Content (Max)		5 % v/v	1 % v/v
Vapor Pressure		55 – 70 kPa	55 – 70 kPa
T10 (Max)		70°C	60°C
T50 (Max)		77 - 110°C	77 - 100°C
T90 (Max)		130 - 190°C	130 – 175°C
EP (Max)		215°C	195°C
E70		15 – 45 %	20 – 45 %
E100		50 – 65 %	50 – 65 %

The volatility characteristic is specified for “B Class” Gasoline (expected ambient temperature in the range of 5 - 15°C).

Table 1.1. Gasoline fuel characteristics regulations - past (Category I) and future (CategoryIV) (Worldwide Fuel Charter 2006).

For the autoignition and combustion process of the HCCI operation the most important fuel characteristics seem to be the fuel reactivities (RON, MON, Cetane Number (Cetane Index)), volatility characteristics and fuel compositions. Because the production scale engine in HCCI mode will most likely be combined with SI (gasoline engine) or CI (diesel engine) operations to cover the required driving cycle envelope, the blend that meets the HCCI requirements would have to fulfill the criteria for the whole engine operating window. In case of commercial gasoline this would mean that it has to readily auto-ignite under homogenous charge compression ignition mode, whereas during spark ignition mode at higher loads it would have to possess good antiknock quality. As mentioned above the operation of HCCI

¹ For oxygenates used, ethers are preferred. Existing regulations permits using up to 10% by volume ethanol (meeting ASTM D 4806), however the blended fuel must meet all other Category I or IV requirements. Higher (C>2) alcohols are limited to 0.1% maximum by volume. Methanol is not permitted.

will have to be realized with standardized fuels in accordance with aforementioned legislations unless others are introduced.

Properties	Diesel Fuel	
	Category I	Category IV
Cetane Number (Min)	48	55
Cetane Index ²	48 (45)	55 (52)
Density @ 15°C	820 kg/m ³	820 kg/m ³
Viscosity @ 40°C	2.0 mm ² /s	2.0 mm ² /s
Sulphur Content (Max)	2000 mg/kg	10 mg/kg
Ash Content (Max)	0.01 % m/m	0.001 % m/m
Carbon Residue	0.3 % m/m	0.2 % m/m
Water Content	500 mg/kg	200 mg/kg
Total Aromatics Content	not determined	15 % m/m
Flash Point (Min)	55°C	55°C
CFPP	Maximum must be equal to or lower than the lowest expected ambient temperature	
T90 (Max)	370°C	320°C
T95 (Max)	not determined	340°C
Final Boiling Point	not determined	350°C

Table 1.2. Diesel fuel characteristics regulations - past (Category I) and future (Category IV)
(Worldwide Fuel Charter 2006).

Operational envelope

Currently, the key focus of HCCI research and development activities is mostly dedicated to determining the best investigational directions and to undertake attempts for further operational window expansion. Today's Homogenous Charge Compression ignition engine operational envelope is significantly *narrow* in comparison to current SI or CI engines operational windows (Figure 1.3. Qiao *et al* 2005).

² Cetane Index is acceptable instead of Cetane Number if a standardized engine to determine the Cetane Number is unavailable and cetane improvers are not used. When cetane improvers are used, the estimated Cetane Number must be greater than or equal to the specified value and the Cetane Index must be greater than or equal to the number in parentheses.

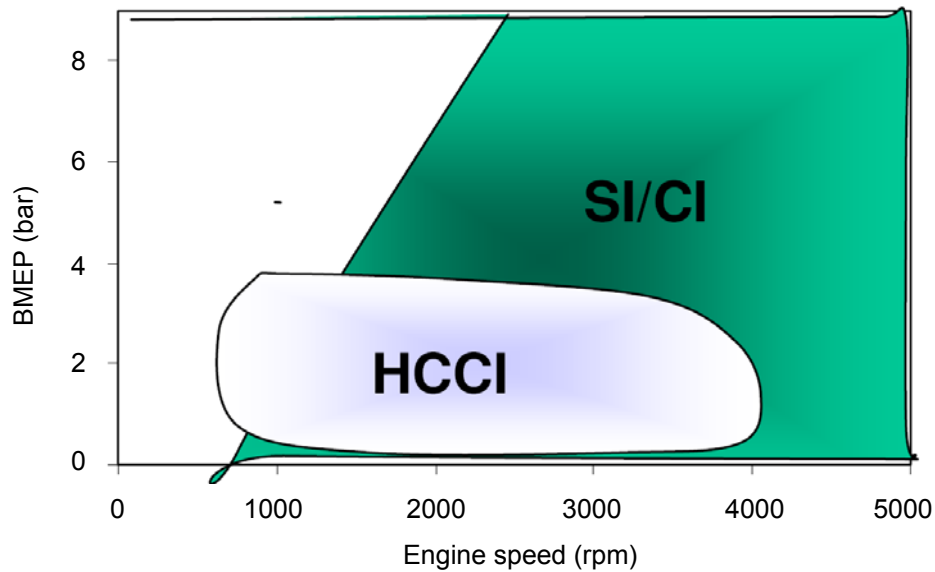


Figure 1.3. Today's representative Homogeneous Charge Compression Ignition engine operational envelope (Qiao *et al* 2005).

Consequently the Homogenous Charge Compression Ignition operation does not cover all the requirements of the speed/load operating points of the European driving cycle (Figure 1.4. Koopmans *et al* 2007).

The exhaustive experimental study (analysis) conducted by Zhao (Zhao *et al* 2002) indicated a narrower (as compared to SI operation) operational window for HCCI (CAI) restricted to 1000-4000 rpm of engine speeds and 0.5-4.0 bar of BMEP (loads) regimes. This was performed for two identical vehicles powered with different engines, one with SI and another with SI/HCCI under European driving cycle schemes (conditions).

Essentially the Homogenous Charge Compression Ignition operation is restricted due to a combination of both shortcomings associated respectively to each envelope 'end' – hardships in operation at higher loads (elevated heat release rates or even knocking phenomena causing higher noise levels or engine damage) and poor autoignition promotion accompanied by high CO and HC emissions and cycle-to-cycle instabilities at light loads operation. Indeed the HCCI operational window size (operating regime covered) is highly dependent on engine operating variables such as dilution, fuelling strategies, intake air temperature or boosting (if applied) and engine geometrical features: the geometrical

compression ratio or valve timing system type (allowing an effective compression ratio to be altered).

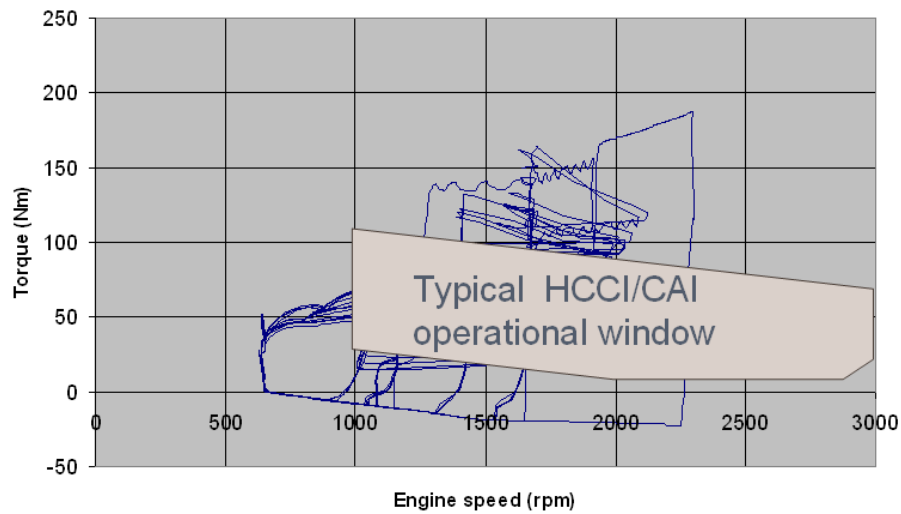


Figure 1.4. Today's European driving cycle and Homogeneous Charge Compression Ignition engine operational envelope (Koopmans *et al* 2007).

Finally, other than to the aforementioned engine features the operational window is very much related to a given fuel type. Moreover often expanding one boundary has an inverse (opposite) effect on the other end of envelope. For instance using low octane number fuels (in contrast to high octane number blends) shifts down the lower boundary, however the upper boundary goes down at the same time.

1.3 Diagnostic techniques for combustion study

The applicability of widespread optical diagnostics techniques in the field of engine research could provide substantial and detailed insight into the characteristics of flow, auto-ignition and combustion processes. Generally this could be gained by aspects of process visualization or chemical species identification with further application of appropriate processing methods e.g. image processing (Heywood 1988 and Zhao *et al* 2001).

The optical measurement techniques utilized in the area of engine research could be broadly classified as passive optical methods such as imaging, emission or chemiluminescence spectroscopy and active optical techniques such as fluorescence or absorption spectroscopy, planar laser induced fluorescence (PLIF) or particle image velocimetry (PIV). Although there are hardships or even limitations for how some optical techniques can be used caused either by engine operating conditions or engine (optical apparatus) specifications or as a combination of both, the advantages of optical diagnostics applications outweigh the shortcomings. This is because of the valuableness of the optical measurements these optical technique were applied in HCCI research field to investigate the flow pattern, autoignition and combustion characteristics as reported in recent open literature studies (Hultqvist *et al* 1999,2002; Wilson *et al* 2005; Persson *et al* 2005,2006; Aleiferis *et al* 20067 or Hwang *et al* 2008).

1.3.1 Passive measurement techniques

A variety of natural light emission (chemiluminescence and thermal radiation) studies were performed for autoignition and combustion analysis throughout this thesis. Passive diagnostics techniques including natural light emission imaging and spectroscopy have been extensively explored for HCCI autoignition and combustion research.

Imaging

The autoignition and combustion process were imaged utilizing two different camera systems – intensified monochromatic CCD (iCDD) and color CMOS. The slow speed monochromatic iCCD camera enabled insight into direct light intensity and light emitted quantification of autoignition, combustion and NVO period activities. Furthermore the obtained characteristics were correlated with pressure based information. The high-speed

color CMOS camera provided detailed information about the autoignition formation and combustion process proceeding of a single cycle and information about cycle-to-cycle variations as a consequence of a few cycles acquired. As importantly, the data from color CMOS camera delivered additional valuable insight into the nature of autoignition and combustion by observing colors with correlation to camera's three channels (RGB color) spectral responsivities curves. It is noteworthy that both the aforementioned camera systems feature spectral responsivities having different wavelength regions of electromagnetic radiation. Further the application of the relevant image processing techniques to the obtained images permitted autoignition and combustion information to be extracted in a qualitative and quantitative ways. These are determinations of autoignition occurrence and combustion proceeding the likelihood of repeatability, the combustion growth rate and the reacting structures spreading velocities.

Spectroscopy

Spectroscopic measurements are methods analysing the electromagnetic radiations emitted, absorbed or fluoresced by molecules or atoms. Principally spectroscopy investigates the emitted or absorbed energy of electromagnetic radiation as the analyte transits from its excited state to ground state or vice versa respectively. The spectroscopic techniques are widely used in analytical chemistry (Skoog *et al* 2004).

Because spectroscopy provides a means of chemical species identifications then its application within the studies covered in this thesis allows an insight to be made into the chemical site of HCCI operation. More specifically an analysis of a major species of autoignition/combustion during negative valve overlap stages could be carried out in qualitative and quantitative (with some limitations) ways. For the spectroscopic measurement the spectrograph coupled with iCCD camera were used. As a result of the identical spectral range acceptance of spectrograph and iCCD imager autoignition/combustion activities pictures obtained from iCCD the observations could be directly correlated. The spectroscopic

measurements conducted were related to emission spectroscopy (heat is a stimulus) and chemiluminescence spectroscopy (analyte excitation by chemical reactions).

1.4 Research objectives, scope and outline

The research work demonstrated in this thesis is a part of CHASE (Controlled Homogeneous Autoignition Supercharged Engine) project at Birmingham University and constitutes a continuation of a research interest in understanding of HCCI operation, which originated during the CHARGE (Controlled Homogenous Autoignition Reformed Gas Supercharged Engine) project also here at University of Birmingham. The key objective of the range of experiments conducted within this thesis scheme was an insightful physico-chemical identification of the nature of Homogenous Charge Compression Ignition autoignition and combustion under various engine operating conditions with different sorts of blends.

The comprehensive studies were carried out utilising nearly identical (matching) thermal and optical Jaguar single cylinder research engines. The configuration of these two experimental single cylinder engines and their facilities are similar (nearly identical), but not the same. A detailed description of these research apparatus is given in section 3.1 of chapter 3. The thermal engine was used to perform general insight into HCCI operation and trends based on conventional engine in-cylinder pressure based measurements. The abilities of the optical engine to allow more insightful measurements to be taken permitted a valuable insight into a frequently predetermined trend and permitted conditions to be gained through imaging process or analysing it from chemical site (spectroscopy).

The main objectives of the experimental work conducted within the scheme of this thesis were:

- a) Investigating the influence of the engine operating conditions such as engine speed and trapped residuals on HCCI operation (ignition process type), more specifically the cool flame activities of a two-step ignition process;
- b) Investigating the effect of fuel type on HCCI operation (ignition process type) and the relevance or meaning of current gasoline-like fuels' antiknock designations (octane numbers) on HCCI operation;
- c) Gaining insight into the physicochemical natures of the one- and two-step ignition process;
- d) Development of relevant image processing techniques, that allow the performance of an appropriate HCCI autoignition-combustion process analysis;
- e) Studies of premixed HCCI operation, more specifically investigating the behaviour of autoignition-combustion of a one-step ignition process using an optical technique;
- f) Studies of the HCCI operation with various direct injection strategies and timings and investigating the effect of injection strategy and timing on HCCI operation, using optical studies.

Therefore the **key research scope** of this thesis can be broken down into several of the following individual investigations:

1) Using a blend of Primary Reference Fuels (PRF40), an insight into the nature of autoignition-combustion was gained during various engine speeds and under internal exhaust gas recirculation rates conditions. This investigation served as a base of an understanding into one- and two-step ignition processes by demonstrating effects of the operating conditions investigated on magnitudes of heat release during cool flame activities (LTHR). With the same fuel and the same operating conditions i.e. speed and two chosen valve timing events the identical experiments were repeated with the optical engine. This was done with the application of imaging and spectroscopy techniques; the chemical

characteristics of particular autoignition/combustion stages under different conditions were determined.

2) A few binary fuel blends including PRF40, PRF80, PRF75.6 and TSF75.6 of various reactivities and compositions have been used to examine the meaning of octane numbers and fuel sensitivity in the HCCI operated engine. This brief analysis was only performed on a thermal engine. Various operating conditions were tested to gain a comprehensive approach.

3) The port fuel injected HCCI stoichiometric and lean operations at low load of operational envelope of a realistic (real-world) engine scenario were optically investigated. This analysis of autoignition and combustion processes was conducted to evaluate autoignition occurrence and combustion proceeding the likelihood of repeatability, combustion growth rate and reacting structures spreading velocities. Indeed this was based on single engine cycle images obtained and appropriate image processing techniques applied. This provided detailed insight into autoignition and combustion activities of a single cycle with identifiable cycle-to-cycle variations.

4) Direct injection HCCI operations were investigated. This includes the single injection and split injections strategies. This was investigated in optical engine applying color high-speed imaging CMOS camera, iCCD camera and spectroscopy. The single injection was realized in induction stroke, and the split injections scheme included fuel injected prior to and during the NVO region (recompression stroke) as with different pilot injection timings.

5) Implementations of developed, modified or adopted image processing techniques.

In addition to those above stated main objectives of this thesis the initial work required some engine test rigs commission activities. Essentially they required hardware (engine and

electronics) and software (engine control) building or modifications to be done. The original engine control software had been modified to accommodate a capability of operating with a high resolution shaft encoder that allowed a fast burn analysis to be performed. Furthermore the VCT system controlling code was developed (built) from scratch. Lastly data acquisition (DAQ) systems - low speed and high speed were developed and implemented. The hardware work concentrated around the commission of the engine with electronics in order to provide successful and necessary control for both research engines used for the tests.

Thesis Outline

This thesis is made up of nine chapters, which cover introduction, literature review, and presentation of research engines, their systems and diagnostics instrumentations. These are followed by experimental results including the conventional pressure transducer based and the optical measurements are presented. Finally, the thesis is summarised and conclusions are drawn with suggestions for future work.

Chapter 2: Literature Review

The relevant literature for the scope of this thesis has been reviewed. This fundamentally includes following topics: physiochemical nature of an HCCI process, influence of fuel molecule type and engine operational conditions on HCCI operation and effect of injection strategy and timing. These topics are presented based on this thesis author's own inferred conclusions and relevant issues noticed from given publications presented as well as corresponding publication authors' thoughts and drawn conclusions.

Chapter 3: Experimental System

A description of optical and thermal single-cylinder engines has been provided. This includes the detailed presentation of the unique engine features, especially in the case of the optical engine. Furthermore the engine control systems are described in details.

Chapter 4: Diagnostic Instrumentation

This chapter presents diagnostic equipment utilised to conduct passive optical measurements in this thesis. The CMOS Phantom v7.1 colour camera, Andor iStar iCCD monochromatic imager, Oriel MS260i imaging spectrograph and lenses used are introduced with their relevant specifications described e.g. transmittance characteristics. This is preceded with a presentation of working principles and relevant attributes with regard to the given camera technology.

Chapter 5: Data Acquisition and Processing

Acquisition systems of conventional data and ways of processing them are discussed in the first part of this chapter. The second part of the chapter is devoted to presentation of optical data acquisition and processing. The developed and adopted image processing methods are introduced and this is done with reference to Matlab[®] programming language and general image processing foundations, as comprehensive image analysis was accomplished by using Matlab[®].

Chapter 6: Characteristic of HCCI Autoignition and Combustion Process

The characteristics of the HCCI autoignition and combustion processes are presented in two ways, i.e. theoretical and practical. The practical part illustrates how the process is dependent on fuel type and engine operational parameters. Then passive optical measurements such as imaging and spectroscopy are applied to visualise the one- and two-stage ignition processes and to gain insight into the chemical natures of these processes.

Chapter 7: Autoignition and Combustion Analysis of Port Fuel Injected HCCI

The characters of HCCI autoignition and combustion with stoichiometric and lean fuel-air equivalence ratios for one-step ignition process were determined based on the autoignition-combustion events images. By using the relevant image processing, the assessments of the likelihood of the process repeatability of autoignition occurrence and combustion development were studied. Further the analysis of combustion growth rates and the front spreading velocities of reacting structures are demonstrated.

Chapter 8: Characteristic of HCCI Operation with Direct Injection Strategies

HCCI operation with various injection strategies and timings is contrasted based on optical measurements. The high-speed colour crank-angle resolved imaging, imaging using the intensified CCD monochromatic camera and spectroscopic measurements were carried out. These optical data and images were used to investigate the characteristics of HCCI operation with various injection strategies. Moreover, the image processing techniques were used to derive information, which were of particular interest to the study.

Chapter 9: Conclusions and Future Work

In this chapter conclusions of the experimental work performed within this thesis's scope are drawn. Then suggestions for future work are presented.

Chapter 2

Literature Review

As HCCI engines have recently gained the interest of the worldwide engine research and development community, many research areas concerning this novel combustion system have so far been explored including flow and autoignition/combustion analysis. Consequently a number of valuable and interesting results have been produced from worldwide research and development facilities. The previous chapter addressed the characteristics of the HCCI concept, demonstrating the most relevant features of this technology in conjunction with a necessary brief literature review. Because of this and because of the broad amount of literature concerning different areas of HCCI research available, the main focus of this literature review is on the most important issues researched, which are in alignment with the scope of this thesis.

The discussion covered in this chapter starts with a demonstration of the physicochemical nature of autoignition and combustion in HCCI operations. This covers a review of literature dealing with conventional pressure transducer based measurements as well as optical research. Following this the second section addresses the impact of fuel type and engine operating conditions on the kind of autoignition and combustion process found in HCCI operation. Then the third section is devoted to an introduction of the most relevant instances reported in the open literature, which shows the potential role and relevance of currently used fuel autoignition designators for HCCI autoignition. More specifically the role of octane and cetane numbers are discussed. Also interestingly attempts to develop new indexing which is more appropriate for an HCCI combustion onset determination than the current fuel autoignition quality designators are demonstrated. Subsequently injection

strategies and injection timings as a means of achieving potential HCCI combustion onset control and process optimisation are addressed in section four. Finally, section five is dedicated to reported soot and particulate emissions from an HCCI operation, followed by a summary.

2.1 Physicochemical nature of an HCCI autoignition and combustion

The fact that the autoignition and combustion process of the Homogenous Charge Compression Ignition mode could traverse either a two-step ignition process with low temperature reactions followed by high temperature reactions or a one-step ignition process with high temperature reactions has been reported as early as 1999 by Hultqvist *et al* (1999). In their study the formaldehyde (CH_2O) was identified as an intermediate or product characteristic of cool flame activities, whereas emission of hydroxyl radicals (OH) were a feature of high temperature heat release. The natural light emission crank-angle resolved single cycle image sequence of HCCI autoignition-combustion was conducted in their study for the first time, to the author's knowledge. They performed imaging of a whole spectrum of electromagnetic radiation including the UV, VIS and NIR regions and isolated particular bands such as CH and OH. From their study it could be inferred that reactions propagate with a particular pattern; therefore, the whole charge does not autoignite simultaneously throughout the combustion chamber. This was found to be a little counterintuitive to the fundamentals of HCCI. Hultqvist *et al* also discovered that the profile of the chemiluminescence intensity of HTHR scales with the profile of the in-cylinder pressure derived heat release rate for the corresponding phase.

A few years later, the pioneering work of Hwang *et al* (2008), clearly showed that instead of two phases for a double-stage ignition process there are three distinguishable phases for a pure HCCI operation. Similarly for a one-step process there are two distinct phases. The

existence of an intermediate temperature heat release phase has been observed in their study. Therefore instead of two classical phases of two-stage ignition there are three distinctive phases and analogously for the one-stage ignition process there are two phases. Their observations are in agreement with the fundamentals of combustion via autoignition initiation described by Bartoek *et al* (1991) who clearly pointed out that there is intermediate temperature heat release separating the LTHR and HTHR regime in a two-step process. Hwang *et al* also reported that low and intermediate temperature heat release phases are associated with low and uniform light emission as compared to the hot temperature heat release phase. Likewise from the investigations of Hultqvist *et al* it could be inferred that cool flame activities are associated with CH_2O emissions and main combustion activities with OH radicals. In their investigation, the formation and then emission of CH_2O was also dominant for an intermediate temperature heat release rate. Nevertheless, contrary to the LTHR formaldehyde emission the one during ITHR was observed to be stronger a five to ten order of magnitudes.

Amneus *et al* (2007) while investigating the nature of an HCCI operation noticed that formaldehyde is formed locally at the initial stage of cool flame activities, which is in contrast to the observations presented by Hwang *et al* (2008). However, this happened at the initial stage and as the cool flame activities progressed the concentration of formaldehyde began to dominate the whole combustion chamber. Therefore, the local character of the formaldehyde formation was presumably an effect of temperature inhomogeneities across the combustion chamber. Moreover, other researchers such as H.Zhao *et al* (2004) have reported a similar character of formaldehyde formation this is in agreement with Amneus *et al* (2007). From their study it could be inferred that this is related to in-cylinder temperature inhomogeneities rather than fuel distribution. Hence the local formation of CH_2O during cool flame activities is highly associated with temperature zones within the combustion chamber. In the same study (H.Zhao *et al* 2004), the influence of isooctane/n-heptane fuel blends with different concentrations on LTHR phasing was investigated. The study showed that there was no

particular effect of fuel blends on LTHR phasing; starting from PRF30, PRF60 and pure n-heptane they showed the same timings for the onset of the formaldehyde formation.

A study by Hildingsson *et al* (2004) employed the planar laser induced fluorescence (PLIF) technique to track the history and distribution of characteristic chemical species formaldehyde and hydroxyl radicals present in the distinctive phases of HCCI process. Their study clearly confirms that formaldehyde is an intermediate or product of cool flame activities. As can be inferred from the graphs plotted in their study the maximum concentration of CH_2O occurs at the LTHR phase. Furthermore when the hot temperature heat release starts, the concentration of formaldehyde drastically decreases. The fraction of hydroxyl radicals was indeed associated with the hot temperature heat release, and the maximum concentration of this species happens roughly at the point of 10% burned charge. Because of this it could be implied that the maximum concentration of OH marks the actual onset of the HTHR phase when a correlation with the study by Hwang *et al* (2008) is made.

Another interesting study concerning the examination of HCCI autoignition and combustion natures was conducted by Hultqvist *et al* (2002). They used a PLIF method as well as chemiluminescence imaging in order to investigate the HCCI operation. The distinguishment of an unburned charge from burned gases zones, the estimation of combustion growth rates and also the reacting structures front spreading velocity were of particular interest in their study. The reported estimated values of the burned area(s) expansion rates were in the range of $3.45 \text{ m}^2/\text{s}$ and the velocity of spreading front reacting structures could reach as high as 82 m/s ; both results are derived from lean combustion. The work of Persson *et al* (2005, 2007) could be considered as an continuation of Hultqvist *et al*'s study. They performed an investigation which aimed to identify the boundary layers between the burning zones and the not yet reacting structures under various engine operating conditions. This was accomplished by acquiring natural light images from two different perspectives of the combustion chamber and by simultaneously incorporating two CCD cameras during their study. To distinguish the burning zones from the not yet reacting

structures, a given criterion for the separation of image pixels intensities was set. They observed that with a retardation of the direct fuel injection the intensity distribution within the combustion chamber was affected. This was presumably a consequence of combustion becoming more inhomogeneous with late injection timings. A further investigation by Persson *et al* (2007) characterised differences and similarities between the pure HCCI and the spark assisted HCCI or SI operations. This comparison was conducted based on optical data; images and further application of image processing were used to quantify the SI flame expansion speed and the reaction front spreading velocities for HCCI. It was found that the magnitudes of the expansion speed for a flame of an SI mode are comparable to the velocities of the reacting structures in HCCI at the initial stage. However, no such comparable values were found for a developed HCCI process; values as high as 120 m/s were observed, whereas for the SI process they were in the range of a few 6-8 m/s.

Kawahara *et al* (2003) undertook an attempt to optically diagnose an autoignition and combustion of dimethyl ether HCCI. This investigation was accomplished by using the high-speed color imaging and spectroscopic measurements. From their experiments it could be seen that the autoignition and combustion activities were blue light dominated. The chemical species identified for a main combustion-activities period were hydroxyl radicals, formaldehyde and CH. Moreover they observed the dominating presence of CO-O during the hot temperature heat release rate. The investigation of Zigler *et al* (2008) would seem to corroborate the findings of Kawahara *et al*; they also observed a similar colour of light emission. Various blends of gasoline-like fuel blends were investigated and it was found that the autoignition and combustion activities were blue light dominated regardless of fuel blend.

The pure HCCI operation, autoignition and combustion process characteristics, more specifically the pattern of autoignition under a different fraction of entrapped residuals were investigated by Aleiferis *et al* (2007). As a key conclusion of their studies they inferred that the onset of combustion becomes more random with an increased fraction of trapped residuals.

2.2 The influence of fuel molecule type and engine operating variables on the character of HCCI autoignition and combustion

As the two-step ignition process claims potential benefits over the *classical* one-step ignition process, recent research on the character of HCCI autoignition-combustion has been focused on understanding the influence of fuel interaction and engine operational parameters on a two-step ignition process, especially the cool flame activities. Examples of the potential claimed benefits of the two-step ignition process over the one-step process are:

- A two-stage auto-ignition process has lower cycle-to-cycle variations under certain engine operating conditions.
- HCCI operation can be achieved with a lower intake air temperature, since the LTHR has the capacity to increase the charge temperature prior to the main combustion (Sjoberg *et al* 2007).

Sjoberg *et al* (2003) tested the influence of engine operating variables such as engine speed and intake air temperature on the magnitude and phasing of cool flame activities. They performed their investigations with a diesel like compression ratio engine, operating with a conventional positive valve overlap and being fuelled with isooctane, gasoline and primary reference fuel blends. The experiments they conducted have shown that both engine speed and intake air temperature have an effect on the phasing and magnitudes of heat release during cool flame activities. With regard to the influence of intake air temperature, it was observed that the magnitude of low temperature heat release decreases as intake air temperature increases. Furthermore, the advancement of the LTHR phase was noted with the intake air temperature increase. They also inferred that the decrease in magnitudes of LTHR was due to the earlier timing of cool flame activities and the occurrence of these activities in lower pressure zones. This is because cool flame activities are favoured by higher pressures. The increase of engine speed caused a reduction in LTHR magnitudes, due to the combined effect of shorter real time available and the contribution of heat transfer.

Similar conclusions concerning the effect of engine speed on cool flame activities were made by Aroonsrisopon *et al* (2002) and Szybist *et al* (2005). Despite the differences in experimental approaches, in the fuel blend used in the engine facilities incorporated, they observed that it is the available residence time that the mixture spends in favourable conditions that contributes and shapes the magnitudes of the cool flame activities. Therefore, the diminishing of cool flame activities with an engine speed increase might be noted. However, the actual trend of magnitudes and phasing appears to vary from engine to engine throughout the engine speeds investigated.

Moreover engine boosting was reported also as an important engine variable, which contributes to the nature of the process type (Christensen *et al* 1999 and Sjoberg *et al* 2007). Principally the investigation of Christensen *et al* has shown that a one-step ignition fuel could traverse a two-stage ignition process as a consequence of intake boosting. Furthermore, this parameter exhibited in work by Sjoberg *et al* (2007) was considered an effective way to control the magnitude of cool flame activities. Both studies reported the rise of magnitudes in LTHR that was associated with the engine boost pressure increase. Further investigations by Sjoberg *et al* (2007) aimed to examine and characterise the influence of the conventional externally and artificially created combustion stoichiometric products of gas recirculation. Apparently both ones systems were classified as cooled ones. They observed that when the fraction of external gas recirculation relative to the fresh charge increases cool flame activities are suppressed. When identifying the influence of an individual species of combustion stoichiometric products on charge temperature they found that CO₂ contributes the most to the charge cooling, as its heat capacity is the largest of these three combustion stoichiometric products, N₂, H₂O and CO₂. They also discovered that diatomic nitrogen elevates compressed gas temperature more effectively than pure air, as a consequence of its lower heat capacity. Water has a moderate heating capacity among the investigated species of stoichiometric combustion products. As this is the case different charge temperatures are experienced when different fractions of EGR are utilised. In fact this might

lead to various phasing and magnitudes of LTHR exhibited throughout the cases of different EGR fractions cases, as pressure-temperature histories are altered.

2.3 Current fuel autoignition quality designators and their role and relevance in the HCCI autoignition process

A number of research studies have been performed to examine the suitability of different fuels for HCCI operation. This includes widespread research involving commercial fuels such as standard gasoline and diesel oil; as well as a great amount of investigations that incorporated the examination of laboratory fuels, single, binary or multi-components blends. The experiments with these so called laboratory blends are especially attractive as they are relatively chemically simple in comparison to multi-component fuels e.g. gasoline or diesel fuel. Also because chemical kinetic mechanisms exist for these simple pure component fuels experiments could be compared with a numerical simulation conducted to gain a further insight. Additionally the experiments with so called laboratory fuels are useful for probing the chemical kinetics of HCCI combustion and investigating the effect of a given fuel property i.e. octane rating isolating other properties in HCCI combustion (F.Zhao *et al* 2003).

Even though a great deal of research has so far been carried out to investigate the fuel interaction of octane and cetane quality relevance for an autoignition initiation in an HCCI operated engine the appropriate designators defining autoignition fuel propensities have not yet been fully and formally established. Research includes the correlation between Research and Motor octane numbers and alternatively cetane measures of fuel and auto-ignition propensities in an HCCI operated engine.

Bradley *et al* (2004) used a CFR engine facility and modeling approach to investigate the relevant fuel properties for HCCI autoignition. The scope of their study included a review of the relationship between RON, MON and the autoignition process in an HCCI operated engine, or the simulations performed. They focused on understanding the effect of toluene/n-

heptane and two primary reference blends on autoignition characteristics. From their study it was noted that the octane indices (actual fuel octane quality) of the sensitive toluene/n-heptane blends are highly dependent on engine operational conditions, and there might be circumstances where the octane index is significantly higher than its RON number. Consequently this would mean that the fuel becomes more resistant for autoignition, than its ignition quality defined by RON numbers. No such evidence was observed for primary reference fuels, presumably as these blends are not sensitive.

Further pioneering work by Kalghatgi (2001) has shown that the auto-ignition quality of fuel is well described by Octane Index $OI = RON - KS$, because it is a correlation between the RON and MON numbers and as importantly the K constant which is an experimentally derived constant dependent on instantaneous engine operating conditions. To obtain this correlation twenty-three different automotive engines were employed. Principally Kalghatgi's study showed that if the higher octane index is the more resistant the fuel is to an autoignition (potential knock). Nevertheless, the actual fuel octane quality is greatly governed by the actual in-cylinder temperature pressure history. It appears that for the sensitive fuel blends autoignition becomes more favoured as the K value increases, the OI decreases.

Kalghatgi *et al's* (2003) subsequent investigation was focused on performing a series of tests with different fuels. When tracking the CA50 (50% burn point) points were assumed to be indications of the fuel autoignition propensities of HCCI, as it shows a crank angle position of 50 % burned charged. They correlated the obtained results with the octane indices of fuels used under investigated engine operational conditions. They observed the retarded onset of the heat release rate for fuels with a higher octane number. Consequently it could be inferred that as the octane number increases the autoignition properties deteriorate. Their study implied that for sensitive fuels with a given in-cylinder pressure, the lower the temperature the more resistant the fuel becomes to an autoignition. When a higher air intake temperature is applied, the autoignition propensities of the sensitive blends are significantly improved in comparison to the non sensitive blends. For this particular research study they found that an

intake temperature of around 120°C, is one for which the fuels' autoignition quality scales with their RON method numbers. In fact their autoignition propensities are equivalent to their RON method numbers. The investigation of Kalghatgi *et al* (2004) attempted to introduce a fuel octane index which could be founded on experimentally derived CA50 and engine operating conditions. High intake air temperatures and engine speed conditions were investigated using different fuels. The empirical correlation among the intake air temperature, fuel-air equivalence ratio and engine speed has been elaborated as a fuel octane index necessary to place the heat release at TDC . However it was found that with an elevated intake air temperature the fuels release heat almost uniformly regardless of the difference in their compositions.

The continuations of the work of Kalghatgi or Kalghatgi *et al* are studies conducted by Risberg *et al*. Risberg *et al* (2003) aimed to compare the autoignition qualities of eleven chemically unlike fuels of various chemistries, and the autoignition propensities meeting the requirements for HCCI autoignition. The fuel blends spanned from simple binary primary reference fuels throughout the toluene addition blends to the commercial multi-component ones with MON and RON values from 73 to 95. These studies were performed with various engine speeds, intake pressures and temperatures, compression ratios and mixture strengths. The key conclusion which could be derived from their work is the following: the autoignition quality of real fuels, which are indeed sensitive fuels containing various common hydrocarbon family components and hundreds of others, can not be described by a current fuel autoignition quality designated by RON or MON numbers unless the engine is operated under conditions equivalent to those tests methods. Moreover sensitive fuels can contribute to expansion of the operational envelope to a greater extent than non sensitive blends of the same RON values.

The objective of the subsequent study by Risberg *et al* (2004) was to identify the influence of exhaust gas recirculation (internal and external) on fuel autoignition quality and propensities in an HCCI operated engine. Clearly, the internal exhaust gas recirculation was

realised by setting the negative valve overlap. In their study it was observed that when a significant amount of residuals are trapped, various fuels start to release heat at the same point. Therefore further assessments of fuel autoignition qualities seem to be impeded. Thus the thermal effect of EGR was pronounced in their study, as one elevating the in-cylinder temperature and thereby impacting the fuel autoignition quality. However, the empirical correlations derived under given engine operating conditions of their currently discussed study scale with their previous studies conducted by Risberg *et al* (2003).

Other work done by Risberg *et al* (2005) aimed to examine the autoignition quality of diesel like blends in an HCCI operated engine. This was done with various injection strategies, including port fuel injection and late direct injection. From their study it could be inferred that cetane designations such as numbers or indices match well with the required fuel autoignition quality in an HCCI operated engine. This was accomplished by correlating the CA50 points and the potential fuel cetane numbers of various investigated commercial and laboratory diesel-like fuels.

Another revolutionary attempt to assess the auto-ignition propensities of hydrocarbon fuels for HCCI requirements has been recently made by Shibata *et al* (2007). In their study, they reviewed the heat release rate where the low temperature heat release fell in particular interest of the study. Hence the autoignition qualities correlate well with the magnitude of low temperature heat release indications. Their study was conducted with a constant engine speed and without exhaust gas recirculation. Therefore the proposed correlation does not account for corrections due to the residual rate. The magnitude of the cool flame activities scaled with the onset of the hot temperature heat release. More specifically, a larger magnitude of LTHR was observed the earlier the mixture started to exhibit heat. This study was preceded by other interesting fuel autoignition quality investigations conducted by Shibata *et al* (2005, 2006). Firstly, in 2005 they reported the apparent influence of aromatic compounds, especially toluene on the magnitudes of cool flame activities. It was observed that if toluene was mixed with other hydrocarbon compounds exhibiting low temperature heat

release, the magnitude of LTHR would be lower than when toluene was replaced with any other non aromatic compound, preserving the same volumetric proportions. As this was the case this phenomenon was named the toluene inhibitor effect. Furthermore, a study by Shibata *et al* (2006) demonstrated that the toluene inhibitor effect is highly charge temperature dependent. As the charge temperature increase the suppressing influence on cool flame activities is reduced. Sjoberg *et al* (2007) reported a similar trend when investigating and comparing toluene blends with others of different chemistries. Their study was performed with different engine operating conditions.

2.4 Injection strategy and timing as a means of controlling the combustion onset and optimising the process

The HCCI operation is chemically kinetically driven and therefore is greatly dependent on the in-cylinder temperature-pressure history, the global and local fuel-air equivalence ratios, fuel reactivities and dilution strategies. As this is the case there is no direct mean of combustion onset control.

Contrary to port fuel injection which seems to have no significant effect on the onset of combustion, a direct fuel injection into the cylinder can help to manage the timing of autoignition initiation. This happens because direct injections have the capability to alter/influence the local fuel-air equivalence ratios and the in-cylinder temperature. Control by way of direct injection refers to varying both the direct injection strategy such as single and split and as importantly varying the injection timings. It is clear that the in-cylinder gas temperature is altered or influenced due to charge cooling caused by fuel evaporation when fuel is injected directly into the cylinder chamber. The injection timings also affect the local fuel equivalence ratios; therefore, the demanded objectives in combustion control can be achieved. Early fuel injections in the induction stroke provide well premixed operations while the late ones occurring in the compression stroke form a rather stratified charge. Hence late

fuel injections drastically increase the local fuel concentration and higher variations in the local equivalence ratios are expected across the combustion chamber. For engines operated with an NVO strategy further promising and significant control of HCCI combustion onset could be gained by injecting fuel into the entrapped residuals. As a result of fuel injection into the hot residuals, intermediates and radicals are formed during this period, which have an impact on the initiation of the main autoignition-combustion process. This is indeed the case when fuel is injected in residual gases which a certain fraction of oxygen (unused air as a result of lean operating engine conditions) (F.Zhao *et al* 2001). However, as direct fuel injection strategies and timings can be used to govern the in-cylinder temperature and local equivalence ratios, they also have a significant influence on emission. Late injection strategies seem to be favourable for NO_x and soot formations as local rich zones are created. Consequently, CO emissions might be lowered as an effect of the elevated local combustion temperature favouring the CO to CO_2 conversion (Dec *et al* 2003). Contrary to this, premixed charges of early injections produce significantly less soot and NO_x , but higher CO emissions. This is the result of the combined effect of more uniform local equivalence ratios and combustion temperatures across the combustion chamber (Dec *et al* 2003).

Until now, various injection strategies, including single and split with different timings, have been widely explored for a HCCI operating engine. This research was undertaken in order to optimise the combustion characteristics such as emissions and as importantly to gain control of combustion onset.

Koopmans *et al* (2003) carried out experiments with a metal (thermal) engine using different split injection strategies to alter the stoichiometry of the fuel-air charge. By introducing some fuel in the recompression stroke, they observed that the combustion activities during that phase were stimulated when the engine was running with a fuel-air equivalence ratio of $\Phi \approx 0.91$ and leaner. Therefore the fuel-air equivalence ratio of $\Phi \approx 0.91$ in their study was identified as a *critical point*. The critical fuel-air equivalence ratio the below which reactions of fuel-air charge leading to a discernible heat release rate during the

negative valve overlap period do not occur. As a consequence of reactions occurring during the NVO, an advanced onset of main autoignition-combustion activities was noted. Furthermore, this advancement scaled well with the amount of oxygen contained by residuals and the capabilities for reactions to happen. Also from their study it could be inferred that under given engine operating conditions, more specifically with fuel-air charge mixtures richer than $\Phi \approx 0.91$, an increase in the quantity of fuel injected during the recompression stroke lowers the in-cylinder pressure. Moreover, the observed reduction in the recompression pressure-temperature caused a retardation of the main autoignition-combustion process.

A study by Berntsson *et al* (2007) demonstrated the distribution of fuel, formaldehyde and hydroxyl radicals using the LIF method with various injection strategies and timings. Their study was conducted under lean engine operating conditions. The optical study they conducted was preceded by investigation of the conventional pressure transducers. It was observed that combustion phasing is advanced as the quantity of fuel injected in NVO is increased. However, this advanced onset of combustion was associated with a higher HC emission. As the advanced onset of combustion was observed, as a result of the fuel injection and reactions during the recompression stroke, the results of Berntsson *et al* seem to be in agreement with the study of Koopmans *et al* (2003).

Urushihara *et al* (2003) tested different direct injection strategies and timings, including split injection and direct injection strategies. With the split injection strategy the fuel was chosen to be injected into the recompression stroke in order to promote reactions. As this was the objective the engine was operated with lean air-fuel charges. Having compared the results of the split injection and single injection strategies of their studies the following can be said. The operational envelope could easily be broadened using the split injection, when fuel injection takes place in the recompression stroke in comparison to the single injection. Moreover they observed an increase in NO_x for a single injection; however, this would have been the effect of the actual single injection strategy investigated, and seems to be optimised

by altering the injection phasing. Also it was noted that this is the load which determines the requirements of the quantity injected during the NVO to obtain the optimal process, for both combustion timing and emission. Furthermore it was observed that there was an excess of fuel presented in the recompression stroke, thus reactions could significantly worsen the fuel consumption. Also based on their investigations, it could be concluded that the pilot injection timing for the NVO period should be appropriately selected for each load and/or fuel-air equivalence ratio to optimise fuel consumption.

Investigations of researchers such as Waldmann *et al* (2007), Aroonsrisopon *et al* (2007) and Song *et al* (2008) provide further evidence that split injection strategies with a pilot injection in the recompression stroke have the capability to control the onset of combustion. They could also contribute to broadening the HCCI operational window. Aroonsrisopon *et al* (2007) while running an engine with pure isooctane, observed that an injection in NVO allowed them to operate an engine at a lower load, which would not be achievable with a single injection strategy. Analogously to Koopmans *et al*'s study (2003) they noted that the heat released during the recompression stroke was highly dependent on the oxygen concentration. Also the optimal timing to set for a pilot injection would be one corresponding to the crank angle position of the exhaust valve closure. Song *et al* (2008) investigated the compression ratio, quantity and timing of fuel injected into the NVO with a split injection strategy. Similarly to Urusihahara *et al* (2003) they noted that there is an optimum in recompression stroke reactions which can impact HCCI operation. They also observed that the recompression reactions are a function of fuel injected at specified engine operational conditions. Moreover, the low boundary of the operational envelope could be shifted down significantly at a low equivalence ratio and high residuals fraction conditions. It was shown that late injection timings during the recompression stroke have a significant impact on the occurrence of reactions, by reducing them. Experiments of Waldmann *et al* (2007), have shown that the injection during the NVO could considerably improve the indicated specific

fuel consumption. However, the pilot injections which are beyond the optimum could cause a loss of combustion stability, which observed by elevated COV of NIMEP values.

2.5 Solid carbonaceous particles and HCCI operation

The fact that particulate matters (soot) emission is drastically reduced from an HCCI engines in comparison to the conventional Compression Ignition (CI) engines is not new. Nevertheless the particulate emission is highly dependent on fuel type, engine operating conditions, injection timings, loads etc. The evidence that soot emission generated by HCCI combustion could be comparable with the emission from SI engines has recently been reported in a study by Price *et al* (2007). This could be done by comparing the engine operating conditions with the same fuel consumption indications, as any other comparison could imply an erroneous indication. Therefore the PM emission from the HCCI engine is not as negligible as one would expect. Moreover, from the investigation of Price *et al* (2007) it is evident that HCCI PM emissions could exceed SI emission under particular operating conditions. In a study performed by Misztal *et al* (2009) investigating Particulate Matter (PM) emission from a multi-cylinder HCCI engine they noted the greatest emission of PM when a quantity of fuel during split injection was introduced close to TDC NVO. In contrast to this, the minimum PM emission was observed for a single injection when fuel was injected in the recompression stroke. Dec *et al* (2003) when investigating emissions observed a progressively higher soot emission with injection timing retardation. The short literature review conducted within this section is dictated by the fact that there is a shortage of technical papers concerning this subject available in open literature.

2.6 Summary

Literary examples from a few different HCCI research areas have been presented in this section. The choice of these particular areas and technical papers was dictated by their relevance for the scope of this thesis. Hence the technical papers related to investigations of fuels, the optical diagnostics and the nature of the process were addressed. Also as some of the literature review was focused on the presentation of HCCI, the literature review is shorter in this chapter to avoid repeating the same things. Indeed other more specific information from technical papers, books or any other available sources were used for referencing in the main body of this thesis.

Chapter 3

Experimental System

3.1 Introduction

This chapter presents nearly identical thermal (all-metal) and optical Jaguar single cylinder research engines. The general features as well as geometrical configurations are given for both research apparatus. Also great attention is focused on unique and important features of the optical engine such as its piston-cylinder lubrication system and the materials of its optical components i.e. windows, mirror and glass liners. Furthermore the engine control systems with their technical aspects are demonstrated. These include simple injection-ignition activities management and more technically sophisticated variable valve timing control system.

3.2 Engine facilities

The experimental part of this thesis was conducted utilising nearly identical thermal (all-metal) and optical single cylinder research engines. The configuration of these two experimental apparatus and their facilities are similar (nearly identical), but not the same. The experimental thermal analysis throughout this research thesis was done on the Jaguar single cylinder thermal engine. In contrast all the experimental optical analysis presented in this research thesis was conducted on the Jaguar single cylinder optical engine.

These two research apparatus are 4-stroke, naturally aspirated, water cooled and double overhead cam (DOHC) engines. The geometrical configurations of these single cylinder

engines derive from the production scale automotive Jaguar V8 spark ignition engine with a displacement of 4.4 L. The production engine is rated to 298 kW at 6100 rpm and 560 Nm at 3500 rpm with a bore of 87 mm, stroke of 91 mm and geometric compression ratio of 9.1. However, a conversion of the traditional spark ignition engine type to an engine providing appropriate HCCI operation required a number of hardware component modifications or replacements to be done. Also home-made controlling systems were implemented as those engines became research ones. In summary, the following key modifications to hardware and software adaptation, development and implementation could be listed:

- 1) Engine head was customised for the single cylinder engine with all aspects and dimensions including intake and exhaust port dimensions remaining unchanged;
- 2) The conventional spark ignition profile camshafts (high-lift valve ones) were replaced with short duration so called HCCI camshafts with low-lift profiles. Generally they are more appropriate for negative valve overlap (NVO) strategy;
- 3) The thermal engine was equipped with a Continuous Variable Cam Timing System (CVCTS);
- 4) Customized intake and exhaust manifolds were installed with the plenum mounted on the intake side for pressure oscillation reduction purposes.
- 5) Both engines were equipped with two fuelling systems :
 - Port Fuel Injection System (PFI) - for intention of premixed operations,
 - Direct Injection System (DI) for high pressure direct single and split injections;
- 6) The optical engine conventional piston was replaced with an utterly flat piston with inserted quartz window in its piston-crown;
- 7) The control systems of injection-ignition events were adapted from Oxford University's and modified by the author of this thesis at the University of Birmingham;
- 8) The control code for continuous valve timing event control system was entirely developed at Birmingham University by the author of this thesis.

Consequently these modifications and replacements along with encountered technical restrictions resulted in some engine geometrical dimensions or features that had not been

originally preserved. Hence their geometries were not identically retained as the Jaguar V8 engine type geometry; also there are some component differences in configurations between these two experimental single cylinder engines such as their camshafts profiles (durations and lifts). Despite all these changes, the geometry of the engine heads remained unchanged and identical to the Jaguar V8 engine type head.

3.2.1 Thermal engine

The original design of this engine is based on the Ricardo Hydra engine. Initially it was re-designed by the internal combustion engine (ICE) research group at Oxford University. Then this engine was modified again to match up with Jaguar V8 engine geometry, sharing among other components the same piston type (bowl-type), cylinder head or variable cam timing system. Figure 3.1 presents a real view picture of all-metal single cylinder engine facility and its specification is listed in Table 3.1.



Figure 3.1. Thermal single cylinder engine.

Parameter	Value
Engine Head Type	Jaguar V8
Cycle	4-stroke
Bore	90 mm
Stroke	88.9 mm
Displacement	0.565 L
Clearance Volume	0.0538 L
Geometric Compression Ratio	11.5:1
Connecting Rod Length	160 mm
Number of Intake Valves	2
Number of Exhaust Valves	2
Intake Valve Lift	2.65 mm
Exhaust Valve Lift	2.1 mm
Intake Camshaft Duration	130° CA
Exhaust Camshaft Duration	110° CA

Table 3.1. Specification of thermal single cylinder engine.

The implemented continuous (within shifting range) variable cam timing system controls both intake and exhaust camshafts simultaneously and independently. For this engine the intake and exhaust camshafts - their profiles and lifts vary are as summarized in Table 3.1. The direct injection system uses a centrally mounted third generation of Bosch[®] gasoline solenoid-operated multi-hole direct injection (GDI) injector type. For a DI system (high-pressure operation) the piston accumulator using nitrogen as a gas was installed to pressurise fuel. As aforementioned, besides the DI system, this engine is also equipped with a port fuel injector located in close vicinity to the intake valves. This PFI system is a low pressure one of about 5 bar operational pressure.

3.2.2 Optical engine

The optically accessed research engine in spark ignition configuration was entirely designed at Ford Motor Company. A real view picture of this research engine facility is shown in Figure 3.2. The Table 3.2 summarises the engine specifications. Principally unlike the conventional thermal single cylinder engine specified in previous sections, this optically accessible engine features several particular arrangements. The piston arrangement is the

conventional Bowditch type with the optical piston screwed into the hollowed extension allowing a fixed 45° mirror to be mounted on the engine crankcase.

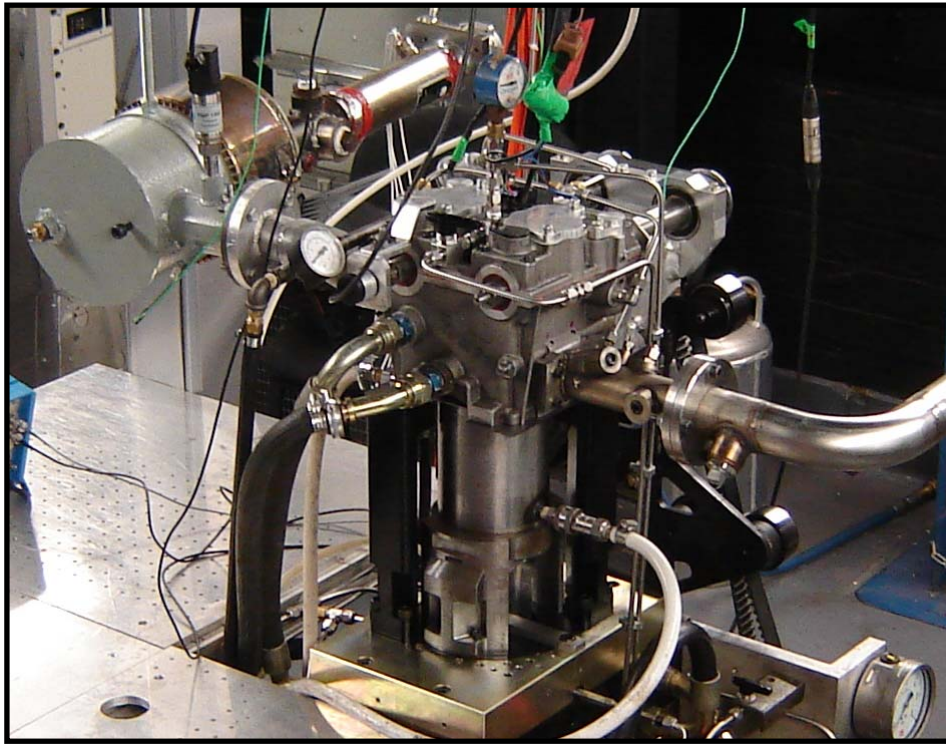


Figure 3.2. Optical single cylinder engine.

Parameter	Value
Engine Head Type	Jaguar V8
Cycle	4-stroke
Bore	89 mm
Stroke	90.3 mm
Displacement	0.562 L
Clearance Volume	0.0562 L
Geometric Compression Ratio	11:1
Connecting Rod Length	148.9 mm
Number of Intake Valves	2
Number of Exhaust Valves	2
Intake Valve Lift	2.5 mm
Exhaust Valve Lift	2.5 mm
Intake Camshaft Duration	150° CA
Exhaust Camshaft Duration	150° CA

Table 3.2. Specification of optical single cylinder engine.

The extended piston is bolted to the conventional piston in the crankcase connected by an ordinary connecting rod with a crankshaft. Additionally this optical research engine has a

pneumatically operated “drop-down” liner allowing quick inspection of the combustion chamber for different purposes e.g. inspections or maintenance (piston, window cleaning).

There are three arrangements for the cylinder liner (whole length) of this optical engine that can possibly form. It can be a full length water cooled liner; a part length of solid glass liner forming the top part of cylinder wall and a short length of water cooled cylinder liner (with 1 to 5 as length proportions) or a full length solid glass liner. With the other two optical accesses which could be constructed, this research apparatus offers three possible optical paths to the combustion chamber:

- 1) Bottom view - through the piston crown equipped with transparent window;
- 2) Side view I - through the vertical triangular window installed in the engine head;
- 3) Side view II - through the solid glass liner if it forms a part of complete cylinder or is a complete liner itself.

The section view of the optical research apparatus with full length water cooled cylinder liner (highlighting only two out of three combustion chamber accesses) is shown in Figure 3.3. As mentioned previously the original (conventional) bowl-shaped piston was replaced with a flat topped piston equipped with transparent disc inserted in the piston crown (see Figure 3.4). This was done for the purpose of optical research because the selection of a flat piston crown window (consequently piston) prevents any image distortion caused by the curvature of the piston crown and it also provides easy optical access to the combustion chamber through the piston crown. The piston-crown window diameter is 64 mm, which is significantly smaller than the piston crown diameter, thereby restricting access to whole combustion chamber area. Therefore the imaged view through the piston crown window (from the below of the engine/cylinder barrel) in this configuration corresponds to only about 52% of the total combustion chamber area. Indeed this limits the research conducted to some extent and should be taken into consideration during experimental results analysis.

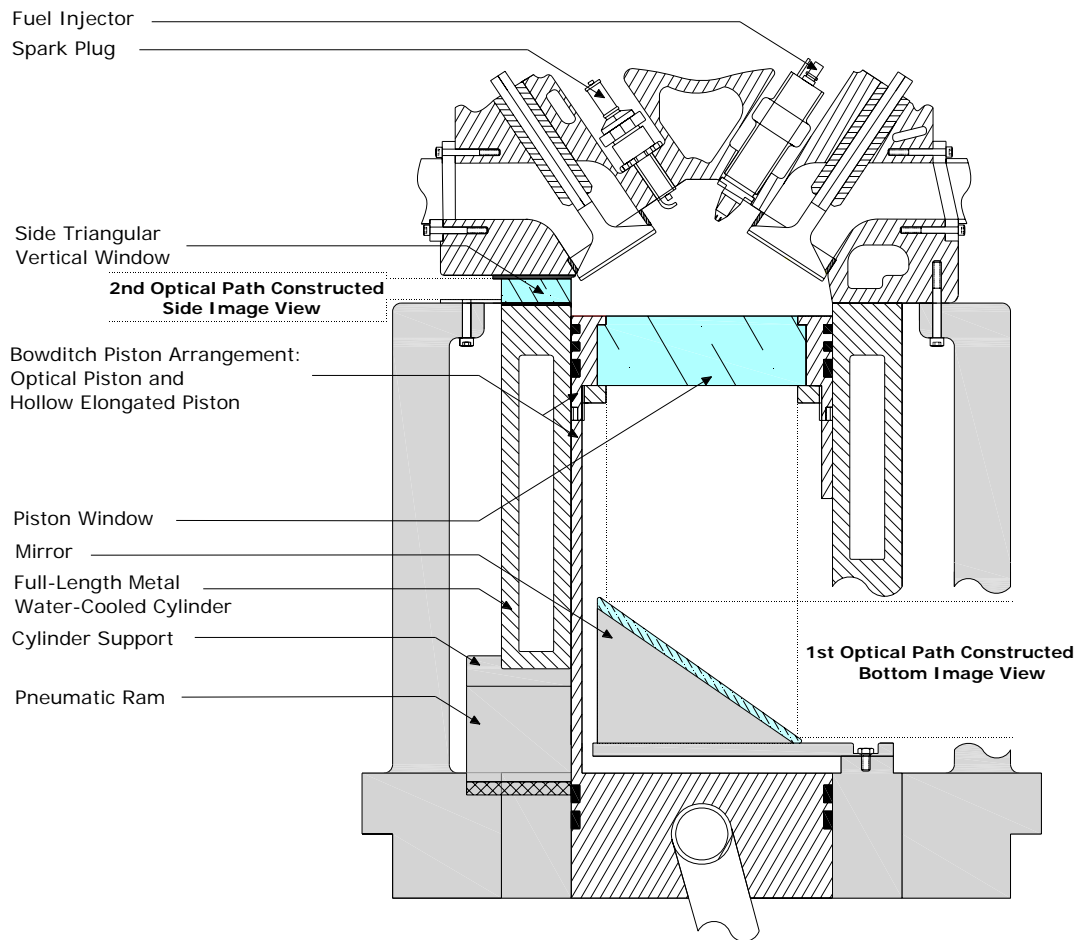


Figure 3.3. Cross section (schematic) of optical research engine. Two constructed optical paths (bottom and view) are illustrated.



Figure 3.4. Flat-topped optical piston with quartz piston-crown insert (window).

Cylinder-piston lubrication system

The subsequent noteworthy unique feature of this optical engine design is the unconventional oil lubrication system between the cylinder and the piston. Lubrication is realized as a 'dry lubrication' by means of piston rings material. Hence proper rings material selection is necessary. The optical piston rings are made of polymers, i.e. polyamid-imide (PAI) known under a commercial name of TORLON[®] offering outstanding properties. All TORLON resins are characterised by flame resistance, high impact strength and exceptional mechanical strength – both tensile and flexural combined with excellent retention of these properties over a wide range of extremely elevated temperatures (Solvay Advanced Polymers). Several TORLON[®] grades are currently available, which can be broadly broken down into two groups: the high-strength grades 4203L, 5030, 7130 and wear-resistant grades 4275, 4301, 4435. Table 3.3 summarises the properties of all grades of TORLON[®].

With their inherent lubricity characteristics further enhanced by special additives, 4301 and 4275 wear resistant grades of PAI constitute the most appropriate resins for piston rings. The gray color column emphasises the properties of PAI grade (4301) selected to manufacture piston rings utilised throughout all these experimental studies covered in this thesis.

This solution (piston to cylinder dry lubrication) contributes significantly to reducing the uncertainties found in the investigational results analysis by eliminating parasitic (unwanted) luminescence recording e.g., burning oil luminescence and/or by changing windows transmission characteristics caused when oil is build-up on the optical element (window).

Property	ASTM Test Method	Grades						Units
		4203L	4301	4275	4435	5030	7130	
General								
Density	D 792	1.42	1.46	1.51	1.59	1.61	1.48	g/cm ³
Hardness, Rockwell E	D 785	86	72	70	62	94	94	
Water Absorption, 24 h	D 570	0.33	0.28	0.33	0.12	0.24	0.26	%
Mechanical								
Tensile Strength								
- 196° C	D 1708	218		130		204	158	MPa
23° C	D 1708	192	164	131	110	205	203	MPa
135° C	D 1708	117	113	116	90	160	158	MPa
232° C	D 1708	66	73	56	52	113	108	MPa
Tensile Elongation								
- 196° C	D 1708	6		3		4	3	%
23° C	D 1708	15	7	7	6	7	6	%
135° C	D 1708	21	20	15	4	15	14	%
232° C	D 1708	22	17	17	3	12	11	%
Tensile Modulus								
23° C	D 1708	4.9	6.6	7.8	9.7	10.8	22.3	GPa
Flexural Strength								
- 196° C	D 709	287		203		381	315	MPa
23° C	D 709	244	219	212	152	338	355	MPa
135° C	D 709	174	165	157	129	251	263	MPa
232° C	D 709	120	113	111	91	184	177	MPa
Flexural Modulus								
23° C	D 709	5.0	6.9	7.3	14.8	11.7	16.5	GPa
Compressive Strength								
23° C	D 695	220	170	120	138	260	250	MPa
Compressive Modulus								
23° C	D 695	4.0	5.3	4.0	8.5	7.9	9.9	GPa
Shear Strength								
23° C	D 732	128	112	77	60	140	120	MPa
Poisson's Ratio								
23° C		0.45	0.39	0.39	0.42	0.43	0.39	
Thermal								
Deflection Temperature 1.82 MPa	D 648	278	279	280	278	282	282	°C
Coefficient of Linear Thermal Expansion	D 696	30.6	25.2	25.2	14.4	16.2	9.0	ppm/°C
Thermal Conductivity	C 177	0.26	0.54	0.65	0.80	0.37	0.53	W/mK
Flammability	UL 94	94 V0	94 V0	94 V0	94 V0	94 V0	94 V0	

Table 3.3. Properties of several TORLON grades (Solvay Advanced Polymers).

Optical materials

The key issue in optical investigation is the appropriate selection of the material for optical components, which meet demanded investigational requirements. More specifically as various materials possess different radiation transmittance characteristics, it is about the

matching radiation transmittance of a material used with region being in the interest of study. For the engine research optical measurements it means that materials for liners, windows, lenses and mirrors should match diagnostic equipment spectral responsivity so that not the observations will not be limited.

Figure 3.5 demonstrates radiation transmittance characteristics of several optical materials. For instance when the low cost silicate glass radiation transmittance characteristics are analysed it is evident that this material is adequate for use in the visible light range. At wavelengths shorter than about 380 nm (UV region) the glass begins to absorb and has to be substituted once this region becomes an interest of study (Skoog *et al* 2004).

The piston crown window, triangular side window and glass liners both short and full length for the single cylinder optical engine were made of fused silica, precisely of full spectrum grade synthetic fused silica. The full spectrum grade fused silica is very flexible material for investigating multi wavelength range that exhibits superior radiation transmittance over a wide spectral range spanning from above 300 nm (near ultraviolet) to approximately 2.5 μm wavelength (short-wave infrared region) (see Figure 3.6). The radiation transmittance of a full spectrum grade fused silica gradually drops below 300 nm and the material becomes significantly absorbant below 200 nm at one spectrum end with cutt-off occurring about above 2.5 μm at the other spectrum end.

Fused quartz and fused silica are made from silicon dioxide (SiO_2). Silicon dioxide occurs naturally as sand or rock and when processed the resulting product is called Fused Quartz (Skoog *et al* 2004). If the silicon dioxide is synthetically derived, the material is often called fused silica. Hence fused silica is a high purity synthetic amorphous silicon dioxide. The main properties of a full spectrum grade fused silica are listed in Table 3.4.

Fused silica as a material for optical components offers a number of following advantages:

- a) excellent optical qualities and wide radiation transmittance spectral range encompassing UV, VIS and IR regions,

- b) a low coefficient of thermal expansion providing stability and resistance to thermal shock over large temperature excursions without cracking,
- c) a wide operating temperature range,
- d) high hardness and resistance to scratching.

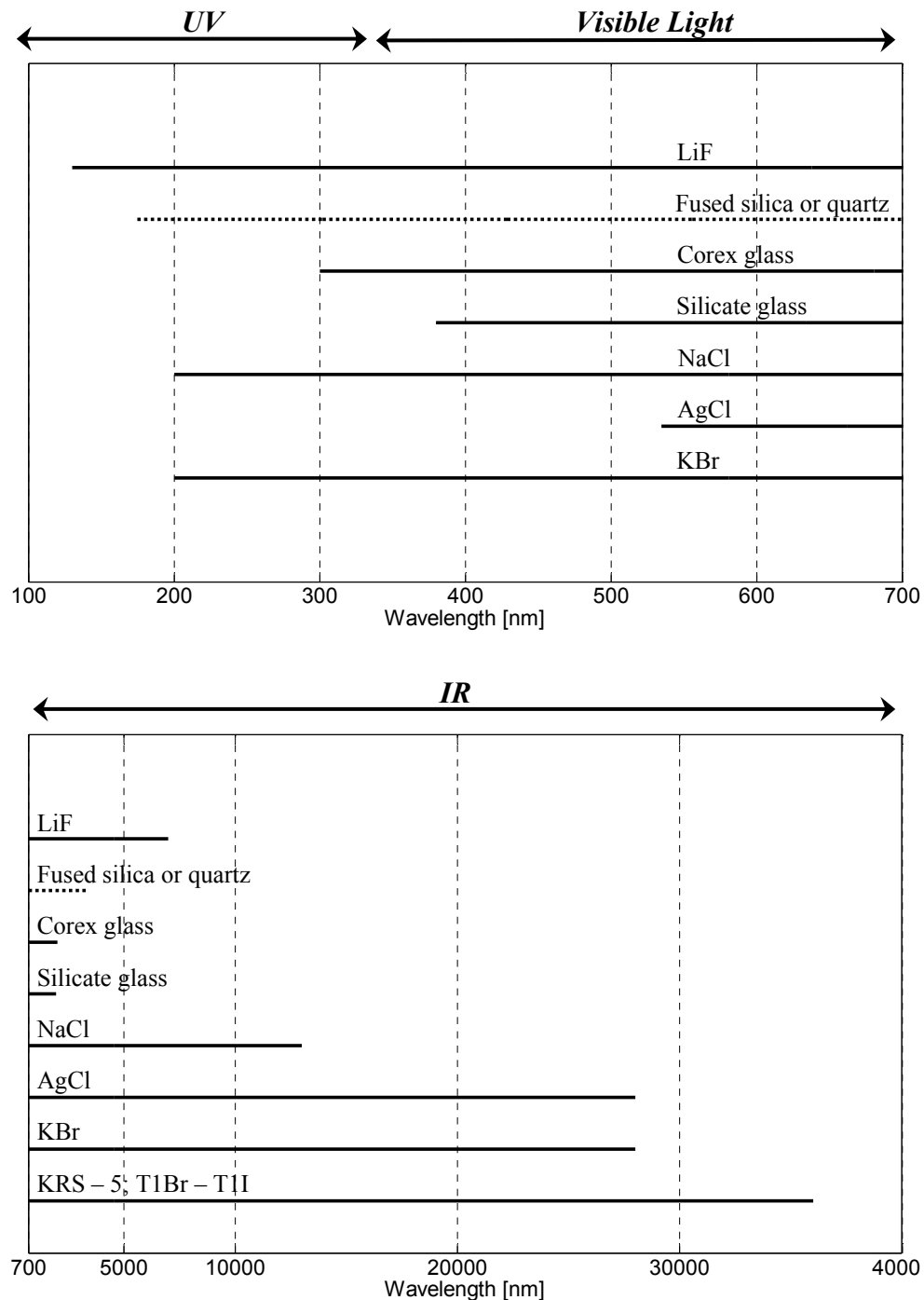


Figure 3.5. Radiation transmittance characteristics of several optical materials for UV, VIS and IR spectral regions (Skoog *et al* 2004).

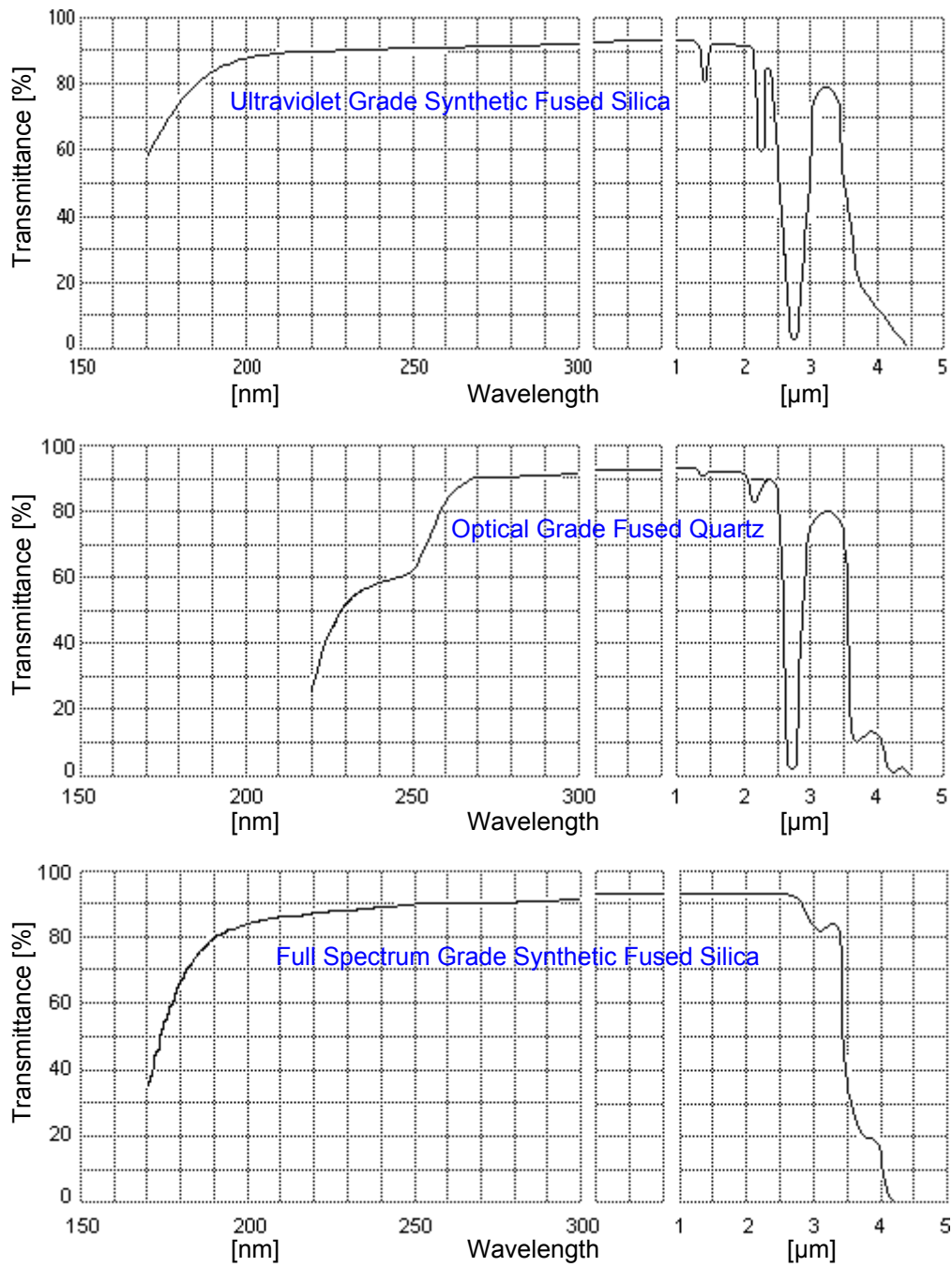


Figure 3.6. Transmittances radiations for ultraviolet grade synthetic fused silica, optical grade fused quartz and full spectrum synthetic fused silica (Alkor).

Property	Full Spectrum Grade Synthetic Fused Silica	Units
General		
<i>Density</i>	2.2	g/cm ³
<i>Hardness, Vickers</i>	1000	kg/mm ²
<i>Water Absorption, 24 h</i>	0	%
Mechanical		
<i>Tensile Strength</i>		
- 196° C	50	MPa
<i>Tensile Modulus</i>		
23° C	73	GPa
<i>Compressive Strength</i>	1100	MPa
<i>Shear Strength</i>		
23° C	70	MPa
<i>Poisson's Ratio</i>	0.17	
<i>Young's Modulus at 25° C</i>	73	GPa
<i>Shear Modulus at 25° C</i>	31	GPa
<i>Rupture Modulus at 25° C</i>	50	MPa
Thermal		
<i>Specific Heat</i>	705	J/kg*K
<i>Coefficient of Thermal Expansion at 20-1000° C</i>	0.54×10^{-6}	K ⁻¹
<i>Thermal Conductivity at 20° C</i>	1.46	W/mK
<i>Melting Point</i>	1715	°C
<i>Maximum Continuous Operating Temperature</i>	950	°C
<i>Maximum Limited Operating Temperature</i>	1200	°C
Chemical		
<i>Chemical Stability</i>	High resistance to water and acids (except hydrofluoric)	

Table 3.4. Properties of full spectrum grade synthetic fused silica (Alkor).

3.3 Engine control systems

An effective and precise control of an engine operation is a resultant matter of engine management (control) system quality. This is undoubtedly a key issue in obtaining trustworthy experimental results. The hardware as well as control codes of these two single cylinder engines are mainly in-house made items, developed at the University of Oxford, Birmingham and Jaguar Cars Ltd. Indeed these include parts and software besides those that are commercially available such as electronic components: incremental encoders, standard NI cards, terminals or cables. The developed complete engine control software primarily is comprised of two separates parts (modules):

- 1) Engine Timing Control System (ETCS);
- 2) Variable Cam Timing Control System (VCTCS).

The ETCS controls the injection - ignition timing and also has the additional capability of synchronising engine run with a camera and/or laser operation. The VCTCS monitors and manages the actual camshafts phasing of the intake and exhaust valves independently. The controlling codes were written in a NI Labview™ graphical programming environment. The choice of Labview™ software was dictated by a rapid, cost-effective and primarily tight integration with most control hardware available.

The implementation of both systems ETCS and VCTCS permitted interesting tests to be conducted *e.g. with different dilution levels*. The complete engine control system was only installed for the thermal engine beacuse the optical research engine design (its design modifications-restrictions) prevented the implementation of VCTCS. A schematic of the systems' components, their arrangement and signals flow is shown in Figure 3.7.

3.3.1 Engine timing control system

The Engine Timing Control System controls the injection (PFI and DI) – ignition timing and laser - camera operation by synchronisation with engine shaft encoders (engine operation) as specified previously in this thesis. The ETCS application code was initially developed at Oxford University by ICE Group. Nevertheless for a desirable fast burn analysis needed under HCCI operation this code had to be modified to accommodate high speed encoder pulses. This was done by the author of this thesis. Consequently the controlling software could manage the injection, ignition, camera or laser triggering with a 0.1° crank angle interval as a combination of both software modifications and encoder (its resolution 3600ppr) selection. It seems clear that ETCS can output or input pulses at any desired crank angle position. An extremely useful feature for optical engine operation is the selectable skip fire mode, which prevents the engine from overheating.

The ETCS involves the following main components:

1) Camshaft and crankshaft encoders;

The camshaft and crankshaft encoders are the same type of encoders – rotary incremental optical encoders. As a cam encoder the widely used Baumer Electric product BDK 16.05A 360-5-4 of a resolution of 360 pulse per revolution (ppr) was selected. This cam encoder only supplies information about one complete revolution of the encoder wheel, which exactly corresponds to one complete engine cycle. For a crankshaft encoder the Baumer Electric manufactured article was chosen, however, from a different family: BDT 16.05A 3600-6-4 with a higher resolution of 3600 ppr. Technical specifications of these encoders are given in Table 3.5. Generally incremental encoders output three series of pulses (the encoder wheel has three rings of segments):

a) The first set of pulses called Channel A define the resolution of the encoder,

- b) The second set of pulses that are offset (out of phase) from the first set of pulses are added in order to determine the spin direction; this is Channel B and the resolution of Channel B is the same as Channel A,
- c) The third is a single pulse indicating each time the encoder wheel has made one complete revolution; this pulse is called Channel Z.

Parameter	BDK 16.05A 360-5-4	BDT 16.05A 3600-6-4
Sensing Method	Optical	Optical
Resolution (ppr)	360	3600
Pulse Tolerance	15 %	15 %
Voltage Supply	5 VDC \pm 10 %	5 VDC \pm 10 %
Maximum Supply Current no load	80 mA	60 mA
Maximum Revolutions	12000 rpm	12000 rpm

Table 3.5. Shaft encoders specifications (Baumer).

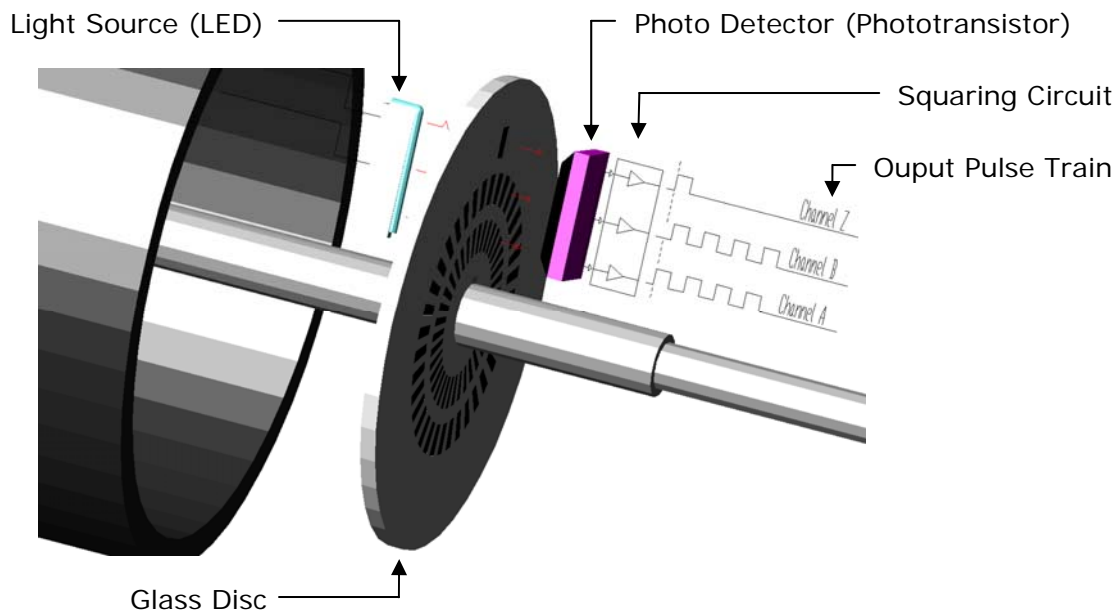


Figure 3.8. Cutaway of incremental encoder.

2) Injector of PFI system;

Standard electromagnetic multi-hole gasoline injector of Bosch® EV 14 type was chosen as a PFI injector, for its premixed operation.

3) Injector of DI system;

The third generation of 8-hole GDI Bosch® direct injector was utilised in direct injection system.

4) Ignition stick coil;

The Denso® ignition stick coil with a part number 5X43-12A366-AA1 was installed in the engine head.

5) ETCS Interface box;

An ETCS interface box provides engine control system with custom made connectivity options. The interface box serves as a communication body between PCI card (code) and the engine components, signal amplifier, noise rejecter, power supply and opto-isolator protection mechanism. The ETCS interface box inputs and outputs TTL pulses or analog signals of 5 and 12 V to and from the engine and the control computer according to the undertaken operation of the control software, indeed matching appropriate electronic components requirements.

6) Connector block;

Screw terminal CB-68LPR was mounted in the ETCS interface box for the convenient connections of inputs and outputs.

7) Cable;

The SH68-68-D1 shielded cable was used.

8) NI Timer counter card;

Parameter	NI PCI - 6602
Counter/Timers	8
Size	32 bits
Maximum Source Frequency	80 MHz
Compatibility	5 V TTL/CMOS
Digital I/O	Up to 32
Pulse Generation	Yes
Buffered Operations	Yes

Table 3.6. NI PCI-6602 technical data (NI).

The NI PCI-6602 timer counter TTL/CMOS compatible module was used for ETCS. Table 3.6 lists the technical specification of the PCI-6602 card

- 9) PC;
- 10) Labview™ application code;

The application code was developed using Labview® version 7.1. A screenshot of ETCS code is shown in Figure 3.9.

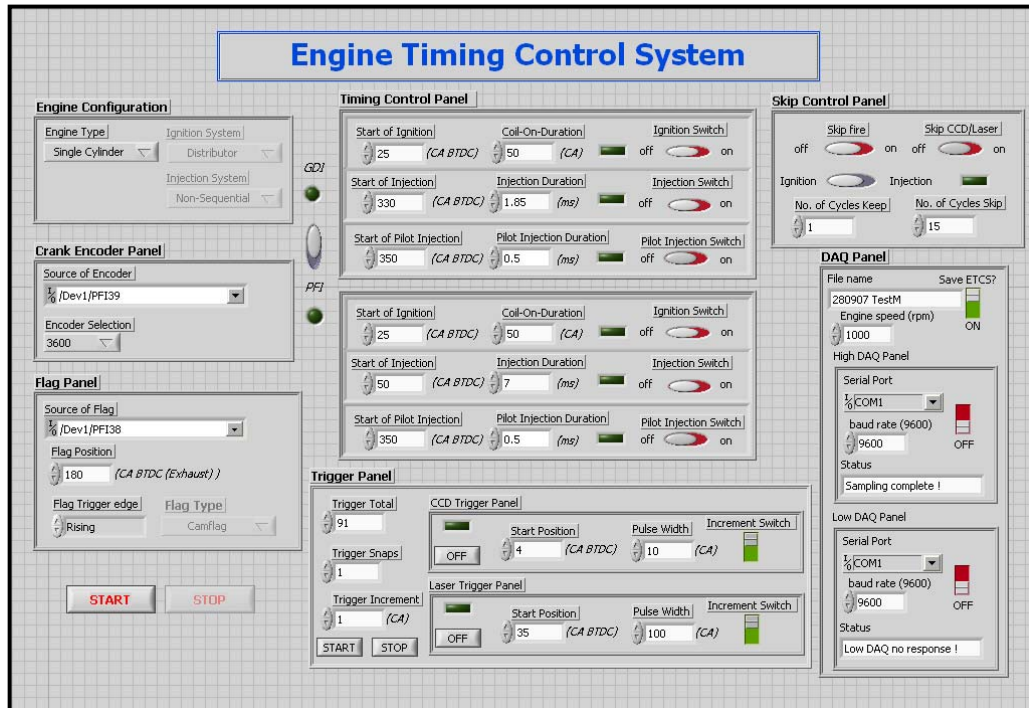


Figure 3.9. Front panel of ETCS.

Any feedback control software operation requires a few inputs to be supplied first before any output can be sent out. The instantaneous crankshaft position is continuously provided by synchronisations with the shaft encoder operations. The crankshaft encoder provides a clock signal (Channel A) and one per revolution signal (Channel Z), whilst the camshaft encoder supplies one per revolution signal (Channel Z) to the interface box. Encoder pulses are TTL ones (transistor to transistor logic). The clock signal is fed via the signal conditioning box namely here the ETCS interface box (signal processing - noise attenuation and signal amplification, power supply) and NI 6602 counter timer card into the ETCS program. The two one per revolution signals coming out from camshaft and crankshaft encoders are processed

by a flip-flop device and the artificially created pulse outputting flip-flop device is the cycle marker named crank flag pulse. This pulse is crucial for appropriate engine operation allowing control software to recognise the actual phase of the engine operation. Once the crank flag and clock pulses are fed into the ETCS, the control application code is able to communicate with electronic devices by sending out control pulses to an interface box according to the desired value set on the crank angle basis of the software front panel. TTL pulses sent out are either sent directly or appropriately processed in the interface box in order to provide efficient operation of components if needed.

3.3.2 Variable cam timing control system

The *continuous* variable cam timing control system simultaneously and independently adjusts intake and exhaust camshafts phasing in relation to the engine's crank angular position in accordance with software demands (set positions). As the engine operates with NVO strategy in HCCI operation the VCTCS can reduce or increase the amount of residuals fraction by controlling the negative valve overlap duration. Hence it is possible to start up an engine with SI operation and then transit to Homogenous Charge Compression Ignition operation on the one hand and to achieve the lowest allowable load of HCCI operation (for the given engine) on the other. The technical data of the developed variable cam timing control system at the University of Birmingham (the Labview™ control code was purely built by the author of this thesis) is tabulated in Table 3.7. A schematic drawing of fundamental VCTCS components and their locations is shown in Figure 3.10.

Performance Data		
	Shifting Range	Angle Tolerance
Intake Phasing System (IPS)	55° CA	Encoder Resolution Dependent i.e. ± 0.1° CA
Exhaust Phasing System (EPS)	50° CA	
Actuation		
Hydraulic Actuation utilizing Engine Lubrication Oil		
Control		
Labview™ Code - Closed Loop with PID Control		
Base Position		
Intake Camshaft	Maximum Advanced Position; 53° CA aTDC	
Exhaust Camshaft	Maximum Advanced Position; - 105° CA aTDC	

TDC is referred to gas exchange TDC

Table 3.7. Technical specifications of variable cam timing control system.

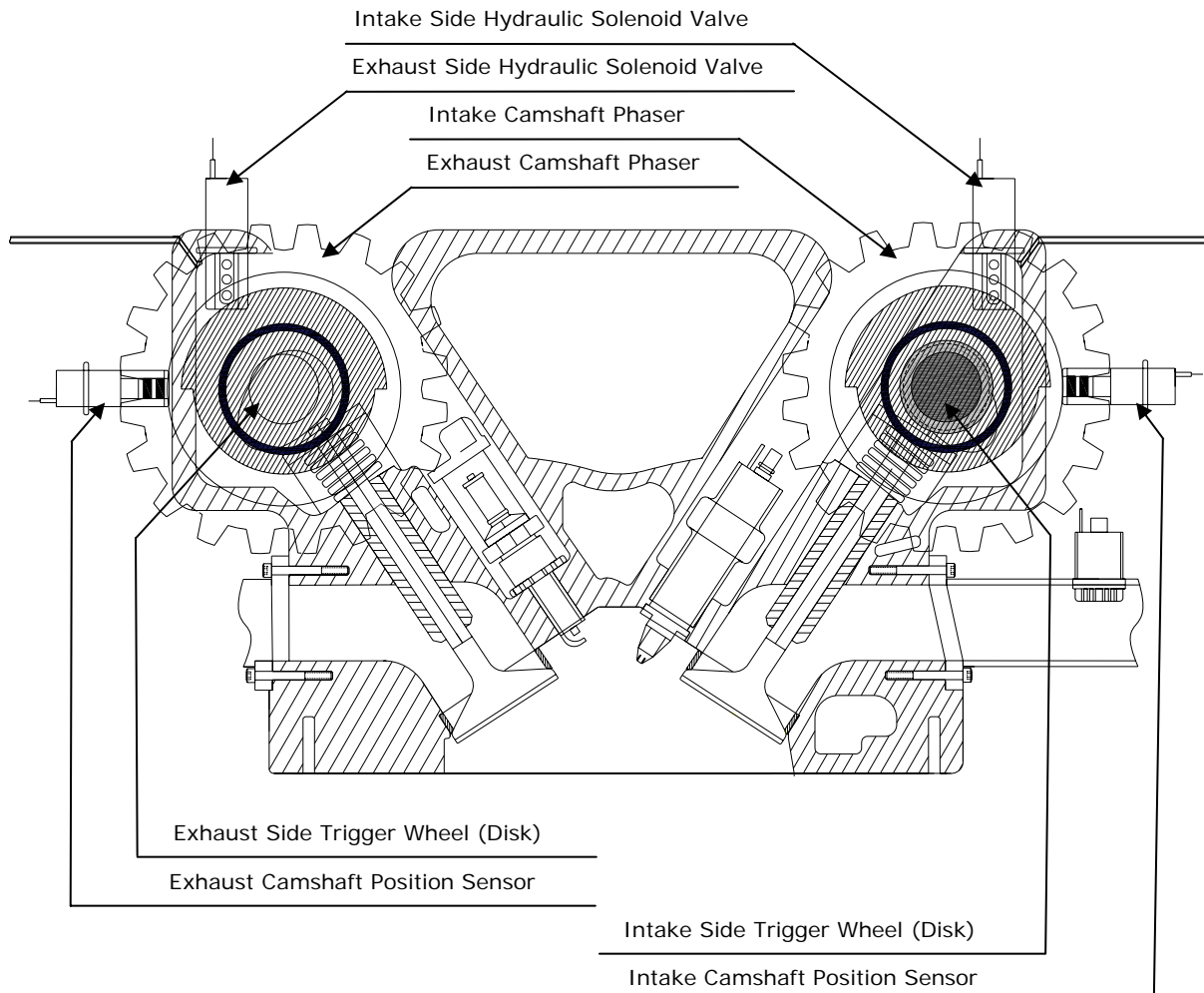


Figure 3.10. Components of VCTCS and their locations.

The variable cam timing control system involves the following key components:

1) Camshaft and crankshaft encoders;

The VCTCS shares (uses) pulses of the same encoders with ETCS. The VCT interface box receives the clock signals and crank flag signals. These TTL pulses are directly outputted from the ETCS interface box. An angle tolerance of variable cam timing control system operation is primarily dependent on the encoder's resolution as it provides time base reference. Because high resolution encoder of 3600 ppr was used the camshaft position could be monitored with a step of 0.1° CA (clock signal interval) within the shifting range.

2) Cam phaser (VCT unit);

The cam phaser unit is integrated into the camshaft gear of the timing belt drive. The principle of operation is based on the rule of sliding helical gears in which a camshaft (its pulley) is connected with the cam timing driven pulley (or sprocket in case of chain driven cam). Helical gears on the interior surface of the camshaft pulley mesh with corresponding helical gears notched on the exterior surface of the inner pulley inside the cam phaser unit.

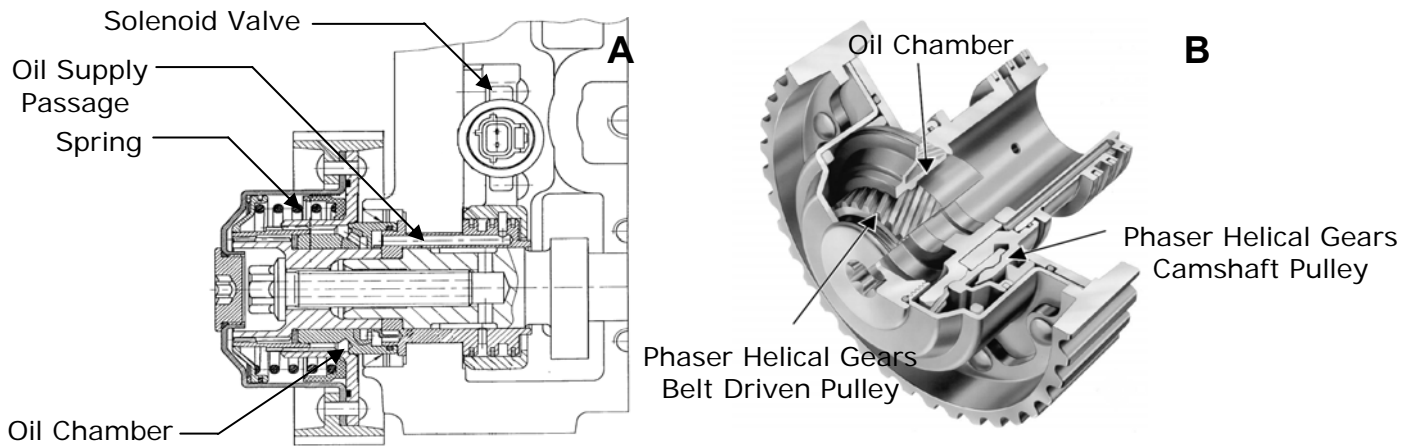


Figure 3.11. Cam phaser (Reproduced from Steinberg *et al* 1998);

A – Cross section; B – Cutaway view.

One side of the cam phaser creates an oil chamber, while the other side is spring loaded as seen in Figure 3.11. The system is hydraulically controlled and the pressurised engine

lubrication oil flow rate is governed by the hydraulic solenoid valve. This in turn controls the axial movement of camshaft rotation relative to the timing pulley through the helical teeth.

3) Hydraulic solenoid valve;

A hydraulic solenoid valve is mounted on the cylinder head and regulates the pressurised flow rate of engine lubrication oil to the oil chamber in order to advance or retard the camshaft position. The solenoid valve is 4/3 type (4 ports 3 positions; off, 50%, 100%). The position of the hydraulic solenoid valve is controlled by a pulse width modulation signal governed by control application software.

4) Camshaft position sensor;

The camshaft position sensor in VCTCS is a Hall Effect type sensor. The cam position sensor is located in close vicinity to the specially shaped disk (trigger wheel) rotating with the camshaft.

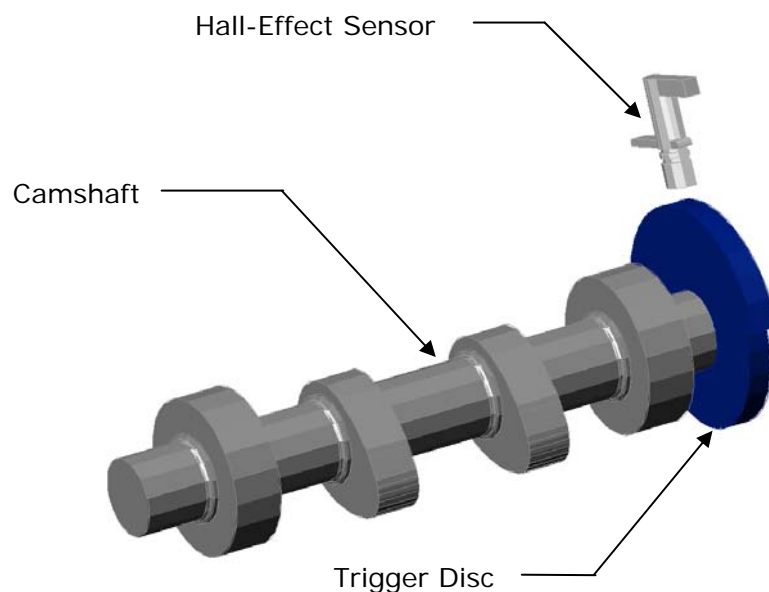


Figure 3.12. Arrangement of camshaft's trigger wheel and position sensor.

The cam position during one cycle is determined by obtaining signals from the camshaft sensor and flip-flop device (encoders' signals).

5) VCTCS Interface box;

The VCTCS interface box mainly consists of two analogous modules:

- Intake camshaft phasing control circuit,
- Exhaust camshaft phasing control circuit.

The relevant circuit of the VCTCS interface box is the processing path of the pulse width modulation (PWM) signal received from the control software. This circuit needs to output an appropriate signal with a rapid response to activate the oil control solenoid valves. The high speed transistor TIP 121 was incorporated into the circuit. The other inputs are cam position sensor signals for both the intake camshaft position and the exhaust camshaft position signal. The VCT system is also a power supply for the Hall Effect cam position sensors.

6) NI Timer counter card, connector block and cable;

The other set of the same type (as in case of ETCS) of NI hardware - timer counter card PCI 6602, shielded cable and CB 68 LPR connector block was used for VCTCS. There is no need to again describe these components since they were presented in the previous section on engine timing control system.

7) Labview™ application code;

The developed Labview™ embedded application is a quick control and fast response code for variable cam timing control. The code is comprised of two identical modules – intake and exhaust camshaft phasing control modules. As stated above this variable cam timing control system operates on a hydraulic working principle and is powered by engine lubrication oil. The system commands the shifting operation in a closed loop control (feedback control). A closed loop, rapid response control in Labview™ software was constructed using two edge separation built-in algorithms and a PID created sub-module. A two edge separation procedure in the VCTCS control code measures the amount of time between the rising edge of the crank flag signal and the rising edge of a camshaft position signal. Therefore the actual camshaft position relative to i.e. TDC gas exchange is defined. Because the clock signal is used as a timebase, the position determined is a crank angle based one.

Then the control code processes the data concerning the actual and the required camshaft position and undertakes an appropriate action. The output PWM is a signal of

constant frequency of 150 Hz with variable duty cycle. This signal is sent to the oil flow control solenoid valve via the interface box. The proportional- integral-derivative sub-module controls and determines the value of the duty cycle based on the difference between the actual and the required camshaft position (error) and importantly based on previous camshaft position history. The PID simulated algorithm consists of four modules - proportional, integral, derivative and ΔT (time constant). The output signal duty cycle is the sum of the outputs of corresponding PID modules proportional, integral and derivative.

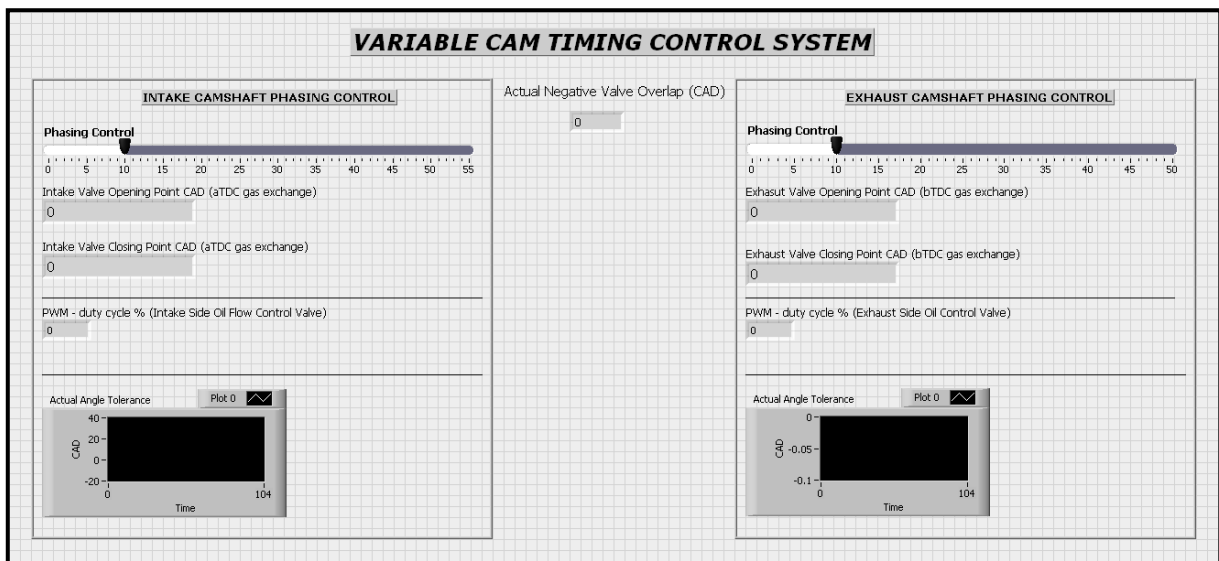


Figure 3.13. Front panel of VCTCS.

This PWM signal was used to move a spool valve that regulates the oil flow by switching the oil path designed between advancement, retardation and holding action to the cam phaser cavity. The phaser cavity changes the valve timing by advancing, retarding or holding camshafts. For an intake camshaft phasing system the base position is the maximum advanced position and the control is managed by retarding the intake camshaft; while for an exhaust camshaft phasing system the base position is the maximum retarded position. Hence the control is managed by advancing the exhaust camshaft. Indeed when the system is deactivated the camshafts remain in their base positions. It is noteworthy that the VCTCS response is affected by other factors such as engine oil pressures and therefore the engine

speed, oil viscosity and increased clearances (temperature dependent) in addition to the control modules and electronic dependencies.

3.4 Summary

Thermal (all-metal) and optical single cylinder research engines have been presented in details. Firstly the necessary modifications required and done for the conventional spark ignition engine type to HCCI engine conversion have been demonstrated, as these engines have been established for Homogenous Charge Compression Ignition operation. Then the unique features of the optical engine including the *dry* lubrication system and optical component materials were presented. The second part of the Chapter was intended to present the engine controlling systems adopted and developed in greater depth. This was accomplished demonstrating the Labview™ application codes modified or purely written in conjunction with hardware (electronics) coupled description.

Chapter 4

Diagnostic Instrumentation

4.1 Introduction

This chapter is dedicated to the presentation of diagnostic equipment (instrumentation) involved in the optical diagnostics of the combustion research covered in this thesis. This demonstrates the relevant features with the particular applicability of monochromatic intensified CCD, high-speed colour CMOS cameras and their lenses as well as the imaging spectrograph. Nevertheless this chapter begins with a brief introduction of scientific cameras, particularly characterising those parameters relevant to engine combustion research. Also potential camera noise sources and a total assessment of image noise content are illustrated in this chapter.

4.2 Fundamentals of scientific cameras

The choice of imager for scientific application is essentially dictated by several main features of a camera. They are spectral responsivity (quantum efficiency), array's sensitivity or allowable minimum light integration period. Nowadays, there are four major leading technologies (types) of scientific cameras:

- Charge Couple Device (CCD),
- Intensified Charge Couple Device (iCCD),
- Complementary Metal-Oxide Semiconductor (CMOS),
- Electron Multiplying Charge Couple Device (EMCCD).

The detectors of CCD, CMOS and EMCCD cameras fundamentally operate in the identical way. Photosensors (detector elements) accumulate charge relative to a local illumination, as photons hitting a detector surface generate the electrical charge (Photonics Spectra 2001). There are distinctions between these various camera types with regards to their charge to voltage conversion and readout processes. Consequently these cameras have diverse structures.

The iCCD camera collects photons by a means of intensifier photocathode (photosensitive surface) and an initial photon to charge conversion (electrons generation) is accomplished by the photocathode. Furthermore located away from the photosensitive area micro-channel plate (MCP) serves as an electron multiplication device. Once a signal is amplified to a demanded level the electrons are passed for detection. This is directly accomplished by a CCD in EBCCD imager (Electron Bombardment Charge Couple Device) or the phosphorus layer and then CCD array in a conventional iCCD imager. The spectral responsivity (quantum efficiency) of iCCD camera is dependent on and determined by radiation transmittance of photocathode and photosensitive array materials.

The CCD or CMOS camera array detector directly captures photons and generate electrons. As this is the case the spectral responsivity is purely determined by the characteristics of the camera's array material's spectral transmittance.

4.2.1 Imager attributes

1) **Array sensitivity** – a quantity of charge accumulated by imager array pixels per unit of input optical energy (Photonics Spectra 2001). Obviously, the more sensitive the camera the better. This is especially relevant for a high-speed or short exposure period imaging application with limited time to capture photons.

2) **Spectral responsivity** – spectral bandwidth of an electromagnetic radiation the imager is sensitive to. This feature is determined by either detector photosensors i.e. silicon

characteristics when silicon photodiodes are used - CCD, CMOS and EMCCD imager or as a combination of photocathode radiation transmittance and detector photosensors in the case of the ICCD camera (Photonik 2005). Spectral sensitivity is typically determined as a QE curve, in which the probability to detect a photon at a particular wavelength is expressed as a percentage.

3) **Fill factor** – the ratio of whole size of imager array area to the sensitive area.

4) **Uniformity** – abilities to record signal uniform across imager array pixels under identical illumination conditions (Photonics Spectra 2001). The imager array might exhibit different non-uniformity patterns under dark conditions and illumination conditions.

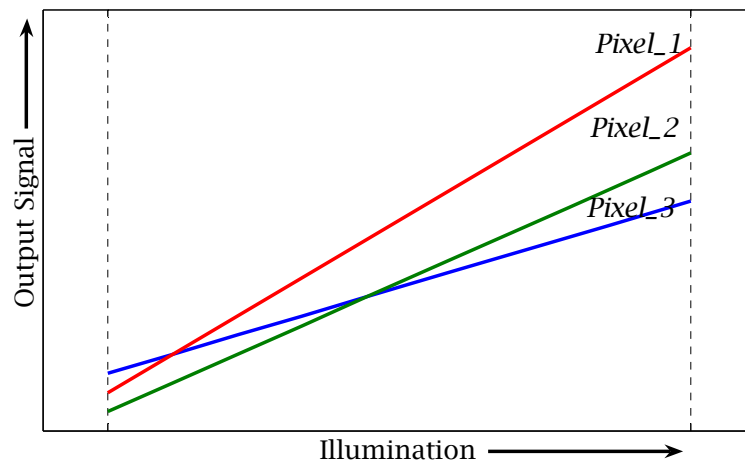


Figure 4.1. Non-uniformity patterns under various illumination conditions for three imager array elements (pixels).

5) **Shuttering** – shuttering system governs the onset and stop of the exposure period (light integration time). There are two main types of shutter systems – rolling shuttering and global shuttering system. Unlike the rolling shuttering system which expose different array parts at different time the global (uniform synchronous) shuttering system starts and stops the light integration period simultaneously for all array pixels (Photonik 2005).

6) **Windowing (sub-imaging - cropped sensor mode)** – this is an imager array ability to read out a certain part of an imager array specified as a number of individual pixels.

Consequently the image resolution is altered at the expense of a frame rate, with the trend being that as resolution decreases the frame rate increases.

4.2.2 Working principles of CCD, ICCD and CMOS imagers

CCD Camera

The comprehensive CCD camera architecture differs according to its detector structure. Hence the CCD imagers can be classified into three main subtypes (Andor Dictionary):

- Full frame CCD,
- Frame-transfer CCD,
- Interline-transfer CCD.

The full frame CCD utilizes an entire detector area in order to capture available photons (charge accumulation). When the image acquisition is completed the readout process is accomplished by consecutively shifting each row to the register output. The readout register then sends each individual pixel horizontally to an output node. Figure 4.2 schematically shows a full frame CCD camera architecture indicating significant components.

The detector area in a frame-transfer CCD is divided into two distinct parts, one collecting photons (charge accumulation) and another (shielded from light) storing collected charge. Once charge is accumulated by a first sensor's area it is immediately sent to a second "storage" zone for a transfer to shift register and finally for the readout process to occur.

The interline-transfer CCD devices are made up of a photosensitive area and charge transfer channels connected and adjacent to each photodiode. The accumulated charge at the end of image acquisition is then quickly transferred to these channels.

The camera detector surface – photosensitive area is composed of individual elements – pixels (photosensors). The light pattern projected onto the photosensitive area is reflected

by single pixels – as a photon to electrical charge (electron) conversion. Subsequently the charge is transferred horizontally by one row to the shift register when image acquisition is finished and the readout process starts. The shift register is made up of a pixels number corresponding to the camera detector surface columns number (row number elements). Also the shift register is protected from any unwanted light impact or light collection. The shift register sends each row sequentially one by one. The charges (electrons) are converted to a voltage and then amplified if required. Finally an analog signal is converted to a digital equivalent, in fact being a digital image representation.

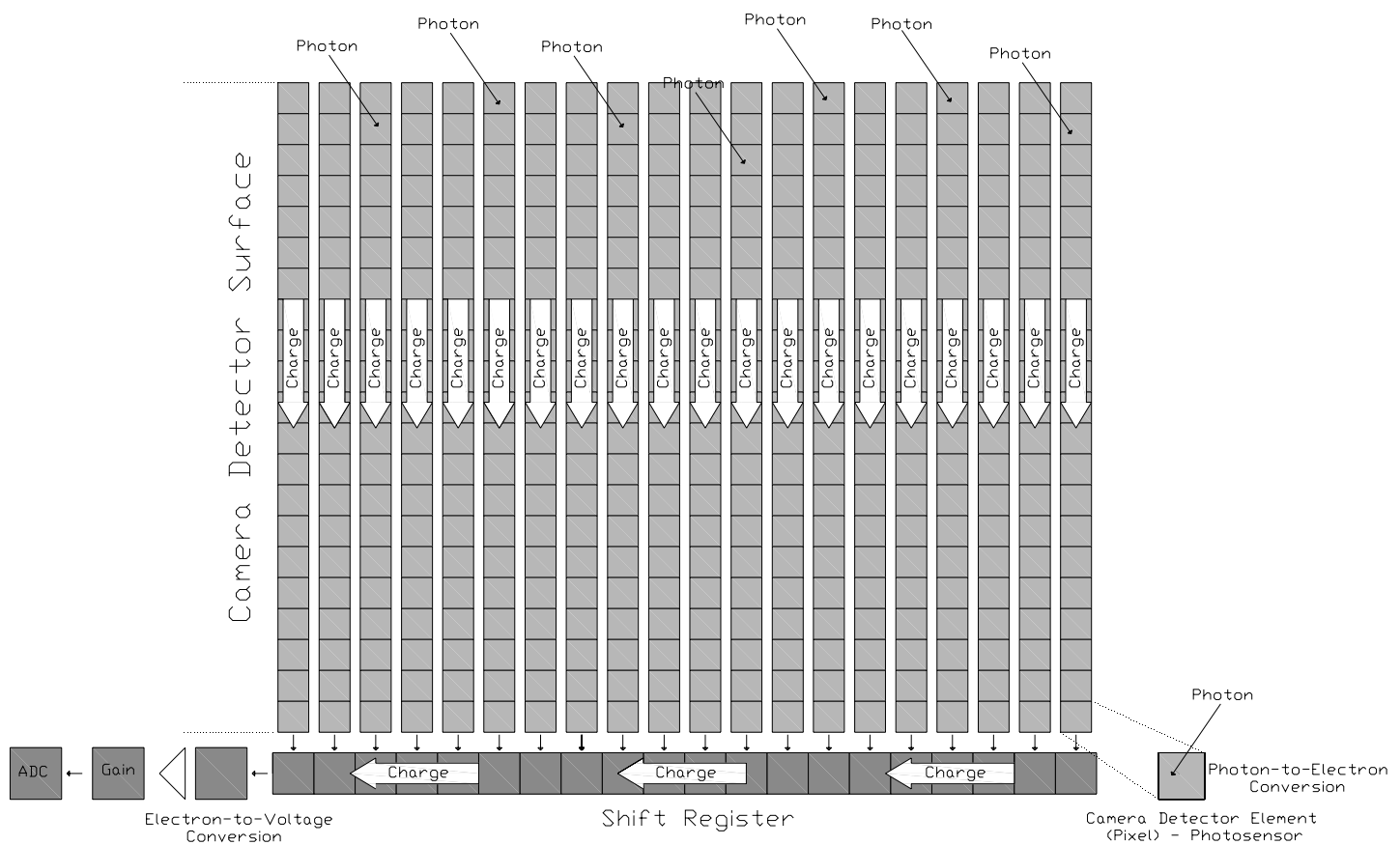


Figure 4.2. Schematic representation of full frame CCD camera architecture.

transfer to a CCD array and the phosphor coated on the optic window coupler converts electrons into a light pattern for a CCD device detection. The device (intensifier) performance is defined by these three main components – photocathode, microchannel plate and phosphor screen. The spectral response of an intensifier is dictated by a combination of an input window and the photocathode installed (coated) material transmittance characteristics - photocathode material's absorption and transmission properties (Andor Dictionary). Fundamentally, the input window defines a lower wavelength limit and the photocathode longer (the other end) wavelength response. The phosphor emission is generally selected to match with the CCD camera response, and ICCD camera spectral response is determined by a combination of both spectral responsivities of an intensifier and a CCD array.

CMOS Camera

The CMOS detector type camera like the pure CCD array integrates light utilising a photosensors area. Photons falling on the sensitive detector are initially converted to electrical charge. Nevertheless, unlike conventional CCD imagers the CMOS pixel charge is further converted to a voltage for an individual pixel independently and simultaneously. Moreover besides photon-to-electron conversion, each individual detector element (pixel) integrated with its own electronics converts charge to voltage and performs other functions e.g. timing control (shuttering – by integrating transistor). The CMOS device features parallel readout i.e. pixels row readout process could be accomplished along with a chosen row by an addressing register or alternatively a column multiplexer is capable of selecting an individual pixel at the same time. The spectral responsivity of CMOS is dictated by transmission properties of photosensitive array material.

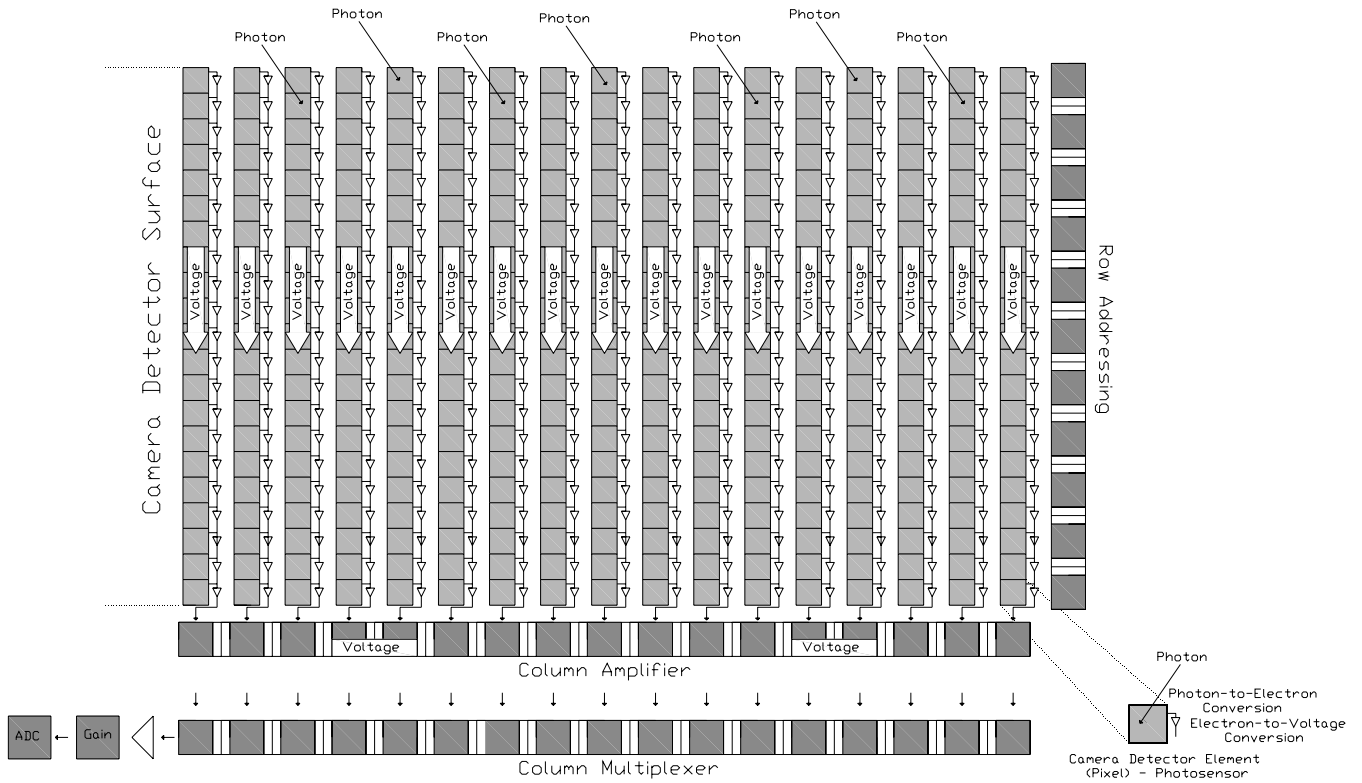


Figure 4.4. Schematic representation of CMOS imager architecture.

4.3 Andor iStar iCCD imager and UV-Nikkor lens

4.3.1 Andor iStar iCCD camera

The application of an intensifier to CCD imager results in an excellent suitability for imaging conditions of an ultra-weak light emission and/or with short light collection periods available. Indeed these conditions are commonly found in an engine combustion research field. Therefore iCCD imagers become precious instruments for those types of research.

The monochromatic Andor iStar iCCD (DH734I – 18 F – 04) was used to conduct significant part of the combustion experiments covered in this thesis. This camera, more specifically a camera model uses the second generation of Andor intensifier with the photocathode coated on a quartz window. This configuration limits the observable electromagnetic radiation to the region of 180 to 850 nm wavelengths. Indeed this is with

different quantum efficiencies as a function of wavelength as shown in Figure 4.6. This is represented by a blue line curve, quartz window with coated on it 'W' photocathode intensifier type of iCCD imager model.



Figure 4.5. Andor iStar iCCD camera (model DH734I – 18 F – 04).

The small modification, namely a replacement of a quartz window onto a magnesium fluoride (MgF_2) would extend the spectral responsivity to 120 nm.

The technical specification of Andor iCCD camera (DH734I – 18 F – 04) are summarized in Table 4.1.

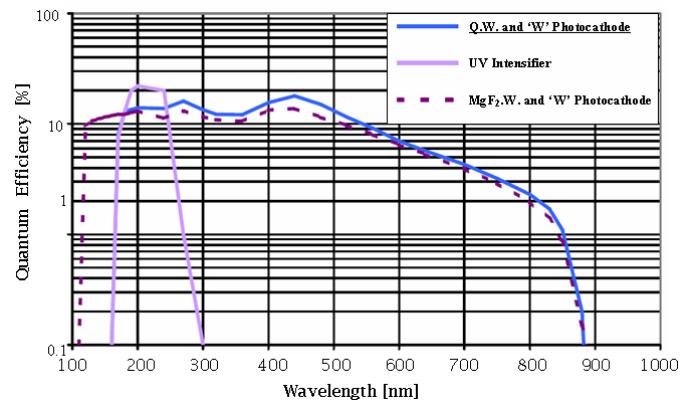


Figure 4.6. The spectral responsivity curves versus wavelength for Andor iStar imagers.

The model Andor iCCD DH734I – 18F – 04 is represented by a blue line curve. (Reproduced from Andor iStar iCCD DH734I Camera Technical Guide).

Technical Data	Andor iStar iCCD DH734I-18F-04 Camera
General Features	
Number of Pixels (CCD Array)	1024 x 1024
Effective Pixel Size (square)	13 μm
Optical Active Area (CCD Array)	13.3 x 13.3 mm
Entire System Spectral Range (Spectral Responsivity)	180 – 850 nm
Peak Quantum Efficiency	up to 18% @ 440 nm
Typical Quantum Efficiency	15 % @ 440 nm
Minimum Quantum Efficiency	13.5 % @ 440 nm
Linearity	1 % maximum
Intensifier Characteristic	
Intensifier Diameter	18 mm
Minimum Optical Gate Width	2 ns
Total Insertion Delay	\approx 35 ns
Input Window Type (Material)	Quartz
Intensifier Spectral Range	180 – 850 nm
Phosphor Type	P46
Phosphor Decay Time (to 10%)	200 ns
Maximum Photocathode Rep Rate	50 kHz
Readout Noise	
Typical and Maximum @ 31 kHz	3 and 6 (e^-)
Typical and Maximum @ 1 MHz	8 and 16 (e^-)
Synchronization/Data Acquisition Control	Internal / External – TTL Type Pulse

Table 4.1. Specification of Andor iStar iCCD camera (DH734I – 18 F – 04).

The iStar iCCD camera control could be accomplished either internally or externally by supplying an external TTL type pulse(s). A number of acquisition types e.g. single scan or accumulation mode are available and constitute a wide suitability for a range of various applications. This particular model DH734I – 18 F – 04 is also equipped with Digital Delay Generator (DDG) and IntelliGate™. The IntelliGate™ system synchronises the photocathode with MCP operation – switches both on and off simultaneously. This is used in order to prevent energetic photons from reaching the CCD sensor while photocathode is in an off state i.e. UV photons might have capabilities of passing through the photocathode when it is off (Andor iStar iCCD DH734I Camera Technical Guide). The camera cooling system was installed in order to reduce dark current noise.

4.3.2 UV-Nikkor 105 mm f/4.5 lens

This UV-Nikkor 105 mm f/4.5 lens was coupled with the recently discussed Andor iStar iCCD camera model for diagnostics of the engine combustion presented in this thesis. This lens was purposely developed for ultraviolet photography with the simultaneous capability of visible light and near infrared regions photography. The lens spectral transmittance spans from 220 to 900 nm. The transmittance curve of 200-900 nm is quite flat approaching as high as 70 % of transmittance. The broad spectral transmittance range of this lens was achieved by appropriate materials selections such as fluorite and quartz lenses to manufacture this lens (Nikon UV-Nikkor 105 mm f/4.5 Lens - Brochure/Manual).



Figure 4.7. UV-Nikkor 105 mm f/4.5 lens.

The UV-Nikkor 105 mm f/4.5 lens does not require additional focusing for UV region imaging, apart from the visible light focus. This is due to the improved chromatic aberration compensation (virtually no variation in the focus position between visible and UV light). Refocusing is needed for infrared photography. The technical specifications of UV-Nikkor 105 mm f/4.5 lens is given in Table 4.2.

As a combination of the Andor iStar iCCD (DH734I – 18 F – 04) camera spectral acceptance and UV-Nikkor 105 mm f/4.5 lens transmittance characteristics the entire system spectral range spans from 220 nm to 850 nm. The lens cuts-off some UV light observation from the camera (iCCD 180 – 850 nm), while some near infrared region observations are restricted by the camera (lens 220 – 900 nm).

iCCD Camera

The intensified CCD performance and operation is primarily affected and governed by an intensifier. This is an intensifier which controls (gates) the light collection period (although the CCD exposure time is also settable separately), and further amplifies the received signal. The intensifier is located before the CCD matrix and is comprised of three major components – photocathode, microchannel plate (MCP) and phosphor screen as seen in Figure 4.3. The photocathode is installed (coated) on the inner surface of a front window.

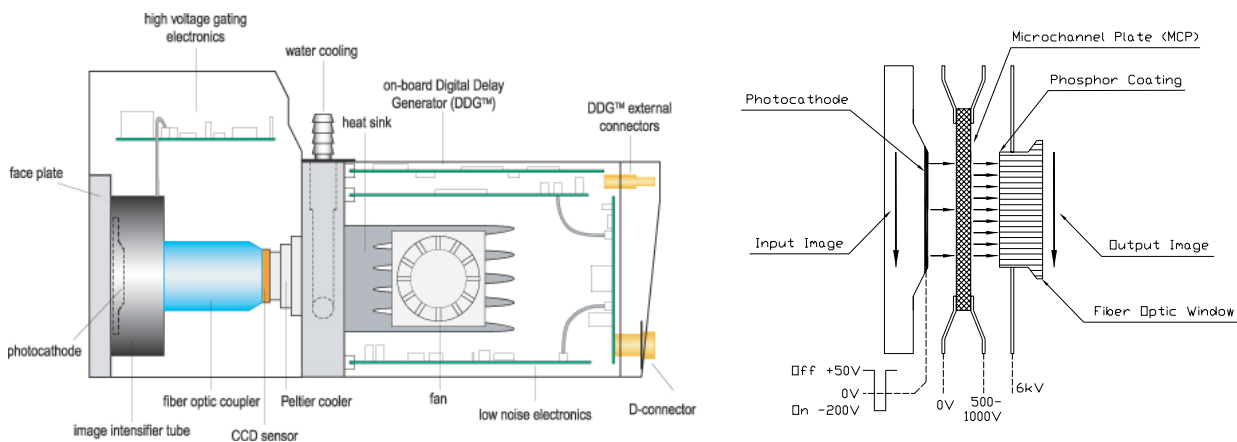


Figure 4.3. Cutaway of iCCD imager (Andor Product Overview) and intensifier cross section.

The light integration period is governed by a photocathode of an intensifier. Applying a negative voltage between photocathode and MCP an operation is commenced and photons hitting the photocathode area liberate photoelectrons. Positive voltage ceases the light acquisition operation – electrons will not have sufficient energy in order to exit photodiode. These liberated electrons are directed to MCP (caused by an electric field) for amplification process. The high potential is applied to microchannel plate in order to amplify the incoming signal. The potential applied to MCP corresponds to the gain selected (the camera system itself – dynamic range or operator). The outgoing electrons then strike a phosphorous coating of a fiber optic widow (coupler). The fiber optic coupler component acts as an image

Technical Data	UV-Nikkor 105 mm f/4.5 Lens
Spectral Transmittance Range	220 – 900 nm
Focal Length	105 mm
Maximum Aperture	f/4.5
Aperture Scale	f/4.5 – f/32
Lens Construction	6 elements 6 groups
Picture Angle	23° 20'
Distance Scales	Graduated 0.48 m to infinity (∞)

Table 4.2. Technical specifications of UV-Nikkor 105 mm f/4.5 lens.

4.4 Phantom CMOS imager and Nikon 24-85 mm lens

4.4.1 Phantom CMOS camera

The color Phantom v 7.1 CMOS detector camera in configuration with RGB 24-bit depth (8-bit per color plane) sensor was used to perform high-speed colour imaging of the engine combustion research observations presented in this thesis. The camera detector spectral responsivity covers the 400 to 1000 nm (VIS and NIR) wavelengths spectral part of electromagnetic radiation (Phantom v7.1 CMOS Color Camera Technical Guide). Indeed this is with various quantum efficiencies for different wavelengths. A graph of quantum efficiency (QE) on wavelength dependency is shown in Figure 4.8A. The imager's area sensitivity (spectral responsivity) to each of the primary RGB color model camera channels (pixel component or just pixel) versus wavelength is depicted in Figure 4.8B. These curves clearly illustrate that the maximum transmittance value of individual colour channel, red, green and blue matches the natural wavelength values of these colours (red 700, green 546.1 and blue 435.8 nm). Technical specification of Phantom v 7.1 type colour camera is listed in Table 4.3.

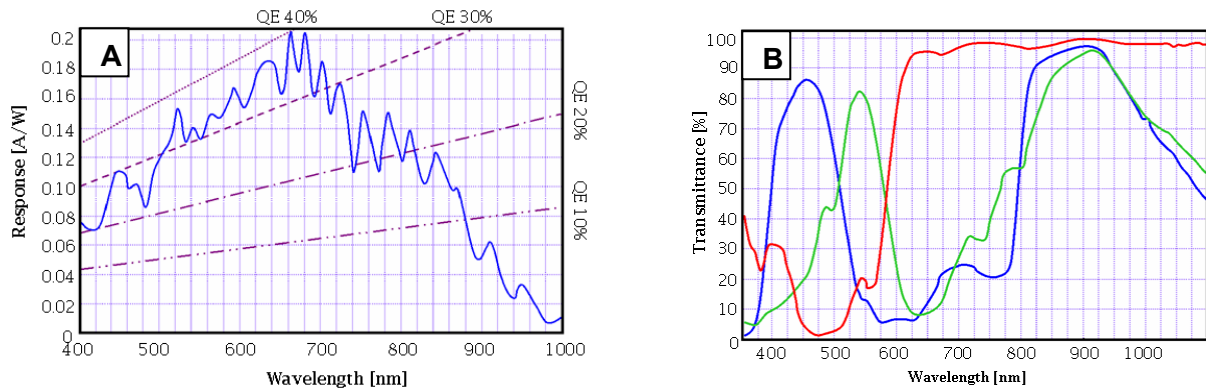


Figure 4.8. Spectral responsivity (quantum efficiency) curves for Phantom v7.1 CMOS color camera: A) General spectral responsivity curve; B) Spectral responsivity curves for each individual color – red, green and blue (Reproduced from Phantom v7.1 CMOS Color Camera Technical Guide).



Figure 4.9. Phantom v7.1 color CMOS camera.

The comprehensive camera Phantom v7.1 operation is synchronized, using the capabilities of accepting two separate TTL inputs to match camera operation with recorded events. The pulse supplied for the first input starts the acquisition while the second input pulse, i.e. more detailed pulse train, drives the camera sampling rate (image separation interval). For the field of engine combustion research this configuration is of significant relevance, because it allows a straightforward crank angle resolved image acquisition, instead of real time basis acquisition which is associated with an inevitable changes of real time crank-angle degrees duration.

Technical Data	Phantom v 7.1 Color CMOS Camera
Sensor	CMOS 24 bit (Color Array)
Number of Pixels	800 x 600
Effective Pixel Size (square)	22 μm
Optical Active Area (CMOS Array)	17.6 x 13.2 mm
Fill Factor	$\approx 65\%$
Spectral Range	400 – 1000 nm
Peak Quantum Efficiency	up to 40% @ 680 nm
Frame Rates @ Resolution	
Maximum @ Minimum Resolution	160000 (fsp) @ 32 x 32
@ Maximum Resolution	4800 (fsp) @ 800 x 600
Resolution System	Continuously Adjustable 16 x 8 Pixel Increment
Minimum Exposure Time	2 μs
Exposure Control	Fixed or/and Extreme Dynamic Range
Shutter System	On Chip Global Shuttering
Readout Noise	≈ 27 (e^- rms)
Synchronization/Image Acquisition Control	Internal / External – TTL Type Pulse
Camera On-Board Memory Size	1024 MB

Table 4.3. Specification of Phantom v7.1 CMOS color camera.

The Phantom v7.1 colour camera was utilised to perform high-speed colour HCCI observations. Reflecting real colors, allowing high-speed crank-angle imaging it provides a powerful tool for a process analysis of a single cycle and analysis of a cycle-to-cycle process, especially when proper image processing methods are applied to the obtained images.

4.4.2 Nikon 24 – 85 mm f/2.8 – 4 IF lens

The Phantom v 7.1 CMOS type colour camera was joined with a standard zoom lens Nikon 24-85mm f/2.8-4D IF of zoom ratio 3.5 and internal focusing. Even though this lens features a maximum reproduction ratio of 1:2 from 35 - 85 mm it is classified as macro lens according to the manufacturer specification (Nikon 24-85 mm f/2.5 – 4D IF Lens - Brochure/Manual). The Nikon 24-85mm f/2.8-4D IF lens technical data are summarized in Table 4.4.

Technical Data	Nikon 24-85mm f/2.8-4D IF Lens
Spectral Transmittance Range	Matching Phantom v7.1 Camera (Exact Spectral Transmittance Range is Confidential)
Focal Length	24-85 mm
Focal Length Scale	24 mm, 28 mm, 35 mm, 50 mm, 70mm, 85 mm
Maximum Aperture	f/2.8-4
Aperture Scale	f/2.8 – f/22
Maximum Reproduction Ratio	1:2 (35-85)
Lens Construction	15 elements 11 groups
Picture Angle (with 35mm format)	84° - 28° 30'
Distance Scales	Graduated 0.5 and 0.21 m to infinity (∞)

Table 4.4. Technical specifications of Nikon 24-85mm f/2.8-4D IF lens.



Figure 4.10. Nikon 24 – 85 mm f/2.8 – 4 IF lens.

The spectral transmittance range of the Nikon 24 -85 mm f/2.8-4D IF lens is confidential and therefore could not be disclosed by the manufacturer. As this lens was used coupled with Phantom v7.1 camera we were only assured (by a Nikon Company) that the lens spectral transmittance covers the Phantom v 7.1 spectral range acceptance. As this is the case the entire system the Phantom v 7.1 CMOS type color and Nikon 24 – 85 mm f/2.8 – 4 IF lens allows observations to be performed with a limited spectral range spanning from 400 nm to 1000 nm - covering generally VIS and some NIR regions.

4.5 Oriel MS260i imaging spectrograph

The Oriel MS260i™ 1/4m Imaging Spectrograph Model 74050 was coupled with the Andor iStar ICCD DH734I – 18F – 04 imager to carry out spectroscopic investigations covered in this thesis. This given imaging spectrograph model is equipped with triple grating mounts of 300, 600 and 1200 lines(grooves)/mm types (Oriel MS260i™ ¼ m Imaging Spectrograph Brochure). Indeed the spectral range, resolution and blaze wavelength or best efficiency are dependent upon the grating (groove density) and operational settings such as slit width. The spectrograph minimises the effect of the stray light. Table 4.5 lists the most relevant technical data of Oriel MS260i™ 1/4m Imaging Spectrograph 74050 model.

Technical Data	<i>Oriel MS260i™ 1/4m 74050 Imaging Spectrograph</i>		
Grating	300 (lines/mm)	600 (lines/mm)	1200 (lines/mm)
Blaze Wavelength	500	400	750
Peak Efficiency (%)	85	80	80
Spectral Resolution ³	0.98 nm	0.5 nm	0.25 nm
Wavelength Region of Grating Efficiency ≥ 20%	250 – 1150 nm	250 – 1300 nm	450 – 1200 nm

Table 4.5. Technical data of Oriel MS260i™ 1/4m 74050 imaging spectrograph.

The communication with the spectrograph such as grating selection or center wavelength is achieved via the ICCD controlling software. By rotating the grating different spectral wavelengths windows are acquired. The slit width is controlled manually. The calibration was performed with 6025 Mercury –Argon Oriel Instruments Spectral Calibration Light, which emits a number of known spectral lines.

³ Spectral Resolution was measured with 10µm x 2mm slit and 26 x 26 µm pixel array (1024 pixels) (Oriel MS260i™ ¼ m Imaging Spectrograph Brochure).

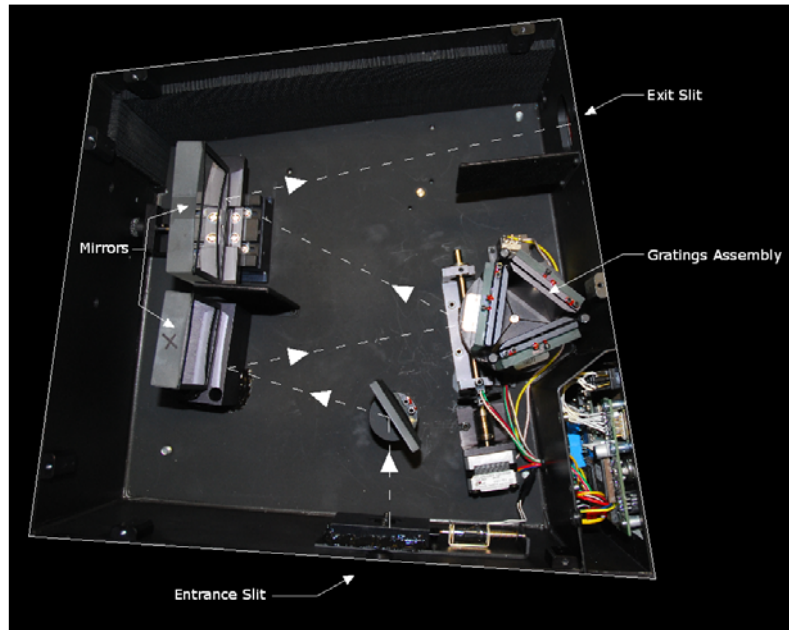


Figure 4.11. Oriel MS260i™ 1/4m Imaging Spectrograph 74050 inside. The dashed line shows the radiation (light) pathway.

4.6 Potential noise sources of imager and image noise content analysis

4.6.1 Potential noise sources of camera

Image noise content is always resultant by a combination of both the imager inherent noise characteristics and its actual operating settings. Potential camera's noise sources are primarily identical for any imager regardless of its technology i.e. CMOS, CCD or EMCCD. Only the particular individual noise contributor characteristic might be different. Despite the fact that the noise characteristic of an imager is a wide and complex theme the potential noise sources could be simplistically classified into three main categories (Photonics Spectra 2001, Photonik 2005 and Andor Dictionary):

- Thermal Noise (Dark Current Noise),

- Readout Noise,
- Photon Noise:
 - Fixed Pattern Noise (FPN),
 - Random Noise (RN).

Thermal noise also alternatively named as dark current noise is one generated by free electrons liberating from imager photosensitive array material as a result of thermal effect (Andor Dictionary). The dark current noise is the camera's array temperature on the one hand and available time dependent on the other. The thermal noise contribution to total noise is intensified with exposure period or temperature increase or as a combination of both.

The readout noise is related to noise originating from the readout process (Andor Dictionary) charge-to-voltage, and then voltage (analog signal)-to-digital conversions. Though readout noise characteristics could vary marginally with camera circuits' temperature (electronics such as analog to digital converter) these changes are so relatively small that it is assumed that readout noise is constant magnitude linked up with the imager regardless of instantaneous settings. Therefore readout noise becomes more prominent at gradually shortened exposure periods.

Photon noise originates from variations caused by photon number count by an array photonsensors (individual array pixels) (Photonics Spectra 2001, Photonik 2005 and Andor Dictionary). This could correspond to variations across array's pixels in one measurement or at the same pixel location in independent consecutive measurements, indeed under identical illumination and exposure period conditions. Further the photon noise can be broken down into two subgroups: fixed pattern noise (FPN) and random noise (RN) (Photonics Spectra 2001). The fixed pattern noise is seen as repeatable irregularities across array pixels from shot-to-shot. The RN occurs with no repeatable pattern in relation to location or time or alternatively as a combination of both. The FPN varies with illumination conditions and could exhibit different patterns (across array's pixels) as illumination conditions change. The photon noise is dependent on signal strength and the exposure period.

The second and third in sequence noise contributors discussed above - readout noise and photon noise can have more pronounced effects for CMOS detector type cameras than for CCD cameras (Photonik 2005). This is because most of the functions performed in CMOS cameras are integrated in singular array's cells as modules. As this is the case it is assumed that CMOS imagers are more prone to noise in general (elevated total noise level) than their counterparts CCD or iCCD cameras. The iCCD imager is also dominated by any sort of the aforementioned individual noise contributor in which dark current noise originates additionally from the thermally generated electrons in the photocathode. As this happens before the MCP plate (amplifier) this initial noise is amplified.

4.6.2 Image noise content analysis

The previous section presented potential imager noise sources in a theoretical way as this constitutes a constructive background for image noise content analysis. The assessment of image noise content is based on the evaluated signal to noise ratio (SNR) indications and is based on visualisation of pixels intensities distributions of images of interest both individual and ensemble-average dark frames. Contrasting a characteristic of a single frame with an ensemble-average image characteristic provides an insight into how the image noise content pattern can be changed by adding a few individual noisy images.

All dark frames presented or used in the analysis were acquired for identical settings of corresponding diagnostic devices under dark room conditions (light off). The dark frame acquisition settings for both imagers are listed in Table 4.5.

Signal to noise magnitudes were estimated according to the following formula:

$$SNR = 20 \log_{10} \left(\frac{\overline{M}(y, x)}{std(M(y, x))} \right);$$

where: $\overline{M}(y, x)$ - Analyzed Image or Region of Interest Global Mean Pixel Intensity,

$std(M(y, x))$ - Analyzed Image or Region of Interest Global Standard Deviation.

The SNR value determined in this way defines the level of pixel intensities non uniformities within the comprehensive image area or eventually image predetermined region of interest (ROI).

Technical Data	CMOS color Phantom v7.1	iCCD Andor i-Star
Number of Pixel	640 x 480	1024 x 1024
Sensor	CMOS 24 bit colour array	iCCD 8bit monochromatic array
Exposure Time	120 μ s	166 μ s
Intensifier Gain	-	50
Exposure Control: Extreme Dynamic Range	Disabled	Disabled
Camera Temperature	Not specified	253 K
Shutter System	On Chip Global Shuttering	
Synchronization	External	External
Trigger and Sync Image	TTL rising edge	TTL rising edge

Table 4.6. Cameras settings of dark frames acquisitions.

The characteristics of dark frames, the individual and ensemble-average acquired by Andor iStar imager, are illustrated Figure 4.12. A similar comparison of Phantom v7.1 camera dark frames is depicted in subsequent figure – Figure 4.13. The left column of Figures 4.12 and 4.13 (Figs 4.12A, 4.13A, 4.13B & 4.13C) shows single dark frame pixels distributions intensities, while right column of the same figures (Figs 4.12B, 4.13D, 4.13E & 4.13F) refers to ensemble-average dark frames characteristics. As RGB color model image is composed of three separate monochromatic images the pixels intensities distributions are shown for each individual colour plane separately for RGB dark images (Phantom v7.1 camera). The numerical representations of dark frames characteristics are summarised in Table 4.6 and 4.7 for iCCD and CMOS imagers' dark frames respectively.

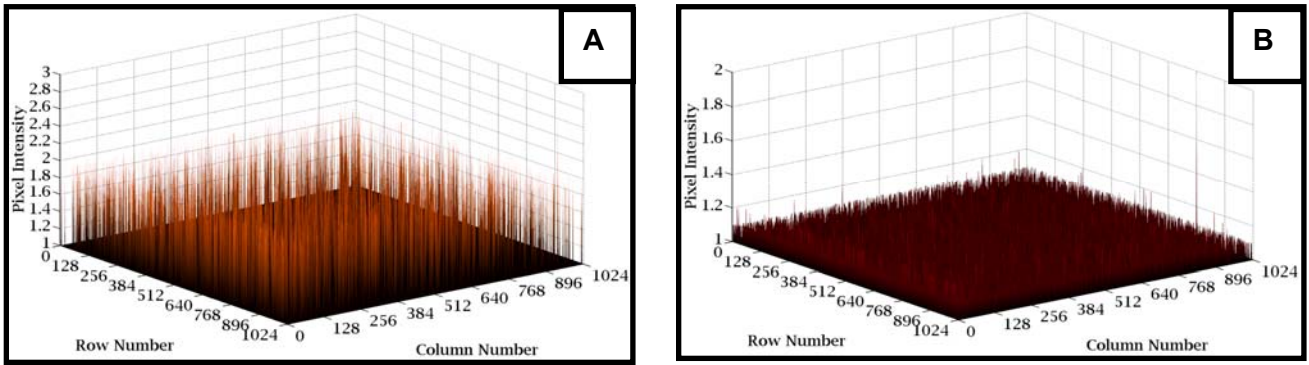


Figure 4.12. Individual (A) and ensemble-average dark frames (B) pixels intensities distributions of iCCD camera.

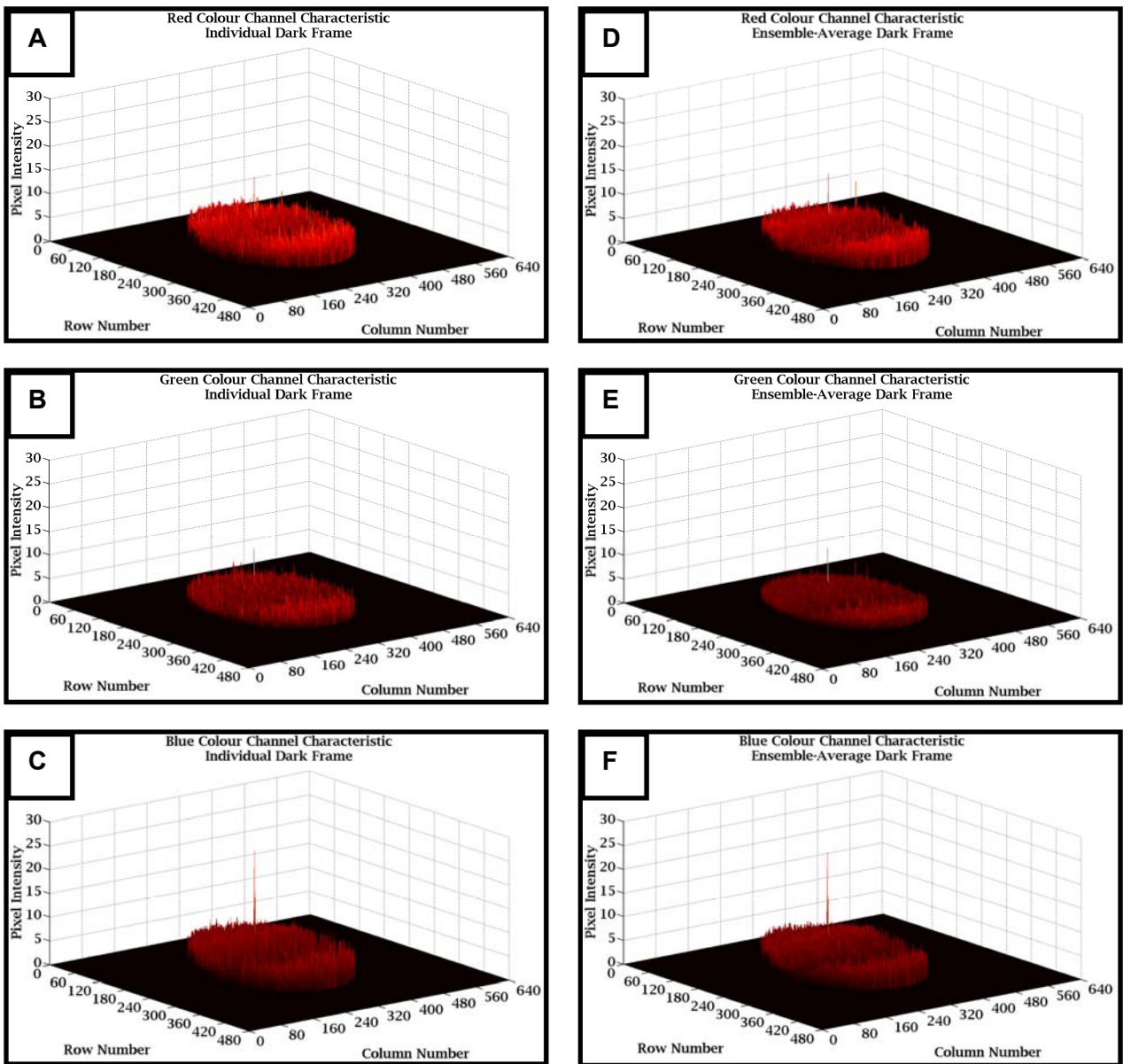


Figure 4.13. Individual (A,B,C) and ensemble-average dark frames (D,E,F) pixels intensities distributions of CMOS camera.

Dark Frame	Characteristic				
	<i>Min. Pixel Intensity</i>	<i>Max. Pixel Intensity</i>	<i>Mean Pixel Intensity</i>	<i>Standard Deviation of Pixel Intensities</i>	<i>SNR [dB]</i>
Individual	1	3	1.0021	0.0458	26.8
Ensemble-Average	1	2	1.0018	0.0136	37.3

Table 4.7. Individual and ensemble-average dark frames characteristics of iCCD camera.

Dark Frame	Channel	Characteristic				
		<i>Min. Pixel Intensity</i>	<i>Max. Pixel Intensity</i>	<i>Mean Pixel Intensity</i>	<i>Standard Deviation of Pixel Intensities</i>	<i>SNR [dB]</i>
Individual	<i>Red</i>	0	14	1.8	1.19	3.6
	<i>Green</i>	0	12	0.97	0.67	3.2
	<i>Blue</i>	0	25	1.98	1.2	4.3
Ensemble-Average	<i>Red</i>	0	15.2	1.92	0.99	5.8
	<i>Green</i>	0	12.2	1	0.51	5.9
	<i>Blue</i>	0	24.5	2.12	1.02	6.4

Table 4.8. Individual and ensemble-average dark frames characteristics of CMOS camera.

The analysis of colour dark frames was limited to the combustion chamber area only as a predetermined region of interest. This was achieved superimposing mask image onto the dark frame and excluding the region beyond the combustion chamber from computational analysis.

Comparing corresponding graphs of Figures 4.12 and 4.13 the different patterns of pixel intensity distributions of a single dark frame versus an ensemble-average frame is evident. The tabulated data listed in Tables 4.6 and 4.7 confirm the observed trend illustrating more uniform pattern of signal intensity distribution for an ensemble-average dark image in contrast to an individual one. Consequently the ensemble-dark frames are characterised by elevated magnitudes of estimated signal to noise ratios than their corresponding single images. As the different noise pattern of the corresponding analysed images has been noticed it is beneficial to refer to the theoretical background of imager noise sources

presented in a past section. As stated, the initial uncorrected image noise content is comprised of the following noise traces - thermal noise, readout noise and photon noise: fixed pattern and random noise. Indeed this seems to be the case for a single image and therefore is valid (relevant) for an individual dark frame, its image noise content. Further the ensemble-average dark frame noise content and observed reduction in pixels non-uniformity are probably due to a random noise smoothing out effect (RN rejection during averaging process). This could be explained from the nature of random noise as it occurs at different locations, and averaging from image to image significantly suppresses its presence in the ensemble-average image. As a result It might be inferred that total noise content of an ensemble-average image is fundamentally restricted to thermal, readout, fixed pattern noise contents with an insignificant suppressed amount of random noise. It also seems that the amount of suppressed thermal noise and thus the amount of its presence in ensemble-average image is highly dependent on the number the ensemble-average image is composed of.

4.7 Summary

The diagnostic instrumentations, monochromatic iCCD and high-speed colour CMOS imagers along with their lenses UV-Nikkor 105 mm f/4.5 and Nikon 24-85 mm f/2.8-4 IF have been presented in detail. Also a MS260i imaging spectrograph system has been described. These instrumentations constitute diagnostic equipments utilized in the optical measurements of engine combustion research conducted within this thesis.

The introduction to working principles and attributes of CCD, iCCD, CMOS imagers including relevant issues such as imager potential noise sources have been addressed in depth. Finally the scrutiny and assessment of dark frame noise contents have been performed.

Chapter 5

Data Acquisition and Processing

5.1 Introduction

This chapter discusses the acquisition systems and processing methods of engine conventional operating variables. The Labview™ developed codes of engine traditional parameters acquisition systems and their instrumentations (hardware) are presented in great depth. Then the devised software for combustion analysis performed also in Labview™ graphical programming environment is addressed. This is presented along with the discussion of data processing ways utilised for extracting relevant combustion analysis (parameters). The second part of this chapter is dedicated to the acquisition and processing of images and optical data of different sorts from optical experiments. As optical data acquisition is straightforward and dependent upon particular diagnostic instrumentation this is only briefly presented. Detailed emphasis is drawn to the optical data processing methods, starting with ways of correcting image noise including several thresholding techniques. For image autoignition and combustion activities analysis three major devised, adopted or modified techniques (image processing) are introduced. As this image processing analysis was preformed in Matlab® programming language these techniques particular assumptions such as area or distance evaluations are addressed in relation to general image processing foundations as well as to those available in Matlab®.

5.2 Engine conventional data acquisition and processing

5.2.1 Data acquisition systems – codes and instrumentation

To log the engine operational variables in order to quantify these engine data and to determine combustion characteristic two data acquisition codes were developed in a Labview™ graphical environment and successfully implemented into the engines systems by the author of this thesis. They are high and low speed data acquisition systems abbreviated to HSDAQ and LSDAQ respectively. These systems - HSDAQ and LSDAQ are principally identical for two single cylinder research engines - thermal and optical. The minor exceptions concern only the channel order or channel number specified because recording of the additional parameter(s) required could vary from engine to engine. The systems instrumentations and measuring devices (transducers or meters) are generally the same kinds for both engines unless otherwise stated.

The high speed data acquisition system was elaborated to record signals of higher natural frequency sensors e.g. in-cylinder pressure transducer. The sampling rate of the HSDAQ system was controlled by an external source i.e. crankshaft encoder clock signal with 0.1° crank angle intervals (3600 ppr shaft encoder). The technical specification of this shaft encoder has been described in detail in section 3.3.1. The gated flag pulse (TDC marker determination) of the crankshaft and the camshaft pulses (one per engine revolution pulses) is used to start the data acquisition. This solution completely eliminates the unavoidable and undesirable changes of the data acquisition start on crank angle basis experienced only if the camshaft one per revolution pulse is used. This is a result of the belt driven camshaft system of the research engine, more specifically the belt flexibility. The flag signal could be defined at any engine cycle position and referred to TDC gas exchange. Then a predetermined required engine cycles number is collected.

The HSDAQ system acquires in-cylinder pressure, intake sensor output and barrel pressure (absolute in-cylinder pressure at given crank angle) histories. Cylinder pressure measurements were made with a Kistler® 6051A piezoelectric pressure transducer mounted on the cylinder head and a Kistler® 5011B charge amplifier for the optical engine. For the thermal engine the same measurements were accomplished with a water-cooled Kistler® 6041 pressure transducer interconnected with the same type of aforementioned charge amplifier. The specifications of Kistler® 6051A and water-cooled 6041 are listed in Table 5.1.

Technical Data	Kistler® Pressure Transducers	
	6051A	6041
Measuring Range	0 – 250 bar	0 – 250 bar
Overload	300 bar	300 bar
Natural Frequency	160 kHz	70 kHz
Sensitivity Change	$\leq \pm 0.5 \%$ (200° C \pm 50°C) $\leq \pm 2 \%$ (23 - 350°C)	$< \pm 0.5 \%$ (200° C \pm 50°C - cooled) $< \pm 2$ (200° C \pm 150°C - noncooled)
Thermal Shock Error (at 1500 1/min, $p_{mi} = 9$ bar)		
Δp (short time drift)	$\leq \pm 0.5$ bar	$< \pm 0.25$ bar
Δp_{mi}	$\leq \pm 2 \%$	$< \pm 2 \%$
Δp_{max}	$\leq \pm 1.5 \%$	$< \pm 1 \%$

Table 5.1. Technical specifications of Kistler® 6051A and 6041 pressure transducers.

The additional in-cylinder absolute pressure values once engine piston is around BDC were monitored by the Druck PMP 1400 pressure transducer installed in the cylinder barrel for optical engine.

Technical Data	Druck® Pressure Transducer PMP 1400
Measuring Range	0 – 4 bar (absolute)
Operating Temperature Range	-20° C to +80°C
Supply Voltage	10 V
Output Voltage	0 – 5 V
Temperature Effect (-20 to +80°C)	
Typical Total Error Band	$\pm 1.5 \%$
Maximum Total Error Band	$\pm 2 \%$

Table 5.2. Technical specifications of Druck® PMP 1400 pressure transducer.

These indications serve for the in-cylinder pressure referencing (pegging) process. For the thermal engine data the pegging process was achieved using intake manifold air pressure measurements. The same kind of pressure transducer Druck PMP 1400 was utilised to track the intake air (intake manifold) pressure history for both engines. The pegging process utilising absolute in-cylinder pressure values as in the case of optical engine solution in this study permits a more precise (accurate) in-cylinder pressure referencing (pegging) process to be achieved. This is due to use of direct cylinder pressure at a corresponding crank angle instead of intake manifold pressure thereby eliminating the influence of unavoidable pressure drops across valves.

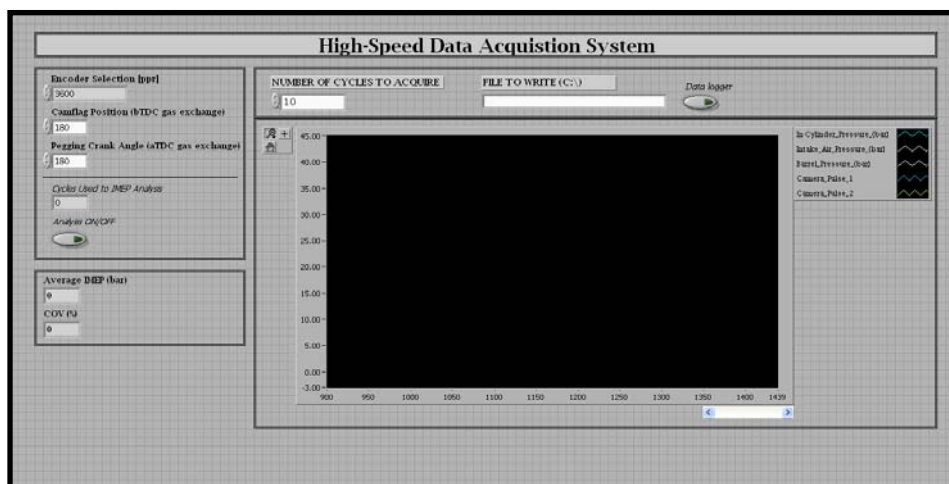


Figure 5.1. Front panel of high-speed data acquisition system.

For optical experiments the high-speed data acquisition system was modified by adding two channels, one to record the image acquisition start and the other camera governing sampling rate (image inter-frame interval) pulses train. This provided a means of actual image acquisition onset and individual image grabbing point verifications as related to the crank angle degree and the in-cylinder pressure history. It is noteworthy that the HSDAQ system was modified to accommodate the indicated mean effective pressure (IMEP) module in order to define on-line the operating point of experiment.

The employment of LSDAQ system was necessary to record the other sensor outputs of lower natural frequencies (response). This low speed data acquisition system was triggered

by a constant internal acquisition rate (internal clock) corresponding to 70 Hz. The LSDAQ system logged volumetric air flow, mixture strength measurements and also standard K-type thermocouple readings such as intake air temperatures (at volumetric air flow meter and in intake manifold), cylinder barrel temperature, coolant temperature, exhaust gases temperature or engine oil temperature. Volumetric air flow was measured using a positive displacement flow meter Romet[®] G40 certified gas meter. The displaced gas volume was monitored electronically by coupling geared shaft encoder (Baumer BDK 16.05A 360-5-4) to a positive displacement air flow meter. The frequency of one per revolution output signal of the encoder provided volumetric air flow indications. The thermocouple readings from one installed in the vicinity of the air-flow meter (intake air line) permitted the air mass flow rate to be evaluated based on the volumetric air flow indications. The mixture strength was monitored by a broadband Bosch[®] Universal Exhaust Gas Oxygen (UEGO) sensor incorporated in ETAS LA3 system.

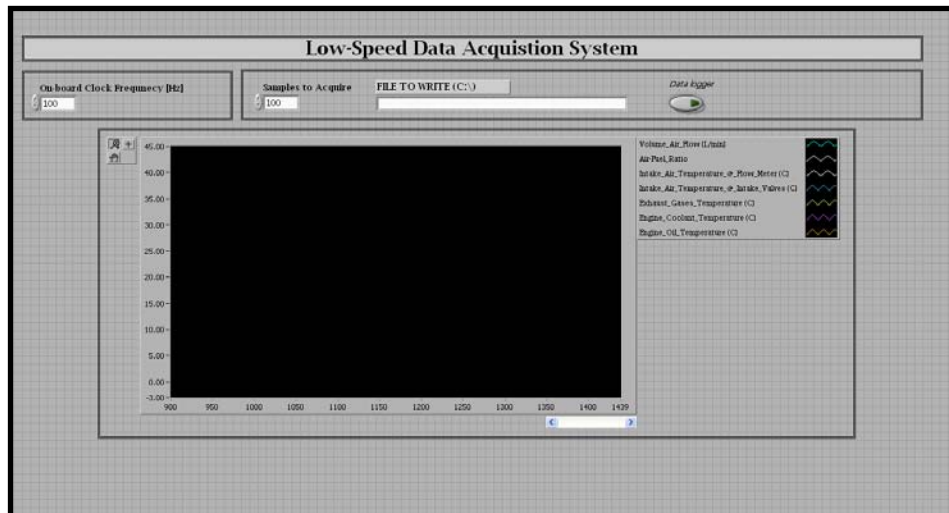


Figure 5.2. Front panel of low-speed data acquisition system.

The signals of both data acquisitions systems were fed to two PCI-6023E interface cards via the BNC 2090 National Instruments shielded rack-mountable connector. Also most of the LSDAQ's signals were conditioned prior to delivery to a connector block and interface card. The brief, relevant technical data of NI PCI-6023E interface card are summarized in Table 5.3.

Interface Card	NI PCI 6023E
Analog Inputs	16SE / 8DI
Input Resolution	12 bits
Maximum Sampling Rate	200 kS/s
Input Range	± 0.05 to ± 10 V
Analog Outputs	0
Digital I/O	8
Counter/Timers	2, 24 –bit
Triggers	Digital

Table 5.3. Technical specifications of NI PCI 6023E interface card.

HSDAQ and LSDQ systems record and store data in a user predetermined pattern. Each single channel measurements is represented by a corresponding column of points (rows) in a saved i.e. chosen text file matrix. The channel configuration and channel order are programmable in Labview™ application or in a NI Measurement and Automation Explorer according to requested user demand. The selected data storage to text file makes a convenient way for further data analysis, which can be conducted in any other programming language.

Figure 5.3 illustrates the overall arrangement of data acquisition systems and signals flow.

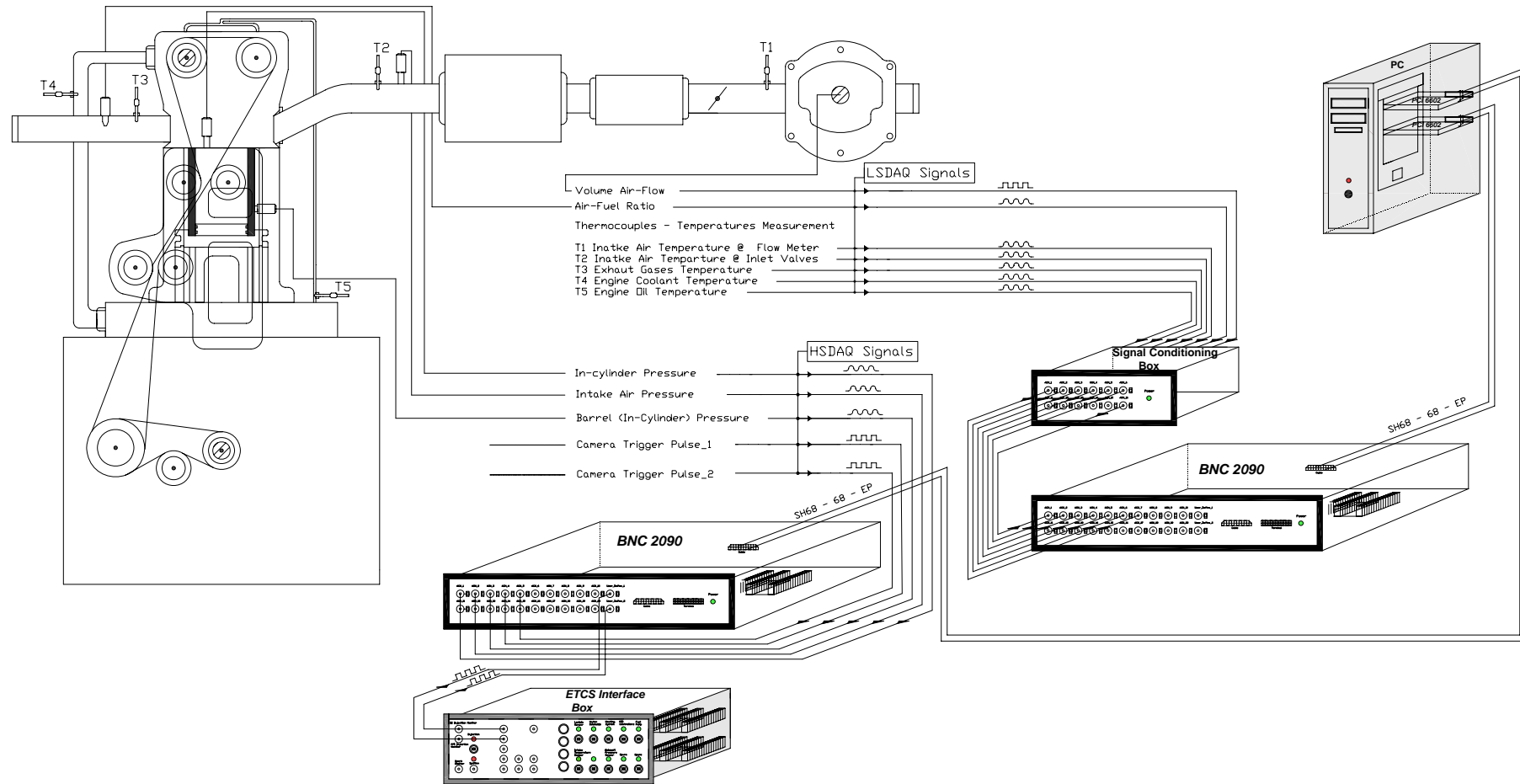


Figure 5.3. Complete arrangement of data acquisition systems and signals flow.

5.2.2 Data analysis

A Labview[™] application was developed in order to process the acquired engine operating variables and extract relevant parameters that define autoignition and combustion characteristics. The code reads saved data from a text file format and display them as an optional function if there is a need; thereby an insight into raw data is provided.

The first approach in data processing is to reference the acquired in-cylinder pressure. The referencing, often called the pegging process is necessary for piezoelectric in-cylinder pressure transducer drift compensation and is necessary to bring forth the in-cylinder pressure transducer readings to the absolute values. The pegging could be accomplished in a number of different ways (H.Zhao *et al* 2001). In our study this was achieved using manifold intake air pressure transducer readings for the thermal engine data and barrel pressure transducer indications for the optical engine. The procedure is straightforward and relies on referencing the raw in-cylinder pressure measurements based on any of the aforementioned pressure transducer readings at the predetermined engine cycle point i.e. induction stroke BDC. This is executed for each individual cycle recorded.

As the in-cylinder pressure is referenced the developed data analysis code is ready to perform comprehensive combustion characteristic analysis. This devised Labview[™] code covers combustion parameters of individual and average cycles with simple statistics, including the determination of standard deviation and coefficient of variation values. The comprehensive data analysis constitutes the determination of the following in-cylinder pressure derived combustion parameters:

- Indicated mean effective pressure (IMEP);
- The magnitude and location of maximum in-cylinder pressure (Pmax);
- Mass fraction burned (MFB) and its cardinal points;
- Heat release rate (HRR) and its characteristic points;
- Rate of pressure rise;

- Trapped residuals mass and ratio to fresh charge;
- Crank angle position of optical data/image start of acquisition and grabbing point.

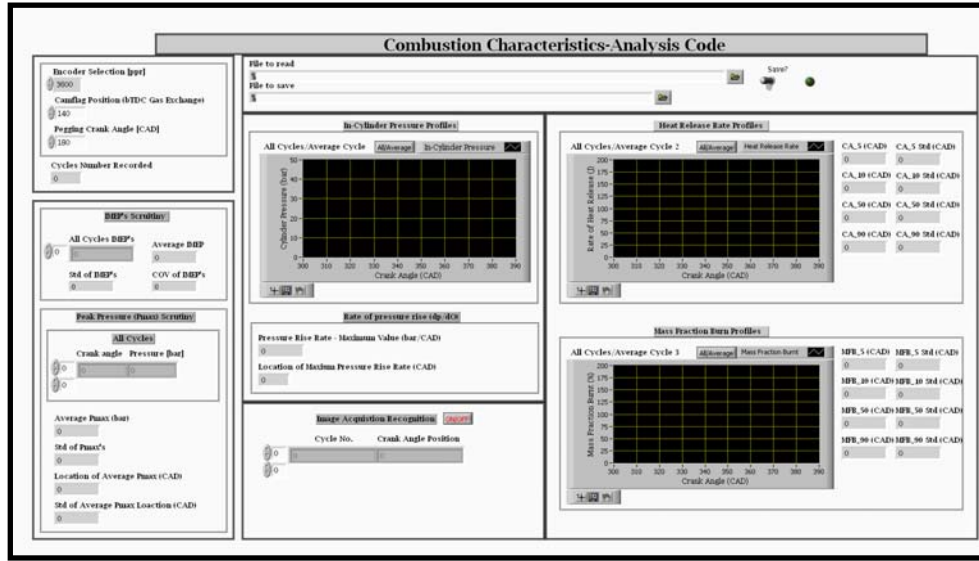


Figure 5.4. Front panel of Labview™ combustion analysis code.

The indicated mean effective pressure is a straightforward procedure of p-V engine cycle integration diagram with a further relation to cylinder swept volume, from

$$W = \int_{V_{BDC}}^{V_{TDC}} p dV$$

$$IMEP = \frac{W}{V_s}.$$

The computational method of mass fraction burn was initially developed and firstly presented by Rassweiler and Withrow (H.Zhao *et al* 2001). This procedure essentially assumes that in-cylinder pressure rise is owing to the combined effect of volume changes and combustion (during combustion period):

$$\Delta p = \Delta p_v + \Delta p_c;$$

Δp – pressure rise

Δp_v – pressure rise due to volume changes

Δp_c – pressure rise due to combustion changes.

$$\Delta p_v = p_i \left[\left(\frac{V_i}{V_{i+1}} \right)^n - 1 \right],$$

p_i – pressure at given crank angle

V_i – volume at given crank angle

V_{i+1} – volume at subsequent crank angle.

Pressure rise due to combustion could be evaluated as follows:

$$\Delta p_c = \Delta p_{i+1} - \Delta p_i \left(\frac{V_i}{V_{i+1}} \right)^n.$$

As combustion typically does not take place at constant volume, the obtained combustion pressure rise data should be referenced to a clearance volume:

$$\Delta p_c^* = \Delta p_c \left(\frac{V_i}{V_c} \right).$$

Once the above parameters are established the mass fraction burned could be estimated according to the following equation:

$$MFB = \frac{\sum_{i=1}^i \Delta p_{*c}}{\sum_{i=1}^N \Delta p_{*c}}.$$

The analysis of heat release rate in a developed Labview™ combustion analysis involved the standard procedure; indeed, based on the first law of thermodynamics differentiating engine swept volume and recorded in-cylinder pressure values. Fundamentally this method is determined as:

$$\frac{dQ}{dt} = \frac{\gamma}{\gamma - 1} p \frac{dV}{dt} + \frac{1}{\gamma - 1} V \frac{dp}{dt}.$$

These heat release rate calculations were performed with fluctuating specific heats ratio γ (c_p/c_v) as engine cycle conditions change i.e. during compression, combustion and expansion.

The mass fraction burn and heat release rate obtained profiles are highly dependent on the polytropic index (exponent) or specific heat ratio chosen (Heywood 1988). The polytropic index (exponent) for MFB calculations was evaluated based on polytropic relationship from known available in-cylinder pressure traces and cylinder volumes (p-V diagram) for compression and expansion stroke separately. The fluctuating specific heat ratios (γ) were obtained with respect to temperature and equivalence ratio dependency. These gamma values used for an analysis were computed for each crank angle independently based on the evaluation of internal energy u and gas constant R according to Krieger *et al* (1967):

$$u = K_1(T) - K_2(T) \cdot \phi; [kJ / kg];$$

$$K_1(T) = 0.692 \cdot T + 39.17 \cdot 10^{-6} \cdot T^2 + 52.9 \cdot 10^{-9} \cdot T^3 - 228.62 \cdot 10^{-13} \cdot T^4 + 277.58 \cdot 10^{17} \cdot T^5;$$

$$K_2(T) = 3049.33 - 5.7 \cdot 10^{-2} \cdot T - 9.5 \cdot 10^{-5} \cdot T^2 + 21.53 \cdot 10^{-9} \cdot T^3 - 200.26 \cdot 10^{-14} \cdot T^4;$$

$$R = 0.287 + 0.020 \cdot \phi; [kJ / kg \cdot K];$$

The trapped residuals mass was estimated using ideal gas law. At the exhaust valves closing point cylinder volume is known and the in-cylinder pressure was recorded. The trapped residuals temperature was assumed to be the same as the exhaust gases temperature, which was measured. The residuals mass to total charge mass (fresh air inducted and residuals mass) ratio constitutes estimated iEGR mass fraction. The residuals gas constant used in the iEGR fraction estimation was taken from Heywood (1988) and corresponds to the isooctane (2,2,4 trimethylpentane) stoichiometric conditions combustion data (combustion products – burned gases). More specifically the gas constants were calculated from the universal gas constant and molecular weights for unburned and burned gases given in Hewyood. Due to the simplicity of the method and thus uncertainties involved, e.g. temperature assumption or gas constant for residual, the computed values should be treated as estimates. Thus in fact this provide more qualitative rather than quantitative insight.

The statistical parameters, standard deviation and coefficient of variation illustrate how the experimental data are spread from the observed mean. The standard deviation magnitudes presented in this thesis were evaluated according to the following formula:

$$Std = \sqrt{\frac{\sum_{i=1}^n (x_i - \bar{x})^2}{n-1}}; COV = \left(\frac{Std}{\bar{x}} \right) \cdot 100\%.$$

x_i – single measurement; \bar{x} – average measurement; n – number of measurements.

5.3 Optical data/image acquisition

The different kind of optical data and images were collected from optical work utilising diagnostic equipment discussed in detail in the previous chapter. Indeed the optical data and images were acquired with a predetermined acquisition mode and stored in a particular file format available for a given measurement equipment. The optical data and image processing were entirely performed using Matlab® programming language. The Matlab® supports the binary, monochromatic, RGB color model and indexed images of the logical, single and double precision floating-point or unsigned integer classes.

The monochromatic iCCD images were stored as a two-dimensional array of raw data with raw grey-level values spanning with the possible signal from 0 to the saturation value across the image matrix. This signal (individual pixel intensity) is a direct form of camera counts. As this camera supports only slow mode of image acquisition only one image per cycle with fifteen cycles skip mode was captured.

The spectroscopic measurements data were also processed as raw data. Each individual matrix column was related to a particular wavelength of electromagnetic radiation.

The colour CMOS camera records and stores true-colour images as a 24bit RGB colour model. Therefore three-dimensional RGB colour model image array is represented by three grey-level (monochromatic) images (3-D array). Each individual pixel colour of true image is

defined by a combination of red, green and blue colour intensity stored in each colour plane at the corresponding pixel location. As images were digitised with 24 bits pixel depth each colour plane is an 8-bit monochromatic image. Hence the total range of values equals 256 levels in each plane, which spans from 0 to 255 for discrete levels or from 0-1 for floating point (continuous) levels. The colour images were stored as TIFF 24-bit images.

5.4 Optical data/image processing

The first approach in optical data or image processing should constitute a removal of a potential noise or errors content. The potential noise sources and final raw image noise content has been shown and analysis performed in sections 4.6.1 and 4.6.2 of the previous chapter. As presented the individual frame or optical data matrix is restricted to the dark current, readout, fixed pattern and random noise traces. It has also been shown that the averaging of a few raw individual images lead to a significant amount of random noise removal (suppression).

Even though there are a number of various image noise correction ways (Gonzales *et al* 2002), the initial step in optical data/image noise reduction is identical – background image from test image subtraction. Apparently this is true for conditions in which the background image(s) e.g. dark frame(s) could be acquired, under the same ambient conditions and equipment settings as test images. Conclusively from the brief image noise content analysis shown and from inferred information it could be said that background image subtraction completely corrects thermal noise, readout noise and fixed pattern noise once ensemble-average background image is used. This leaves some or even most of the random noise portion of a resultant image. This happens because the ensemble-average image contains smoothed out RN traces. The same operation conducted with an individual background image i.e. dark frame, could be directed to erroneous pixel intensity distribution of the resultant image due to the nature of random noise, which occurs at different locations from

image to image. Any initial and raw optical data and image noise corrections were performed as an ensemble-average dark frame subtraction in this thesis. Thus it appears that any presented optical data or image noises were limited to random noise pattern content after dark frame subtraction.

The remaining optical data or image noise content or alternatively any initial noise could also be eliminated by applying appropriate mathematical operations such as filters (linear and non-linear) or segmentation techniques (Gonzales *et al* 2002). Nevertheless the selection of the appropriate method is not trivial; frequently the enhancing of the total image quality may lead to the deterioration or changing of other inherent image aspects. Schiessl *et al* (Schiessl *et al* 1999) reported that using filters in the image noise rejection process requires a proper mask size (pixels number neighbour) to be chosen and the obtained results are dependent on this aforementioned parameter.

As the some image processing computational operations could only be performed in Matlab[®] on the binary (two-level) images, the thresholding techniques were applied to define appropriate threshold levels for images. The threshold level was determined as a single-level global one. The thresholding techniques were only applied for the high-speed camera images, since only they provided a means for a single and a cycle-to-cycle autoignition and combustion analysis to be performed. In fact image thresholding of those images might have contributed considerably to the elimination or partial reduction of the remaining uncorrected random noise traces. Because the determination of an appropriate threshold level is not a trivial process in some cases, four various widespread known image thresholding techniques (Gonzales *et al* 2002; Malina *et al* 2008; and Otsu 1979) were examined for our purposes. These are following methods:

- Image Histogram based Triangle Algorithm Procedure,
- Otsu Technique,
- Gray Level Gradient Technique,
- Iterative Method.

The detailed procedures of these utilised image thresholding techniques are discussed in Appendix B.

These four segmentation techniques were employed to the test image shown in Figure 5.5 A & C have produced two significantly different threshold levels. Three of these four techniques: Otsu, Gray Level Gradient and Iterative generated consistent results: an identical threshold level value. This was the only Image Histogram based Triangle Algorithm Procedure which produced significantly elevated segmentation level value. Plotting thresholded images along with primary image in Figure 5.5 clearly shows how variations in image derived information e.g. area size, combustion area(s) contours are thresholding value dependent. Also noteworthy is that a proper evaluation of threshold level is essentially more important for images containing first auto-ignition or combustion sites than at a later combustion stage, since minor changes in threshold level can significantly contribute to over or under estimation of the analysis parameters at these initial stages.

The purpose of examining these four techniques in our study was to gain insight into the results and derive the most proper threshold value. It is noted that the applicability of any of these aforementioned segmentation techniques is restricted to a two-dimensional image size array. However, the segmentation process of a colour image (3D image array) could be performed by employing a thresholding technique to each individual monochromatic image (2D array) separately, thereby the threshold level for each individual colour plane is established. But this stands beyond the scope of this study, because the further image processing methods and their operations are mostly based on binary images. Thus the color images (24-bit images) were firstly converted to 8-bit grey-scale (monochromatic) images with predetermined coefficients of red, green and blue pixel intensity plane conversion.

As one of the further presented devised image processing techniques to a great extent relies on an image normalised histogram and its statistical descriptors, it is worthwhile to present theme beforehand. Also the general and Matlab[®] supported assumptions of the image area object and image objects distance are described further. They are addressed

here as a computational approaches basis for a particular image processing techniques introduced also in this chapter.

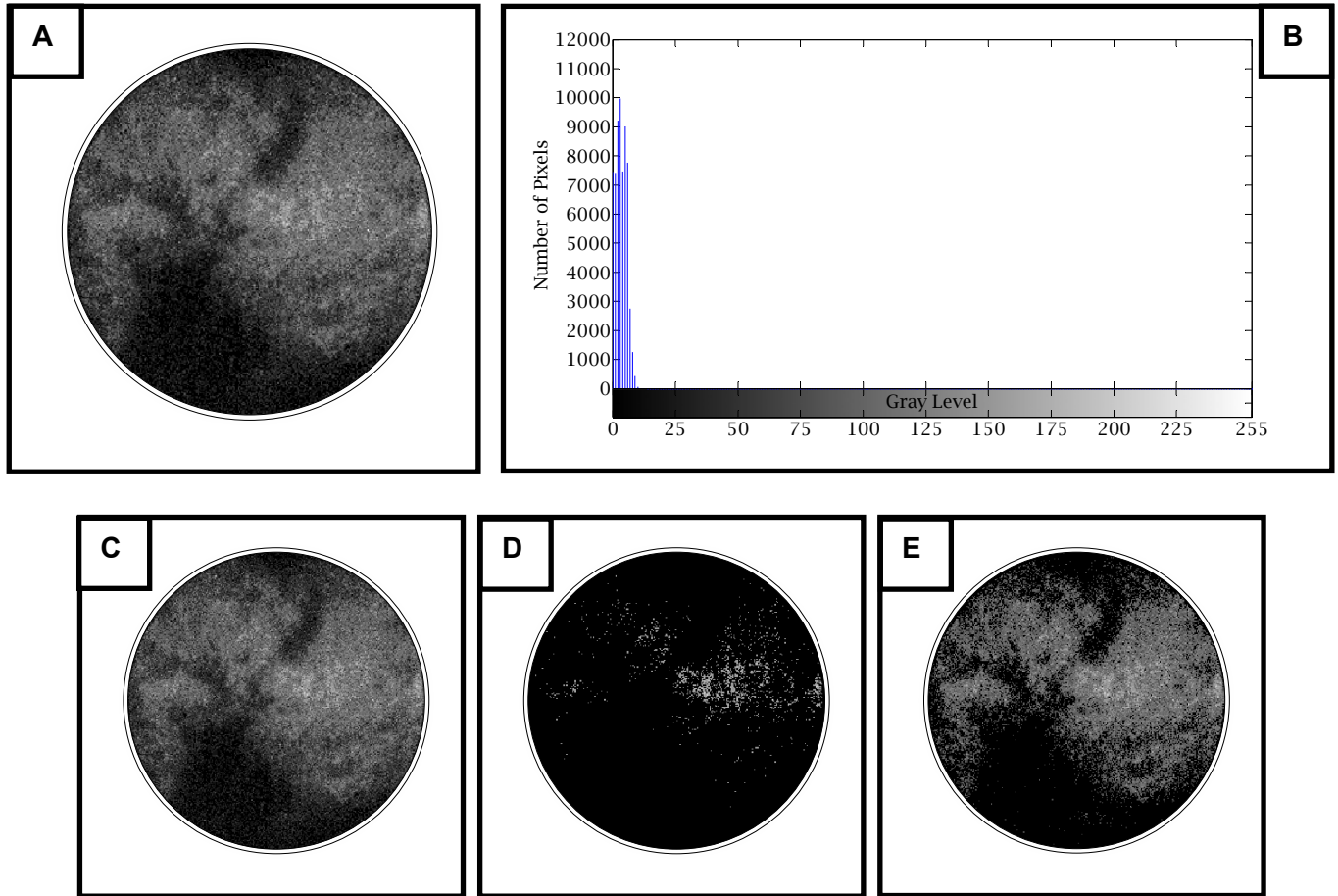


Figure 5.5. Test image (A & C), and its histogram (B) and thresholded images (D & E). Thresholded image (D) represents image appearance of test image (c) segmented with threshold level ($TL = 8$) indicated by Image Histogram based on Triangle Algorithm Procedure. The thresholded image (E) corresponds to test image appearance (c) segmented with consistent indication of $TL=4$ delivered by three other methods utilized: Otsu, Gray Level Gradient and Iterative Techniques. As a test image is featured by dark grey level characteristics, what is seen on its histogram (B), image array elements of all images included in A,C,D & E were multiplied by a factor of 19, obviously after thresholding level determination or segmentation process.

5.4.1 Image normalised histogram and its statistics

The image normalised histogram is a straightforward representation of pixel intensity occurrence probability of an image (probability mass function for discrete values or probability density function for continuous values). The procedure to obtain and plot the normalised histogram refers to a simple division of pixel numbers having identical intensities by a total image pixels number. This is performed for all distinctive presented intensity values of the analysed image:

$$p_i = \frac{n_i}{n}; \quad i = 0, 1, 2, \dots, L-1$$

n_i – number of pixels having given (the same) intensity – level in an analyzed image,

n – total number of pixels in an analyzed image,

i – intensity level,

L – possible number of intensities levels i.e. 256.

$$\sum_{i=0}^{L-1} p_i = 1;$$

The normalised image histogram profile provides valuable insights into an image's intensity value distribution. Further, the applicability of simple descriptors and statistical moments complete this insight by providing valuable information regarding central tendency, data spread measurement, histogram shape or highest occurrence probability intensity value.

I. Simple descriptors of image normalised histogram:

- a) *Mode* – mode defines the intensity level associated with the greatest probability of occurrence value;
- b) *The highest occurrence probability* - occurrence probability value represented by the mode.

II. Statistical moments of image normalized histogram:*a) The first common statistical moment – mean;*

Mean determines the center of a distribution i.e. the mean intensity value in the probability distribution pattern. The mean is specified as a:

$$\mu_T = \sum_{i=1}^{L-1} i \cdot p_i \quad (\text{Gonzales et al 2002})$$

b) The second central statistical moment – variance;

Variance determines the distribution broadness. Because the distribution broadness quantified is linked to an observed mean, the variance value delivers qualitative insight into intensity levels and their occurrence distribution probabilities around the observed mean. The variance is specified as a second central moment (around the observed mean):

$$\sigma^2 = \sum_{i=1}^{L-1} (i - \mu_T)^2 \cdot p_i \quad (\text{Gonzales et al 2002})$$

The larger the variance, the more scattered data are around the observed expectance. Conversely lesser variances indicate data concentrated near the observed mean and point out higher occurrence probabilities in a close vicinity to the mean as opposed comparison to a distribution that *tails* occurrence probabilities. Undisputedly the variance equals zero while the distribution is represented by one intensity level variable occurrence probability. Also at this instance the intensity level of that occurrence probability becomes a mode and mean.

c) The third central statistical moment and skewness;

Skewness defines the potential asymmetry direction and its degree of the distribution. Generally whilst the variance determines the spread measure (distribution broadness) the skewness identifies the distribution outcomes bias. Although a normalised histogram is a sufficient technique for the distribution shape illustration, the precise identification of a potential distribution asymmetry requires a skewness to be determined mathematically. The skewness is computed as a ratio of (dividing) third statistical central moment and (by) standard deviation (square root of variance) to the power of three.

$$M_3 = \sum_{i=0}^{L-1} (i - \mu_T)^3 \cdot p_i \quad (\text{Gonzales et al 2002; Dobosz 2004})$$

$$S = \frac{M_3}{\sigma^3} \quad (\text{Gonzales et al 2002; Dobosz 2004})$$

σ – standard deviation (square root of variance)

The symmetrical distribution skewness is determined by zero value and data are equally distributed on either side around the observed mean. Positively-skewed distribution, also named as a right-skewed distribution is one with the data concentration massed to the left side also in relation to the mean where the right tail is longer than the left one both could be determined by the data spreads (variances) around the observed global mean in corresponding directions. This distribution is also featured by the mean being larger than mode. The negatively-skewed distribution, the left-skewed distribution is the opposing scenario (one) with contrasting relationships. A representative illustration of both distribution scenarios are plotted in Figure 5.6.

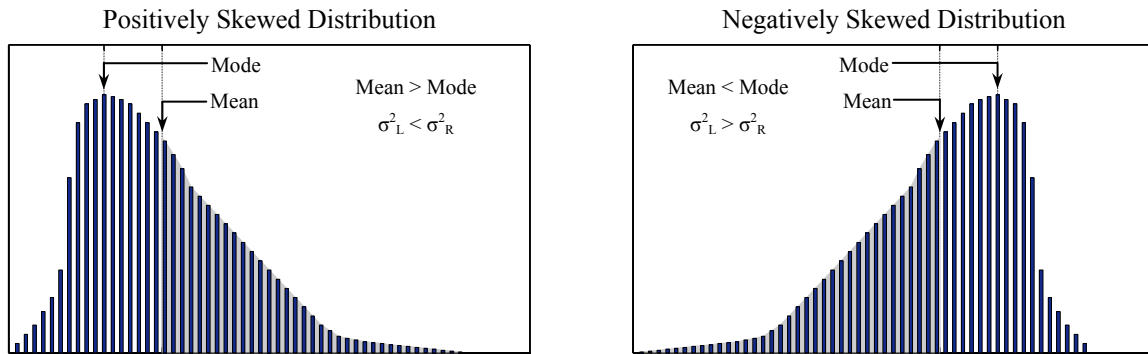


Figure 5.6. Illustrations of asymmetrical distributions - a positively and negatively skewed distribution of the identical skewness degree of opposing signs. σ_L^2 – left-hand side (below mean) data distribution variance; σ_R^2 – right-hand side (above mean) data distribution variance.

d) *The fourth central statistical moment and kurtosis;*

Kurtosis verifies distribution flatness with reference to a normal distribution, a bell-shaped curve determined by specified criterion. The kurtosis is calculated as a ratio of fourth statistical central moment and (by) square variance.

$$M_4 = \sum_{i=0}^{L-1} (i - \mu_T)^4 \cdot p_i \quad (\text{Gonzales } et al \ 2002; \text{Dobosz } 2004)$$

$$K = \frac{M_4}{\sigma^4} - 3 \quad (\text{Gonzales } et al \ 2002; \text{Dobosz } 2004)$$

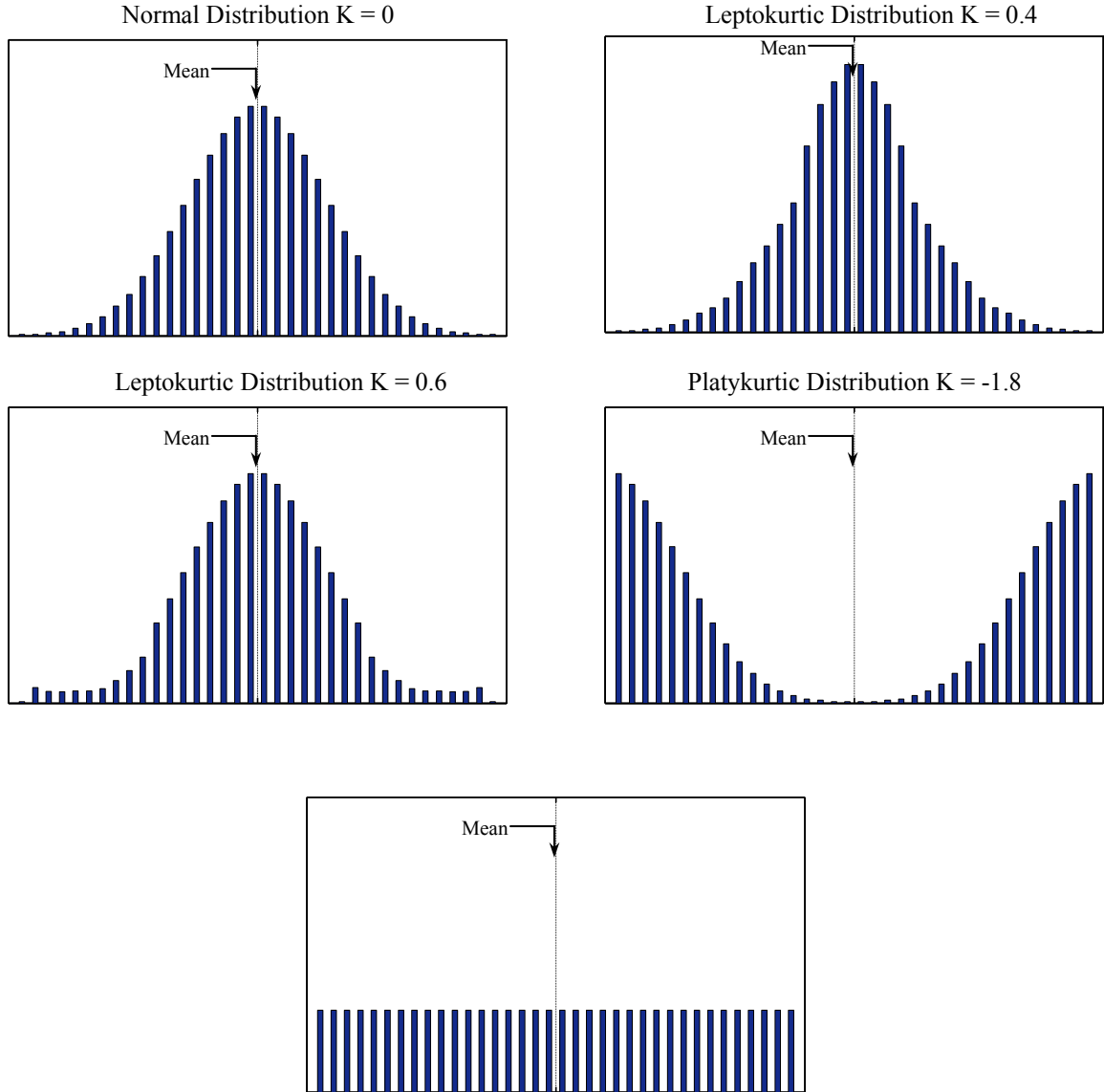


Figure 5.7. Illustrations of various distribution characteristics with different kurtosis indications.

Kurtosis zero value is assumed and reserved for a normal distribution. The kurtosis larger than zero indicates peaked distribution falling off rapidly near the observed mean with relatively long and/or heavy extreme points of a distribution curve in comparison to normal distribution or distribution with the central part corresponding to the normal distribution

central part. It also has tails *heavier* than ones that come across in a normal distribution curve shape.

This distribution pattern (any characterised via kurtosis greater than normal distribution kurtosis) is also called a *leptokurtic distribution*. The negative kurtosis features the flatter (dipped, more rounded) distribution (*platykurtic distribution*) in a central part near the mean in comparison to the normal distribution. Figure 5.7 illustrates various distribution patterns with corresponding computed kurtosis including normal distribution, two leptokurtic distributions and two platykurtic with one uniform distribution.

5.4.2 Image object area determination

The pixel based object area size is generally estimated as one which should exactly correspond to (1's) object's pixels in a binary image, or alternatively to a number of pixels above the predetermined pixel's level intensity for a monochromatic image area estimation. However this might not always be the case once analysis of image object area size is conducted in a Matlab® programming environment. This happens since there are two different methods available in the aforementioned software - *sum* and *bwarea* functions (Matlab Image Processing Toolbox Tutorials and Help, Wrobel et al 2004). The *sum function* returns area size corresponding precisely to a total number of (1's) pixels of the binary image irrespective of the object shape, whereas *bwarea function* returns the estimated total area size determined by an individual pixel area by analysing its 2-by-2 neighbourhood (Matlab Image Processing Toolbox Tutorials and Help) according to Matlab® implemented algorithm:

- area of single 2-by-2 neighbourhoods with zero 1's pixels returns 0;
- area of single 2-by-2 neighbourhoods with one 1's pixel returns 1/4;
- area of single 2-by-2 neighbourhoods with two adjacent 1's pixels returns 1/2;
- area of single 2-by-2 neighbourhoods with two diagonal 1's pixels returns 3/4;
- area of single 2-by-2 neighbourhoods with three 1's pixel returns 7/8;

- area of single 2-by-2 neighbourhoods with four 1's pixel returns 1.

So it appears that area determined by utilising *bwarea function* is object shape dependent because this function considers pixel neighbourhood and may not always correspond to (1's) pixels numbers of the binary image. To investigate this problem the analysis of two artificially created binary images objects sizes – one with a circular object and the other with a square was performed. This is illustrated in Figure 5.8 with tabulated form summarising the objects' area results.

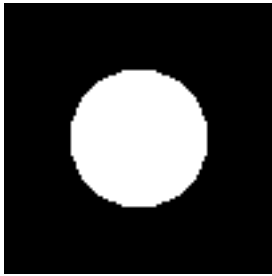
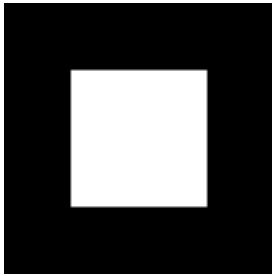
<i>Image with Circular Shape Object</i>		<i>Image with Square Shape Object</i>	
			
<i>Function</i>	<i>Area Size Estimated [Pixels]</i>	<i>Function</i>	<i>Area Size Estimated [Pixels]</i>
sum function	2085	sum function	2601
bwarea function	2092	bwarea function	2601

Figure 5.8. Comparison illustrating area size determination upon function used and image object shape.

Now it is evident that estimated area size is function dependent; more specifically the potential differences that emerge in between these results of these two aforementioned functions are due to objects shapes and different approaches. This simple analysis has shown that both functions could produce identical or different results because of essentially object shape dependency. The reported area sizes of autoignition and/or combustion zones in this thesis were estimated using *sum function*, whereby the returned area size corresponds to the actual size regardless of an object's shape.

5.4.3 Image objects distance determination

There are four major distance measures metrics available in image processing foundations: Euclidean, Quasi-Euclidean, City-Block and Chessboard (Gonzales *et al* 2002). Also these four metrics are supported by Matlab® *bwdist* function utilised to image points distance evaluation (Matlab Image Processing Toolbox Tutorials and Help).

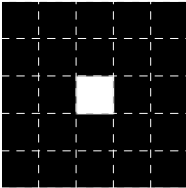
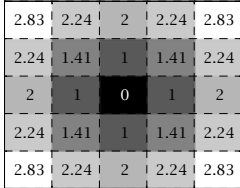
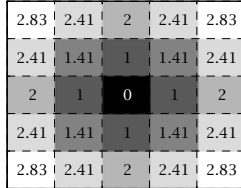
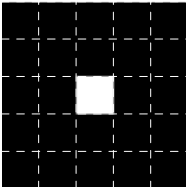
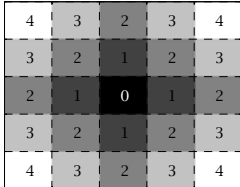
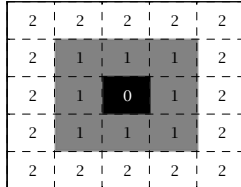
Distance Method	Euclidean	Quasi-Euclidean
Distance Estimation Formula (between Two Arbitrary Image Points $G(x,y)$ and $H(s,t)$)	$D = \sqrt{(x-s)^2 + (y-t)^2}$	$D = x-s + (\sqrt{2}-1) y-t , \text{ if } x-s > y-t ,$ $\text{otherwise } (\sqrt{2}-1) x-s + y-t $
Binary Image	Distance Distribution	Distance Distribution
		
Distance Method	City-Block	Chessboard
Distance Estimation Formula (between Two Arbitrary Image Points $G(x,y)$ and $H(s,t)$)	$D = x-s + y-t $	$D = \max(x-s , y-t)$
Binary Image	Distance Distribution	Distance Distribution
		

Figure 5.9. Review of image distance measurement metrics (methods).

These four computational distance measures metrics, their approaches in image points (pixels) distances measurements along with exemplary distances distributions are depicted in tabulated form in Figure 5.9.

As their formulas indicate in conjunction with the visualizations of distances distributions it is apparent that there are differences in measured distances among these metrics with regard the to diagonal image directions from base point (nonzero point in binary image). This in fact could easily lead to under or overestimating results i.e. distances measured between image points.

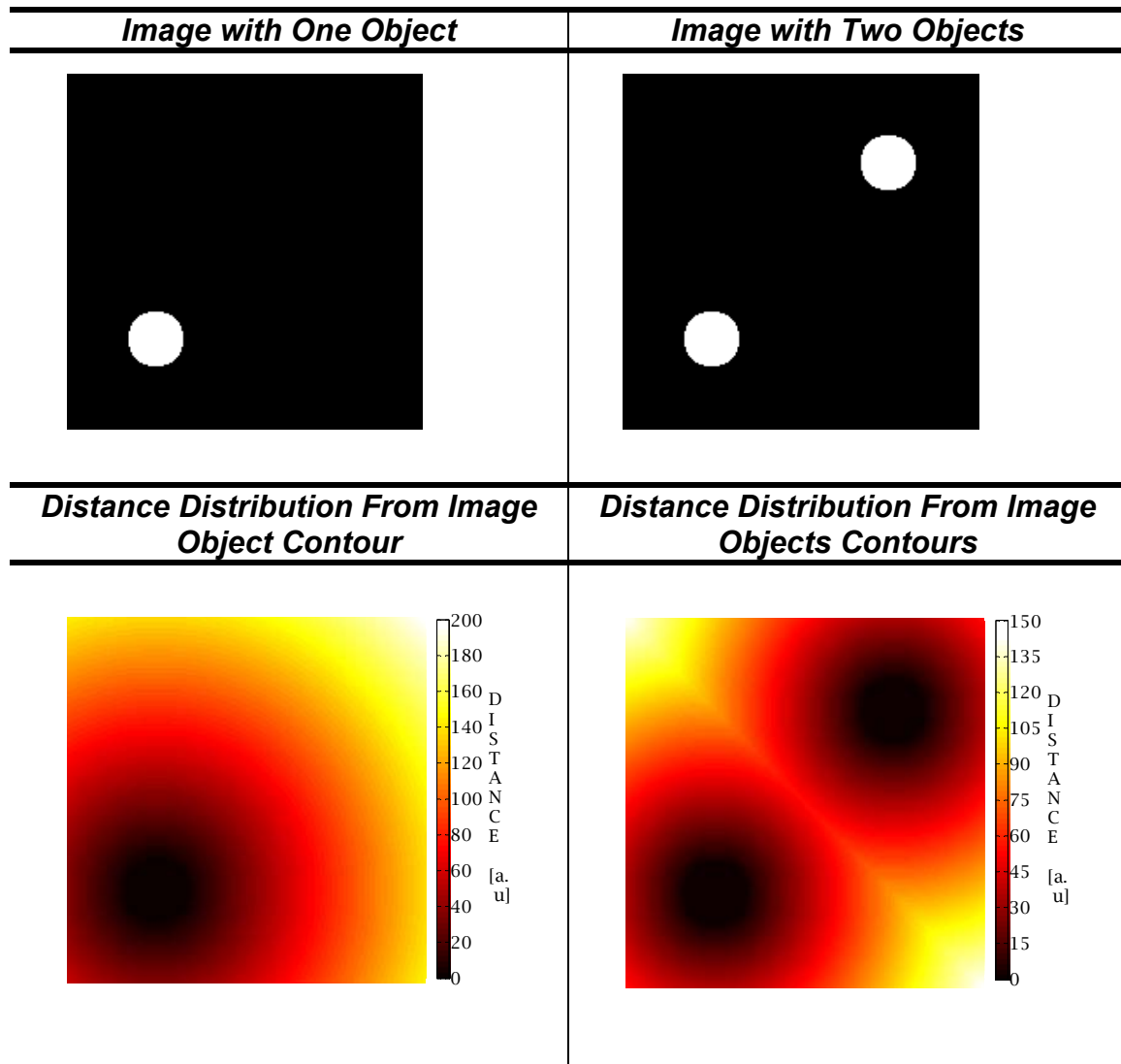


Figure 5.10. Representative illustration of *bwdist* function operation – its difference in distance evaluation and distribution for single object and double objects images contents. The distance was determined using *euclidean distance* metric.

The distance distributions shown in Figure 5.9 were conducted for a binary image presented in the same figure. For the image objects distance evaluation in this thesis the Euclidean metrics were selected which correspond to real-life distance measurements between image

points, since any other method chosen would have caused under or overestimation of a distance measured.

The other key issue in evaluating object distances in the image by using *bwdist* function in Matlab environment is the distance computation when more than one object is presented in an image. This is exemplarily demonstrated in Figure 5.10, which illustrates two binary images with their corresponding distance arrays evaluated. Since the algorithm computes the distance between the nonzero and zero pixels, two objects in the image cause the maximum distances to be determined halfway between them (uniform distance distribution).

5.4.4 Image processing techniques for autoignition and combustion analysis

The three major image processing techniques for autoignition and combustion processes analysis are introduced in this section. This is accomplished by presenting pure technique assumptions used and also in relation to image processing foundations, general and those aspects available in Matlab®.

5.4.4.1 Autoignition occurrence and combustion development pattern likelihood of repeatability technique

The devised method named 'Autoignition Occurrence and Combustion Development Pattern Likelihood of Repeatability Technique' provides a means of investigating the likelihood of the repeatability nature of autoignition occurrence and combustion development pattern with reference to planar optical observation i.e. the analysed image. This is accomplished by inspecting grey-level probability distribution of an ensemble⁴ image (image

⁴ The ensemble image is an 8-bit grey-level (monochromatic) image composed of addition of twelve individual cycle images captured at the same crank angle degree in this study. The individual images were binarized before

normalised histogram). The assessment of grey-level probability distribution (of an ensemble image) is obtained by employing statistics, more specifically statistical descriptors defining normalised histogram central tendency (1st common statistical moment – mean) , data spread (2nd central statistical moment - variance) and shape (skewness and kurtosis based on 3rd and 4th central statistical moments respectively), whereby the insight into process likelihood of repeatability is gained corresponding to either auto-ignition or combustion ensemble image content area. These general and statistical descriptors were discussed in detail in section 5.2.4. So here they will only be addressed in direct relation to a technique being presented. Also it appears that besides the general information of global⁵ process repeatability likelihood indicated by the mean value, further facts are gained concerning the process nature across the distinguished combustion chamber zones of total autoignition/combustion marked. They determine local process assessments (local information) thereby completing the comprehensive analysis. These are variance, skewness and kurtosis, all computed in relation to central tendency.

Generally an 8-bit (integer class) ensemble image contains discrete array elements values spanning in interval [0,255]. However, as a consequence of only twelve images (each represented with two discrete available levels 0 and 1) taken in formation of the ensemble image in this study, the ensemble image values are potentially within the limited interval [0,12]. This is also because that the images addition operation is realized between corresponding pixels. Then to conduct statistical analysis the ensemble image grey-levels are assigned numerically corresponding to random variables. This approach allows a straightforward interpretation of results since a given random variable corresponds to its grey level counterpart. The grey-level probability distribution of an ensemble image (image normalised histogram) is accomplished by dividing a number of pixels having the same grey level by the total number of pixels taken for analysis from ensemble image i.e. pixels having grey level within the interval analysed. Mathematically this is expressed as:

converted to 8-bit images and therefore each individual 8-bit image comprised of only two image array elements intensities allowable 0 or 1 (pixels intensities).

⁵ Global refers to a comprehensive (total) image content (area) marked by autoignition/combustion zones.

$$p_i = \frac{n_i}{n}; \quad i = 1, 2, 3, \dots, L$$

and $\sum_{i=1}^L p_i = 1;$

where: n_i - pixels number having given, the same grey level,

n - total number of pixels taken for analysis i.e. from [1,12] interval in this study ,

i - random variable corresponding to grey level,

L - possible number of grey levels i.e. 12 in this study.

The indicators and statistical descriptors used to characterise ensemble image grey-level probability distribution are listed below:

a) Mode (M);

The global process nature likelihood of repeatability is higher, thus the process is more predictive with the greater mode for a given probability distribution.

b) The Greatest Occurrence Probability Magnitude (P.o.O_{max});

The probability of occurrence value indicated by the mode.

c) Range (R);

Range which defines the difference in the greatest and lowest occurrence probabilities in a distribution could essentially point out the presence of random variable(s) featured with zero occurrence probability in a distribution when contrasted to the mode's occurrence probability.

d) Mean - Expected Value or Expectance (μ_T);

The mean is the first (1st) common statistical moment of random variables. Defining the center of distribution in probability distribution, an average grey-level (random variable) determines the global process likelihood of repeatability corresponding to the autoignition/combustion marked area(s). Apparently the process likelihood of repeatability increases as indicated by greater expectance.

e) Variance (σ^2);

Variance, the second statistical central moment (around the observed mean) determines distribution broadness. Because this indication is directly linked to an observed mean, variance provides a qualitative insight into the random variables and their occurrence probabilities distribution in relation to the observed mean of the normalised histogram for the purpose of this analysis. The larger the variance value the more scattered data are around the observed expectance. Hence for this study it means that the nature of the global process likelihood of repeatability, its main indicator – mean is influenced and formed from more random variables and their occurrence probabilities, which are located further from the observed mean. Contrary to this, lower variance indications point out data concentrated near the observed mean. Consequently the nature of process likelihood of repeatability is reflected to a greater extent through random variables (and their occurrence probabilities) located closer to the observed mean for this distribution. The variance equals zero for single random variable distribution probability and the mode becomes mean in this case.

f) Skewness (S);

Skewness determines potential distribution asymmetry, its direction and degree. Primarily while variance defines spread measure (distribution broadness), skewness identifies distribution outcome bias. The skewness values presented throughout this entire study were computed as a ratio of the third statistical central moment to standard deviation (the square root of variance) to the power of three. The symmetrical distribution with equally spaced data around the observed mean is determined by a zero skewness value indication. The skewness pointing out a character of distribution – data mass concentration and distribution tail orientation in relation to observed mean provides valuable information in a form of site to site random variables that are associated with the identification of higher versus lower occurrence probabilities distribution. This practically distinguishes two classes of random variables, one having a more significant impact on the obtained observed mean i.e. the process likelihood of repeatability nature than the other. For our analysis it is clear that those random variables of distribution on the right-hand side (as referenced to observed mean

sides) enhance the greater nature of the process repeatability likelihood than their left-hand side counterparts at identical occurrence probabilities.

g) Kurtosis (K);

Kurtosis is a descriptor verifying the actual distribution pattern (shape) with reference to normal distribution – bell shaped curve (precisely determined). The kurtosis was calculated as a ratio of fourth statistical central moment and square variance:

Zero kurtosis value distribution indicates that distribution matches the normal distribution shape; in other words, a normal, bell shaped distribution is featured by a kurtosis zero. The kurtosis greater than this value points out so called leptokurtic distribution with peaks falling off rapidly near the observed mean having a relatively long and/or heavy tail in contrast to normal distribution. However, it could also indicate distribution characterised by central part matching to the normal distribution and tails heavier than in a normal distribution curve shape. The negative kurtosis indicates flatter (dipped, more rounded) in a central part near observed mean distribution (platykurtic distribution) as compared to normal distribution. For the intention of this analysis kurtosis along with skewness serve as distribution shape indications, and the kurtosis itself identifies the mass of the distribution in relation to normal distribution as mentioned above. Pointing out this fact the indication of random variables with greater occurrence probabilities is gained, where kurtosis unlike skewness defines their peakness (thus contribution to process repeatability likelihood) around the observed mean.

In summary, with regards to the approaches and ways undertaken to analyse the autoignition occurrence and combustion development pattern likelihood of repeatability within this study the following facts are noteworthy. Firstly the process repeatability likelihood was assessed disregarding individual image autoignition/combustion zone(s) original pixels intensities. This is the case because as stated above the ensemble image was created of individual images after the binarisation process. Secondly and as importantly this analysis would be more valuable if a greater number of individual images were available. Also for an analysis of HCCI such as the one conducted in this study, the observed trend would be more

valuable if the combustion phasing was kept constant thus eliminating cycl-to-cycle variations affecting combustion onset and development, as analysis in not accounted for this changes.

5.4.4.2 Expansion rate of burned areas

The real size of the autoignition and/or combustion area(s) within the accessible imaged part of the combustion chamber was computed by defining the area size on a pixel basis first. Then this pixel based area was converted into the real size area with the knowledge of the predetermined individual pixel physical (real) size. For the determination of the real pixel size, the piston-crown window diameter value (64 mm) and the number of pixels along this diameter on the image (the imaged part of the combustion chamber diameter) were taken corresponding to either number of columns or number of rows in y-axis and x-axis image orientation respectively. Both measurements indicated an identical number of pixels along the diameter – 283, with the aforementioned diameter size this corresponds to 0.226×0.226 mm physical size of an individual pixel – square size since camera array pixels for both imager use iCCD and CMOS. The reported area sizes of the autoignition and/or combustion zones in this study were estimated using *sum function*, whereby the returned area size corresponds to the actual size regardless of an object's shape. Once this was estimated and converted to the real size area, combustion growth (expansion rate of the burned area) was computed based on the numerical differentiation between each pair of consecutive images dA/dt , their areas with respect to elapsed time between corresponding images.

The expansion rate of burned areas is one of a few steps required to compute within a comprehensive mean flame front expansion speed analysis for spark ignited combustion process (Heywood 1988) determination. The application of this burned areas expansion rate estimation technique was reported by Hultqvist *et al* (2002) for the first time in the HCCI combustion field (according to the author's knowledge). In the current study (section) the objective of this detailed presentation of a seemingly simple technique arose from different computation approaches offered by Matlab®, which consequently and importantly could

produce various results. Hence it is evident that obtained results are very much area computational methods dependent as performed or related to Matlab® available functions.

5.4.4.3 Reacting structure front spreading velocity

In this study the developed and proposed analysis for HCCI reactions fronts spreading velocities tracking (estimation) provides an insight into instantaneous magnitudes of reactions velocities along the reactions contours at any single contour's node as well as average value. This is accomplished based on a procedure which corresponds to the numerical differentiation of the distance which the individual reaction front contour has moved in each node with respect to elapsed time of two consecutive considered images – image pair.

The first attempts and results estimating reactions front spreading velocities shown in open literature concerning HCCI research were undertaken by Hultqvist *et al* (Hultqvist *et al* 2002). This was further investigated by other researches e.g. Persson *et al* (Persson *et al* 2007) using this same technique. The procedure they utilised to derive reaction front spreading velocities was based on the flame front velocity calculation method for spark ignition combustion process (Heywood 1988) with a proposed replacement of the arc length of the best-fit circle onto the straight reaction front length. The aforementioned replacement was necessary due to the fact that there was no apparent flame front propagation in HCCI combustion. More precisely the straight reaction front length was computed as a distance from the image edge i.e. initial reaction location to the reaction front.

The need for a new procedure capable of tracking each single 'burning zone' spreading velocities individually, independently of others and also along the contour delivering instantaneous values, appeared during the initial observation of HCCI autoignition and combustion images. They revealed highly wrinkled reactions fronts, also frequently occurring and promoting from a number of loci within the accessible part of the combustion chamber.

Unfortunately the behaviour (pattern) of these reacting structures prevented the applicability of the method proposed by Hultqvist *et al* (2002).

The proposed procedure in this study requires three main steps in order to obtain reactions fronts spreading velocities indications. Firstly distances from the image object contour – autoignition or combustion zone front (of an initial image in images pair analysis) to image edges are evaluated by using Matlab[®] *bwdist function*. The gained results (distances) are in the form of an array, which size corresponds to the image containing the object size and distances located in the corresponding array cells matching actual distances from the object's contour in given directions. These distances are pixel based ones, however, once the real pixel size is determined the conversion to real distances is straightforward as stated in the previous subsection. Then the edge detection function is applied to the object i.e. autoignition or combustion zone of the second image, whereby the object contour is defined. Finally this object contour of a second image is superimposed on the first image object distances array in order to filter values along the contour only. These values referring to the time elapsed between the analysed images constitute the reaction front spreading velocities indications at any image contour location. It is noteworthy that analysis of a single island reaction front spreading velocities with an image containing a few burning zone and not overlapping requires an individual distance array measurement and contours detection for each single island to be performed separately. This is a consequence of *bwdist function* distances computation when more than one object is presented on an image as presented in the previous section. The reacting structures front spreading velocities were estimated by selecting Euclidean metrics corresponding to real-life distance measurements between image points. Any other method chosen would cause under or overestimation of reactions fronts spreading velocities for this analysis.

5.5 Summary

The traditional engine operating variables data acquisition systems have been discussed in detail. Further the engine data analysis and methods utilised for conventional in-cylinder pressure derived information were presented. The second part of the chapter introduced the optical data and image processing techniques. At the beginning systematic noise content removal techniques such as background subtraction were presented. Then four image thresholding methods were examined. Finally the relevant image processing methods for autoignition and combustion analysis such as ones assessing the likelihood of the repeatability of combustion onset and development patterns, estimating expansion rates of burned areas or evaluating reacting structures front spreading velocities have been demonstrated in detail. It has been also demonstrated how the image computation approaches could significantly affect the obtained analysis results. Different ways of area of distances of an image object have been illustrated concerning to Matlab[®] available functions as well as in accordance with general image processing foundations. As has been demonstrated, the results are very much image processing approach dependent and careful selection of an area and distance calculation ways for an introduced image processing techniques is required.

Chapter 6

Characteristic of HCCI Autoignition and Combustion Process

6.1 Introduction

This chapter is dedicated to the presentation of the characteristics of the Homogeneous Charge Compression Ignition autoignition and combustion processes. At first, a background to the HCCI autoignition and combustion is addressed in two ways: a theoretical one including the study of reaction pathways leading to autoignition and particular engine autoignition/combustion, and then the study of the thermal engine. The thermal study was conducted in order to gain insight into the characteristic of HCCI mode under predetermined engine conditions. The findings include the influence of engine operational parameters on autoignition and the combustion process type. More specifically it has been demonstrated that the nature of the HCCI autoignition/combustion process (one- or two-stage ignition) is highly dependent on engine operating variables. Furthermore an optical study including imaging and spectroscopy techniques has been carried out, which provides a means to understand the physicochemical nature of the one- and two-stage ignition process of HCCI. This analysis was performed for particular engine operating conditions, where the transition of a one- to a two-stage ignition process was caused by different amounts of trapped internal residuals. This was investigated using the same fuel blend with the engine running under the same operating conditions: engine speed, equivalence ratio and intake air temperature. The last part of this chapter briefly discusses the character of the autoignition with different fuels under various engine operating conditions. This analysis provides an insight into how

relevant the current fuel antiknock rating indicators as well as the fuel blend composition are for an engine operating conditions in HCCI mode.

6.2 Fundamentals of HCCI autoignition and combustion

An autoignition and combustion process can essentially proceed as a one- or two-stage ignition mode in an HCCI operated engine. The process type is highly conditioned by the kind of fuel, more specifically its composition and engine operational variables. The two-step ignition process is characterised by an early low temperature chemistry, also referred to as cool flame activities, followed by the main autoignition and combustion activities i.e. hot temperature heat release (HTHR) stage. The cool flame activities are exothermic reactions, associated with the occurrence of a negative temperature coefficient (NTC) regime – reversing the reactions period. The onset of NTC happens once the temperature conditions are favourable for ceasing the reactions leading to cool flame activities. Therefore the low temperature heat release (LTHR) is only favoured within a particular temperature window. Generally the one-step ignition process is *described* by only a hot temperature heat release phase. Nevertheless for both ignition processes i.e. one- and two-step a so called intermediate temperature heat release (ITHR) phase is distinguishable (Bartok *et al* 1991). A recent study by Hwang *et al* (2008) clearly depicts the existence of an ITHR regime with other phases for the one- and two-stage ignition process in an HCCI operated engine. This was investigated using a range of various fuels. The representation of one- versus two-step ignition processes based on their heat release profiles is shown in Figure 6.1. This was accomplished by running the engine at identical operating conditions and by varying the fuel composition, replacing commercial gasoline with a 75% isooctane and 25% n-heptane, Primary Reference Fuel blend (PRF75).

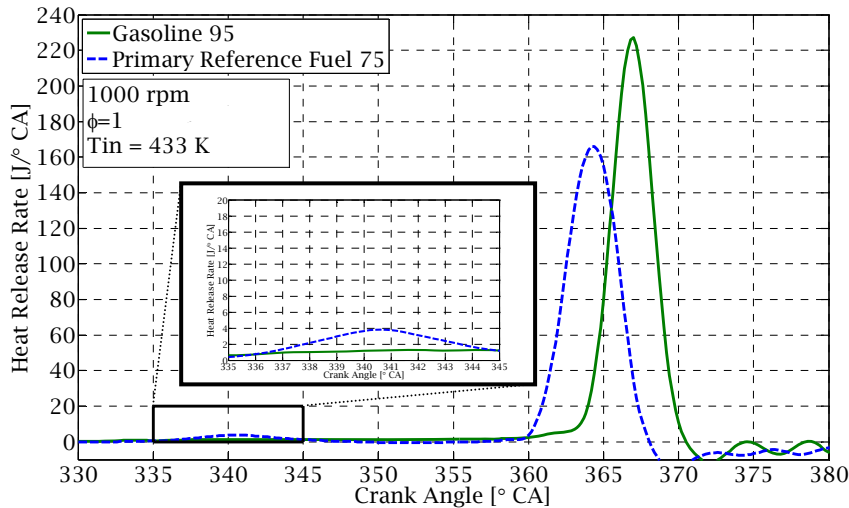


Figure 6.1. Representation of one- versus two-step ignition process.

As the autoignition and combustion type in a practical combustion system such as HCCI is conditioned to a high extent by fuel type, thereof fuels could then be broadly broken down into two groups (Sjoberg *et al* 2003):

- one-stage ignition fuels – e.g. natural gas, aromatics or straight chain paraffinic fuels with lower carbon number;
- two-stage ignition fuels – e.g. diesel fuel or straight chain paraffinic fuels with a higher carbon number.

The influence of the molecular structure of hydrocarbon fuels on low temperature heat release activities reported by Shibata (2004) composed the following order (sequence) which has been presented in diagram form in Figure 6.2. Indeed this is among the most common type of hydrocarbon family; hydrocarbons of the greatest influence are located at the top of the diagram with these having little or no contribution at the bottom.

An understanding of the chemical nature of an auto-ignition and combustion process constitutes valuable background, knowledge and further insight could be gained by reviewing the reactions pathway. This is shown here in Table 6.1 based on the simplified model presented by Bartok *et al* (Bartok *et al* 1991). This simplified reactions pathway model is for a paraffinic like hydrocarbons and because of this the low temperature heat release

reactions are included. The initiation of the auto-ignition process is accomplished by hydrogen abstraction from the parent fuel – reaction (1). This step forms the alkyl radical and hydroperoxy. The second reaction depicts the further, subsequent abstraction of hydrogen from the alkyl radical (2) and consequently the olefins formation.

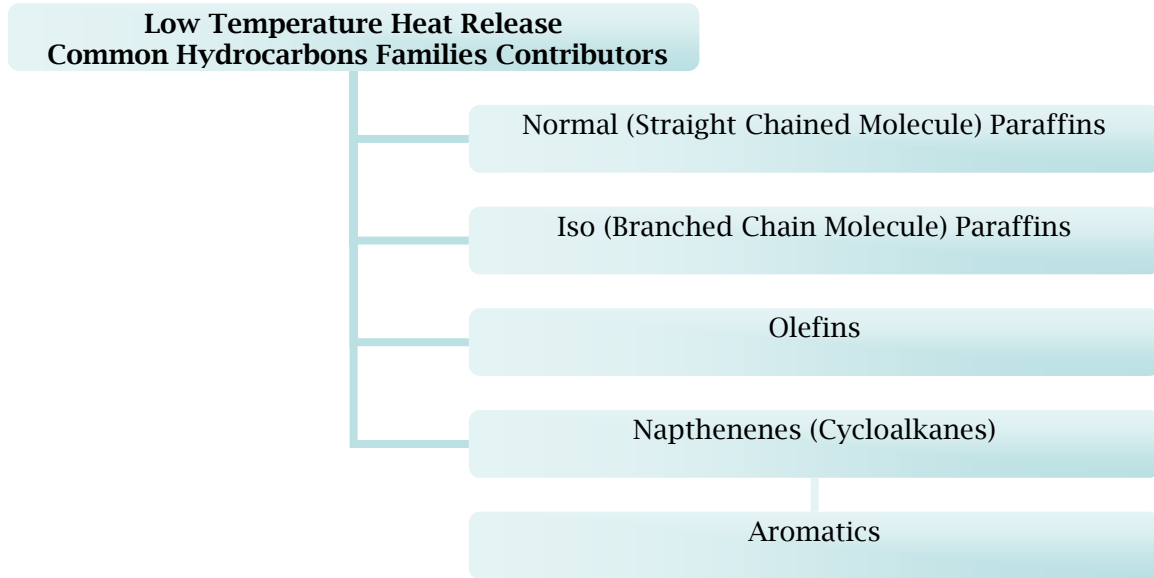


Figure 6.2. Influence of hydrocarbon fuel type on low temperature heat release.

$RH + O_2 \rightarrow R^* + HO_2^*$ (1)
$R^* + O_2 \rightarrow \text{olefin} + HO_2^*$ (2)
$R^* + O_2 \leftrightarrow RO_2^*$ (3)
$R^* + O_2 \rightarrow RO_2^*$ (3a)
$RO_2^* + M \rightarrow RO_2^* + M$ (3b)
$RO_2^* \rightarrow \text{olefin} + HO_2^*$ (3c)
$RO_2^* \rightarrow ROOH^*$ (4)
$RH + RO_2^* \rightarrow ROOH + R$ (5)
$ROOH^* \rightarrow \text{carbonyl} + R^* + OH^*$ (6)
$ROOH^* + O_2 \leftrightarrow OOROOH^*$ (7)
$OOROOH^* \rightarrow HOOROOH$ (8)
$HOOROOH \rightarrow RCHO + R'O + OH^* + OH^*$ (9)
$RH + HO_2^* \rightarrow R^* + H_2O_2$ (10)
$H_2O_2 \rightarrow \text{destruction (H}_2\text{O, O}_2\text{)}$ (11)
$H_2O_2 + M \rightarrow OH^* + OH^*$ (12)

Table 6.1. Reactions pathway leading to an autoignition process.

On the other hand in reaction (3) alkylperoxy is formed by the addition of oxygen to the alkyl radical. Reactions (2) and (3) are parallel propagating reactions occurring at low temperature governed by a temperature. Reaction (3) is the one leading to cool flame activities. At low temperatures reaction (3) is more favorable than the olefins production. Furthermore there are reactions (3a-3c) which occur parallel to (2) and (3) and these show the different way that olefin forms. The alkylperoxy radical, the product of reaction (3) can either undergo internal isomerisation (4) or could form hydroperoxylalkyl by the next hydrogen addition abstracted from parent fuel (5). Decomposition of hydroperoxylalkyl yields carbonyl, alkyl radical and hydroxyl (6). Alternatively there is an oxygen addition to ROOH (7), and then due to subsequent isomerisation of hydroperoxylalkylperoxide the alkylhydroperoxide is formed (8). The alkylhydroperoxide decomposes into aldehyde and two hydroxyl radicals (9). This depicts a complete pathway to the low temperature heat release. These low temperature reactions and their occurrence have significant importance in a practical combustion system which is the main scope of this chapter. These low temperature reactions occur in the particular temperature window 750-850 K (G.Shibata *et al* 2004). As the temperature increases due to the reactions of exothermicity and compressive heating, the reverse of reaction (3) and (7) takes place; in other words the formation of olefins becomes dominant. This is the beginning of a NTC (negative temperature coefficient) regime, the time when the reactions rates decrease with temperature increase. The NTC region separates the low-temperature and intermediate-temperature regimes. Hydroperoxy formed in reaction (2) leads to the formation of hydrogen peroxide in reaction (10) by means of hydrogen abstraction from the parent fuel. The faith of hydrogen peroxide formed during low temperature zone could have led to the destruction of water and oxygen presented by reaction (11), however, hydrogen peroxide is quite stable at low temperatures associated with LTHR. The hydroxyl radicals produced in reaction (9) are desperately seeking to form species – they are not stable at these temperatures. Also these hydroxyl radicals formed according to reaction (12) – hydrogen peroxide breaking down at these temperatures shares the aforementioned faith. Subsequently the NTC region ends as the increasing temperature

and pressure activate significant hydrogen peroxide accumulation (10). This is the point when the intermediate temperature heat release commences. This regime is characterised by a significant hydrogen peroxide accumulation and further decomposition. Hwang *et al* (2008) suggested that hydroxyl radicals formed at the early stage of the ITHR phase are absorbed by a fuel decomposition process. As this happens a large part of fuel needs to be decomposed before a significant concentration of hydrogen peroxide is accumulated, which in fact is necessary to trigger the hot temperature heat release. Consequently it is believed that this is an onset of the hot temperature heat release period occurring once in-cylinder temperature reaches about 950-1000 K, however, it is also fuel type dependent. Hwang *et al* (2008) observed that this is a point in an engine cycle matching roughly with the 10% burn point of the main heat release rate profile, regardless of the sort of fuel used. Also it was suggested that precise separation of successive phases could not be purely and well defined based on cardinal points of the heat release rate profile.

6.3 Effects of engine operational variables

6.3.1 Experimental aspects

The autoignition and combustion study has been conducted with an HCCI operated single cylinder thermal engine. The aim of this research and further analysis performed was to gain an understanding of engine operation parameters, engine speed and residual rate trapped influence on process type, essentially on low temperature heat release activities present in the two-step ignition process. This analysis is based on the average cycles results of 100 engine cycles which were acquired at each investigated engine operating point.

The engine was fuelled with a mixture of Primary Reference Fuel 40 (PRF40) composed of 40% of isooctane and 60% of n-heptane volumetrically. The fuel blends specifications are listed in the fuel table in the appendix A. The fuel was injected using a direct injection system

and single injection scheme with injection timing in induction stroke set constant to 110° CA after TDC gas exchange (recompression). For the engine speed effect experiments, indeed engine speed was varied with the constant valve timing event set. These experiments were conducted with a constant fuelling rate. The valve timing event was varied and engine speed was kept constant for research on the influence of internal exhaust gas recirculation. This research was conducted while retaining a constant fuelling rate for one set of tests and fuel-air equivalence ratio for the other. Thus by varying two parameters 20 various engine operating conditions were investigated:

- 6 different engine speeds from 800 to 1800 rpm with 200 rpm step at a constant fuelling rate;
- 9 different valve timing events settings at a constant fuelling rate;
- 5 different valve timing events settings at a constant equivalence ratio.

The engine operating conditions for engine speed and residual rate experiments are summarised in Table 6.2. The research dealing with different engine speeds and the residual rates tests conducted cover (share) the same valve timing events matrix listed in Table 6.3.

Experiments	Engine Speed Influence	Residual Rates Influence
Intake Air Temperature	305 K	305 K
Intake Air Pressure	100 kPa	100 kPa
Coolant Temperature	363 K	363 K
Injection Timing	110° CA aTDC	110° CA aTDC
Injection Pressure	100 bar	100 bar
Engine Speed	Variable (800 – 1800 rpm)	1000 rpm
Valve Timing Event	Corresponding to VTE#3 of Table 6.2	Variable of Table 6.2

TDC is referred to Top Dead Centre of gas exchange (recompression)

Table 6.2. Engine operating conditions for test of engine speed and residual rates influence.

Valve Timing Event (VTE)	Intake Valves Timing		Exhaust Valves Timing		Estimated iEGR Mass Fraction	
	Intake Valves Opening (IVO)	Intake Valves Closing (IVC)	Exhaust Valves Opening (EVO)	Exhaust Valves Closing (EVC)	Constant Fuelling Rate Tests	Constant Fuel-Air Equivalence Ratio Tests
VTE-1	50°CA aTDC	180°CA aTDC	170°CA bTDC	60°CA bTDC	≈ 36.7 %	≈ 36.5 %
VTE-2			175°CA bTDC	65°CA bTDC	≈ 40 %	-
VTE-3			180°CA bTDC	70°CA bTDC	≈ 44.2 %	≈ 45.7 %
VTE-4			185°CA bTDC	75°CA bTDC	≈ 47.6 %	-
VTE-5			190°CA bTDC	80°CA bTDC	≈ 51.2 %	≈ 51 %
VTE-6			195°CA bTDC	85°CA bTDC	≈ 54.8 %	-
VTE-7			200°CA bTDC	90°CA bTDC	≈ 57.5 %	≈ 57.4 %
VTE-8			205°CA bTDC	95°CA bTDC	≈ 59.6 %	-
VTE-9			210°CA bTDC	100°CA bTDC	≈ 60.4 %	≈ 59.8 %

TDC is referred to Top Dead Centre of gas exchange (recompression)

Table 6.3. Engine valve timing events matrix.

6.3.2 Engine speed influence

As has previously been stated the experiments investigating the influence of engine speed on process type, fundamentally the magnitude of LTHR exhibited during the two-step process, were conducted by varying engine speed from 800 to 1800 rpm in a 200 manner step with a constant fuelling rate. The fuelling rate was chosen to provide lean engine operations under any investigated conditions, thereby eliminating parasitic and unwanted effects of incomplete fuel conversion due to lack of oxygen, under rich conditions.

The obtained results, the heat release rate profiles demonstrated in Figure 6.3 indicate the significant influence of engine speed on autoignition and combustion with an HCCI operated engine – the magnitude of low temperature heat release exhibited. There is a monotonic trend – a gradual low temperature heat release drop, both peak and magnitude of energy released during that phase with an increase in engine speed. The highest speed investigated i.e. 1800 rpm revealed great LTHR phase suppression and consequently could serve as a representation of a transition from a two- to –one step auto-ignition process.

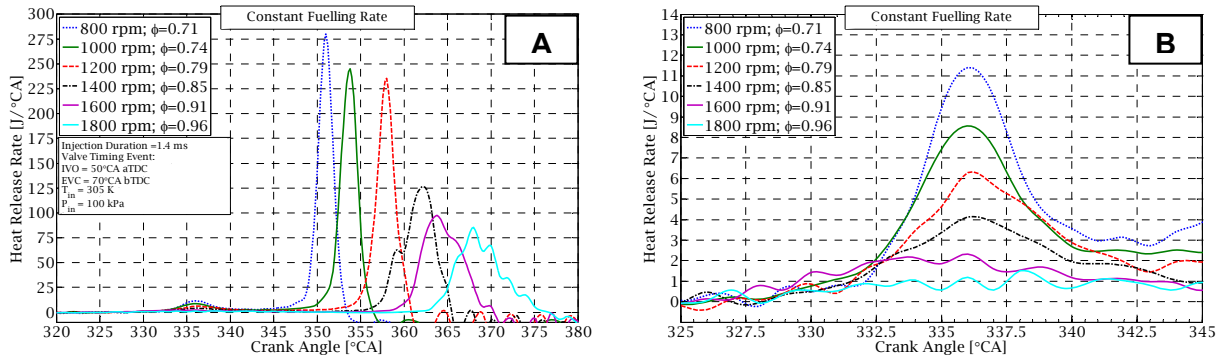


Figure 6.3. Engine speed effect on autoignition and combustion proceeding at constant fuelling rate; Total heat release profiles (A) and low temperature heat release profiles (B).

Fundamentally an engine speed increase leads to real time cycle reduction – shorter real time of crank angle interval. As this is the case and due to the fact that low temperature reactions are active at a specific temperature window i.e. 750 – 850 K, it can be stated that there is less time for these reactions to take place as speed increases. The progression from the initial temperature to the temperature terminating the LTHR activities is shortened, on a real time basis. Cool flame reactions are time dependent (Bartok *et al* 1991) and are conductive in a particular temperature window. Any increase in engine speed that reduces the amount of residence time availability for air-fuel mixture could therefore diminish the heat exhibited pending the LTHR phase. To gain a better understanding of this, a numerical analysis of the low temperature heat release phase activities has been conducted for engine speeds of 800, 1000, 1200 and 1200. The results are listed in Table 6.4.

Characteristic of LTHR Phase	Engine Speed			
	800 rpm	1000 rpm	1200 rpm	1400 rpm
Estimated Total Energy of LTHR [J]	≈ 63.3	≈ 53.1	≈ 42.3	≈ 33.3
LTHR Period [°CA]	14.6	17	16.2	16.6
Energy of LTHR Exhibited on Real Time Basis [J/ms]	20	18.7	18.8	16.8

Table 6.4. Characteristic of LTHR phases for engine speeds instances of 800 -1400 rpm.

The analysis confirms that the total heat released during LTHR phase is highly dependent on the real time available. Having compared two extreme cases analysed i.e. 800 and 1400 rpm, it could be inferred that for the available time of 800 rpm with 1400 rpm of energy

exhibiting during the LTHR on a real time basis there would be approximately a 65% increase in the total energy of cool flame activities as compared the to actual one. Also this analysis reveals the drop in estimated energy on real time base of the LTHR phase with an increase in engine speed. This is further explained in conjunction with the observed trend of a gradual fuel-air ratio increase as engine speed increases.

The evident variations in air-fuel ratio suggest that there must have been changes in the fresh charge mass induced per engine cycle as the fuelling rate was kept constant. As this is the case there is strong evidence that the fresh charge mass to trapped residuals ratios are varied for these different engine speeds. If this occurs it could contribute to variations in low temperature heat release activities. Figure 6.4 illustrates the recorded average mass of the fresh charge induced, the mass of trapped residuals per engine cycle and their ratios as a function of engine speed.

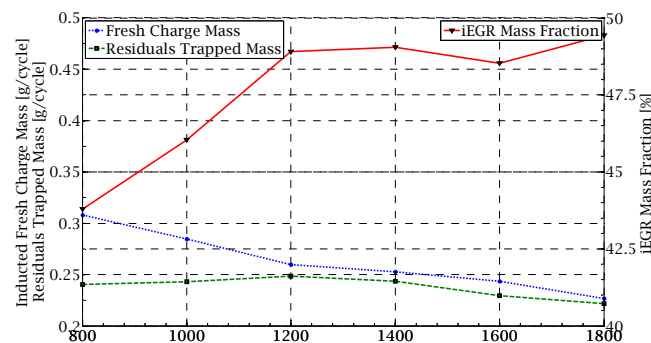


Figure 6.4. Mass of fresh charge induced, entrapped residuals and their ratios as a function of engine speeds investigated.

The data plotted in Figure 6.4 demonstrate the monotonic drop in drawn fresh charge mass per individual engine cycle with an increase in engine speed. The estimated residuals mass does not indicate a clear trend; initially at 800 rpm it increases reaching its maximum for 1200 rpm and then starts to decline. The estimated iEGR mass fraction rises with an engine speed increase (excluding the 1600 rpm point) presumably as a consequence of the drop in fresh charge mass with engine speed increment. The noticed trend of a fresh charge drop as engine speed increases may be a consequence of the valve timing event set. The intake

valves close at the bottom dead centre of the induction stroke which, in fact eliminate the reversing flow into the intake manifold and enhance cylinder filling at low speeds. At higher engine speeds the ram effect which improves the cylinder filling is significantly suppressed, therefore the inducted fresh charge mass is reduced (Heywood 1988).

At identical residuals and incoming fresh charge temperatures, the larger the iEGR mass fraction the higher the induction stroke BDC temperature is. This happens as the fresh charge and exhaust gases mix together. As a combination of both higher combustion temperatures (peak) and less time for heat transfer, the temperature of residual gases rises as engine speed increases. The effect of higher combustion temperatures is even more pronounced and further *boosted* by a drop in the air-fuel ratio with the increase in speed in our study, at a constant fuelling rate with this particular valve timing event. Consequently the higher temperatures of BDC indication stroke are expected for higher speeds investigated. Furthermore, they are raised quicker in comparison to low engine speed cases due to decreased heat losses as compressive heating progresses. This trend prevails prior to the low temperature heat release phase. At low speeds the higher heat released during LTHR can compensate for this temperature difference.

The cylinder pressure and the estimated average temperatures of cylinder charge curves prior to and during the LTHR phase for the investigated engine speed are shown in Figure 6.5.

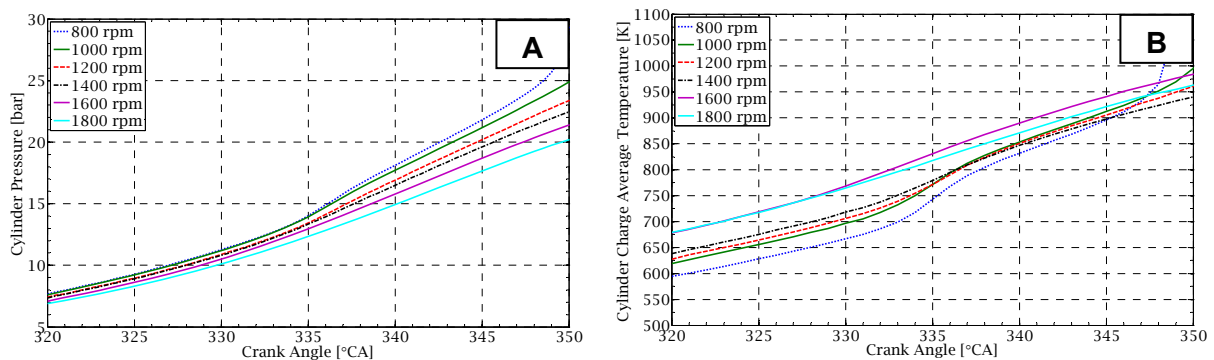


Figure 6.5. Cylinder pressures histories (A) and estimated cylinder charge average temperatures (B).

The data plotted in Figure 6.5 (B) suggest that at higher engine speeds higher BDC temperatures and additional aforementioned speed effects contribute to higher in-cylinder temperatures encountered at the same crank angle prior to low temperature heat release activities. To compensate for the initial temperature (BDC induction stroke), correction concerning various amount of residuals trapped was included into the estimation of these in-cylinder temperature profiles. This was achieved according to a procedure proposed by Sjöberg (2004). Although the temperature which initiates cool flame activities is encountered at earlier crank angle degrees for a higher engine speed, there is no apparent trend of LTHR shifts (on a crank angle basis) with engine speed variations; if one compares Figures 6.3 and 6.5(B). Moreover the peak positions of cool flames activities with different examined engine speeds are well matched on a crank angle basis. Correlating these activities with in-cylinder pressure traces plotted in Figure 6.5(A) it is seen that higher engine speed LTHR activities proceed at gradually lower cylinder pressure zones. As the reactions of cool flames activities are highly pressure dependent (Bartok *et al* 1991), this can clarify the observed trend of the position of LTHR peaks. The fraction of heat released pending cool flame activities is higher at gradually elevated pressures, therefore the initial stage of LTHR could exhibit less heat than a later stage of LTHR. Thus the peaks of LTHR for different engine speeds could match.

The reduction of magnitude exhibited by LTHR as engine speed increases is mostly due to the amount of time available for reactions to develop. Also the possible contributing effect of temperature-pressure histories to LTHR timing was observed. This was investigated and noted under the predetermined engine operating conditions.

During the early days of Homogenous Charge Compression Ignition engines, the effect of engine speed on cool flames activities was extensively investigated by Leppard (1990). He observed the monotonic and gradual drop of intermediates concentration formed during low temperature heat release, which was in fact an indication of LTHR magnitude with engine speed increments. The latest observations of this subject reported in open literature by Sjöberg *et al* (2003) pointed out also available time for reactions as a main consequence. They operated their engine without a negative valve overlap strategy and therefore the study

can not be directly correlated as they did not experience the effect of trapped residuals. As their engine was operated with variable intake air temperature to maintain constant combustion phasing (CA50) the influence of various intake air temperatures was extensively considered.

6.3.3 Residuals rate influence

Tests examining residuals rate (iEGR) effect on the process type - LTHR exhibited during the two-step process were carried out with various valve timing events listed in Table 6.2 at a constant engine speed of 1000 rpm. To gain a comprehensive insight one set of tests was performed with a constant fuelling rate and the other with a constant fuel-air equivalence ratio. The study with a constant fuelling rate was conducted using each valve timing event in Table 6.3, thus autoignition and combustion were examined under nine various levels of trapped residuals. Tests with a constant fuel-air equivalence ratio involved a study with five of these predetermined valve timing events. This could provide a direct and straightforward comparison between the constant fuelling rate tests and the fuel-air equivalence ratio tests.

As seen from Table 6.3 the different valve timing events and thus residuals rates were done by varying only the exhaust camshaft position. Gradual advancement of the closing point of the exhaust valves results in a relatively higher mass and volume of trapped residuals from one case to another. With fixed conditions of incoming charge i.e. intake air temperature and pressure, the gradual drop in volumetric air-flow yields lower fresh charge mass and higher iEGR mass fraction values.

The obtained results for constant fuelling rate tests are plotted in Figure 6.6. The corresponding in-cylinder pressure and average temperature of cylinder charge profiles are demonstrated in Figure 6.7. The constant air-fuel equivalence ratio tests results are presented in Figure 6.8 and their corresponding in-cylinder pressure and average temperature of cylinder charge profiles are plotted in the subsequent figure – Figure 6.9.

Constant fuelling rate experiments were conducted with a selected fuelling rate providing lean engine operating conditions so that a case with the highest iEGR fraction could be investigated.

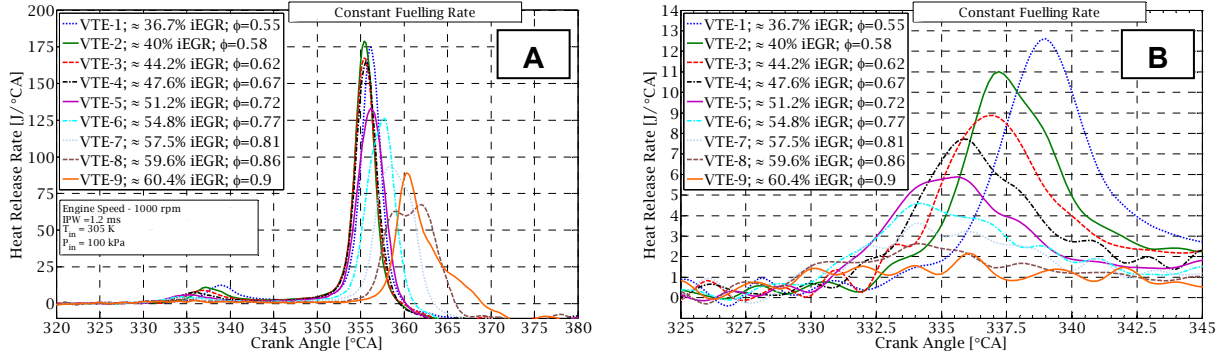


Figure 6.6. Influence of internal exhaust gases on autoignition and combustion proceeding at constant fuelling rate; Total heat release profiles (A) and low temperature heat release profiles (B).

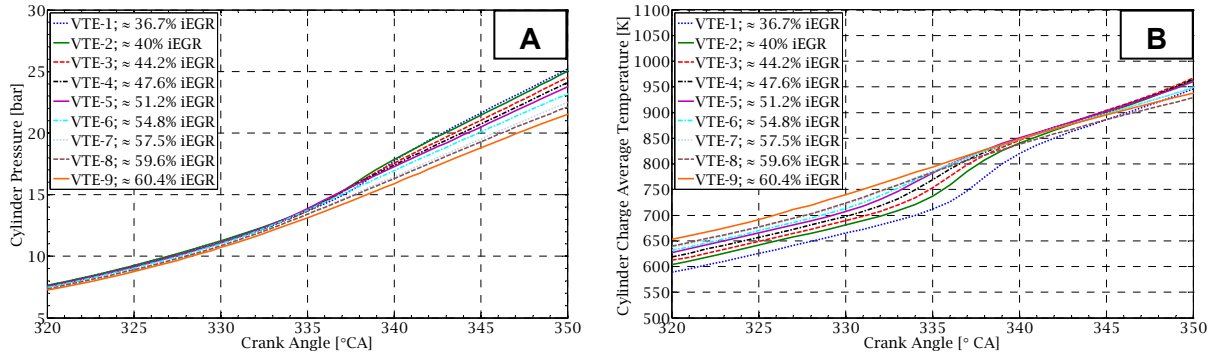


Figure 6.7. Cylinder pressures histories (A) and estimated cylinder charge average temperatures (B) prior to HTHR activities for constant fuelling rate tests.

The plotted heat release curves of autoignition and combustion activities in Figures 6.6 and 6.7 under various fractions of trapped residuals conditions indicate an apparent trend. The monotonic gradual advancement in the onset of low temperature heat release associated with a reduction in its magnitude is observed as the amount of trapped residuals increases relatively to the fresh charge. This is the case for both sets of tests, with a constant fuelling rate and a constant air-fuel equivalence ratio. The transition from a one- to a two-step ignition process is observed for around 60% trapped residuals of the total charge mass. Also after

comparing Figures 6.6(B) and 6.7(B) another important observation could be made; there are no significant rises or drops in LTHR magnitudes or peaks with different fuel-air ratio conditions as corresponding cases of the same valve timing event are considered.

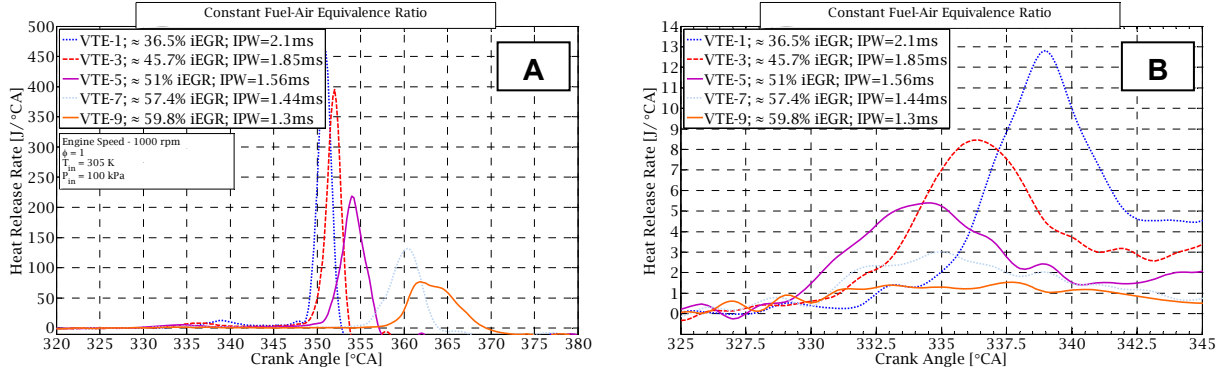


Figure 6.8. Influence of internal exhaust gases on autoignition and combustion proceeding at constant fuel-air equivalence ratio; Total heat release profiles (A) and low temperature heat release profiles (B).

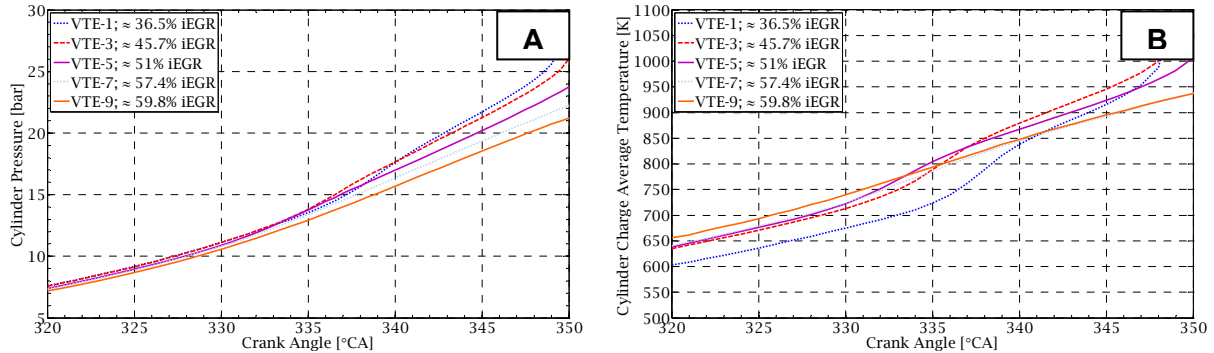


Figure 6.9. Cylinder pressures histories (A) and estimated cylinder charge average temperatures (B) prior to HTHR activities for constant fuel-air equivalence ratio tests.

The observed influence of internal exhaust gas recirculation on the HCCI autoignition and combustion should be considered on two key planes. Firstly as exhaust gases recirculation is internal and utilises trapped residuals, the thermal effect should be addressed. Secondly the chemical effect, relating to the difference in charge composition as the residual fraction is varied, needs to be taken account. Also as importantly this chemical effect may be more pronounced during the constant fuelling rate tests because the composition of residuals is significantly changed by changes to the fuel-air equivalence ratio under these conditions.

As low temperature heat release activities are shifted towards the earlier crank angle with an increase in residuals fractions for both a constant fuelling rate and an fuel-air equivalence ratio tests this would indicate that the LTHR phase conductive window is altered on a crank angle basis. For the constant fuelling rate with a fixed incoming air temperature and pressure the higher fraction of entrapped residuals leads to elevated induction stroke BDC temperatures. The same might be stated for a constant fuel-air equivalence ratio; however, the compensation for progressively elevated temperatures of residuals as the iEGR fraction is reduced should not be disregarded. This happens since the amount of fresh charge increases and in order to provide the equivalent fuel-air ratio more fuel needs to be injected. On the other hand although the trapped residuals are at higher temperatures there is more fresh charge, which needs to be heated up as well. As Figure 6.10 shows this is the case. Higher residuals temperatures encountered at lower iEGR fractions have not produced higher charge temperatures (estimated at BDC induction stroke) than cases of lower residuals temperatures with a higher iEGR, even at a constant fuel-air ratio. This indicates that the gain due to the elevated temperature of residuals was significantly used for heating up more of the fresh charge mass.

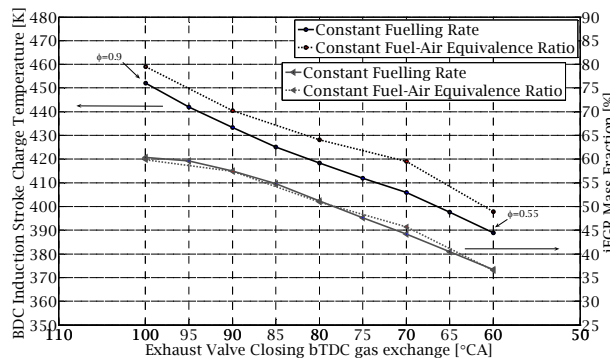


Figure 6.10. Induction stroke BDC temperature and iEGR mass fraction as a function of exhaust valve closing point for constant fuelling rate and fuel-air ratios.

Also the evident progressive increase in BDC induction stroke temperature with an increase in the iEGR mass fraction is presented. This is the case for both the constant fuelling rate tests and the fuel-air equivalence ratio tests' points. Further as this happens the higher

temperatures are encountered at an earlier crank angle for a higher fraction of trapped residuals. Indeed this would justify the behaviour of an advanced onset of cool flame activities with an increase in residuals fractions, as the LTHR phase is active within the particular conductive temperature window. Furthermore correlating this observed trend of LTHR activities phasing with the corresponding cylinder pressure curves of Figures 6.7(A) and 6.9(B) one can see that the cool flame activities proceed at various in-cylinder pressure zones. It appears that air-fuel mixtures traverse very similar pressure histories prior to the onset of cool flame activities for a given set of experiments. Therefore, with an increased in the trapped residuals fraction advancing the initiation of cool flame activities (on a crank angle basis), this phase occurs in a lower cylinder pressure zone. This could have contributed to a progressive reduction in the LTHR magnitude exhibited with increasing the trapped residuals fraction, as elevated pressure favours the low temperature reactions. This discovery of low temperature reactions on pressure dependency has been recently noticed in HCCI operated engine study by Christensen *et al* (1998). and Sjöberg *et al* (2003). Also it was well described as one of the general combustion fundamentals by Bartok *et al* (1991). The above discussion identifies the thermal influence of the residuals on the observed variations in the magnitude and timings of LTHR activities during the two-step ignition process.

As neither emission tests nor particular thermodynamic studies were conducted, the chemical effect of the residuals on the observed trend could only be addressed based on theoretical consideration in conjunction with a review of available literature. However, further insight into the chemical site of a one- and a two-stage ignition process is also gained when the spectroscopic data are demonstrated in the subsequent section, as the transition from a one to a two-stage ignition process was achieved by trapping a higher fraction of residuals. Precisely speaking this is a chemical analysis of thermodynamic properties of residual constituents (species) which influence the charge temperature i.e. heat capacity (Sjöberg *et al* 2007). Also it should be noted that not only the thermodynamic analysis of residuals species should be considered but also of fresh charge as the total charge is composed of

both at various proportions under different conditions in our study. Sjöberg *et al* (Sjöberg *et al* 2007) investigating the heat capacity of individual species of stoichiometric combustion products i.e. carbon dioxide, water and nitrogen, noting that the CO_2 contributes the most to the charge cooling, thus its heat capacity is the largest of these three aforementioned species. They also discovered that diatomic nitrogen elevates compressed gas temperature more effectively than pure air, as a consequence of its lower heat capacity. Water has moderate heating capacity among the investigated species of stoichiometric combustion products.

It is clear that real residuals could contain other chemicals such as carbon monoxide, unused oxygen, unburned hydrocarbons or nitrogen oxides species beyond the stoichiometric combustion products. Also the composition of actual residuals is highly dependent on combustion stoichiometry and other relevant engine operating conditions that bring about the combustion process. It is true that at a constant fuelling rate the increase of the trapped residuals relative to fresh charge elevates the total concentration of carbon dioxide in the charge. In parallel the concentration of water, nitrogen and nitrogen oxides increases. There is a reduction in oxygen concentration as a result of both less fresh air drawn and less of an unused oxygen presence in residuals coming from richer combustion. As more concentration of both carbon dioxide and nitrogen are retained as a result of an iEGR fraction increase it is hard to distinguish how the charge has been influenced by their presence as they exhibit opposite effects to charge temperature. At constant air-fuel ratio conditions, the residuals composition remains constant regardless of combustion inefficiencies. This is the fraction of residuals to fresh charge which defines the whole concentration of the species. Indeed as the iEGR mass fraction increases there is more CO_2 , water and nitrogen or nitrogen oxide concentration associated with a pure oxygen drop. Similarly as stated above it is hard to predict the trend of how the charge has been influenced by the presence of the residuals based on this theoretical consideration. All these theoretical studies addressed above including the literature review were dedicated to point

out the chemical effect of residuals which could give an additional potential contribution to the observed trend in this study.

The third finding of this study is that the amount of fuel injected appears to have no influence on the magnitude or peak of the LTHR phase for the investigated fuelling rate under a constant fraction of trapped residuals. This is shown in Figure 6.11 using three different fuelling rates, which in fact form three different combustion stoichiometry conditions i.e. fuel-air ratio.

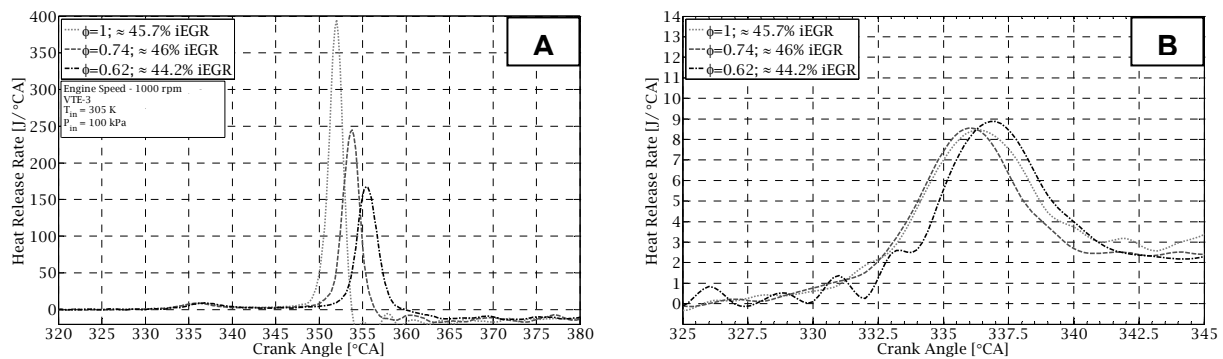


Figure 6.11. Effect of fuelling rate on autoignition and combustion proceeding at nearly identical residuals fraction; Total heat release profiles (A) and low temperature heat release profiles (B).

Plotted curves of the LTHR activities in Figures 6.11(B) show similar peaks, magnitudes and also timings of this phase, regardless of significant changes in air-fuel ratios. Therefore it could be inferred or hypothesised that this amount of iEGR rate considerably limits the development of low temperature reactions and is independent of fuelling rate within the specified range of fuel-air ratio. Furthermore this would imply that only part of the injected fuel precedes the cool flame activities and contributes to the magnitude of the LTHR exhibited, whereas within the fuelling rates investigated this has not had a pronounced effect. Regardless of the precise nature of this behaviour, this finding has crucial importance for studying the ignition type processes of HCCI operation.

6.4 Physicochemical characteristics of one- and two-step ignition processes

6.4.1 Experimental aspects

The research identifying the physiochemical nature of the one and two-step ignition process has been conducted using an optical engine, the detailed description of which can be found in section 3.2.2. To conduct the analysis of the physicochemical nature two passive optical diagnostics techniques were employed with simultaneous in-cylinder pressure records. Firstly imaging with an Andor iStar iCCD camera and then spectroscopy measurements utilising an Oriel MS260i imaging spectrograph coupled with the aforementioned camera was performed. These two diagnostic instruments along with their detailed technical specifications were introduced and presented in sections 4.3 and 4.5.

The optical engine was running on Primary Reference Fuel 40 (PRF40) with a constant engine speed of 1000 rpm. The transition from a one- to a two-step ignition process or vice versa was realised by varying the valve timing event, more specifically the exhaust valves closing point. As a result of the elevated residuals fraction trapped at a particular studied engine speed and intake air temperature the blend of PRF40, a potential two-step ignition fuel was undergoing one-stage ignition process. Apparently the reduction of entrapped residuals forced a transition from a one- to a two-step process to occur. This was a subject of investigation within the previous section and was addressed in greater depth. Hence the study of the one- and two-stage ignition processes was conducted by varying only the fractions of residuals entrapped, while keeping all the other engine operation parameters constant i.e. intake air temperature, pressure or injection timing and pressure. Indeed this was done to avoid any parasitic unwanted influence on its observed nature. The research

was conducted with a constant fuelling rate for two different valve timing events strategies.

The engine operating conditions are listed in Table 6.5.

Engine Operating Variables	Experiments	
	One- and two-step ignition process – - physicochemical nature	
Intake Air Temperature	313 K	
Intake Air Pressure	100 kPa	
Coolant Temperature	363 K	
Injection Timing	140° CA aTDC	
Injection Pressure	100 bar	
Engine Speed	1000 rpm	
Valve Timing Event	VTE#1	VTE#2
Intake Valves Opening	55° CA aTDC	55° CA aTDC
Intake Valves Closing	205° CA aTDC	205° CA aTDC
Exhaust Valves Opening	220° CA bTDC	240° CA bTDC
Exhaust Valves Closing	70° CA bTDC	90° CA bTDC
Estimated iEGR Mass Fraction	≈ 42%	≈ 57%

TDC is referred to Top Dead Centre of gas exchange (recompression)

Table 6.5. Optical engine operating conditions.

The spectroscopic data and images were acquired throughout the triangular vertical window of the engine head as an optical access. The spectrometer was positioned perpendicularly to the optical engine axis so that the slit of constant height was located across the triangular head window, thereby recording light from the whole of combustion chamber. Also the plano-convex lens was mounted in between the spectrometer and engine to focus the light into the spectrometer slit. This lens was made of silica fused material. Figure 6.12 shows the triangular optical access to the combustion chamber with reference to location of its artifacts the spark plug and valves.

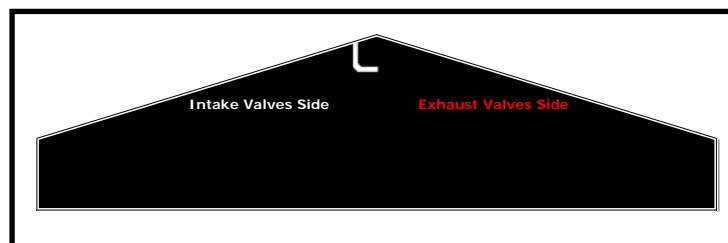


Figure 6.12. Access through triangular vertical head window in reference to combustion chamber artifacts locations.

For the imaging experiments the Andor iStar iCCD monochromatic camera was coupled with a UV-Nikkor 105 mm f/4.5 lens. The lens aperture was set to f/5.6 and the focus distance equaled 0.7 m during the experiments. With these parameters chosen the depth of field equaled the value of 6 mm (0.697 – 0.703 m). The focusing was performed only for a visible light.

The spectroscopic measurements were conducted using an Oriel MS260i™ 1/4m Imaging Spectrograph with 300 lines/mm grating and 0.5 mm slit width set. The slit width was set manually, and grating selection was accomplished via the iCCD controlling software. By rotating the grating windows with different spectral wavelengths, comprehensive spectra were acquired. The calibration was performed with a 6025 Mercury –Argon Oriel Instruments Spectral Calibration Light, which emits a number of known spectral lines.

The spectroscopic data as well as the image acquisitions were controlled by the intensifier operation. With the constant values of light integration (gate pulse width) 166 μ s and 332 μ s (corresponding to 1 and 2° CA at studied engine speeds) for image and spectroscopic data acquisitions respectively and an MCP gain of 50 and 250 settings a straightforward comparison of corresponding obtained results could be achieved. The IntelligaGate system was enabled for image acquisition. The camera temperature was set to -20°C in order to reduce dark current noise. The camera settings for imaging experiments are summarised in Table 6.6. Table 6.7 summarises settings for the spectroscopic measurements of both the spectrograph and the iCCD, as the imaging spectrograph was coupled with the aforementioned imager.

The camera recorded optical data and images as a single scan acquisition and was controlled externally when the start of individual image acquisition (grabbing point) was synchronised with the engine operation. This was accomplished via the engine controlling software which has the capability to send out a single signal every engine cycle to initiate image acquisition. At the engine operating conditions studied and the above specified parameters of acquisition the low camera frame rate of 0.72 Hz resulted in only one image per engine cycle being acquired skipping 15 cycles. The one image at each corresponding

crank angle was captured during the imaging acquisition; for the spectroscopy 10 measurements were taken at the corresponding crank angle of the cycle (10 various cycles) and then averaged.

iCCD Camera Settings	Set Value
Number of Pixels (CCD Array)	1024 x 1024
Optical Active Area (CCD Array)	13,3 x 13,3 mm
Optical Gate Pulse Width	166 μ s ($\approx 1^\circ$ CA)
CCD Exposure Time	1000 μ s
Synchronization	External
Trigger and Sync Image Acquisition Inputs	TTL Pulse Rising edge
MCP Gain	50
Gate Pulse Delay	0
Camera Temperature	-20° C

Table 6.6. Settings of iCCD Andor iStar monochromatic imager.

Device and Its Settings	Set Value
<i>Oriel MS260i™ 1/4m 74050 Imaging Spectrograph</i>	
Grating	300 lines/mm
Slit Width	0.5 mm
<i>iCCD Camera</i>	
Gate pulse Width	332 μ s ($\approx 2^\circ$ CA)
CCD Exposure Time	1000 μ s
Gate Pulse Delay	0
MCP Gain	250
Frame Rate	0.85 Hz
Camera Temperature	- 20° C
Acquisition Type	Single Scan

Table 6.7. Settings of Oriel MS260i™ spectrograph and iCCD imager.

The analysis of iCCD camera images used raw gray-level (monochromatic) images with spanning with the signal from 0 to the saturation value directly corresponding to camera counts. Indeed a part of the combustion chamber only was distinguished from the whole image for quantifying the peak or total light emission (TL). The spectroscopic data were also processed as raw data with no correction to the different quantum efficiencies of iCCD imager and the spectrograph versus wavelength correction.

6.4.2 Physicochemical analysis of one- and two-step ignition processes

In the previous section of this chapter we concentrated on thermal observations regarding the dependency of ignition process type on engine operating variables, more specifically the LTHR activities of the two-step process. The qualitative and quantitative influence as well as the transition states from a one-to a two-step ignition process or vice versa were defined with regard to engine speed and the residuals rates for this particular engine. This section focuses on the understanding of the physicochemical natures of one- and two-step ignition processes, based on the analysis of the quantification of intensity of light emitted and the identification of chemical species at corresponding phases via the spectroscopic measurements. For spectroscopic measurements the emissions of formaldehyde, with the strongest bands of 370-480 nm region and hydroxyl – with the most intense head of 306.4 nm (Gaydon 1974) were of particular interest. The formaldehyde (CH_2O) emission serves as an indication of cool flame activities, and initially was observed by Emeleus (Gaydon 1974). as a dominant species in a spectra of cool flames The engine experiments of HCCI evidently showed that a low temperature heat release region is associated with the emission of CH_2O (Hultqvist *et al* 1999; Hildingsson *et al* 2004; H.Zhao *et al* 2004; Amneus *et al* 2007; Hwang *et al* 2008). While the formaldehyde emission scales well with cool flame activities, OH was identified as a tracer of hot temperature heat release regime by all the aforementioned researchers. Interesting findings have been recently reported by Hwang *et al* (2008) regarding the precise identification of distinctive HCCI phases. They showed that apart from one or two key phases of the one- and two-step ignition process respectively there is clearly another identifiable one called intermediate temperature heat release. As a result the one-step process has two distinctive phases, and the two-step process is made up of three distinctive phases as the ITHR is considered to occur.

The analysis of the physicochemical nature of one- and two-step ignition processes was conducted using the same fuel blend (PRF40) and the same engine operating conditions such as engine speed, fuel-air ratio, intake air temperature or pressure etc. The process transition from two- to one-step was accomplished by varying the valve timing event thereby facilitating the investigational analysis. Hence a comprehensive analysis of the autoignition and combustion activities characterisation was conducted under two different valve timing events. Figure 6.13 demonstrates two average heat release profiles under these two different valve timing events investigated.

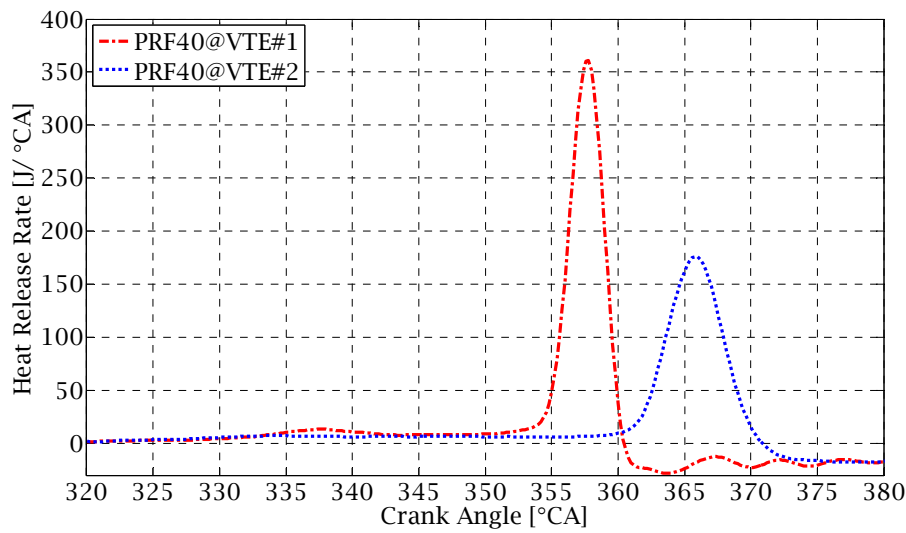


Figure 6.13. Profiles of heat release rates for two different valve timing events activities.

For the valve timing event referred to first the mixture undergoes a two-step ignition process, whereas for the second, LTHR period is significantly suppressed. Therefore it is believed that the process is a one-step ignition process. Nevertheless the minor exhibition of cool flames activities might still be detectable. Because of this three distinctive phases for each investigated valve timing event are analysed and considered in this study. Figures 6.14 and 6.15 demonstrate the characteristics of autoignition and combustion activities of their particular corresponding phases, indeed for two valve timing events examined. The light intensity of activities of potential low and intermediate temperature heat release rates are scaled on the same basis for these two cases examined. This provides a straightforward

insight. The same was done for the HTHR period. Further the analysis of the intensity of light emitted in a quantitative way as a function of crank angle for a particular engine cycle region is presented in Figures 6.15 and 6.17 for the two valve timing events investigated.

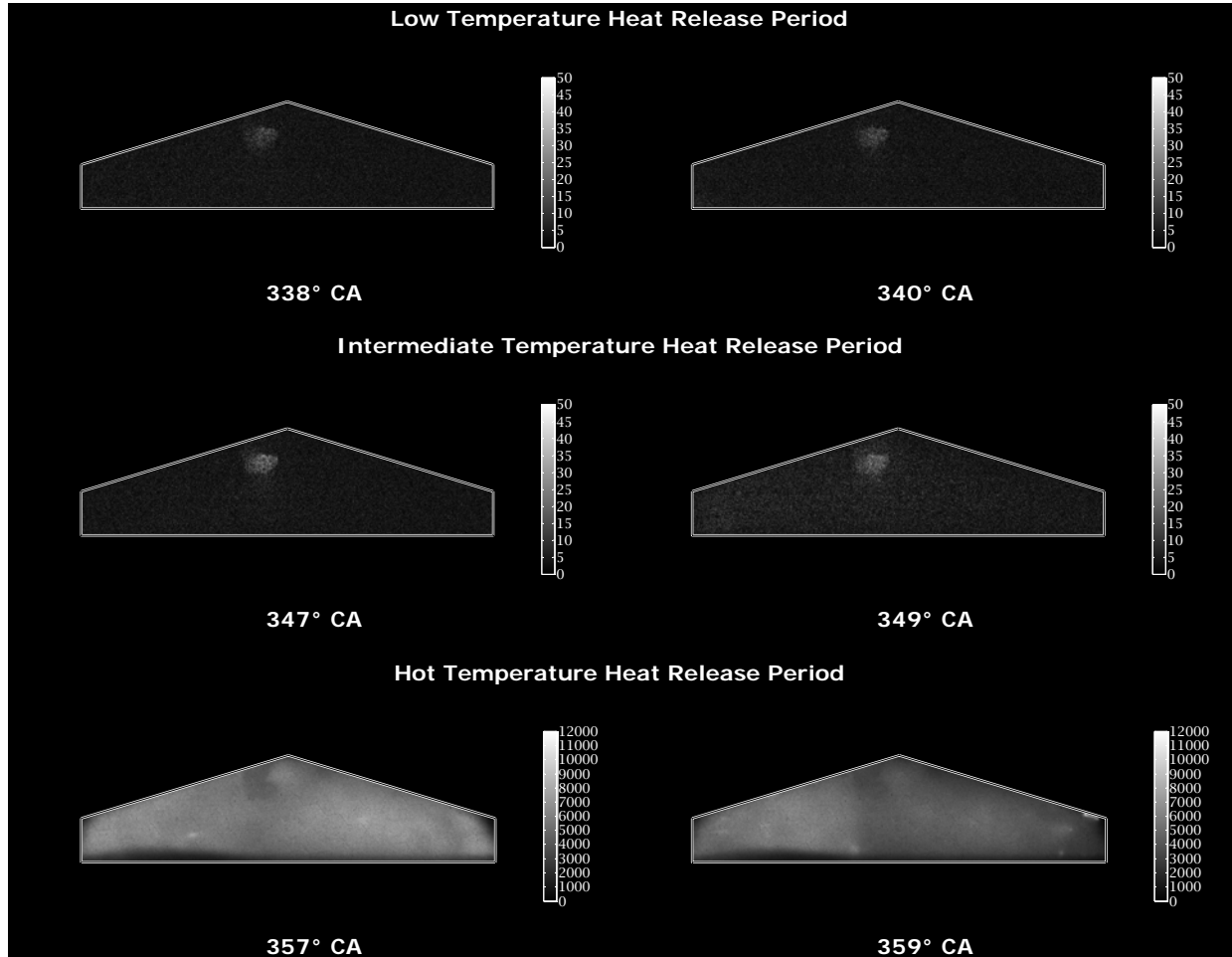


Figure 6.14. Single images of various crank angles, illustrating different phases of autoignition and combustion process proceeding at investigated VTE#1.

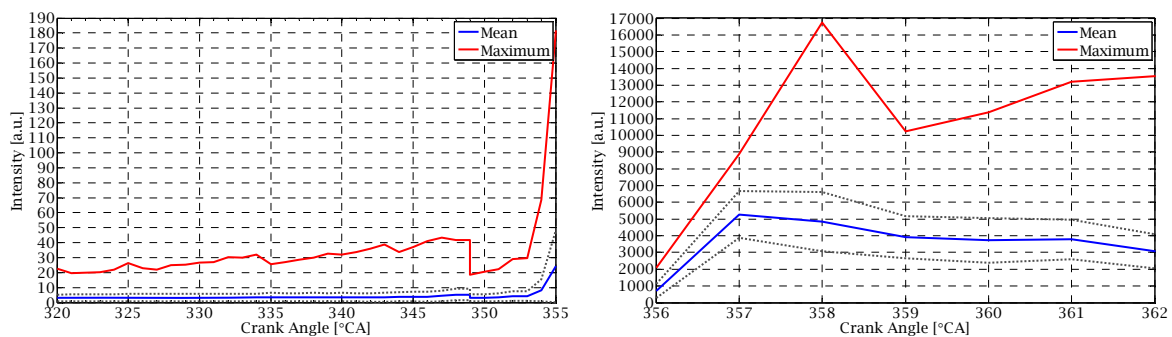


Figure 6.15. Light emission intensity as a function of crank angle for autoignition and combustion activities at investigated VTE#1.

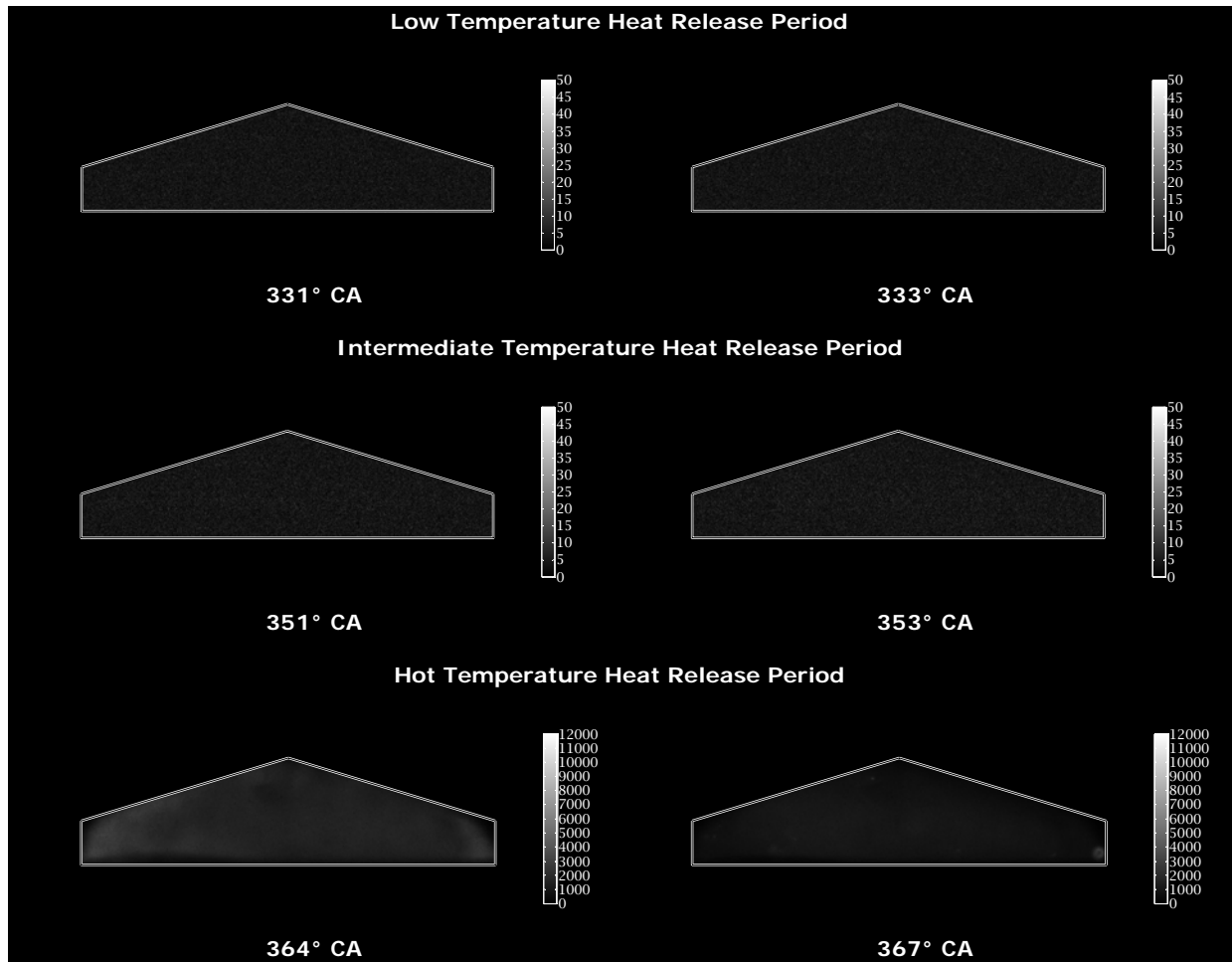


Figure 6.16. Single images of various crank angles, illustrating different phases of autoignition and combustion process proceeding at investigated VTE#2.

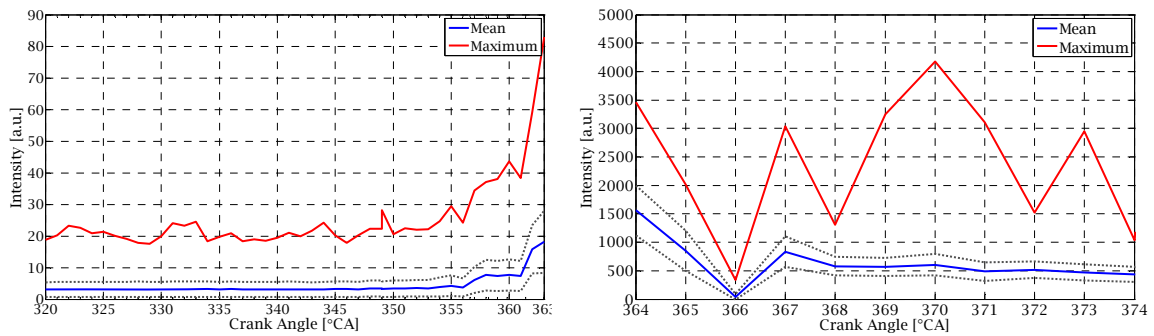


Figure 6.17. Light emission intensity as a function of crank angle for autoignition and combustion activities at investigated VTE#2.

This shows both the average and peak values of observed (recorder) natural light emission intensity. Comparing experimental results, more specifically the characteristics of their corresponding phases plotted in Figures 6.14, 6.15, 6.16 and 6.17 two main

observations can be made. Firstly the light emitted intensity varies when the corresponding phases of these two autoignition and combustion processes are compared. Secondly the successive phases of the given process vary among them, and the significant difference is the amount of light emitted between the LTHR or ITHR and the main combustion HTHR phase.

Having examined the corresponding phases between investigated phases the lower intensity of light during the potential cool flame activities could be justified as a suppressing effect of residuals, and it generally precedes the one-step ignition process under VTE#2 in comparison to VTE#1. As an effect of proper cool flame activities the two-step process emits the light more intensely during this period. Further analysing the HTHR activities a similar trend is noticeable, the light intensity emission is considerably higher for valve timing event one than for the second case investigated. However, this is not surprising as experiments were carried out with a constant fuel-air ratio. As fewer amounts of residuals are trapped, more air is inducted and so more fuel is injected to provide the same fuel-air equivalence ratio i.e. stoichiometric one in this study. Essentially the light emission intensity is highly dependent on the concentration of the chemical species taking part in chemiluminescence reactions (Garcia-Campana *et al* 2001) i.e. fuel and air in this case and the reaction rate. Also, the reaction rate is a function of the chemical analysis. This would justify the differences in light intensity emitted between the HTHR activities of the two examined cases. Persson *et al* (2005) observed that the light intensity becomes smaller quantitatively as when the engine works progressively under the lower load. Also Persson *et al* (2005) and Hultqvist *et al* (1999) reported that the light emission intensity profile during the HTHR period scales well with the profile of the pressure derived heat release rate.

From the Figure 6.16 it would appear that any potential lower temperature and intermediate temperature heat release periods are quite uniform and low light emission intensity phases. This was also observed by Hwang *et al* (2008). However, by analysing Figure 6.14 the local zone of higher light intensity is observed for each individual picture presented of LTHR and ITHR phases. This could indicate that the characteristic chemical

species for LTHR and ITHR phases might develop locally. By characteristics chemical species we mean the formaldehyde emission as one which has been identified for both phases of low and intermediate temperature, with higher emission for the ITHR than the LTHR phase by Hwang *et al* (2008). The various studies of light emission or CH_2O concentration reveal that formaldehyde could occupy the whole combustion chamber on one hand or could be formed locally (Zhao *et al* 2004; Amneus *et al* 2007; and Hwang *et al* 2008), at least at the initial stage. The interesting and relevant finding of the CH_2O investigation reported by Zhao *et al* (2004) for our study seems to be that when the formaldehyde emission was observed locally its development was highly dependent on a local charge temperature not a global one. Hence correlating our study images of 338, 340, 347 and 349°CA of Figure 6.14 with their investigation finding the higher light intensity zone distinguishable within the combustion chamber would indicate the existence of a local temperature zone. More precisely, this zone might be favourable temperature regime for reactions to occur, presumably the formation of formaldehyde.

The spectrum of the low and high temperature heat release periods at corresponding crank angles is demonstrated in Figure 6.18 and 6.19 for the cases VTE#1 and VTE#2. It appears that the cool flame activities are characterised well by an emission of formaldehyde with Emeleus formaldehyde bands in the region 370-480 nm. As seen from Figure 6.19 (A) the emission of the CH_2O is drastically reduced in comparison to Figure 6.18 (A), as the low temperature is significantly suppressed due to elevated percentage of residuals. Hence this spectrum is characteristic more for a one-step ignition. The high temperature heat release is characterised by an emission of hydroxyl with its peak at 306.4 nm. Indeed the emission is elevated for the first valve timing event investigated in comparison to the second valve timing event, which is presumably the consequence of fuel concentration. This reason was discussed above in the light emission intensity analysis. The finding of this investigation i.e. the presence of formaldehyde during the LTHR and hydroxyl for HTHR are in agreement with studies conducted by other researchers i.e. Hultqvist *et al* (1999), Kawahara *et al* (2003) and Hwang *et al* (2008).

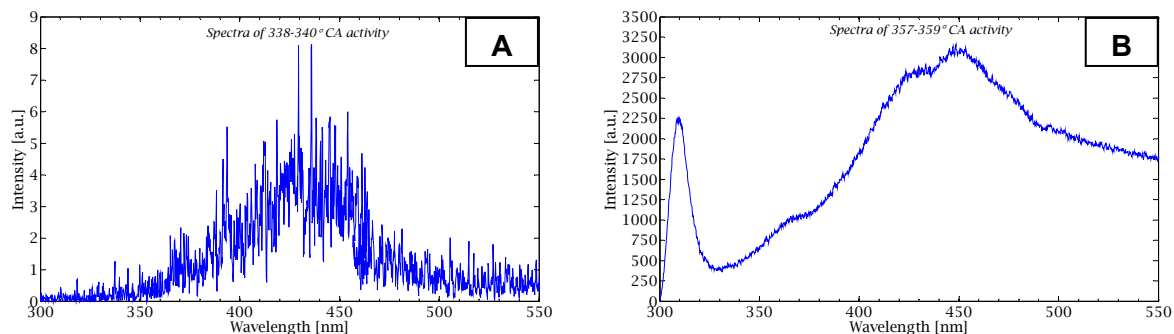


Figure 6.18. Spectra of potential low temperature heat release activities (A) and heat release activities (B) at corresponding crank angle degrees – VTE#1.

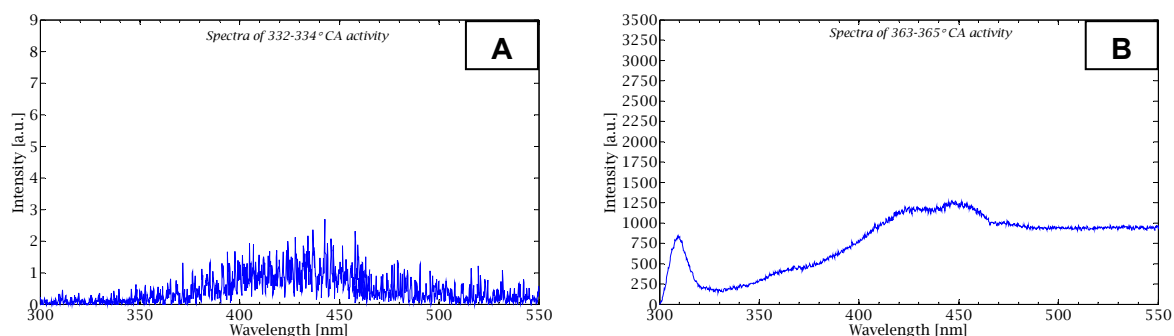


Figure 6.19. Spectra of potential low temperature heat release activities (A) and heat release activities (B) at corresponding crank angle degrees – VTE#2.

6.5 Correlation of ignition process type with fuel octane quality

6.5.1 Experimental aspects

A study correlating ignition process type with potential fuel autoignition qualities determined by fuel octane numbers and fuel sensitivity has been conducted using a thermal engine and four various blends. Three of these blends were nonsensitive Primary Reference Fuels with different octane numbers varying from 40 to 80 (PRF40, PRF75.6 and PRF80). The fourth fuel blend was the sensitive Toluene Standardization Fuel blend (TSF75.6) of the same RON as PRF75.6 (75.6) and different MON, with a sensitivity value equal to 8.7. The compositions and other relevant properties (for this study) of these blends are listed in the common fuel data table in the Appendix.

By contrasting the behaviour of PRF40 and PRF80 an understanding of the influence of fuel octane quality on ignition process type was gained. Moreover by comparing the process characteristics exhibited by the two alike chemical blends of PRF75.6 and TSF75.6 an insight into the role of fuel sensitivity was gained. Hence two sets of experiments were conducted.

The first set of tests were carried out under various engine speeds and residual rates (valve timing events) using PRF40 and PRF80. These were performed with a constant fueling rate (for a given blend), intake air temperature, pressure and injection pressure-timing. Table 6.8 summarises engine operating variables for these experiments.

The second set of tests were conducted using blends of PRF75.6 and TSF75.6 under a constant engine speed of 600 rpm, a fuel-air equivalence ratio (stoichiometric) injection pressure and timing. The fuel blends used, more specifically their compositions were strictly standardised ones according to ASTM D2699 and D2700 to reflect the same antiknock

(autoignition) propensities at RON method conditions. By varying the intake air temperature an insight into the effect of octane sensitivity was gained with a range of temperatures investigated, as one of the two key parameters distinguishing RON and MON procedures is different temperature. The MON and RON method procedures are specified in the appropriate tests methods standards ASTM D2699 and D2700 respectively.

Engine Operating Variables	Experiments
	Influence of Fuel Octane Number on Type of Ignition Process
Intake Air Temperature	313 K
Intake Air Pressure	100 kPa
Coolant Temperature	363 K
Injection Timing	110° CA aTDC
Injection Pressure	100 bar
Engine Speed	Variable
Valve Timing Event	Variable

TDC is referred to Top Dead Centre of gas exchange (recompression)

Table 6.8. Engine operating conditions for PRF40 and PRF80 tests.

Engine Operating Variables	Experiments
	Influence of Fuel Octane Sensitivity on Type of Ignition Process
Intake Air Temperature	Variable
Intake Air Pressure	100 kPa
Coolant Temperature	363 K
Injection Timing	110° CA aTDC
Injection Pressure	100 bar
Engine Speed	600 rpm
Valve Timing Event	
Intake Valves Opening	50° CA aTDC
Intake Valves Closing	180° CA aTDC
Exhaust Valves Opening	180° CA bTDC
Exhaust Valves Closing	70° CA bTDC

TDC is referred to Top Dead Centre of gas exchange (recompression)

Table 6.9. Engine operating conditions for PRF75.6 and TSF75.6 tests.

6.5.2 Fuel octane number and ignition process

Research and Motor Octane Numbers are the most extensively and common used laboratory ratings methods for determining the anti-knock (auto-ignition) quality of liquid fuel for spark-ignition engines. The octane number scale is defined by the volumetric composition of two paraffinic hydrocarbons, isooctane (2,2,4 trimethylpentane) and n-heptane. Isooctane was assigned a value of 100 and n-heptane zero octane numbers. Volumetrically proportioned mixtures of isooctane and n-heptane are named Primary Reference Fuels, which by definition have zero fuel sensitivity. This means that their antiknock (auto-ignition) resistance is identical for RON and MON test conditions.

The data analysis of the autoignition and combustion of PRF40 and PRF80 blends under various operating conditions is presented in Figure 6.20. Two plotted graphs show the magnitude of the LTHR phase exhibited under various engine speeds (A) and valve timing events (B) for two investigated blends. The engine speed investigation experiments were conducted with a constant valve timing event set, while various tests were conducted with the influence of residuals at a constant engine speed.

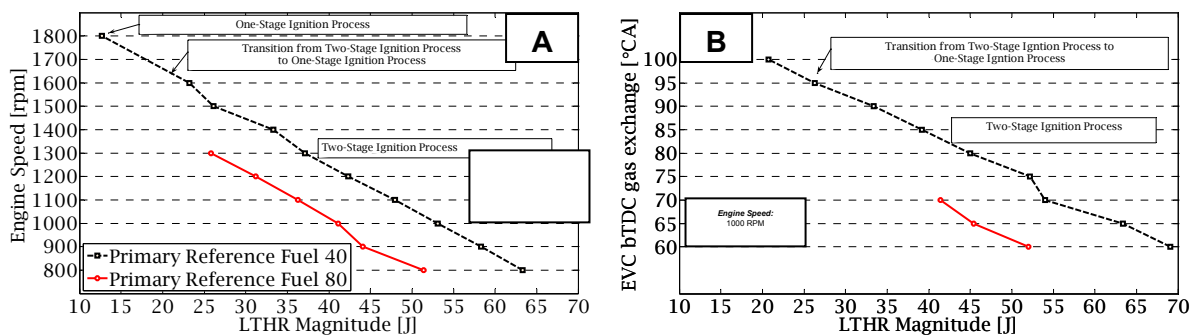


Figure 6.20. Magnitudes of cool flame activities of PRF40 and PRF80 blends for a range of various engine speeds and residuals fractions conditions.

By analysing these results two main observations could be made. Firstly and most importantly for this analysis the magnitude of cool flame activities exhibited by PRF80 is always lower than that of PRF40 under any investigated engine operating conditions, speeds

or residuals rates. However, this is not surprising because the cool-flame activities are very much dependent on a reactive n-heptane concentration (Bartok *et al* 1991, Sjoberg *et al* 2003). Hence for Primary Reference Fuel blends this would imply that the heat release of low temperature reactions is dependent on the fuel octane number, and with a gradual fuel octane increase a progressive drop in the LTHR phase should be observed. Furthermore as a combination of both a reduction in the concentration of reactive n-heptane and its diminished contribution to low temperature heat release, the autoignition propensities deteriorate as fuel octane number increases. This particularly happens when the energy released pending cool flame activities acts as an additional source of temperature increase (Sjoberg *et al* 2003). Therefore the low temperature heat release is crucial in defining autoignition propensities for an HCCI operated engine.

Secondly a higher octane number blend would show a transition from a two- to a one-step process or vice versa at the point at which the PRF40 still proceeds the two-step ignition process. However, above the engine speed 1300 rpm with a valve timing – EVC 70° bTDC and IVO - 50° aTDC; the PRF80 started to misfire and impeded further experiments. The same this occurred for the tests when constant engine speed 1000 rpm was maintained while the retard of EVC 70° bTDC point was made. Presumably this was an effect of deteriorated fuel autoignition characteristics because the LTHR phase becomes completely suppressed with an elevated engine speed or residual fraction. Thus as a consequence the HCCI operating regime with higher octane PRF blends is restricted with regard to engine speeds and the residuals rate in contrast to what is possible with lower octane PRF blends.

6.5.3 Fuel octane sensitivity and ignition process

As discussed in the section on experimental aspects, the effect of fuel octane sensitivity on ignition process type in a NVO HCCI operated engine was investigated by utilising two chemically unlike blends – nonsensitive PRF and sensitive TSF of the same RON's and

different MONs. Three types of pure hydrocarbon with different auto-ignition reactivities were used in order to compose these two blends. TSF75.6 with RON of 75.6 and MON of 66.9 consists of 58% toluene and 42% n-heptane volumetrically. To reflect the same research method octane quality as TSF 75.6 the PRF 75.6 blend was made up of 75.6% isooctane and 24.4% n-heptane volumetrically. The experiments were conducted with a constant valve timing event, an engine speed of 600 rpm and a fuel-air equivalence ratio (stoichiometric) varying intake air temperature in order to change the cylinder charge temperature.

Data plotted in Figure 6.21 show the observed experimental trends. It appears that an increase in intake air temperature is associated with a decrease in the magnitude of low temperature heat release for both blends. This was expected since the increased temperature disfavours cool flame activities (Sjoberg *et al* 2003). However, in addition to this behaviour careful scrutiny reveals a significant trend between these two experimental blends.

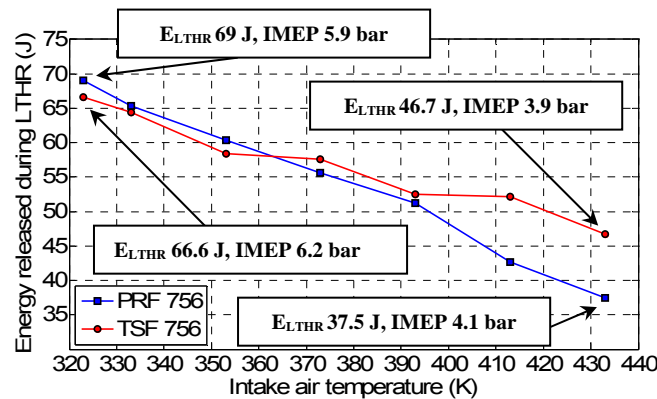


Figure 6.21. Magnitudes of cool flame activities of PRF75.6 and TSF75.6 blends for a range of intake air temperatures at constant valve timing event, engine speed and stoichiometric fuel-air ratio.

At the instance of the lowest intake air temperature i.e. 323 K the magnitude of low temperature heat release is marginally larger for PRF75.6 than for TSF75.6. With a further increase of intake air temperature the lines representing the magnitude of LTHR for both blends converge. This is a transition point where the trend reverses when a higher intake air temperature is applied. Finally, at the instance of the highest intake air temperature there is a much greater value of magnitude of LTHR exhibited by TSF75.6 than by PRF75.6. It should

be noted that the proportion of reactive n-heptane which leads to low temperature reactions in low temperature heat release is nearly double in a mixture with toluene than in a mixture with isooctane, though the magnitude of LTHR is not greater at all conditions investigated for TSF75.6.

From a chemical standpoint this trend is named as a suppressing effect on low temperature reactions of an aromatic compound that is contained in the blend with other compounds having the capacity to exhibit an LTHR. Hence not only does toluene exhibit low temperature reactions during LTHR but also acts as a suppressant of low temperature heat releases. Furthermore this observation suggests that the suppressing effect of methylbenzene in a mixture with n-heptane is highly dependent on intake temperature, in fact on charge temperature. It appears to be stronger at a low intake air temperature and becomes weaker with increasing intake air temperature. This toluene inhibitor effect was first noted by Shibata *et al* (2005). In our study it appears that this toluene inhibitor effect becomes less pronounced with incoming air temperature – thus with charge temperature. This is also in agreement with further work done by Shibata *et al* (2006) who briefly reported this behaviour. Nevertheless these observations are important in a fuel auto-ignition evaluation process among different fuel types. As the inhibitor effect changes with temperature there is an indication that it might also change as the residuals fraction is changed, and particular fuel blends are used.

6.6 Summary

The fundamental characteristics of the autoignition and combustion process in Homogenous Charge Compression Ignition engine have been presented. Initially the relevant theory and literature review classifying the ignition processes types have been introduced. Then the influences of engine operational variables on ignition process types have been investigated. This included the investigation of the effect of engine speed and

entrapped residuals rate on the magnitude of cool flame activities exhibited during the two-step ignition process exhibited. The suppressing effect of LTHR as engine speed or residuals rates increase has been identified. As a consequence the transition from a two- to a one-step ignition process have been noted due to unfavourable engine operating conditions i.e. either engine speed or residuals rate or as a combination of both. Importantly the physicochemical insight into the HCCI autoignition and combustion process was gained, more specifically insight into its corresponding distinctive phases. This was accomplished using the imaging and spectroscopic measurements. Finally the last section, apart from the summary, was devoted to the investigation of the correlation between fuel octane numbers and process type for a Primary Reference Fuel under various operating conditions. It was found that the octane number scales well with the LTHR magnitude exhibited for the given engine operating conditions. The octane sensitivity was investigated by using a nonsensitive Primary Reference blend and sensitive Toluene/n-Heptane blend with various intake air temperatures. The aforementioned blends were of the same Research Octane Numbers and different Motor Octane Numbers.

Chapter 7

Autoignition and Combustion Analysis of Port Fuel Injected HCCI

7.1 Introduction

This chapter is focused on a discussion of the behaviours of autoignition and combustion activities inherent in the single-step ignition process under stoichiometric and lean engine operating conditions. The work reported here utilised an optical engine and employed the high-speed Phantom v7.1 camera to carry out the imaging. The aforementioned imager was synchronised with engine operation. Crank-angle resolved images of the autoignition and combustion phases were acquired along with simultaneous in-cylinder pressure data. Thus the comprehensive analysis of this study was based on a combination of image and pressure derived information. The relevant image derived data analysis characterising an autoignition and combustion behaviour of Homogeneous Charge Compression Ignition operation was accomplished by involving the major image processing methods presented in section 5.4.4. Therefore autoignition occurrence and combustion development patterns including the identifications of preferential autoignition sites and their likelihood of repeatability have been investigated with the available data. Further the combustion growth rates were estimated at each crank angle degree for each individual cycle based on acquired images. Lastly this chapter demonstrates estimated magnitudes and their distribution of reacting structures instantaneous front spreading velocities along the reacting structures contour(s). This is shown by analysing consecutive crank-angle images (data) of two single cycles, representing one of each engine operational conditions.

7.2 Experimental aspects

The study was performed using an optical engine, which operated with a negative valve overlap strategy by fuelling with one-step ignition fuel, standard gasoline. In other words this fuel preceded a single-step autoignition and combustion process under the engine operational conditions investigated. The investigation was conducted for stoichiometric ($\Phi=1$) and lean ($\Phi\approx 0.83$) fuel-air conditions. The fuel was introduced with an injection timing set to a constant value of 50° CA before combustion TDC (against closed intake valves) for both conditions studied. Also the other engine operational variables such as engine speed, intake air temperature, and pressure or valve timing events were set and maintained for both sets of tests conducted i.e. under stoichiometric and lean conditions as listed in Table 7.1.

Engine Operating Variables	Experiments
	PFI HCCI High-Speed Imaging
Intake Air Temperature	313 K
Intake Air Pressure	100 kPa
Coolant Temperature	363 K
Injection Timing	310° CA aTDC
Injection Pressure	5 bar
Engine Speed	1000 rpm
Valve Timing Event	
Intake Valves Opening	55° CA aTDC
Intake Valves Closing	205° CA aTDC
Exhaust Valves Opening	240° CA bTDC
Exhaust Valves Closing	90° CA bTDC
<i>iEGR Mass Fraction</i>	
$\Phi=1$	$\approx 57\%$
$\Phi\approx 0.83$	$\approx 56\%$

TDC is referred to Top Dead Centre of gas exchange (recompression)

Table 7.1. Optical engine operational conditions.

For the acquisition of crank-angle images the high-speed Phantom v7.1 camera coupled with a Nikon 24-85 mm f/2.8-4D IF lens, the specifications of which have been described in section 4.4, was utilised. The focal length was set to 50 mm with the f/5.6 aperture chosen

for this study. Observations conducted are restricted to wavelengths region corresponding to spectral bandwidth of electromagnetic radiation of camera-lens acceptance-transmittance, as no filters were used to block out particular wavelength(s) and characteristics of piston crown window and reflecting 45° mirror spectral transmittances cover the entire aforementioned region. The focus adjustment was performed for visible light only in this study.

The acquisition of images was controlled by a CMOS array with a single image constant exposure period set to 120 μ s (corresponding approximately to 0.71° CA at a studied engine speed). The dynamic range exposure operation was disabled and therefore image acquisition was running with constant values of light integration period. Also as imager features global shuttering system process, which eliminates variations in light integration time across imager array points for single image or seen as shot-to-shot (image-to-image) at the same array location under identical illuminating conditions, thus a straightforward comparison of the obtained images could have been performed. The camera's frame rate was monitored by the pulse train (crank-angle resolved) of one crank angle degree corresponding with the separation of successive edges of the same type. This in fact constitutes an image separation interval (inter-frame period) in this study. This image acquisition synchronisation engine operation was accomplished by utilising a Labview™ in-house developed code which employs National Instruments (NI) PCI 6602 counter/timer card. The camera was brought into line using two available inputs (TTL pulse/ pulse train) – one (first) camera's input commenced the imaging acquisition process whereas the second (single pulse or pulse train) was governing the camera's frame rate (externally driven frame rate mode). This synchronisation provides a means of complete camera control mode usage since both the start of image acquisition and the camera's frame rate are both synchronised by externally supplied pulses. Table 7.2 summarises Phantom v7.1 camera settings for the discussed experiments.

Images were acquired below the cylinder barrel and they are line-of-sight images, meaning that the camera array integrated light came from various depths of the combustion chamber during the exposure time period. The resultant image contains some third

dimension of information which can not be distinguished and disregarded. Figure 7.1 shows part of an imaged combustion chamber in relation to combustion chamber artefacts.

CMOS Camera Settings	Set Value
Pixels Number (Resolution)	640 x 480
Optical Active Area (CMOS Array)	14,08 x 10,56 mm
Physical Estimated Image Pixel Size	0.226 x 0.226 mm
Digitization	8 bits per colour component
Frame Rate	7207 fps
Exposure Control	Fixed
Exposure Duration	120 μ s
Synchronization	External
Trigger and Sync Image Acquisition Inputs	TTL Pulse Rising edge
Recording	Post-trigger Recording

Table 7.2. Settings of Phantom v7.1.

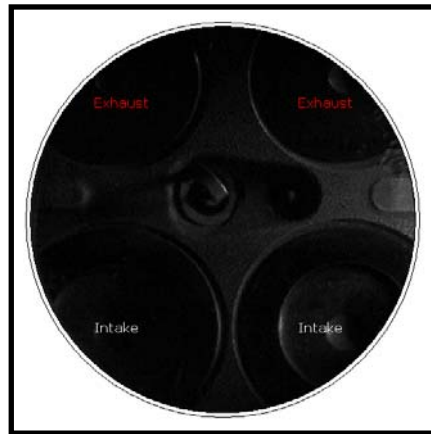


Figure 7.1. Imaged combustion chamber part with reference to its artifacts.

The camera records and stores images in a form of 3-dimensional array comprised of three monochromatic individual images of the RGB colour model. This is recorded with 24 bit pixel depth. At the selected camera operational parameters i.e. frame rate, resolution etc. 9286 images were able to be stored in the on-board memory, corresponding to the twelve individual consecutive engine cycles to be captured. Hence the statistical analysis is based on these twelve cycles. The start of image acquisition and the frame rate controlling pulse train (defining the individual image grabbing point) were additionally recorded by HSDAQ for actual image acquisition correctability and verifications purposes.

7.3 Insight into autoignition occurrence and combustion progress patterns

The visualisation of autoignition occurrence and combustion progress is purely achieved here demonstrating an ensemble images sequence of a cycle. The ensemble image represents autoignition and combustion activities occurring at the same crank angle degree from various cycles as a result of the unification of single image activities to a collective representation form. Therefore the individual ensemble image, more specifically its normalised histogram statistics review delivers potential insight into process characteristics i.e. the likelihood of repeatability tendency at a given stage of investigation. The ensemble image of the total enflamed area is depicted in the form of a colourmap with particular colour assignments depending on grey-level intensity, determined with the identical criterion for the entire ensemble image sequence.

The evaluation of process repeatability likelihood is performed with regards to the total enflamed area of the ensemble image. This is accomplished by statistical descriptor indications supplied by the *Autoignition Occurrence and Combustion Development Pattern Likelihood of Repeatability Technique* described in section 5.4.4.1. Besides the fact that the observed mean indicates a global tendency of process repeatability, other statistical descriptors such as variance, skewness or kurtosis allow a more detailed investigation of the process to be performed with a manner specified in the aforementioned introductory section of this technique. Additional important information about the ensemble image activities are gained by observing following statistical descriptors: variance which informs about data spread around the observed mean; skewness which indicates the side and degree of data asymmetry around the observed mean (random variables with higher vs. lower occurrence probabilities location and their *ratios*) and kurtosis which points out the higher probability occurrence data in relation to expectance. More specifically they inform about the occurrence probability distribution of random variables corresponding to the grey level distribution

(characteristics) of total enflamed area. Then, this image derived information is completed with a correlation of in-cylinder pressure derived parameters such as cardinal points of heat release rates or mass fraction burned. At this point two facts which could further facilitate better understanding of observed trends are noteworthy. Firstly each individual image activity and ensemble image activity corresponds to approximately 0.72° CA duration (camera's integration light period). Secondly as indications of CA5, CA10 and CA50 standard deviations combustion onset timing is associated with cycle-to-cycle variations, which could considerably contribute to changes in the global process likelihood of repeatability assessments. This happened despite the fact that intake air temperature was maintained constant.

The experimental results are presented in Figure 7.2 in the form of a sequence of autoignition and combustion ensemble images for $\Phi=1$ engine operating conditions. The statistical descriptors corresponding to each individual ensemble image are summarised in Table 7.3. The first autoignition traces (sites) are marked by a collective activities image at 358° CA – 2° CA before TDC combustion. The area occupied by these autoignition zones is significantly undersized in comparison to the whole imaged combustion chamber area. As related to the corresponding heat release rate profiles plotted in Figure 7.3, it is evident that these ensemble image activities reflect autoignition/combustion behaviour before a mean 5 % burn point is accomplished (mean CA5 -360.7° CA with std 1.02° CA). The poor process repeatability tendency is fundamentally indicated by an observed low mean value ($\mu_T = 1.11$). Further this could easily be noticed by observing the ensemble image colourmap (colours distribution). Marginally low variance and high positive skewness values pointed out data concentrated around the observed mean, with a great data concentration on the left side as in relation to the observed mean -1.11 grey-level (random variable). Furthermore the weak process likelihood or repeatability is also confirmed with determined magnitudes of mode and maximum probability of occurrence equal to 1 and 0.94 respectively. This information also indicates that the total enflamed area is mostly dominated by one area of grey-level intensity pixels.

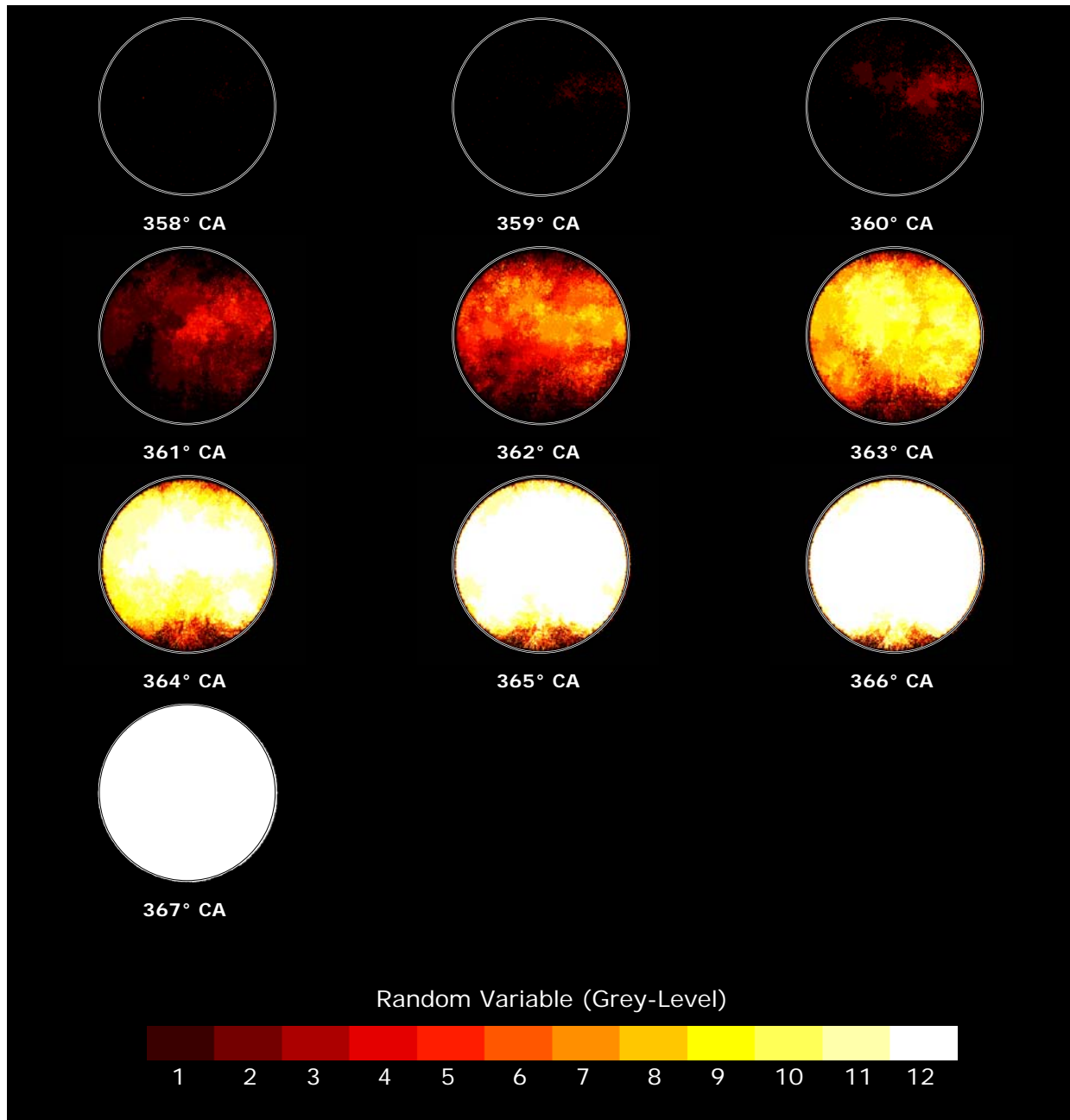


Figure 7.2. Sequence of ensemble images showing autoignition and combustion at $\Phi=1$.

The slight rise in global process repeatability tendency is observed for the next image in the sequence exhibiting activities at 359° CA. This corresponds to the larger total enflamed area size marked. Then the skewness value is an indication of more uniform grey-level distribution around the observed mean. Presumably the observed behaviour is a consequence of the autoignition progress. However, despite these marginally improved statistical descriptors that tend to enhance the overall process likelihood of repeatability, it is

not an exaggeration to assert that the process likelihood of repeatability is still poor at this cycle point.

Ensemble Image °CA	Statistical Descriptors						
	Mode (M)	Maximum Probability	Range (R)	Mean (μ_T)	Variance (σ^2)	Skewness (S)	Kurtosis (K)
358° CA	1	0.94	0.94	1.11	0.3	5.63	N.D.
359° CA	1	0.9	0.9	1.12	0.14	4.1	N.D.
360° CA	1	0.64	0.64	1.44	0.44	1.42	N.D.
361° CA	1	0.49	0.49	1.95	1.46	1.24	0.82
362° CA	6	0.16	0.16	4.62	4.6	-0.16	-0.99
363° CA	8	0.22	0.219	7.73	6.04	-1.2	0.87
364° CA	12	0.36	0.35	10.13	6.6	-1.96	3.38
365° CA	12	0.76	0.75	11.11	5.13	-3.05	8.77
366° CA	12	0.86	0.85	11.4	3.8	-3.85	14.7
367° CA	12	1	1	12	0	0	N.D.

N.D. – Not Defined

Table 7.3. Statistical descriptors of ensemble images of stoichiometric ($\Phi=1$) conditions.

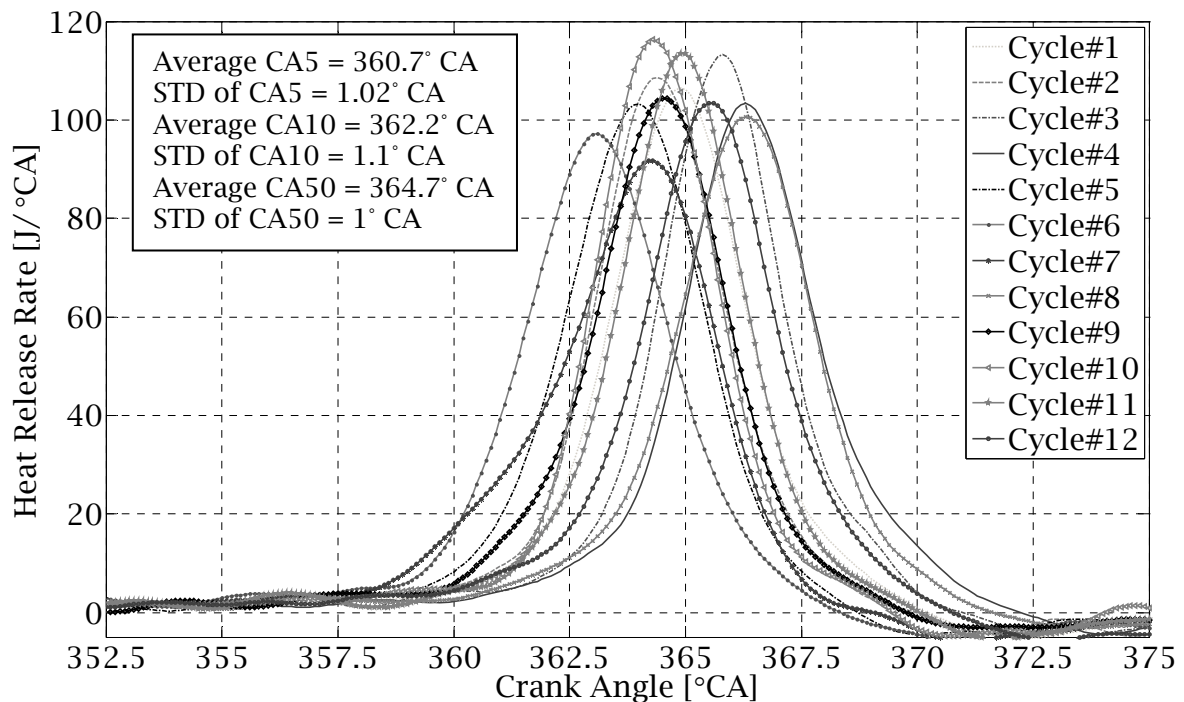


Figure 7.3. Heat release rate profiles of individual imaged cycle at $\Phi=1$.

The TDC combustion image ($360^\circ - 360.72^\circ$ CA) demonstrates autoignition or combustion activities which scale well with the mean 5% burn point (mean imaged cycles CA5). After comparing this image with the two preceding ones, the uniform distribution shape becomes more evident. As this happens the observed mean and variance are elevated. The greatest occurrence probability of a distribution is still associated with the lowest possible mode. The nature of a distribution with a higher observed expectance contributes to improving the global process likelihood of repeatability tendency.

The above analysis of these first three images is fundamental to gaining an understanding of the autoignition occurrence in this study. The initial observations made would essentially imply a random character (location) of cycle-to-cycle autoignition occurrence within the imaged part of the combustion chamber. However, at this point of the study it may seem too early to draw any adequate conclusions, since the random nature of the autoignition could be affected by other factors such as combustion timing variations. Further in this analysis the initial observations will either be confirmed or denied as the ensemble image is a collective representation showing preferential places. Also despite the fact that these first three autoignition or combustion activity images showed a poor process likelihood of repeatability, these activities occur mainly in one distinguishable part of the combustion chamber. As Figure 7.1 presents as orientation of the imaged part of the combustion chamber in relation to combustion chamber artifacts, this evidently corresponds to the exhaust valves.

As autoignition and combustion processes gradually progress the greater area fraction of the whole imaged part becomes enflamed. This is noticeable for the 361° CA ensemble image presented. The greater enflamed fraction is also associated with the progressively increased value of the global process likelihood of repeatability, for this particular image equaling to $\mu_T = 1.95$. The remaining statistical descriptors: variance, skewness (still positive) and kurtosis determine a more equalised occurrence probability distribution. This would mean that different individual areas of grey-levels, more specifically their sizes become more equalised in an ensemble image. However, the greater part was still occupied by areas of

grey-levels (random variables) from the left of the observed mean. As the important and unique feature of this ensemble image, the required number of random variables (≥ 5) needed for the kurtosis calculations has been presented for the first. The determined kurtosis value indicates a rather peaked data concentration around the observed mean (random variables with high occurrence probabilities) in reference to normal distribution.

The statistics of the subsequent image in sequence reveals distinctive characteristics. The activities of this 362° CA ensemble image correlate with the mean 10 % burned point (CA10 - 362.2° CA with std 1.1° CA). As unique aspects of these image activities have a considerably higher observed mean value, great variance and negative skewness in comparison to preceding images. Also the mode is no longer the lowest possible for the first time in this analysis. Taking together these various statistical indications, especially the mean value, the improved tendency of process repeatability likelihood is noted. The total enflamed area is comprised of a higher fraction occupied by areas of random variables (grey-levels) located from right of the observed mean.

The next image of the cycle sequence 363° CA shows primarily the whole accessible combustion chamber enflamed. At this point of the cycle the enflamed area is occupied by all possible various grey-levels (random variables) i.e. from an interval [1,12], with different fractions corresponding to magnitudes of individual grey-levels occurrence probabilities. At this point it becomes clearer that a gradually slower combustion growth rate as nearly the whole combustion chamber is enflamed. Obviously this is true for the comprehensive area enflamed with any random variable, thus the combustion development should be considered by tracking the highest possible grey-level area development now. In comparison to previously discussed image, the elevated observed mean, lower skewness (negative value) and higher mode's probability magnitude clearly imply a greater tendency of process repeatability.

The autoignition and combustion activities presented in 364° CA ensemble image shows a greater fraction of enflamed area occupied by grey-level twelve than any other individual grey-level. This is an indication of mode and its occurrence probability value – 12 and 0.36

respectively. Consequently, due to autoignition and combustion progress, the likelihood repeatability is improved.

The lastly investigated images confirmed the initially noted observations regarding the location of the preferential autoignition sites. There is a consistent and constant common place favouring autoignition or initial stage combustion activities. During the earlier cycle crank angle period i.e. 358 - 360° CA those activities were featured with a rather poor global likelihood repeatability. However, as the process progressed (361 - 364° CA) the likelihood of repeatability considerably increased for this location. Presumably low process repeatability nature at the initial cycle's crank angles was affected by the combustion onset timing variations. Once the autoignition and combustion period progresses, the early initiated cycles are gradually *completed* with autoignition or combustion reacting structures of late initiated cycles. This in fact points out preferential areas for autoignition and therefore progressively elevates observed mean magnitudes. Also there is no evidence to say that the initially observed tendency for low process repeatability was caused by a pure mismatching of single image preferential autoignition sites.

The last three images in the activities of 365 - 367° CA at $\lambda=1$ are instances depicting a progressive global likelihood of repeatability improvement. The occurrence probability tends to be a single random variable distribution. Moreover a whole imaged part of the combustion chamber is being dominated by a single grey-level. The indications of gradually higher kurtosis magnitudes and means of ensemble images 364-366° CA potentially show that this is the case. Also these images show direction for further combustion development preferential. The last image in sequence i.e. 367° CA reveals the occurrence probability distribution featured by the greatest possible single random variable. This implies that the whole accessible part of the combustion chamber is enflamed at this cycle point.

The straightforward insight into the likelihood of process repeatability of the considered period is gained by contrasting the divergence (misalignment) of total enflamed area fraction and 'Bright Object(s) Area' fraction profiles. These are shown in Figure 7.4 for both operating conditions studied $\Phi=1$ and $\Phi\approx 0.83$. The so named 'Bright Object(s) Area' fraction was

calculated as an area fraction corresponding to the random variable (grey-level) 12 marked area(s) of the enflamed combustion chamber area at any crank angle image. Also the misalignment between them is reflected by the enflamed area ratio calculated as a ratio of 'Brightest Object(s) Area' and total enflamed area.

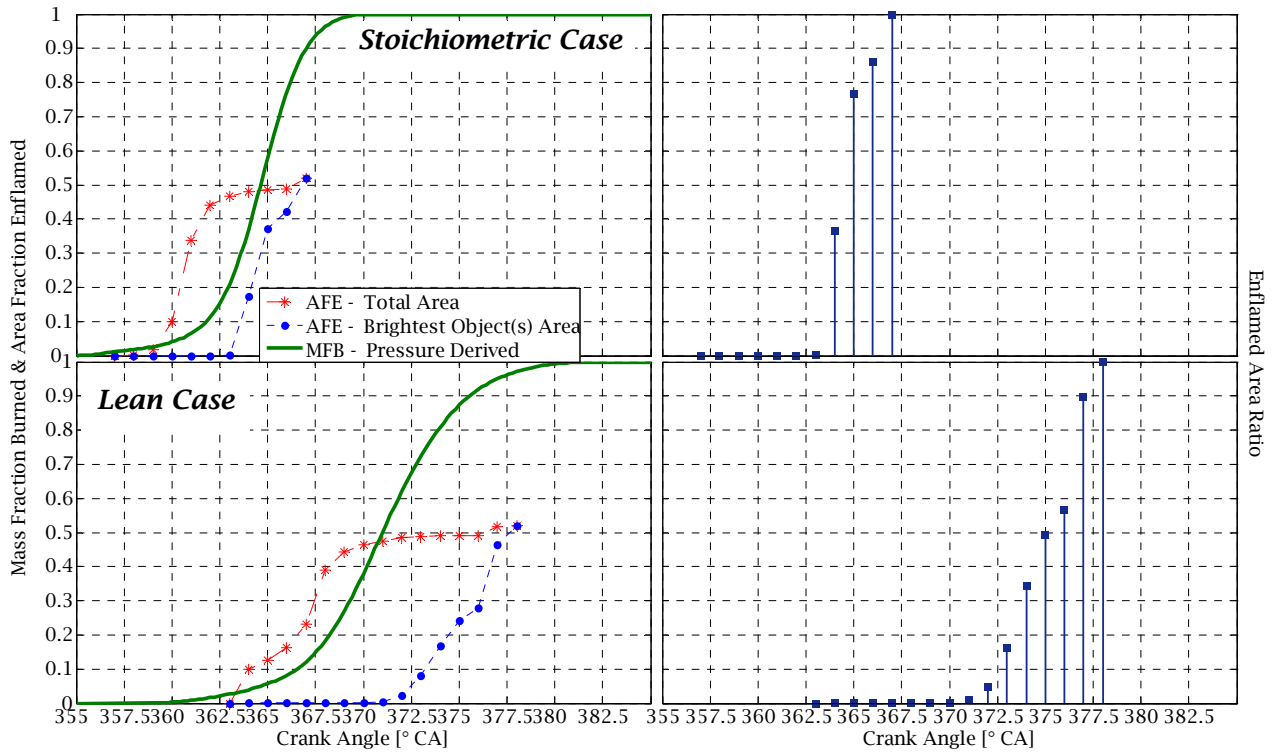


Figure 7.4. Traditional cylinder pressure traces mass fraction burned derived (MFB), area fraction enflamed (AFE) profiles and enflamed areas ratios. The total area enflamed (fraction) is entire autoignition/combustion area occupied in ensemble image regardless of ensemble image pixels intensities within the interval [1, 12]. The so called 'Brightest Object(s) Area' corresponds to grey-level pixel intensity (random variable) of 12 indicated area of the entire autoignition/combustion area in the ensemble image. The enflamed area ratio was computed as 'Brightest Object(s) Area' and total enflamed area indications.

A discussion of HCCI autoignition and combustion behaviour at lean ($\Phi \approx 0.83$) operating conditions is essentially based on process visualisation using images plotted in Figure 7.5 along with corresponding image statistical descriptors listed in Table 7.4.

Starting from 364° CA, initial autoignition sites are observable. Any preceding ensemble image (not shown here) revealed autoignition activities and therefore the 364° CA ensemble image constitutes a first image in the autoignition and combustion images sequence presented for lean operating conditions. As this happens the retarded combustion onset is pronounced at $\Phi \approx 0.83$ operating conditions in comparison to $\Phi \approx 1$ case studied. This is conceivable from the standpoint of the mixture strength reaction rate dependencies, therefore it was expected. Similar to repeatability likelihood tendency of the initial autoignition activities at stoichiometric conditions, the first autoignition sites at $\Phi \approx 0.83$ case also have a weak process repeatability nature. This may be an indication of obtained statistical descriptors determining the process likelihood of repeatability nature – the mean yielding a value of 1.02, mode being 1 and mode's occurrence probability 0.976. However, at this point in the study it is noteworthy that the combustion onset (autoignition timing) points specified as CA5 (mean 365.2°CA) or CA10 (mean 367.1°CA) are joined with high standard deviations of 2.3 and 2.1°CA respectively as seen in Figure 7.6. Presumably this fact itself contributes to a decreased expectance value. This is because the activities of early and late (presumably not exhibiting activities at this cycle point) initiated cycles are combined together in a collective form (ensemble image).

The next image presented in sequence, 365°CA shows activities correlating well with a mean burn point of 5 %. The observed mean value tends to achieve a slightly higher magnitude than expectance of preceding image. It is interesting that the number of different random variables (grey-levels) presented on its normalised histogram (not shown here) clearly indicate the minimum number of three single images exhibiting autoignition or combustion sites at this cycle point. This would suggest that the process likelihood of repeatability tends to be quite weak. However, the fairly low observed mean could be an effect of mismatch between the bigger autoignition/combustion areas of early initiated cycles

and the smaller areas of late initiated cycles. Consequently this leads to only some fractions of the comprehensive area(s) forming common place(s). Despite the fact that observed means are quite low at this initial stage the autoignition activities occurred in a common discernible location of imaged combustion chamber.

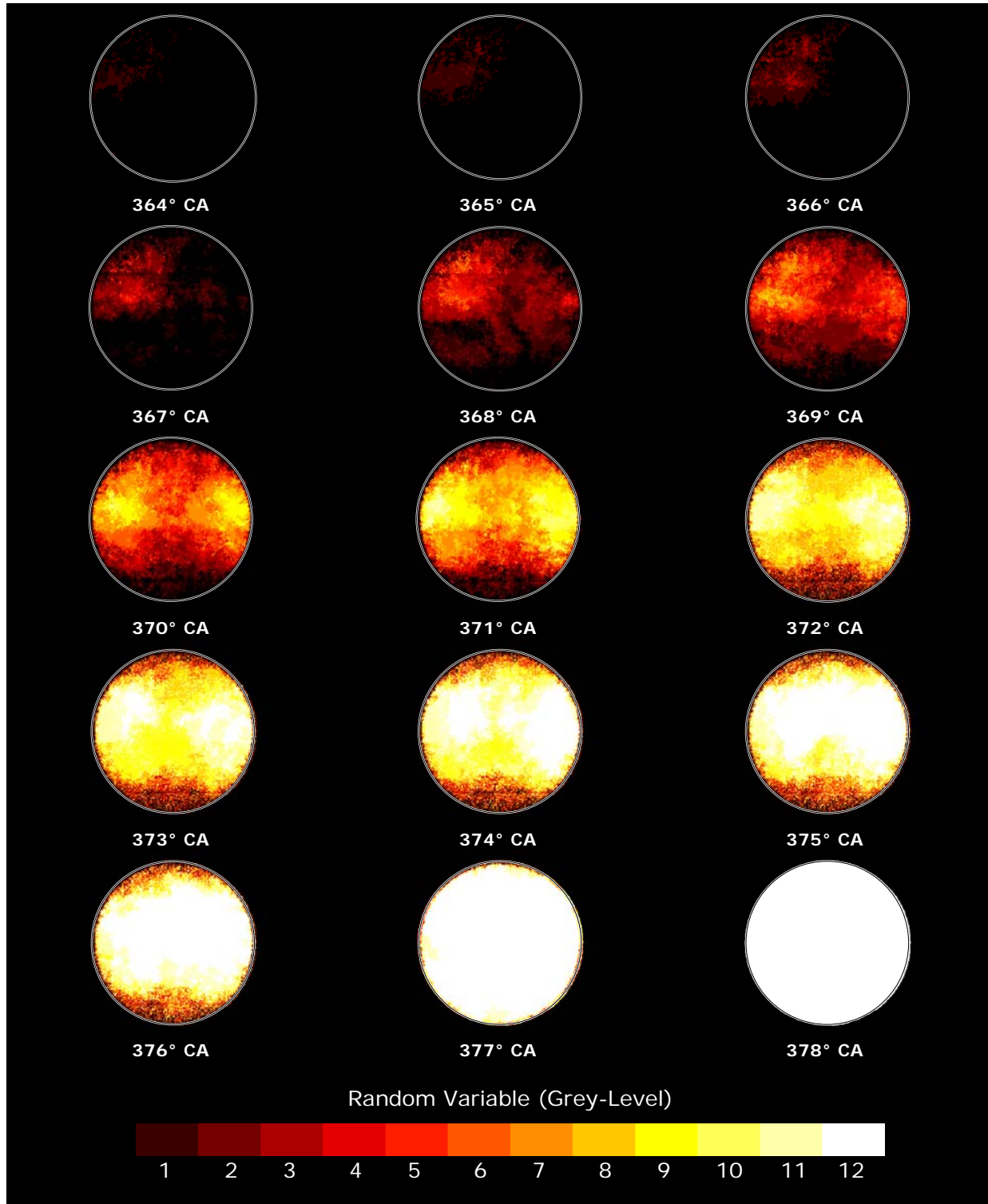


Figure 7.5. Sequence of ensemble images showing autoignition and combustion at $\Phi \approx 0.83$.

Ensemble Image °CA	Statistical Descriptors						
	<i>Mode (M)</i>	<i>Maximum Probability</i>	<i>Range (R)</i>	<i>Mean (μ_T)</i>	<i>Variance (σ^2)</i>	<i>Skewness (S)</i>	<i>Kurtosis (K)</i>
364° CA	1	0.976	0.976	1.02	0.023	6.24	N.D.
365° CA	1	0.919	0.919	1.09	0.1	3.92	N.D.
366° CA	1	0.714	0.714	1.37	0.41	1.79	N.D.
367° CA	1	0.509	0.509	1.82	1.1	1.25	1.15
368° CA	1	0.347	0.347	2.3	1.88	1.1	0.78
369° CA	2	0.218	0.218	3.4	3.2	0.49	-0.53
370° CA	6	0.161	0.161	5.1	5.56	-0.08	-0.96
371° CA	7	0.189	0.188	6.56	6.8	-0.6	-0.5
372° CA	9	0.195	0.163	8.07	8.1	-0.98	0.22
373° CA	11	0.199	0.174	8.91	8.3	-1.195	0.71
374° CA	12	0.34	0.32	9.65	8.5	-1.48	1.34
375° CA	12	0.493	0.472	9.99	8.4	-1.61	1.54
376° CA	12	0.567	0.548	10.2	8.4	-1.79	2.15
377° CA	12	0.897	0.893	11.6	2.5	-4.8	23.8
378° CA	12	1	1	12	0	0	N.D.

N.D. – Not Defined

Table 7.4. Statistical descriptors of ensemble images of lean ($\Phi \approx 0.83$) conditions.

The further two images 366 and 367° CA illustrate evident, gradual growth of enflamed areas. These area growths are highlighted with progressively increased magnitudes of the observed means. At the 367° CA point of the cycle the occurrence of new preferential autoignition or combustion progress locations becomes apparent. It could not be clearly stated whether this is a favoured place for an autoignition occurrence or combustion development since some cycles traverse the autoignition and others traverse the combustion at this cycle point (367° CA corresponds to mean 10% burn point with std 2.1°CA). The literature reported (Hwang *et al* 2008) that this is around CA10 point where fuel goes into main combustion (HTHR), generally for any fuel type. Therefore, CA10 seems to be a point in a cycle that separates autoignition from combustion processes. This initial investigation of autoignition nature at $\Phi \approx 0.83$ operating conditions has shown a poor tendency of process repeatability with presumable evidences justifying the given trend.

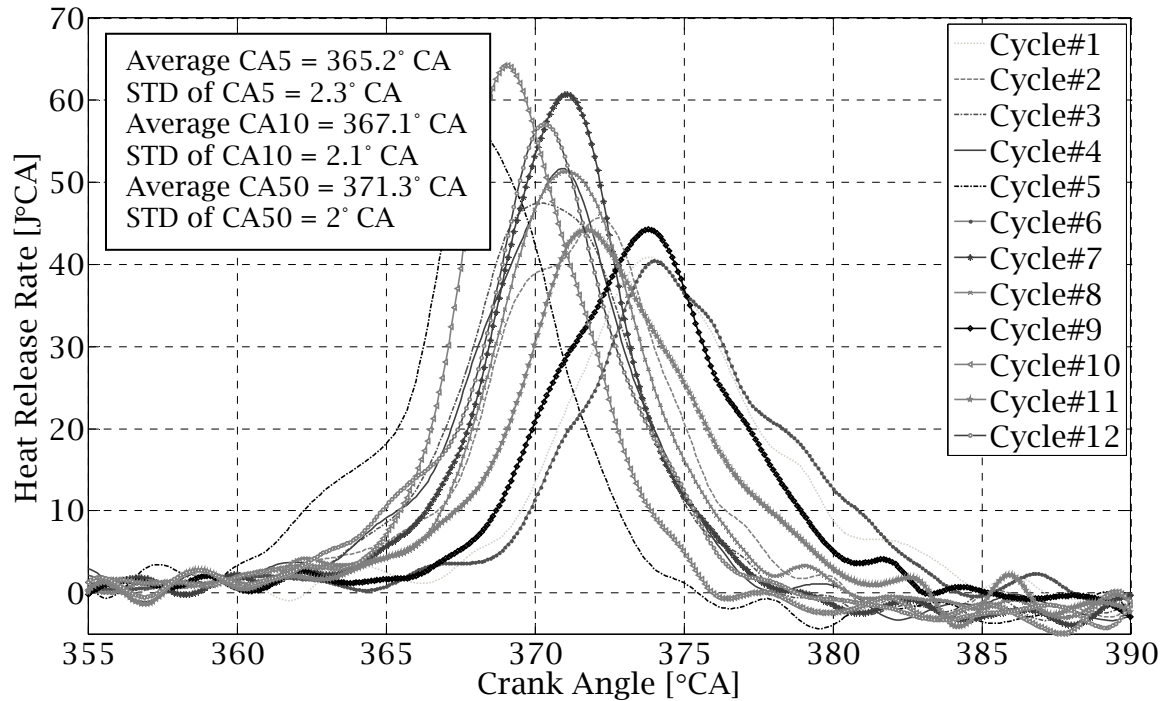


Figure 7.6. Heat release rate profiles of individual imaged cycle at $\Phi \approx 0.83$.

Like in the case of stoichiometric study the favoured location for autoignition occurrence is identifiable. This area corresponds to underneath the exhaust valves. However, unlike the favoured autoignition occurrence at $\Phi=1$ case, the one that is preferential at lean conditions is located at a different exhaust valve (from engine perspective – timing belt and dyno valves sides).

Ensemble images of 368° and 369° CA cycle points are yet characterised with data of occurrence probability distributions concentrated more to the left side of the observed means as indications of their skewness – 1.1 and 0.49 respectively. This means that for both these images the greater fractions of whole enflamed areas are still occupied with lower grey-level (random variables) pixels or individual areas. Indeed global process repeatabilities tend to be gradually improved, with high random variable areas occupying autoignition or combustion development zones respectively. The second distinguished area becomes more dominant at this point. Also at the 369° CA cycle's point the nearly whole combustion chamber in field of view is already enflamed.

The next images i.e. 370 - 373° CA show activities, combustion activities progressing from these two aforementioned preferential sites. These zones are constantly and consistently marked with the presence of the highest random variables (highest of all presented in normalised histogram). Starting from 370° CA, this is the first image in sequence showing negatively skewed occurrence probability distribution. This corresponds to a greater fraction of the enflamed area occupied by higher grey-level intensities pixels. In fact most of the single image activities form a common location that is greater than half of the enflamed area. As a consequence of this behaviour the global process likelihood of repeatability increases, which is not surprising. Also it is interesting to note that the subsequently identified preferential location for autoignition occurrence or combustion development matches quite well with one favourable and distinguished at $\Phi \approx 1$ operating conditions.

The last five images in sequence present combustion activities of 374 - 378° CA cycle points. Each individual cycle image tends to gradually enflame the accessible combustion chamber. This evidently occurs with a distinguishable combustion progress pattern. As combustion process progresses it results in progressively improved process repeatability nature. For both conditions studied, complete repeatability of the process was accomplished only while the whole visible part of the combustion chamber was enflamed. Furthermore at the initial stages i.e. autoignition activities the process likelihood of repeatability was identified as quite weak. However as the variations in combustion onset timing are taken into account this fact might lead to justify the poor process repeatability nature observed at this initial stage. The assessment of process repeatability tendency during the overall cycle period studied above could also be gained by analysing the corresponding plots in Figure 7.4.

The investigation carried out in this subsection of this study clearly suggests that there are preferential, favoured locations and *directions* for autoignition occurrence and further combustion development processes. The utilised technique allowed an accurate assessment of process likelihood repeatability to be performed at any engine cycle point imaged; and this

was done. With evidence given, it is believed that the quite weak pronounced nature of the process repeatability at initial stages is due to cycle-to-cycle combustion onset variations that deteriorate the tendency of the observed means. Also these favourable locations for autoignition formations are presumably caused by temperature or mixture inhomogeneity effects or as a combination of both across the combustion chamber. The effect of nonuniform temperature distribution within the combustion chamber would support this observed favoured pattern of autoignition, as they occur in close location to the exhaust valves. However, with data at hand it is quite difficult to point out an exact reason for this pattern. Also when the mixture strength was varied autoignition occurrence zones were located on opposite sides of the combustion chamber valves, left to right but still underneath the exhaust valves' area.

Then the identified favoured location for an autoignition occurrence at $\Phi=1$ operating conditions matched with a second (subsequent) autoignition or combustion area identified at lean operating conditions. It is noteworthy that this analysis was performed under specified conditions by trapping a significant amount of residuals. Despite the differences in operating conditions, fuel used etc. this study could be compared or even completed with the work of Aleiferis *et al* (2006), who investigated the influence of iEGR rate on the spatial randomness of the autoignition formation in an HCCI operated engine fuelled with a two-step ignition fuel - n-heptane. They observed that the autoignition behaviour becomes more difficult to predict once the amount of trapped residuals increase. In this current study the favoured places for autoignition to occur were identified with assessments given in relation to mixture strength dependency for HCCI PFI operating conditions. The obtained results clearly highlighted the effect of mixture strength on autoignition nature, and spatial initiation within combustion chamber influence.

7.4 Analysis of the combustion growth rate

The nature of HCCI process and its potential differences and similarities under premixed operating conditions studied at $\Phi=1$ and $\Phi\approx 0.83$ are further gained by investigating the expansion rates of burned area(s) (combustion growth rates). Figures 7.7 and 7.8 present combustion growth rate distributions for consecutive individual imaged cycles at $\Phi=1$ and $\Phi\approx 0.83$ operating conditions respectively. The 5, 10 and 50% burn points of corresponding heat release rate profiles are plotted on these figures in order to provide a correlation of combustion growth rates distribution with autoignition, combustion stages, and their durations. Indeed these rates of burned areas expansions were obtained based on the numerical differentiation of areas of two consecutive images – a method described in more detail in section 5.4.4.2. Also important to mention is the fact that this computational procedure was programmed to terminate calculations once the entire accessible combustion chamber area was enflamed. This could cause deviations in the obtained values of real combustion growth rates presumably and this is especially perceptible at latter combustion stages. This is because the significant portion of combustion progresses is beyond the field of view (restricted combustion chamber field of view due to the piston crown window), and only minor changes (expansion) occurring in the visible combustion chamber part are analysed. This drawback prevents an appropriate evaluation from being performed at later combustion stages. Nevertheless engine cylinder processes such as autoignition or combustion are largely three-dimensional ones and a real estimation producing realistic, unquestionable results of burned area expansion rates should be accomplished by studying third dimension information simultaneously. Despite the fact that these images contain some third dimension information (line-of-sight image), which could not be distinguished, the analysis carried out is a planar, 2-D analysis thus producing planar combustion expansion rates.

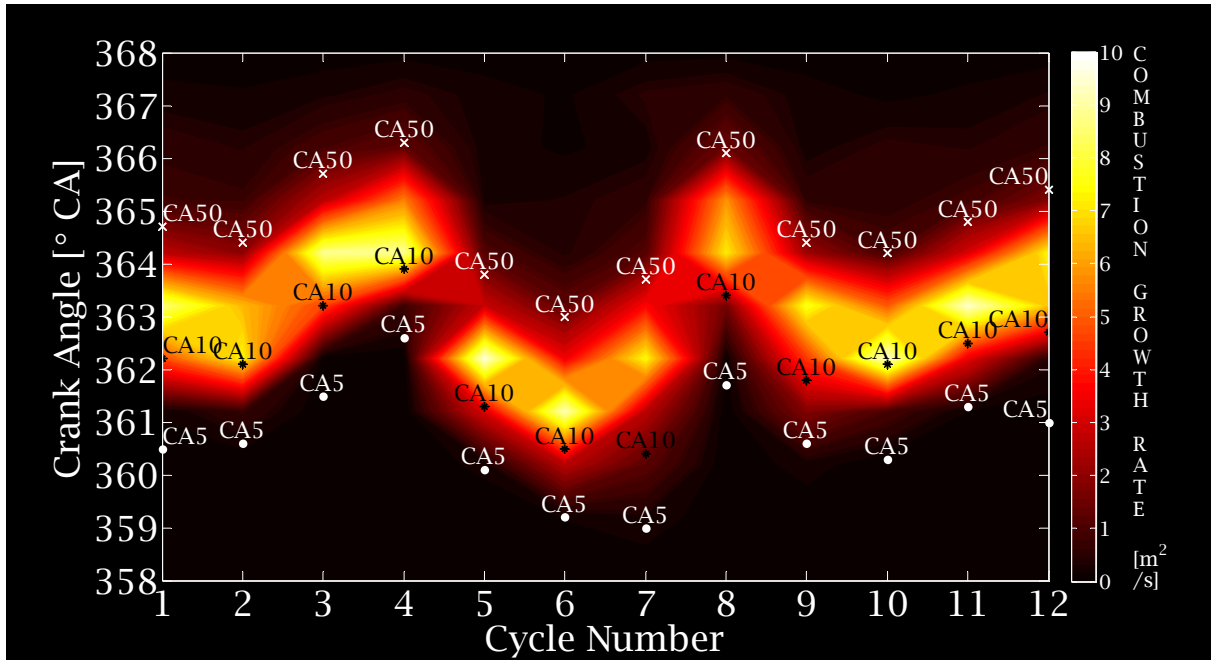


Figure 7.7. Expansion rate of burned areas distribution for each individual imaged engine cycle at $\Phi=1$.

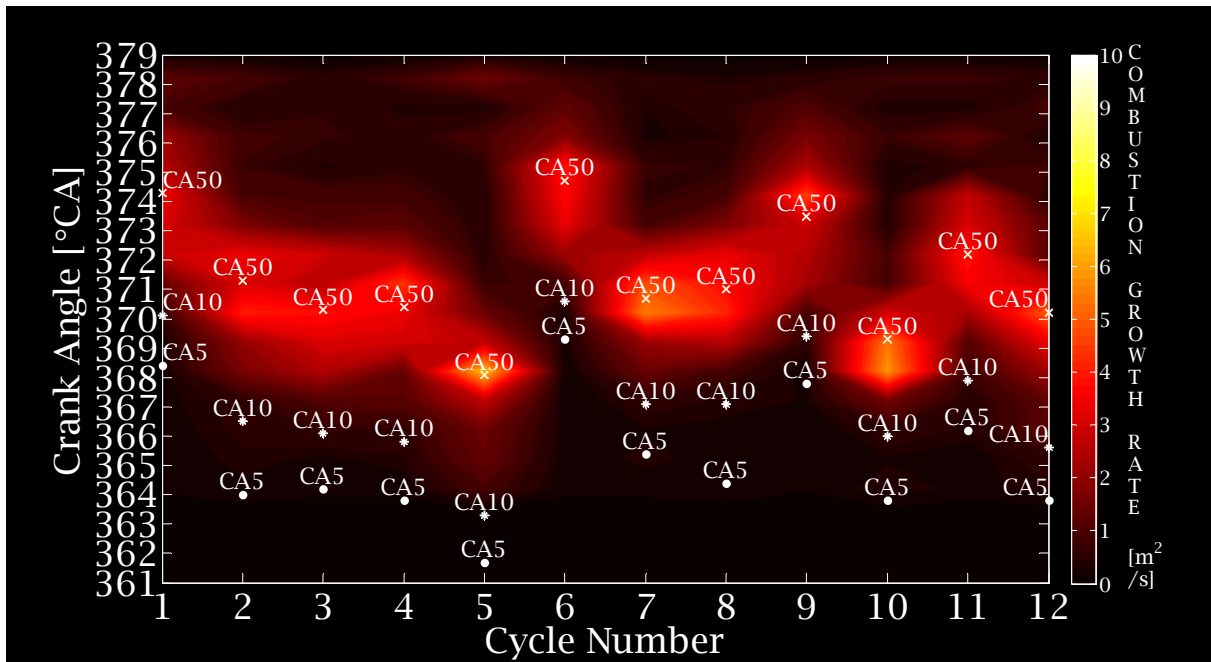


Figure 7.8. Expansion rate of burned areas distribution for each individual imaged engine cycle at $\Phi \approx 0.83$.

Having compared Figures 7.7 and 7.8 two key observations can be made. Firstly results show evident, considerable differences in the magnitudes of the greatest combustion growth rates and initial stages combustion growth rates encountered in distributions of $\Phi=1$ and $\Phi\approx 0.83$ operating conditions investigated. Secondly, there are various combustion growth rates distributions with burned points' correlations of these two cases scrutinised. The faster planar burned areas expansion rates and their maximum magnitudes observed at $\Phi=1$ conditions are most likely caused by an actual air-fuel ratio. More specifically elevated reactions rates are due to higher fuel concentration. This consequently leads to a more rapid progressing combustion process. Thus this was anticipated to some extent because pressure derived data, heat release rate profiles (Figure 7.3 and 7.6) or mass fraction burned profiles (Figure 7.4) revealed a steeper slope, indicating a faster progressing process at $\Phi=1$ operating conditions of the cases studied. It implies that the combustion chamber must have been entirely enflamed in a relatively shorter period of time (on a crank angle as well as real time basis) for the stoichiometric than the lean operating conditions. As a result the difference in the fraction of the enflamed per one crank angle degree duration must be higher for a richer mixture. The obtained magnitudes of combustion growth rates in this study are in agreement with the expansion of the areas reported by Hultqvist *et al* (2002) . With extremely lean operating conditions ($\Phi=0.25$ to 0.35) in contrast to our study ($\Phi=1$ and $\Phi\approx 0.83$) they observed combustion growth rates in the order of $3.45 \text{ m}^2/\text{s}$. In the current study we observed a drop in the maximum expansion rates of burned areas with Φ decrease, which would itself clarify (beyond the different characteristics of fuels used) variations in combustion growth rates reported by the current study and theirs.

A correlation of characteristic points of the heat release profile with combustion growth rate distribution showed various patterns of burned area expansion rate distribution at $\Phi=1$ and $\Phi\approx 0.83$ operating conditions. This was performed by identifying combustion growth rates of particular windows of heat release cardinal points specified as CA5-CA10, CA10-CA50. Similarly for both cases the CA5-CA10 window is characterised by observed slow combustion growth rates. Obviously combustion growth rates of CA5-CA10 at $\Phi=1$

conditions are higher than those at $\Phi \approx 0.83$. The reason explaining this observed trend was previously mentioned in this discussion. Further, when burned areas expansion rate distributions of CA10-CA50 windows in Figures 7.7 and 7.8 are tracked it is seen that the greatest magnitudes at stoichiometric conditions are exhibited just after; close to 10 % burned point is reached. Certainly prior to CA50 point, while $\Phi \approx 0.83$ the maximum values of combustion growth rates primarily match with CA50's points. There are two substantial, possible reasons that might justify the observed trend. As the imaged part of the combustion chamber does not cover the area of the entire combustion chamber nor its volume, the greatest combustion growth rate magnitudes could have been observed at different locations (heat release profiles points) beyond the field of view if the whole area of the combustion chamber area (preferably the volume) had been analysed. This might be more pronounced as the process becomes more rapid with a fuel-air ratio increase that quickly enflamed the accessible part of the combustion. Consequently higher increments of enflamed area fractions are observed at earlier stage of combustion with a further gradual drop in the burned areas expansion rate. This is purely due to minor area changes as the access to combustion chamber part is limited. This would suggest that most of the combustion portion is developing beyond this field of view as the mixture is enriched. Secondly it should be stated that a significant part of the combustion chamber area (not the volume) might be enflamed before CA50's are reached in two dimensional perspectives as the fuel-air ratio is increased. This would match with observations conducted (images).

These two aforementioned reasons regarding equipment limitations (engine piston window size) and the diagnostics technique chosen – imaging (2-D information) preventing any further conclusion concerning the pure combustion nature. Therefore it might be said that *realistic* maximum combustion growth magnitudes could correlate well with CA50's at $\Phi=1$, as in the case of $\Phi \approx 0.83$ operating conditions. Another interesting finding of this investigation is the fact that *below* the CA5's points there are no discernible combustion growth rates. The pioneering work of Hwang *et al* (2007) concerning the HCCI autoignition and combustion phases identification reported a visible weak and uniform light emission for

the whole combustion chamber which is imaged at the early stage until approximately 10 % burn point of heat release rate. They identified this stage as an intermediate temperature heat release (ITHR) period. The onset of hot temperature heat release (HTHR) in their study was consistently marked with a bright single location(s) chemiluminescence point(s) with light intensity and nature comparable to the ITHR phase emission. As mentioned earlier in this chapter they also reported that the heat release rate burn point distinguishing these two phases (ITHR and HTHR) is around CA10 for any fuel investigated (one and two stage ignition fuels). However, they also noted that the precise determination is not a trivial process. Based on these exceptionally valuable facts, our current study results showing activities roughly *above* CA5 as considered for an individual cycle (characteristic *insignificant* sizes of these first detected reacting structures), there is a strong indication that the HCCI process observations conducted within this study regard only the HTHR phase. Furthermore this is emphasised because of the camera settings used - short exposure periods without gain operation. With these settings presumably there are no possibilities to detect any ITHR activities, as for an instance Hwang *et al* operated their camera with a variable gain intensifier to capture these activities. It is interesting to point out that equipment acceptance spectral ranges were nearly identical in our and their equipments. These ranges allowed observations of VIS and NIR light regions with various quantum efficiencies throughout this entire region and varying between these cameras.

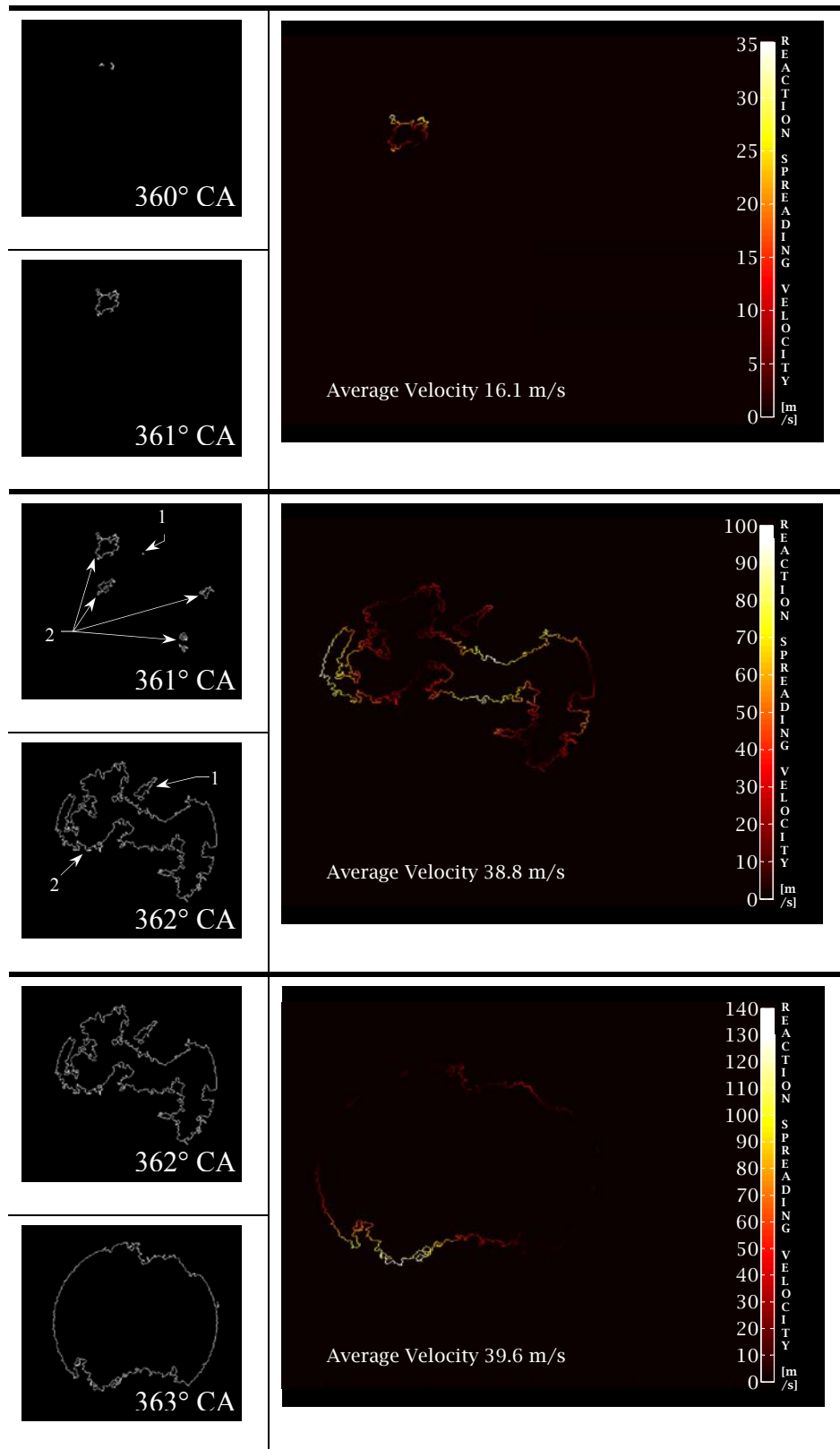
Briefly summarising the analysis conducted in this subsection would suggest an evident trend of prolonged slow combustion growth rates as mixture strength is leaned off. However, with some of the uncertainties presented above regarding optical diagnostic limitations this would need further studies to be conducted in order to support this finding and to lead to draw more certain conclusions.

7.5 Analysis of the front spreading velocities of reacting structures

The reacting structures fronts spreading velocities distributions along the reacting structures contours (local velocities) with mean values are presented in Figures 7.9 and 7.10 for stoichiometric ($\Phi=1$) and lean ($\Phi\approx 0.83$) operating conditions respectively. Because the comprehensive illustration requires an image pair of consecutive crank angles with highlighted reacting structures and also the distribution along the reacting structures contours to be presented thus only one cycle of each operating condition are shown and discussed. This provides a detailed insight into local values and their distribution during the whole cycle period, although with a limited comparison of mixture strength dependency as reaction fronts spreading velocities magnitudes of one cycle of operating conditions are illustrated. The emphasis on single burning *islands* (with the image containing multiple islands) is given to show how the velocities were estimated, more precisely speaking showing which initial image reacting structure contour corresponds to successive image contours. Then each of these single structures velocities along the contours were computed separately as it could result in underestimation of values computed (distances and consequently velocities) with more details given in 5.4.3 section. Indeed the reacting structures front spreading velocities were estimated according to the procedure introduced and specified in section 5.4.4.3.

For both cases, the analysis clearly indicated the low mean values for the initial combustion (autoignition) process reaching as high as approximately 16 m/s at $\Phi=1$ (images 360-361° CA), and 14.5 at $\Phi\approx 0.83$ (images 364-365° CA) operating conditions with maximum local values of 35 and 55 m/s for the corresponding conditions respectively. This is observed in comparison with subsequent combustion stages. As correlated to heat release rate points for these corresponding single cycles (Figures 7.3 and 7.6), the aforementioned velocities magnitudes obtained are representations of about (slightly further) CA5 and CA10

points for stoichiometric and lean conditions respectively, since each image accounts for the activities of additional 0.71° CA duration.



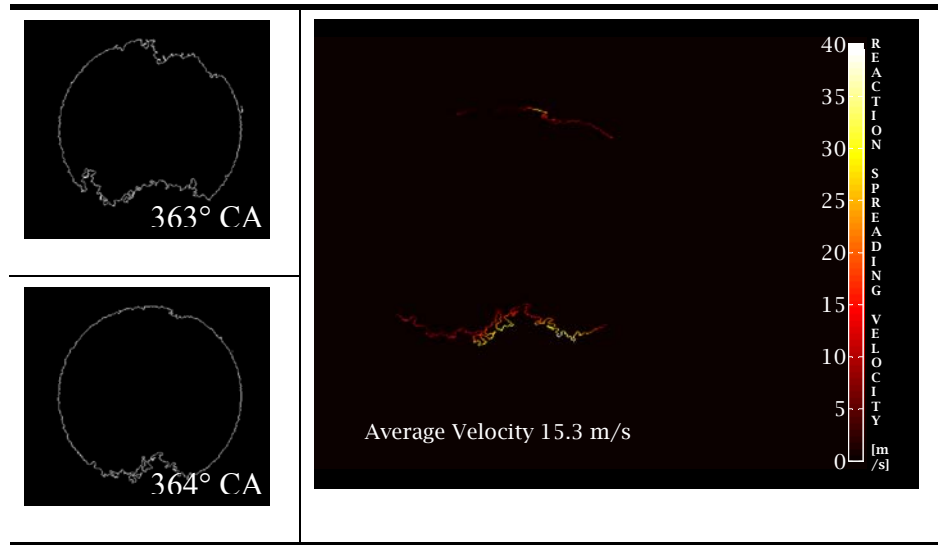
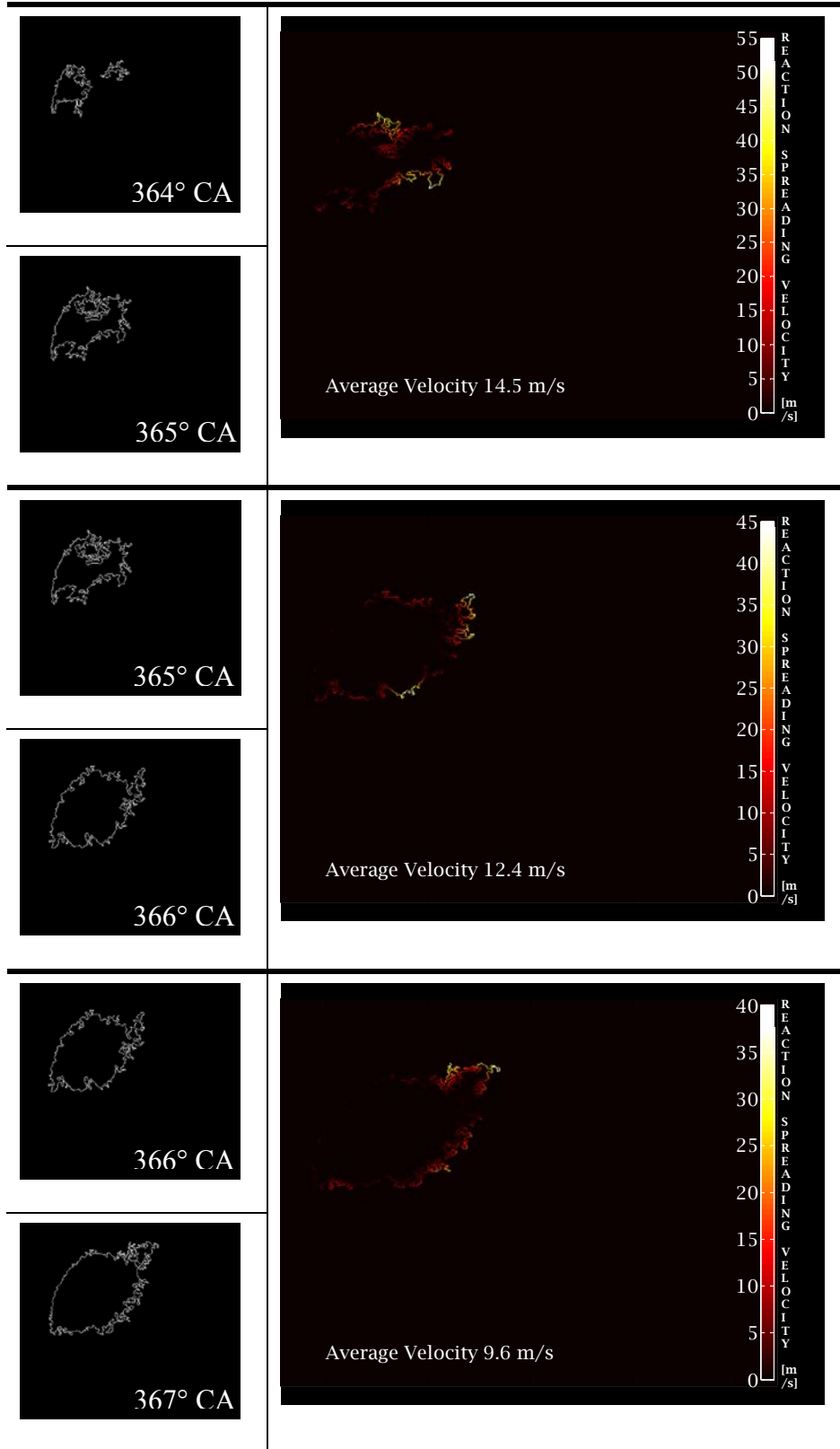


Figure 7.9. Reactions fronts spreading velocities distribution along the reactions contours for an individual cycle at $\Phi=1$ operating conditions. The left column shows the reacting structures (their contours) of the image pair taken into the analysis and the right column illustrates the velocities distribution along the reacting structure contour(s). Numerated are single reactions structures development, which were computed separately.

Further, as the combustion progresses the reactions fronts spreading velocities become gradually higher up to a given point and then start to decline. This is noticeable for both cycles of velocities examined. The greatest average (39.6 m/s) with local (up to 140 m/s) reactions front spreading velocities is seen for an image pair of 362-363° CA at $\Phi=1$ operating conditions. Before this happens, the preceding image pair (361-362°) CA reveals maximum local values up to 100 m/s and a mean value of approximately 38.8 m/s, for the same operating conditions considered. For the burned points of this individual cycle, this is a region located somewhere between CA10 and CA50 points on the heat release rate profile, significantly closer to CA10 than to CA50.

By analysing the single cycle reactions fronts spreading velocities at lean conditions, the highest values are observable for 367-368° CA image pair reaching a mean value of approximately 31.2 m/s and maximum local values of 110 m/s. Roughly speaking this period corresponds to CA50 of the heat release rate. Further at 368-369° CA period the reactions

fronts spreading velocities start to decrease and the maximum local values of 60 m/s are reached. The further combustion stages beyond these reported above are characterised by a gradual drop in reactions fronts spreading velocities for both cycles shown in this study.



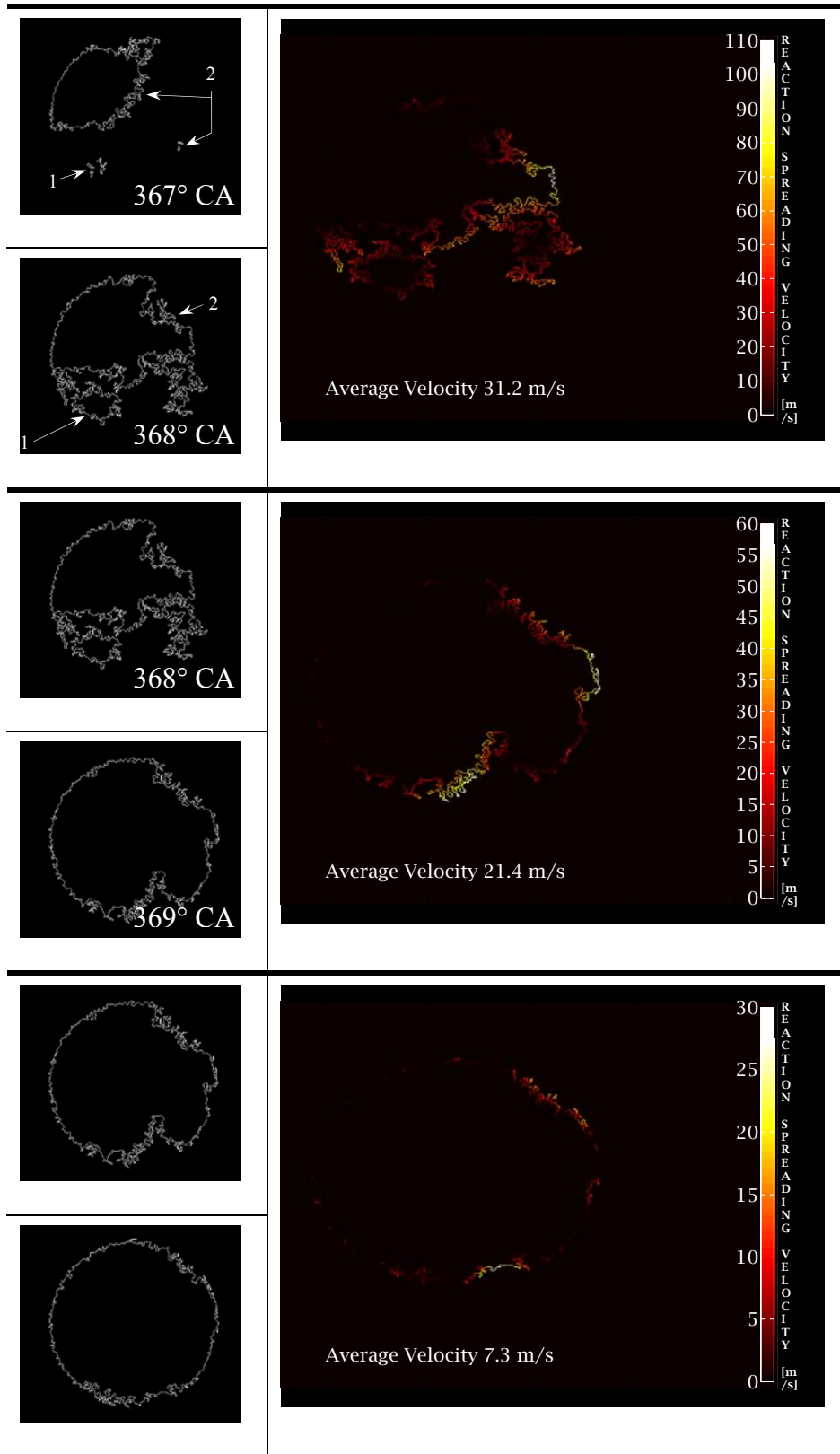


Figure 7.10. Reactions fronts spreading velocities distribution along the reactions contours for an individual cycle at $\Phi \approx 0.83$ operating conditions. The left column shows the reacting

structures (their contours) of the image pair taken into analysis and the right column illustrates the velocities distribution along the reacting structure contour(s). Numerated are single reactions structures development, which were computed separately.

The analysis conducted and covered here, produced three main observations. First, the initial stage of combustion (autoignition) exhibits significantly lower local and mean velocities magnitudes of reacting structures. Secondly, at $\Phi=1$ operating conditions the highest magnitudes encountered in the whole cycle analysis are for the region CA10-CA50 of heat release rate, while at $\Phi\approx 0.83$ these scale well with an approximately CA50 point region. Third, maximum reacting structures fronts spreading velocities, both local and mean values were shown to be higher at $\Phi=1$ than at $\Phi\approx 0.83$ operating conditions, although this is stated based on a single representative cycle of each case studied. The natures of autoignition and combustion processes in this section revealed analogous behaviour to the previous section's observations which investigated the similarities and differences of combustion growth rate distributions at stoichiometric and lean conditions. Therefore reasons clarifying each behaviour in this section could be found as ones corresponding to the preceding section's justification.

Hultqvist *et al* (2002) noticed reaction front spreading velocities values of approximately 82 m/s for a developed combustion at $\Phi=0.25-0.24$ lean operating conditions. These velocities magnitudes correspond to mean values observed and were the first ones reported in HCCI technology to the author's knowledge. Then Persson *et al* (2007) reported reacting structures spreading speeds reaching up to 110 m/s at $\lambda=1.03$ operating conditions, apparently these magnitudes also constitute mean values of one direction, since their values were estimated using the analogous technique of Hultqvist *et al* (2002). Despite the fact that different techniques (assumptions) were utilised to estimate reacting structures fronts spreading velocities for the current study and for cited aforementioned studies (regardless of other differences in investigational approaches e.g. fuels characteristics), a direct comparison could or even should not be performed. However, it is noticeable that local

values of current studies scale well with their reactions fronts spreading values reported. As comparison of the mean values of reacting structures fronts spreading velocities of the current study with reported aforementioned results of references Hultqvist *et al* 2002 and Persson *et al* 2007 would indicate an underestimation of current results.

7.6 Summary

Optical diagnostics and a further analysis of autoignition and combustion processes of the port fuel injected Homogenous Charge Compression Ignition engine operation mode under lean and stoichiometric conditions were conducted. The optical diagnostics were conducted using a Phantom v7.1 CMOS colour camera, and a further analysis employed relevant image processing techniques to derive image information. The study has examined and yielded the following issues and conclusions.

The predictable nature of the autoignition occurrence and combustion progress at $\Phi=1$ than at $\Phi\approx 0.83$ operating conditions were evaluated. For both aforementioned cases, the initial stages (autoignitions) exhibited a low process likelihood of repeatabilities with improved indications as combustion progresses. Presumed evidences were identified responsible for this nature. Also, despite the indications of poor global process repeatability, preferential first autoignition sites were clearly identified for both cases studied. It was found that the preferential side of combustion chamber for an autoignition to occur (combustion onset) is one corresponding to the exhaust valves side.

The analysis of combustion growth rates revealed a faster expansion rate of burned areas at $\Phi=1$ than at $\Phi\approx 0.83$ operating conditions. This is observable contrasting initial as well as developed combustion stages. Also different patterns of combustion growth rates distributions were noted between these two cases for the same heat release rate points windows specified as CA10-CA50.

The estimated reacting structures fronts spreading velocities were illustrated showing local velocities along the burning island(s) contour(s) with mean magnitudes computed. The local highest magnitudes evaluated reached the 110 m/s, and they are associated with the developed combustion stage. At the same stage the mean values were found to be in the range of approximately 38.8 m/s. Initial combustion stages were indeed shown significantly lower values than the developed combustion stages. The mixture strength was noted having influence on the magnitudes of both local and mean values estimated of reacting structures front spreading velocities.

Chapter 8

Characteristic of HCCI Operation with Direct Injection Strategies

8.1 Introduction

This chapter demonstrates the influence of injection strategy, single and split with different injection timings on the recompression stroke and main autoignition-combustion activities of HCCI operation. Various direct injection strategies have been investigated including a single injection strategy and a split injection strategy that introduces fuel significantly prior to TDC negative valve overlap period. This was accomplished using optical engine which run with a stoichiometric fuel-air ratio. Three diagnostic instruments: the Complementary Metal-Oxide Semiconductor (CMOS) high-speed colour imager, the intensified Charge Couple Device (CCD) and the imaging spectrograph were utilised to perform passive optical measurements. It was found that the colour and the intensity of the autoignition-combustion is completely different when some of fuel is injected prior to TDC NVO with the split (double) injection, than for other cases investigated including even one with a pilot injection occurring during the TDC recompression stroke. For this particular case autoignition-combustion activities were dominated by a bright yellowish colour emission, while the other injection strategies studied have shown a consistently dark bluish colour emission during the autoignition-combustion period. Furthermore with an injection strategy that introduces fuel prior to TDC NVO, a bright light intensity emission was identified as persisting for a long period of time corresponding to approximately 25°CA during recompression stroke. In conjunction with spectroscopic measurements conducted during

this period (NVO) showing classical continuum spectra of thermal radiation of solid materials and preceding one with some traces of C_2 , C_3 and CH there is evidence that this light emission derives from incandescence of solid carbonaceous particles. Therefore it is thought that the soot formation during the negative valve overlap occurs as a result of the pyrolysis of fuel molecules; the thermal breakdown of fuel molecules into hydrogen and carbon. As the entire study was conducted using standard gasoline and a blend of PRF40 the impact of fuel type on potential soot formation during the NVO period has been noted. Further the insights into the autoignition-combustion activities in qualitative as well as quantitative ways are gained by the application of relevant image processing techniques. The combustion onset and its development are investigated, with a quantifiable analysis performed concerning the likelihood of the repeatability. Then the magnitudes of combustion growth rates are estimated and scaled with their corresponding cardinal points of heat release activities.

8.2 Experimental aspects

The engine was operated with a constant speed of 1000 rpm and a negative valve overlap period of 145°CA , fired every cycle (skip-fire mode disabled) during the experiments. Prior to the start of tests the engine operational conditions such as its coolant temperature, oil temperature and intake air temperature were stabilised to determine levels according to the engine operating conditions listed in Table 8.1. The valve timing event and other relevant engine operational variables yielded a significant estimated value of 57% of the trapped residuals. The research was carried out with different split injection and single injection strategies. The main injection's phasing of split injection strategies was kept fixed and only the pilot injection timing was varied. By varying its timing from -40 to 40°CA after the TDC recompression stroke with a step of 40°CA , three various split injection strategies were investigated. The injection timing noted here refers to the start of injection, and the designation 0°CA corresponds to TDC NVO, and consequently 360°CA to TDC combustion.

Hence the pilot injection timings of the split injection strategies studied are designated as 680°CA (prior to NVO), 0°CA (TDC NVO) and 40°CA (after NVO) with the main injection timing set to the induction stroke as 140°CA.

Engine Operational Conditions	
General Engine Operational Variables	
Engine Speed	1000 rpm
Intake Air Temperature	313K
Intake Air Pressure	100 kPa
Coolant Temperature	363 K
Oil Temperature	353 K
Fuel/Air Equivalence Ratio	1
Fuel Injection	
Injection System	DI
Injection Pressure	100 bar
Fuel	ULG95 and PRF40
Injection Strategy and Timing	
Single Injection	140° CA
Split (Double) Injection	Pilot Injection / Main Injection
Strategy I	SOI at 680° / 140° CA
Strategy II	SOI at 0° / 140° CA
Strategy III	SOI at 40° / 140° CA
Valve Timing Specification	
Intake Valves Opening	55° CA
Intake Valves Closing	205° CA
Exhaust Valves Opening	480° CA
Exhaust Valves Closing	610° CA
iEGR Mass Fraction	
$\Phi=1$	$\approx 57\%$

Table 8.1. Engine operational conditions.

Also they refer to the single injection strategies I, II and III respectively and this terminology will be used throughout the remainder of this chapter. A representation of the injection strategies studied in relation to the cylinder pressure (motoring case) is illustrated in Figure 8.1. The split injection ratio and also the quantity of fuel injected remained constant for all three cases investigated. They yielded the same stoichiometric fuel-air equivalence ratio. The injection timing of only one single injection case examined within the investigational scheme of this chapter was set to correspond to the crank-angle position for the main

injection of split injection. With these selected injections for the split injection strategies the same fuel quantities were introduced during the main injection in the compression stroke.

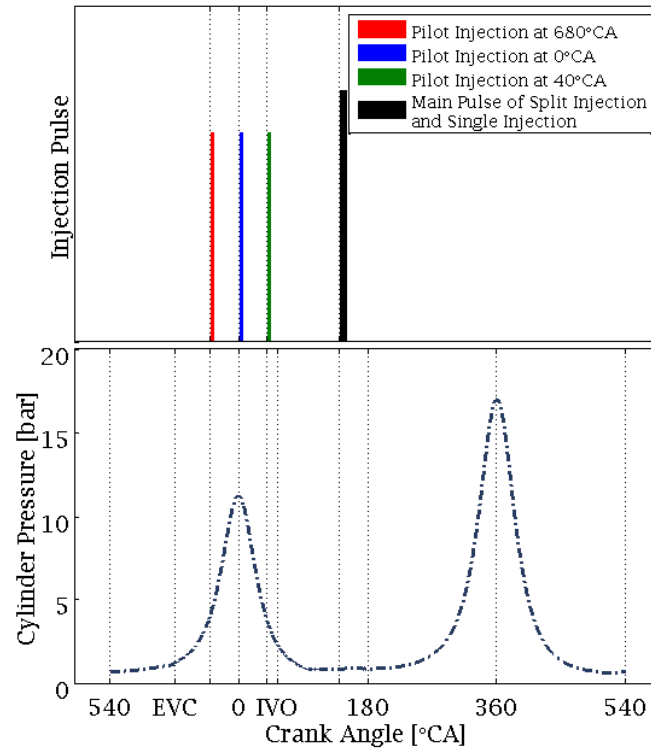


Figure 8.1. A representative presentation of injection strategies investigated in reference to engine cycle cylinder pressure. EVC and IVO plotted designate exhaust valves closing and intake valve opening points respectively.

Using the same sort of fuel was to provide the identical charge cooling and resulting in an identical volumetric efficiency (in-cylinder filling process). However, with split injection strategies there is additional charge cooling which occurs when fuel injected in the NVO period. This is apparently highly dependent on the pilot fuel injection timing. Nevertheless, this charge cooling effect could be compensated by an occurrence of any potential reactions taking place in NVO; reactions which are in fact also injection timing dependent.

Two chemically unlike blends, commercial gasoline (ULG95) and the Primary Reference Fuel (PRF40) were utilised to conduct a comprehensive set of tests in this study. The data of these blends are summarised in the fuel table of appendix A. Firstly traditional gasoline was

utilised as a commercially available fuel to diagnose the HCCI process with different injection strategies. The fuel and operating conditions were chosen to imitate a real-life (realistic) HCCI engine operating conditions scenario. A second blend of PRF40 was selected to gain further insight into the process by using optical diagnostics such as iCCD imaging and spectroscopic measurements, still under the same engine operating conditions. In this case a usage of a fuel blend with a known autoignition chemistry such as binary PRF40 is advantageous and convenient for interpreting experimental results. The selection of a blend with the volumetric proportion of 60% reactive n-heptane to 40% 2,2,4 trimethylpentane (PRF40) was primarily dictated by an attempt to reflect the ignition process type one exhibited by unleaded gasoline under the same engine operating conditions. As ULG95 exhibited no cool flame activities under the specified engine operating conditions pre-research was performed by varying the proportion of n-heptane to isooctane to form a mixture, which provided a one-step ignition process under the identical studied engine operating conditions. Thus this was a blend of PRF40 which exhibited primarily a one-step ignition process under investigated engine operational variables. That particular fuel blend potentially a two-step ignition process was forced to undergo a one-step ignition process as a consequence of engine operating conditions, mainly speed, intake air temperature and the rate of trapped residuals (Sjoberg *et al* 2003,2007; chapter 6) , with then rate of trapped residuals being the most prominent contributor.

The acquisition of crank-angle resolved colour images was performed with a CMOS Phantom v7.1 camera with the identical settings as in chapter 7. This is presented in a section 7.2. The images were captured throughout the piston-crown window (bottom view), with the same orientation to combustion chamber artifacts as shown in Figure 7.1.

The Andor iStar iCCD monochromatic imager model was further utilised to carry out the imaging of this study. For experiments the camera was coupled with a UV-Nikkor 105 mm f/4.5 lens. The lens aperture was set to f/5.6 and the focus distance equaled to 0.7 m during for the experimental setup. With these parameters chosen the depth of field equals to the value of 6 mm (0.697 – 0.703 m). The focusing was accomplished for a visible light. The

comprehensive system, camera (Andor iStar DH734I – 18F – 04) and lens (UV-Nikkor 105 mm f/4.5) wavelength spectral acceptance range features a broader spectral range down to UV than a colour CMOS camera with corresponding Nikon lens covering a UV region. At the engine operating conditions studied one image per engine cycle could only be gained by skipping 15 cycles. The data (images) were acquired as single scan grey-level (monochromatic) images. The image acquisition was controlled by the intensifier operation. With the constant value of light integration (gate pulse width) 166 μ s, corresponding to 1° CA at the engine speed studied and the MCP gain set to 50, the values of the light intensity of raw images recorded vary from 0 to saturation level. The settings were kept the same for the entire image acquisition, thus allowing a straightforward quantifiable comparison to be performed. The IntelligaGate system was enabled for the image acquisition. The camera temperature was set to -20°C in order to reduce dark current noise.

The Oriel MS260i™ 1/4m Imaging Spectrograph Model 74050 coupled with the Andor iStar iCCD DH734I – 18F – 04 camera was used to carry out spectroscopic measurements. The grating 300 lines/mm and slit width to 0.5 mm were selected and set for the measurement. The calibration was performed with 6025 Mercury –Argon Oriel Instruments Spectral Calibration Light, which emits a number of known spectral lines. The spectrometer was positioned perpendicular to the optical engine so that the slit of the constant height was located across the triangular head window. The plano-convex lens between the spectrometer and engine was mounted to focus the light onto the spectrometer slit. This lens was made of fused silica.

8.3 Analysis of gasoline HCCI operation with various injection strategies and timings

The work that is presented in this section aims to characterise main autoignition-combustion of HCCI in an engine fuelled with gasoline, under different predetermined injection strategies. It also deals with the potential activities that occur during recompression stroke activities.

The optical diagnostics of this section were accomplished with high-speed crank-angle resolved color imaging in conjunction with additional and simultaneous conventional in-cylinder pressure transducer measurements. For this study, an image sequence of twelve complete individual engine cycles with an inter-frame rate separation of 1°CA was taken for each investigated operating condition i.e. injection strategy. The consistent (constant) imager settings and identical quantity of fuel injection preserved (for split injection strategies) resulted in the ability to perform a direct quantifiable comparison of emitted light. The preservation of the same amount of fuel injected during the examined cases was of particular importance as the light intensity emission of chemiluminescence reactions is highly dependent on the concentration of reagent and the reaction rate (Garcia-Campana *et al* 2001). In fact, reaction rates scale proportionally with reagent concentration. Indeed this is the case for HCCI operations, for which it has been demonstrated that the light intensity emitted depends greatly on the concentration of fuel in the fuel-air mixture (Persson *et al* 2005; chapter 6) and therefore is correlated with engine load (Persson *et al* 2005). Also an excellent relationship between the profiles of the hot temperature heat release (HTHR) phase and the intensity of natural light emission in this phase has recently been presented from work done with HCCI operated engines (Persson *et al* 2005; Hultqvist *et al* 1999).

The experimental results are summarised in Figures 8.2 -8.18 and are in various forms. Firstly an individual cycle, ensemble-average and ensemble images are shown in Figures 8.2-8.9 for each individual investigated injection case. Further Figures 8.10 – 8.13 complete

these observations with a characterisation of a presentation of the light intensity distribution for only one ensemble-average image from each sequence. The most intense image of a corresponding sequence is selected for this characterisation. As noted both single cycle and ensemble-average images were shown. This is done in order to gain detailed insight into the investigated phenomena. The single cycle images might not illustrate the actual trend e.g. colour, therefore there was a need to create a sequence of ensemble-average images. On the other hand as ensemble-average images may significantly contribute to the attenuation of the light intensity, and it seems that the problem becomes more prominent for those activities which exhibit a local character e.g. combustion onset, therefore it is more profitable to show single cycle images also, indeed for one representative cycle here. The aforementioned ensemble images are those referring to a statistical analysis of autoignition occurrence and combustion development patterns and are combined with their corresponding statistical descriptors summarised in Tables 8.2-8.5. Further the experimental results are focused on the analysis of estimated combustion growth rates and their crank-angle distribution in relation to the burn points for each imaged cycle of the cases studied.

Having compared periods of autoignition-combustion activities for different investigated cases shown in Figures 8.2-8.9 it is discernible that a distinct atypical colour for autoignition-combustion activities for a split injection strategy that introduce fuel (pilot injection) prior to the TDC recompression stroke. Both the intensity and the colour of the light emitted are unique when compared to the other investigated cases in this study. When some portion of fuel is introduced prior to TDC NVO bright yellow dominated autoignition-combustion activities are observable in contrast to dark bluish autoignition-combustion activities of other injection cases studied. This happens despite the differences in injection timings among those cases. It is especially interesting that even with fuel injected in hot residuals at the top dead centre of the recompressions stroke the activities of autoignition-combustion are completely different from those occurring when fuel is introduced prior to TDC.

Furthermore it is not only the colour scheme, but also the light intensity which sets these investigated cases apart. The autoignition-combustion activities of split injection strategies

with timings 0/140°CA and 40/140°CA as well as autoignition-combustion activities of the single injection case exhibited such a low luminosity that for visual enhancement the intensities of all the pixels at any RGB image location had to be multiplied by factor five. This was the case for single cycle and ensemble-average images of the autoignition-combustion period. Obviously the other analyses presented in this section and regarding those activities were performed by using raw images, and the visual enhancement was done only for an improved, clearer presentation of investigated results.

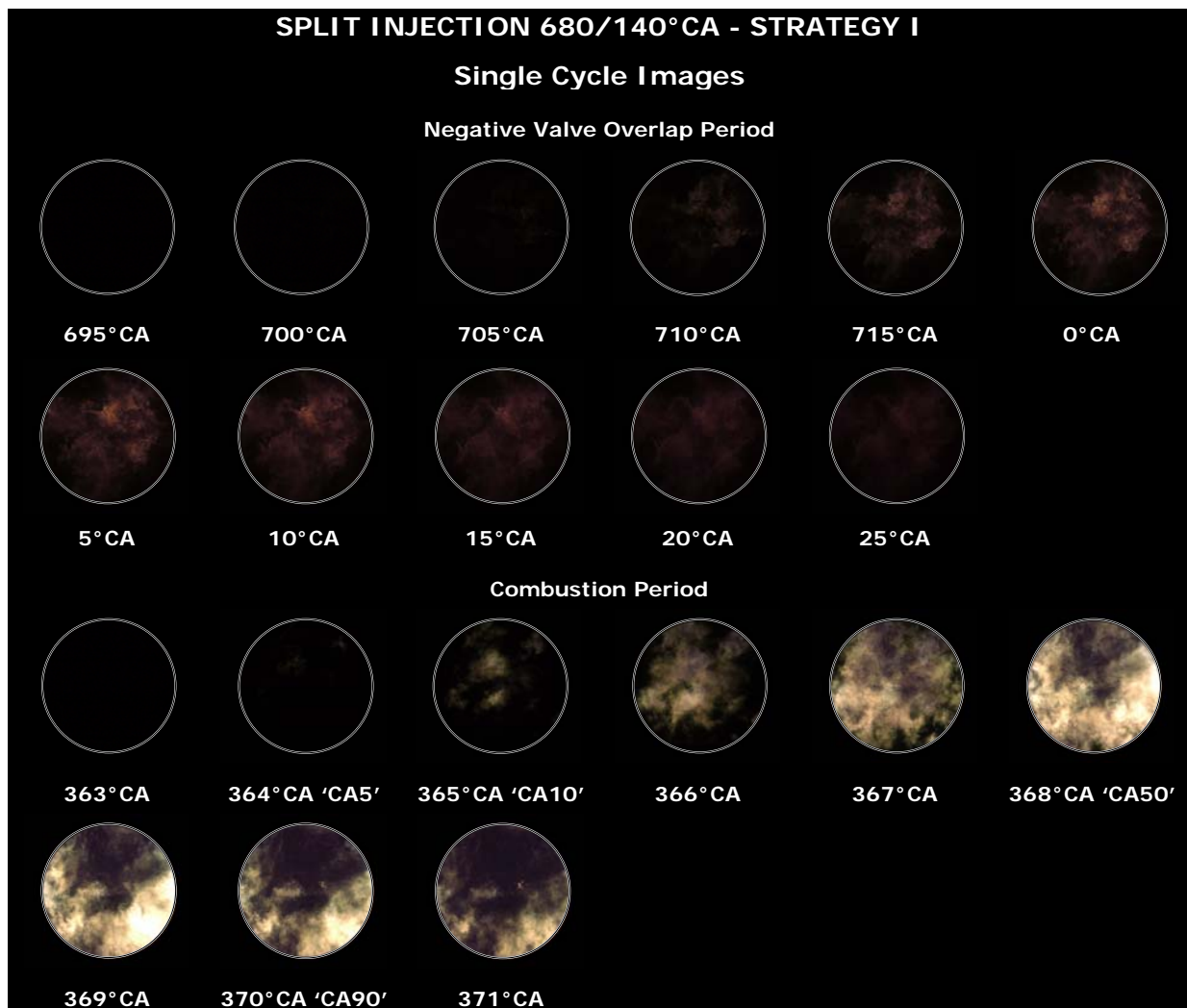


Figure 8.2. Single cycle image sequence of *negative valve overlap* and *main autoignition-combustion* periods of split gasoline injection with timing of 680/140° CA at $\Phi=1$. Images were acquired throughout the piston-crown window with Phantom v7.1 camera. Symbols in quotations refer to heat release rate burn point.

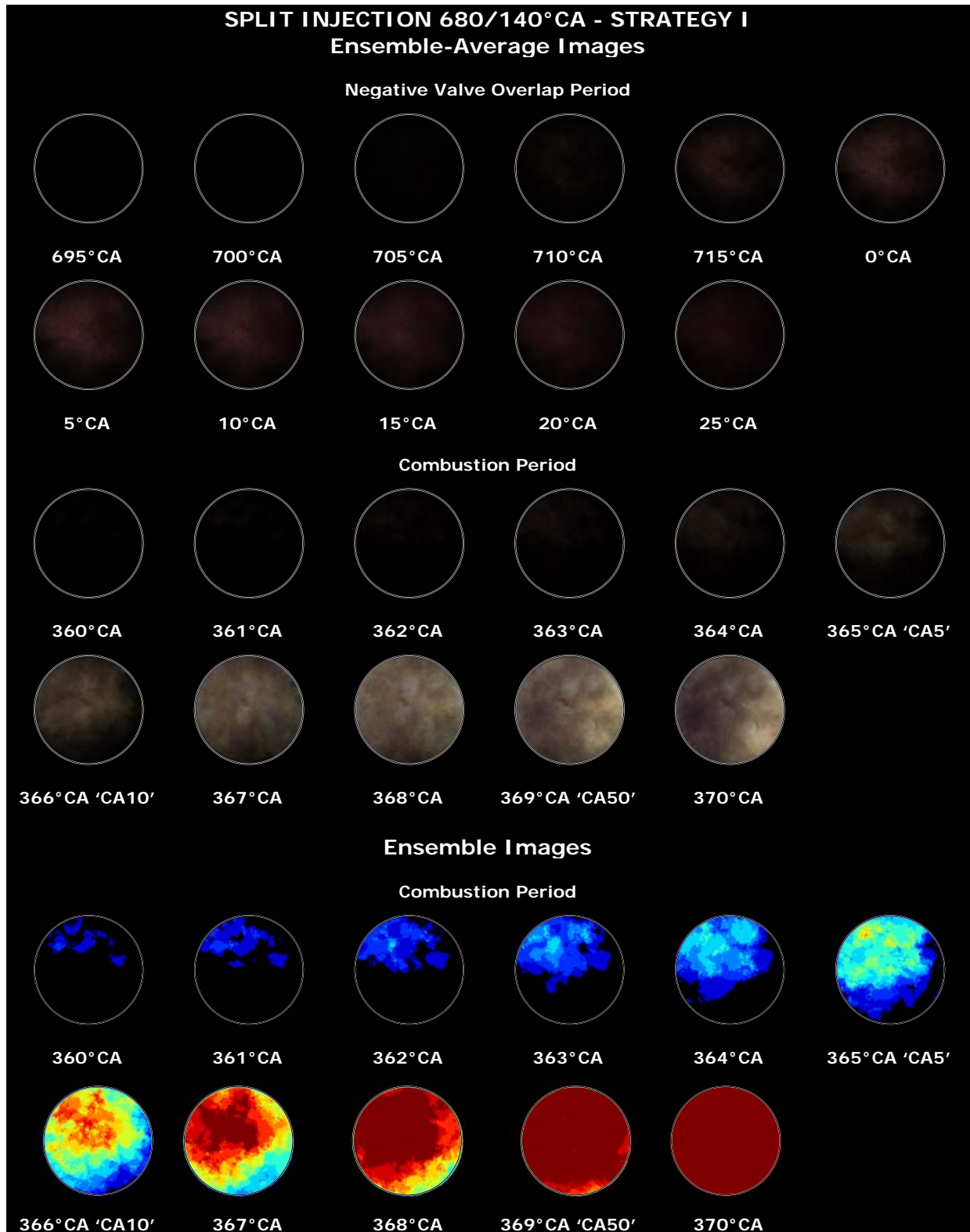


Figure 8.3. Ensemble-average image sequence of *negative valve overlap* and *main autoignition- combustion* periods of split gasoline injection with timing of 680/140° CA at $\Phi=1$. An ensemble image sequence of *main autoignition- combustion* period is also included. Symbols in quotations refer to average heat release rate burn points. Standard deviations of these corresponding burn points are 1.2, 1.1 and 1 for CA5, CA10 and CA50 respectively.

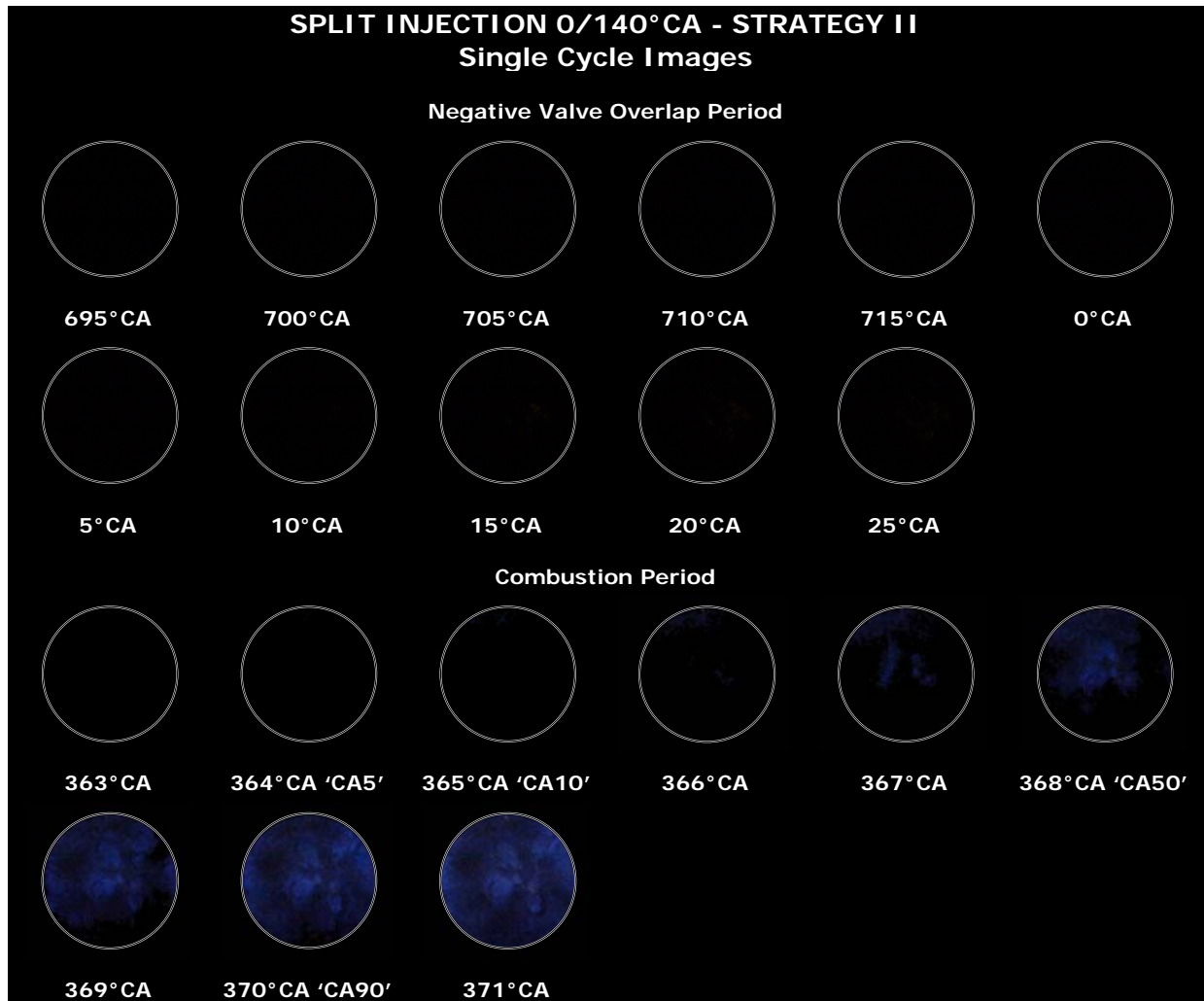
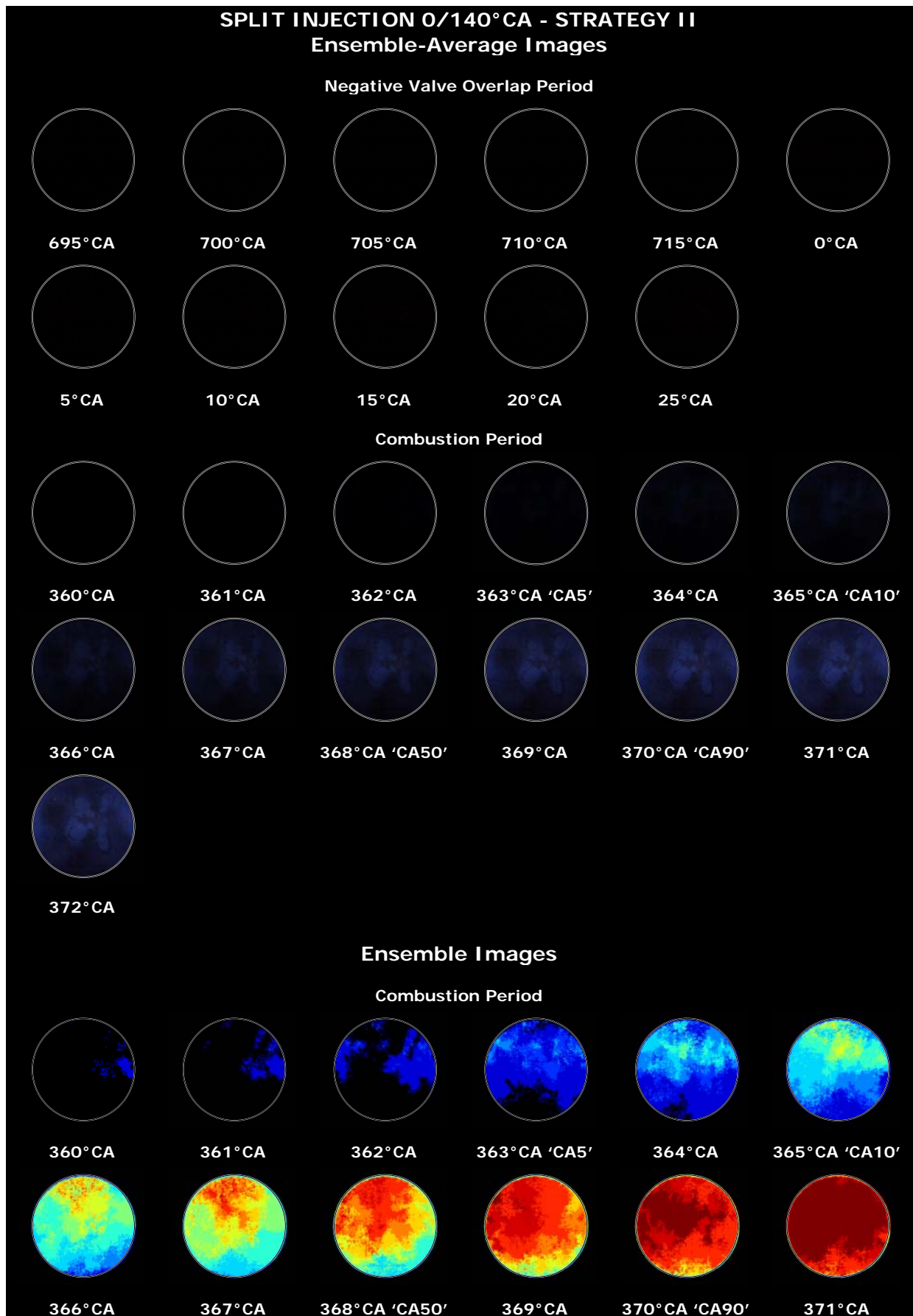


Figure 8.4. Single cycle image sequence of *negative valve overlap* and *main autoignition-combustion* periods of split gasoline injection with timing of 0/140° CA at $\Phi=1$. Images were acquired throughout the piston-crown window with Phantom v7.1 camera. Symbols in quotations refer to heat release rate burn points. In order to enhance visibility of the presented *main autoignition-combustion* period images, the intensities of all pixels at any RGB image location were multiplied by factor five.

Further, an analysis of the light captured by the three colour channels of the camera during the autoignition-combustion period was conducted in order to derive quantitative indications of recorded signals. This analysis is presented in Figures 8.10-8.13 for each studied case. As stated above the most intense ensemble-average image from a corresponding sequence was chosen for that scrutiny. Evaluated mean values and their standard deviations are given in captions (descriptions) under each corresponding figure.



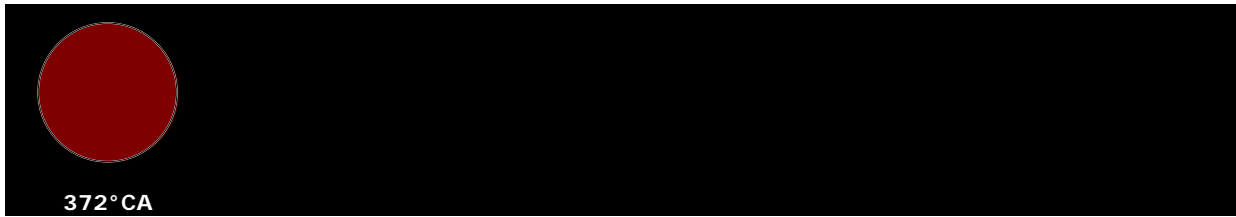


Figure 8.5. Ensemble-average image sequence of *negative valve overlap* and *main autoignition-combustion* periods of split gasoline injection with timing of 0/140° CA at $\Phi=1$. An ensemble image sequence of *main autoignition-combustion* period is also included. Symbols in quotations refer to average heat release rate burn points. Standard deviations of these corresponding burn points are 2.3, 2.3, 2.5 and 2.6 for CA5, CA10, CA50 and CA90 respectively. In order to enhance visibility of the presented *main autoignition-combustion* period images, the intensities of all pixels at any RGB image location were multiplied by factor five.

An analysis of Fig.8.10 and its computed mean values indicates that bright yellow luminous autoignition-combustion activities are red-channel dominated. In other words when there is a red-channel light dominance the colour will be yellow (under particular color scheme as one found in this investigation). Contrary to this, the dark bluish autoignition-combustion activities of split injection strategies II and III and of the single injection strategy consistently show a blue channel dominated signal intensity. Furthermore, when one compares the corresponding mean values of split injection I with other cases it is evident that the differences are not about only the colour scheme but as importantly they concern the light intensities. They emitted different colours of the autoignition-combustion activities are from opposite spectrum ends as blue and red. It might be worth noting here the fact that all these results were captured with identical camera settings where the light integration time seemed to be the most relevant factor.

The observed blue chemiluminescence of HCCI autoignition-combustion activities in the current study is not surprising as it has recently been noted by other researchers e.g. Zigler *et al* 2008 and Kawahara *et al* 2003. In direct comparison to the current study Zigler *et al* 2008 conducted a high-speed investigation of HCCI autoignition-combustion by using an identical imager, although with a light integration period set roughly twice as long. They

operated their engine with gasoline (as one among the other blends examined) at lean operating conditions, while introducing fuel into the intake manifold. Their study showed a continuous blue emission for any distinctive phase of HCCI autoignition-combustion (Hwang *et al* 2008) regardless of the fuel blend investigated. The similarities between the current study's observations and theirs clearly indicate that HCCI autoignition- combustion activities are blue chemiluminescence dominated.

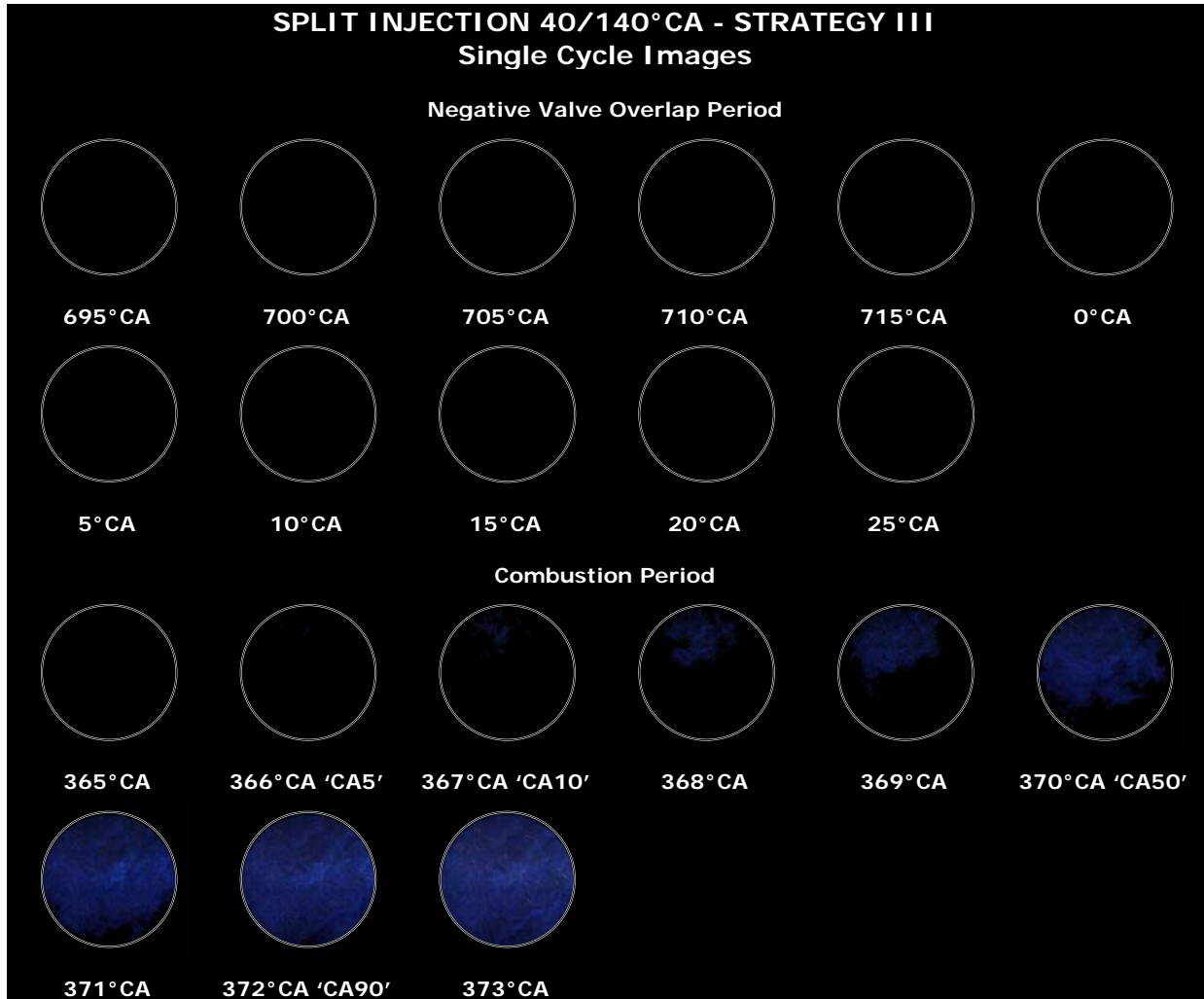
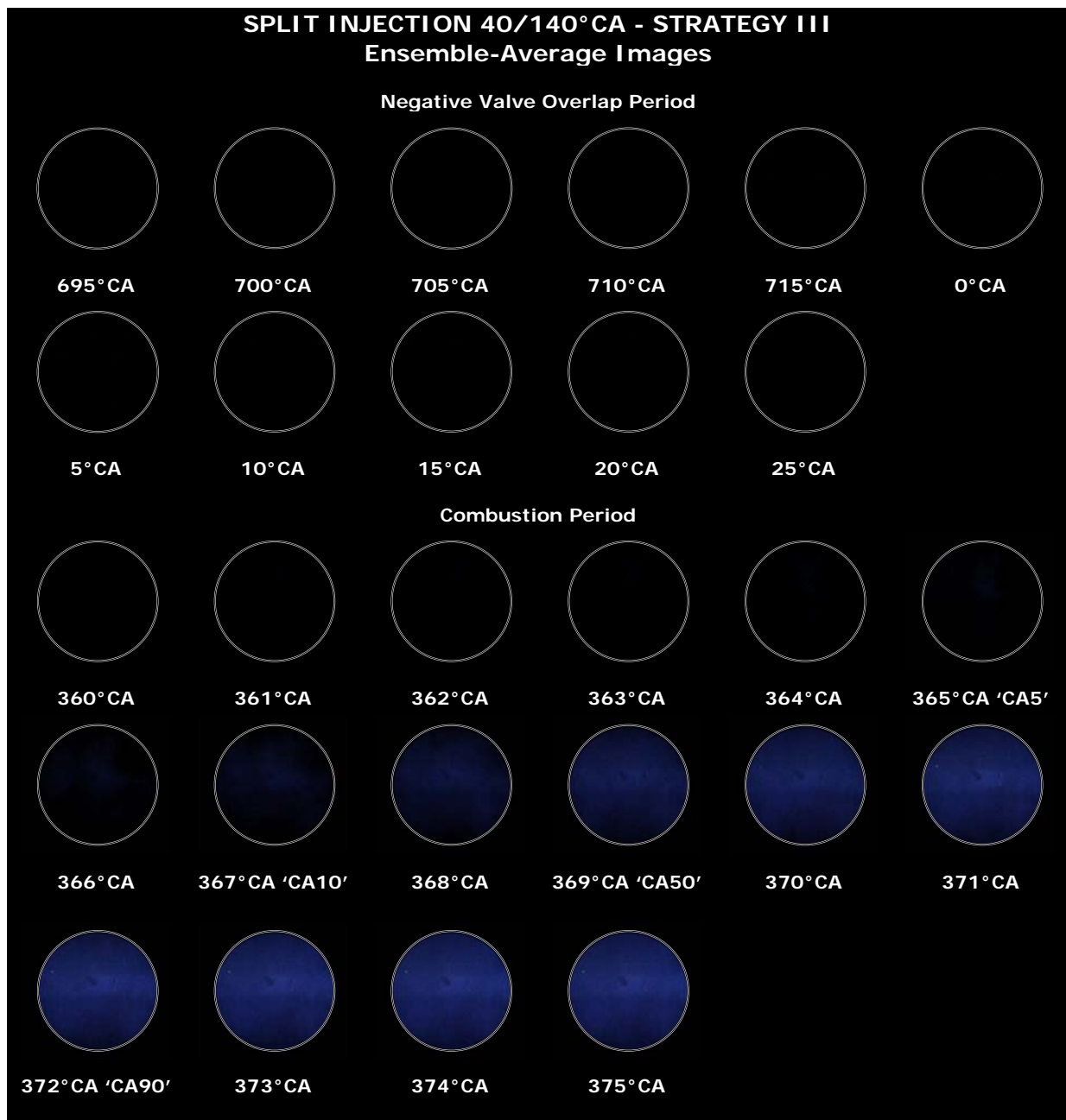


Figure 8.6. Single cycle image sequence of *negative valve overlap* and *main autoignition-combustion* periods of split gasoline injection with timing of 40/140° CA at $\Phi=1$. Images were acquired throughout the piston-crown window with Phantom v7.1 camera. Symbols in quotations refer to heat release rate burn points. In order to enhance visibility of the presented *main autoignition-combustion* period images, the intensities of all pixels at any RGB image location were multiplied by factor five.

However, the current study also shows that this may be declared true for particular engine operating conditions, more specifically with an injection timing strategy. There are conditions where these blue colour dominated autoignition-combustion activities are either significantly changed or masked in terms of the natural colour light emission. It is also noteworthy that the author of this thesis also observed blue light dominated activities for port fuel injected HCCI autoignition and combustion (Luszcz *et al* 2009). Kawahara *et al* (Kawahara *et al* 2008) by conducting an investigation of dimethyl ether HCCI and by introducing fuel into the intake manifold they noted the blue light emission of corresponding autoignition and combustion phases. No bright emission, more specifically no white-ish colours were reported in their study. Another investigation showing the blue light emission isooctane autoignition and combustion was performed by He *et al* (He *et al* 2006). They derived this from rapid compression facility measurements. Although the study was not dealing with engine combustion it is interesting to note here, from the standpoint of the autoignition-combustion chemiluminescence character.

It is necessary to scrutinise the negative valve overlap period of this case and contrast potential NVO's activities with the other cases studied to gain an understanding of what has contributed or caused that atypical observed autoignition and combustion behaviour i.e. the emitted light colour and intensity when fuel is introduced prior to the TDC recompression stroke. This is accomplished by contrasting the corresponding images shown in Figures 8.2-8.9. After comparing the potential activities of the recompression stroke it is clearly noticeable that only split injection with a pilot injection at 680°CA exhibits discernible activities during this period. Surprisingly, when a pilot fuel injection occurs at TDC NVO, no significant activities appear. This is especially true when compared to the case when a pilot injection occurs prior to the TDC recompression stroke. Nevertheless by carefully analysing individual cycle images for O period included in Figure 8.4, distinguishable local activities at 10°CA after NVO and onwards are observable. They are of a dark light emission intensity that is really hard to notice. Also these activities (in the case of a pilot injection at TDC NVO) show a local character with a potential random distribution. Therefore they might not be

clearly presented in the ensemble-average images; this is the effect of signal attenuation. Similarly, the attenuated light intensity of NVO activities can be seen when equivalent images of the ensemble-average and single cycle sequences are contrasted for the case when a pilot injection occurs prior to TDC. Finally, the split injection strategy of inserting fuel after TDC of recompression stroke did not reveal any recompression stroke activities nor did the single injection strategy investigated. This was expected as fuel was primarily injected during the introduction stroke for both of these cases; thus no favourable conditions were encountered for the air-fuel mixture to undergo activities.



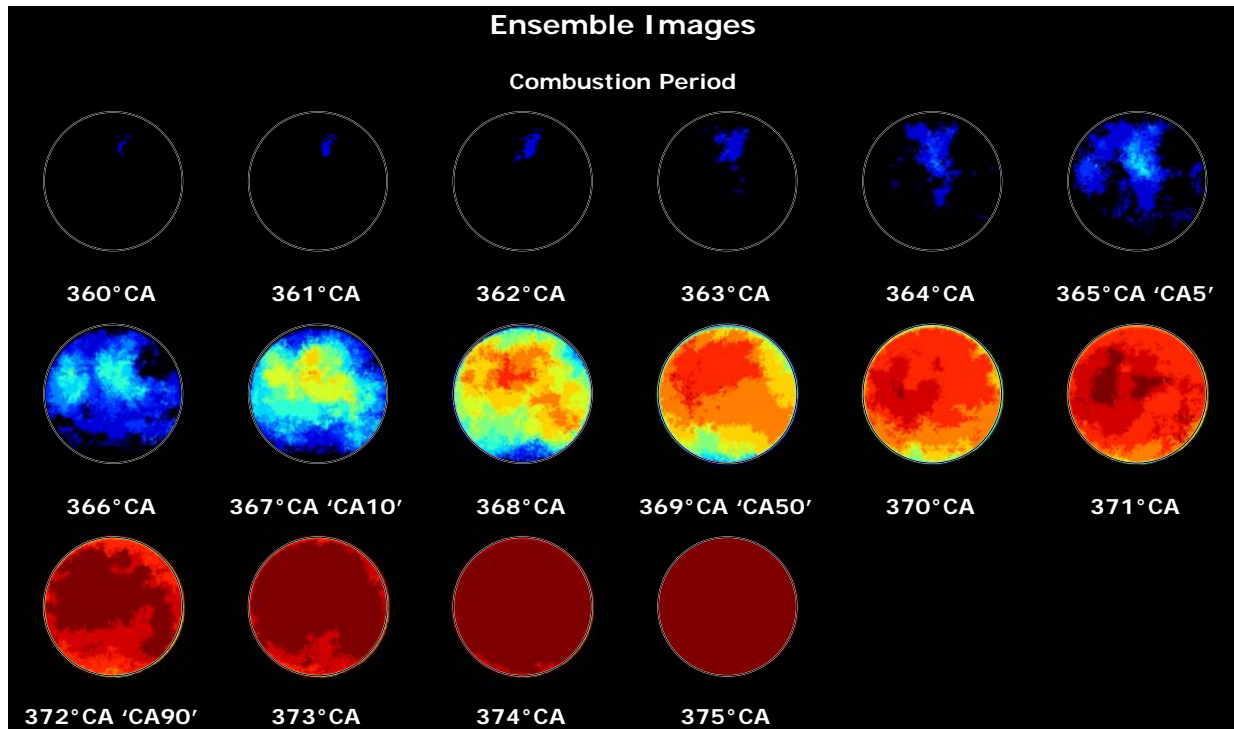


Figure 8.7. Ensemble-average image sequence of *negative valve overlap* and *main autoignition- combustion* periods of split gasoline injection with timing of 0/140° CA at $\Phi=1$. An ensemble image sequence of *main autoignition- combustion* period is also included. Symbols in quotations refer to average heat release rate burn points. Standard deviations of these corresponding burn points are 2.3, 2.3, 2.5 and 2.6 for CA5, CA10, CA50 and CA90 respectively. In order to enhance visibility of the presented *main autoignition-combustion* period images, the intensities of all pixels at any RGB image location were multiplied by factor five.

Now that the activities of the negative valve overlap period for all investigated injection events have been briefly contrasted there it is time to identify the considerable ones. The activities of the recompression stroke were revealed once the pilot fuel occurred prior to TDC NVO. As the engine was running under stoichiometric operating conditions, there was no potential for a reactions leading to heat release. Also it is when these NVO activities affect the main autoignition-combustion period that they become of particular interest. Negligible recompression stroke activities with a pilot injection case of TDC NVO showed be ascribed to the same origin as those exhibited by a case with a 680°CA pilot injection. This can be done especially because the engine operating variables such as the fuel-air equivalence ratio, split

injection ratio and fuel type were kept constant. During the recompression stroke when fuel is introduced prior to TDC the activities first become visible at 10°CA before TDC. They appear to persist for roughly another thirty crank angle degree period. Moreover different light intensity emissions are observable throughout as seen in Figures 8.2 and 8.3. Because the engine was operating at $\Phi=1$ and therefore there were no oxygen leftovers (unused air) in the trapped residuals that might constitute opportunities for reactions to occur during the NVO, there is evidence that the emitted light recorded is not chemiluminescence.

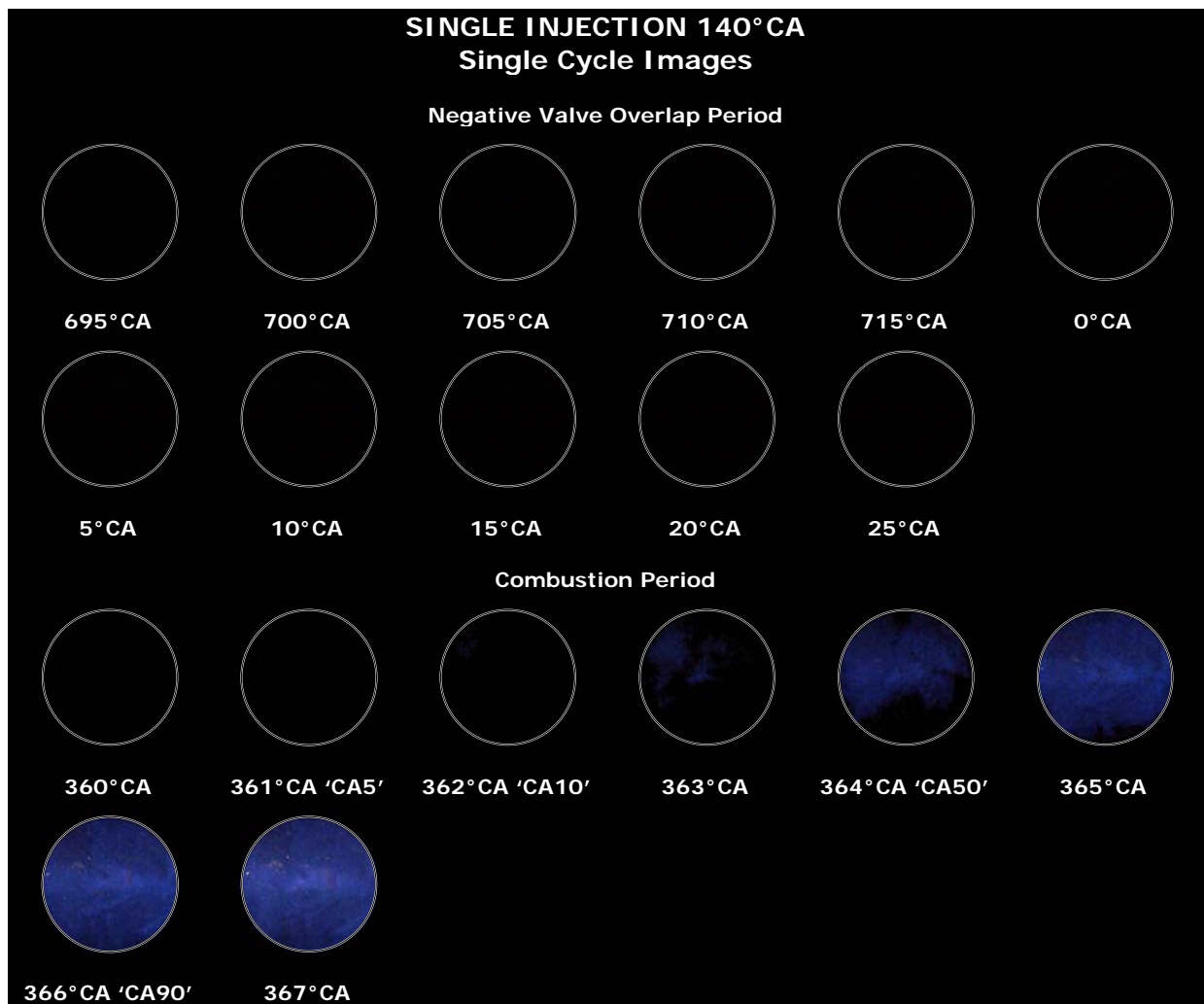
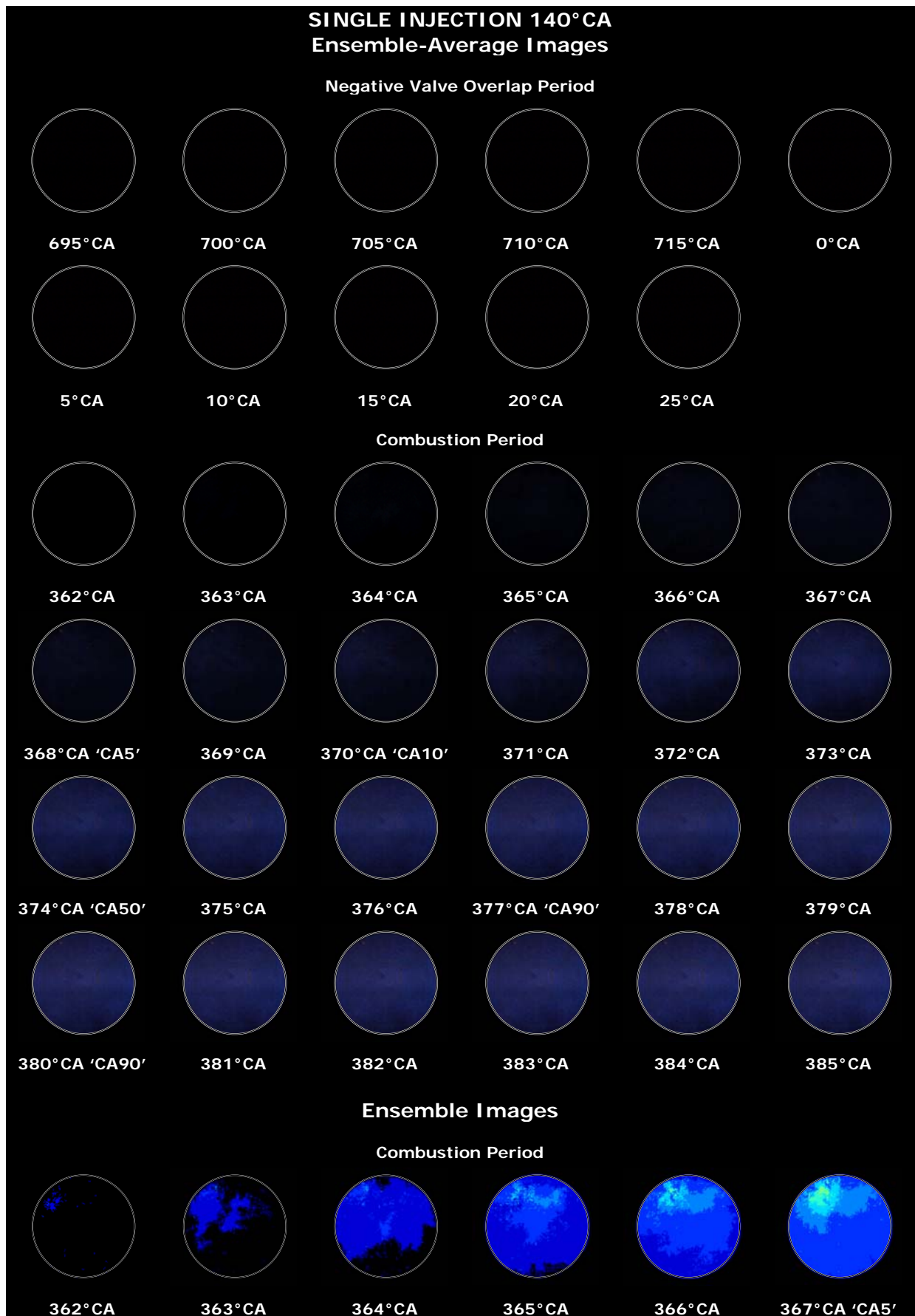


Figure 8.8. Single cycle image sequence of *negative valve overlap* and *main autoignition-combustion* periods of single gasoline injection with timing of 140° CA at $\Phi=1$. Images were acquired throughout the piston-crown window with Phantom v7.1 camera. Symbols in quotations refer to heat release rate burn points. In order to enhance visibility of the presented *main autoignition-combustion* period images, the intensities of all pixels at any RGB image location were multiplied by factor five.



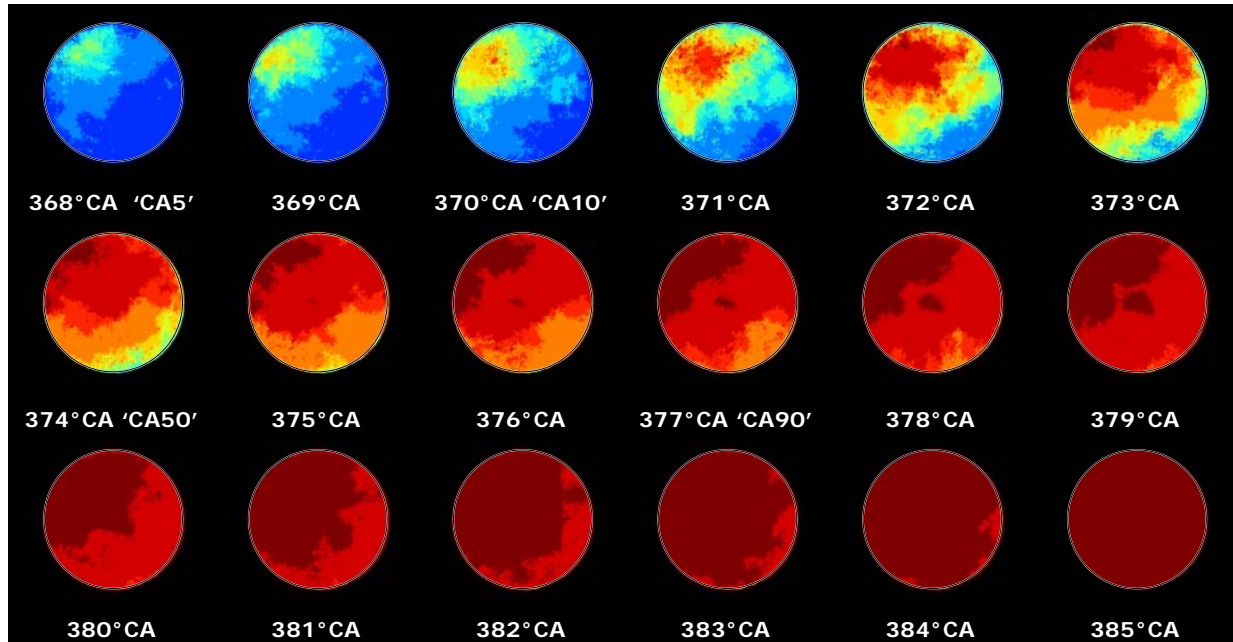


Figure 8.9. Ensemble-average image sequence of *negative valve overlap* and *main autoignition-combustion* periods of single gasoline injection with timing of 140° CA at $\Phi=1$. An ensemble image sequence of *main autoignition-combustion* period is also included. Symbols in quotations refer to average heat release rate burn points. Standard deviations of these corresponding burn points are 3.2, 3.4, 4.8 and 6.1 for CA5, CA10, CA50 and CA90 respectively. In order to enhance visibility of the presented *main autoignition-combustion* period images, the intensities of all pixels at any RGB image location were multiplied by factor five.

After investigating the potential for reactions to occur during the negative valve overlap with various fuel-air equivalence ratios, Koopmans *et al* (2003) observed no reactions contributing to heat release with conditions of $\Phi \approx 0.91$ and richer. Indeed, this study was conducted with fuel injection occurring during the recompression stroke. Further, the time interval in which this light is emitted seems to corroborate the opinion that the recorded light and its intensity are not chemiluminescence. It is unlikely that a chemiluminescence could have lasted for such a considerable length of time as the transition from an excited state to the ground state of an atom or molecule after excitation which yields chemiluminescence is a short period of time (Garcia-Campana *et al* 2001). Because of these reasons it is believed that the observed light emission during NVO period in this study might have come from an

incandescence of solid carbonaceous particles, or more specifically the effect of thermal radiation emitted by solid carbonaceous particles.

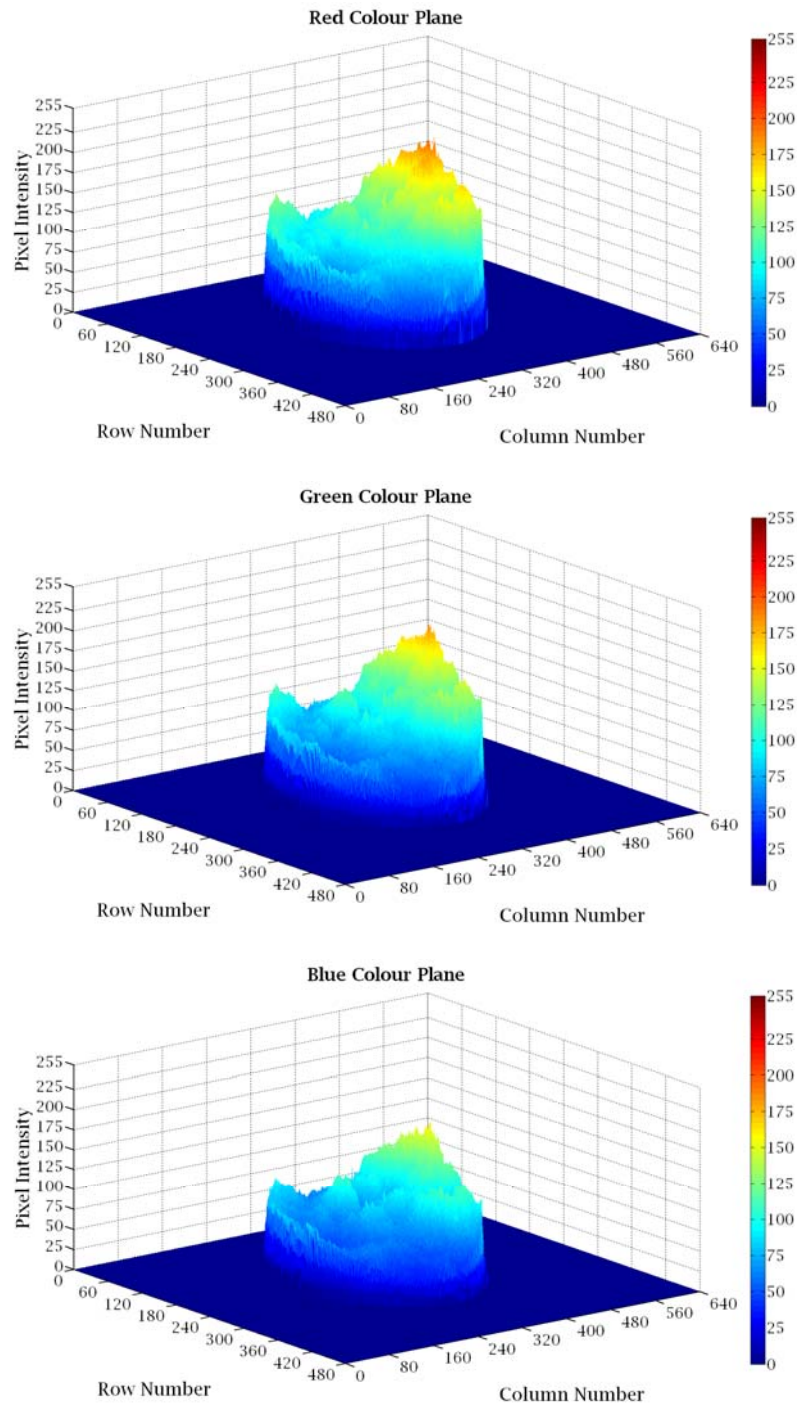


Figure 8.10. Light intensity distribution for three individual planes of RGB ensemble-average image at 369°CA of split gasoline injection with timing of 680/140° CA. Means estimated for each plane equal to 98.7, 82.9 and 69.3 with their standard deviations of 30.7, 28.9 and 21.3 for red, green and blue plane respectively, calculated within the distinguished combustion chamber area.

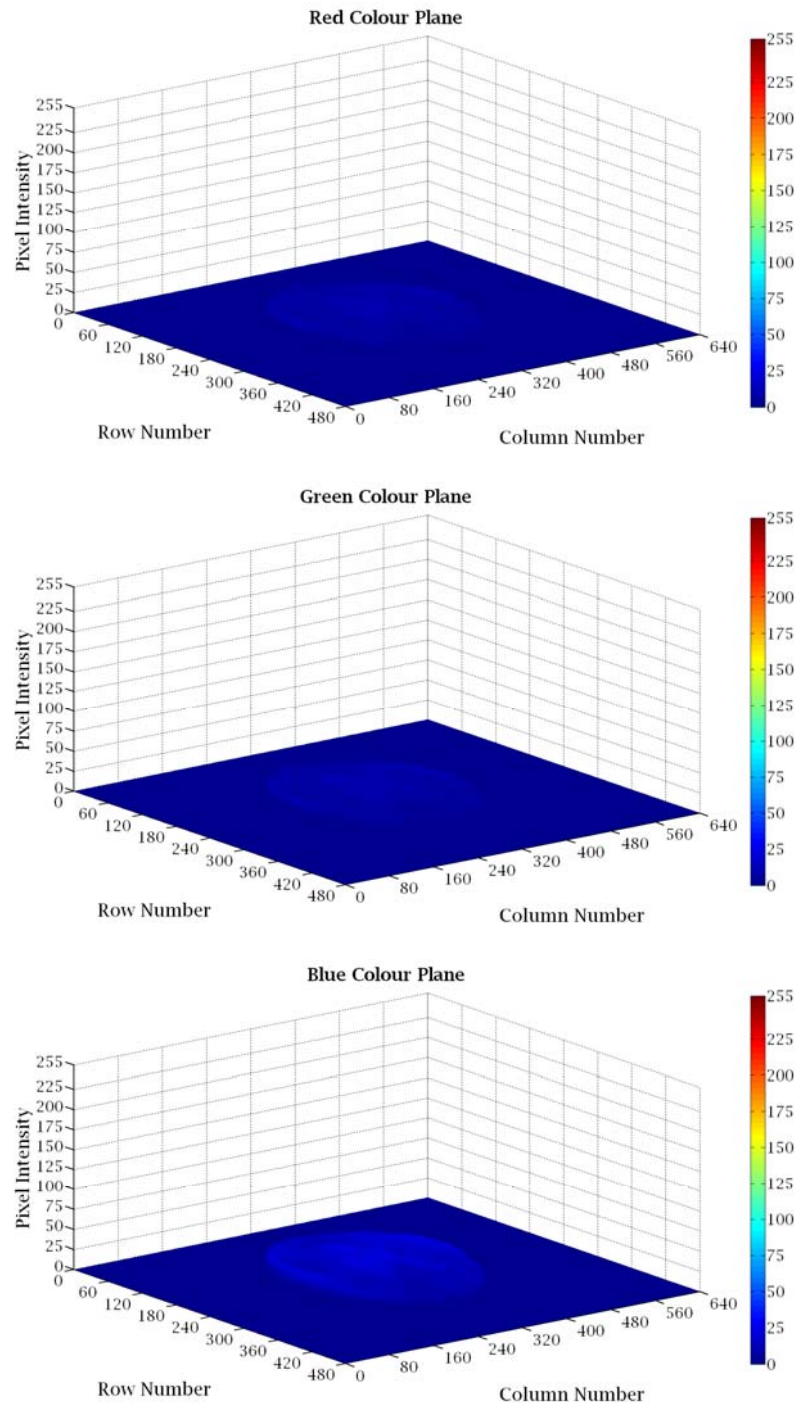


Figure 8.11. Light intensity distribution for three individual planes of RGB ensemble-average image at 372°CA of split gasoline injection with timing of $0/140^{\circ}\text{CA}$. Means estimated for each plane equal to 5.7, 5.8 and 12.5 with their standard deviations of 2.1, 2.2 and 4.3 for red, green and blue plane respectively, calculated within the distinguished combustion chamber area.

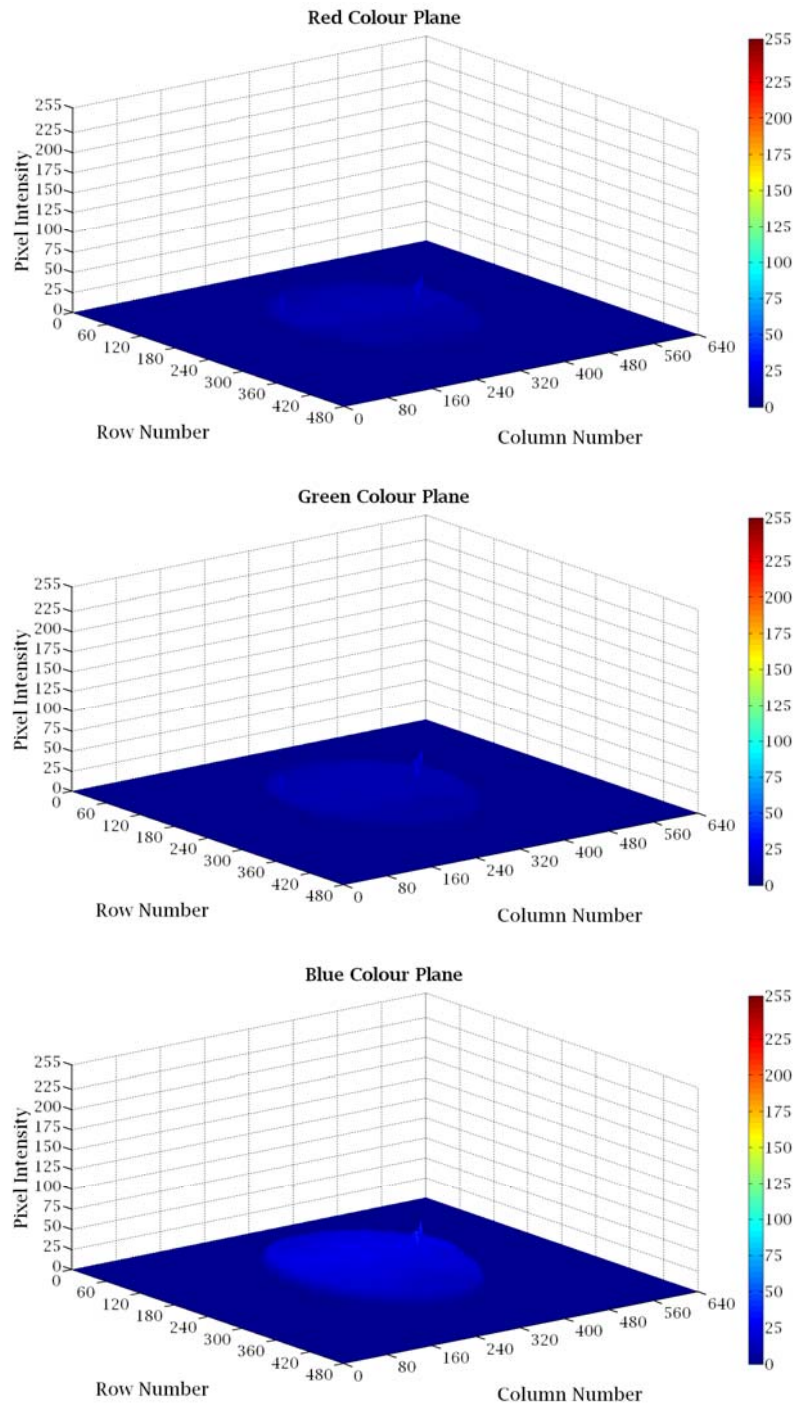


Figure 8.12. Light intensity distribution for three individual planes of RGB ensemble-average image at 374°CA of split gasoline injection with timing of $40/140^{\circ}\text{CA}$. Means estimated for each plane equal to 7, 7.9 and 18.4 with their standard deviations of 2.5, 2.4 and 4.2 for red, green and blue plane respectively, calculated within the distinguished combustion chamber area.

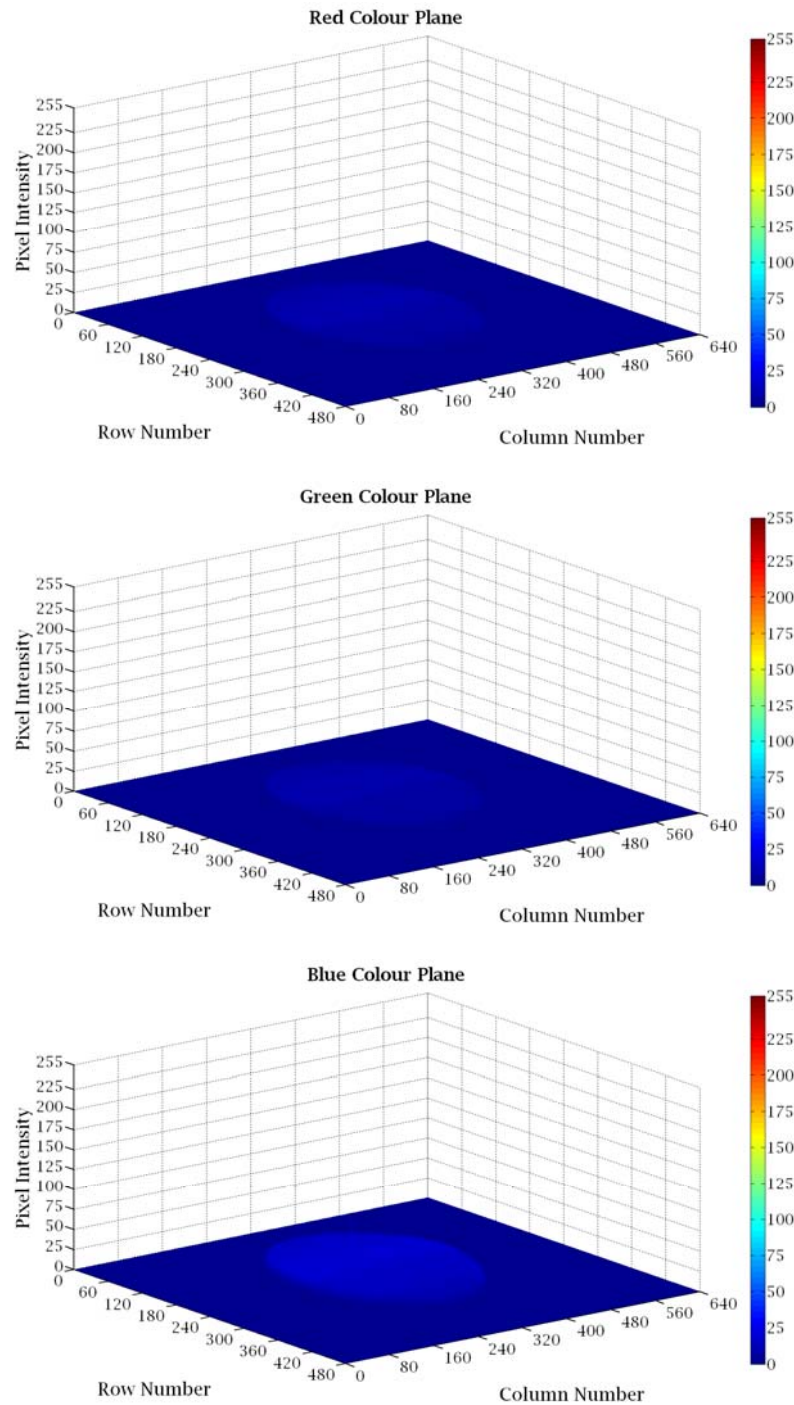


Figure 8.13. Light intensity distribution for three individual planes of RGB ensemble-average image at 374°CA of single gasoline injection with timing of 140°CA . Means estimated for each plane equal to 6.8, 6.5 and 14.2 with their standard deviations of 2.1, 1.8 and 3 for red, green and blue plane respectively, calculated within the distinguished combustion chamber area.

During the negative valve overlap interval, at the particular engine operating conditions studied it is believed that the soot is formed as an effect of pyrolysis of the fuel molecules, which most likely constitutes the first step in soot forming process. Essentially pyrolysis of the fuel is considered as an important source of the soot formation process (Heywood 1988). The pyrolysis process during the NVO at the operating conditions investigated would seem to be favorable, especially due to the high temperatures caused by large fraction of residuals trapped and lack of oxygen. Fuel molecules breaking down thermally could form different carbon-ring structures, smaller hydrocarbon molecules or eventually carbon and monatomic or diatomic hydrogen. As the pyrolysis occurs, it considerably contributes to dehydrogenation of hydrocarbon molecules and finally soot particles having an appropriate low hydrocarbon content with H/C ratio in the range of 0.1-0.2 (Heywood 1988) could be formed via the other further conventional routes. These routes of soot formation as a particle growth could include conventional processes: polymerization, surface growth, coagulation and aggregation. Worth noting here is also that the soot particles of higher H/C ratios than the aforementioned specified are also encountered in soot emission analysis (Heywood 1988). With the current study using standard gasoline, which includes significant aromatics content ($\approx 30\%$ vol.) the formation of solid carbons might be further favorable, as at the temperatures ≤ 1700 K aromatics were noted as effective compounds in forming soot through pyrolysis (Heywood 1988). Also the aromatic hydrocarbons could significantly contribute to formation of polycyclic aromatic hydrocarbons considered as precursors of soot formation. Unlike to the soot formation during the diffusion or premixed flame combustion the soot formation process during the NVO at the conditions studied seems to be more stable (constant) as there is no competition between the soot formation process and oxidation of fuel or soot particles. However as the residuals contain some water traces, the carbon could be attacked by H_2O to produce carbon monoxide and hydrogen (Heywood 1988; Gaydon 1974), which could constitute the only possible way to oxidise some fraction of soot formed during the NVO period. As it is thought that soot is formed during the NVO via the conventional ways; thus the particle numbers, their sizes and as importantly their volume fraction are all dependent

on the temperature-pressure history and amount of time available. If this is the case this would contribute to a decrease in the volume fraction of pyrolysed fuel molecules and consequently soot formed, for instance when the fuel is injected at TDC NVO in contrast to cases when the pilot injection occurs prior to the TDC recompression stroke. Consequently, this helps to clarify the observed reduction in light intensity emission during the NVO. Also as this soot is formed at later crank angle degrees the temperatures are lower and the higher thermal radiation intensity is moved towards longer wavelengths, thereby greater incandescence strength is lower at shorter wavelengths, the spectral region more suitable for currently used imager to be captured.

The analysis of the light emission during the NVO for a pilot injection at 680°CA case has been performed and is shown in Fig. 8.14. This was conducted by extracting data from three

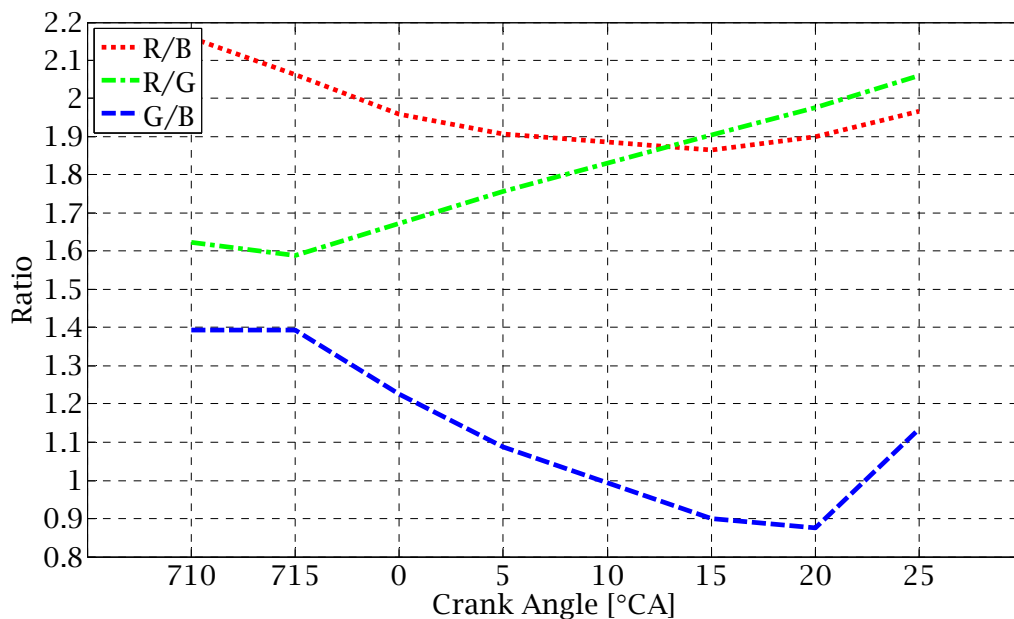


Figure 8.14. Responses of three camera channels as a from of corresponding channels signals ratios during the NVO activities of investigated split gasoline injection with timing of $680/140^{\circ}\text{CA}$ at $\Phi=1$. Presented ratios abbreviated to R/B, R/G and G/B designate ratios between signals of respective channels - red-to-blue, red-to-green and green-to-blue.

camera channels (red, green and blue) and by calculating the ratios between the corresponding channels. Firstly based on red-to-blue and red-to-green channel ratios there is

a clear indication that the potential incandescence of soot is red light (red camera channel) dominated. This would be in agreement with Ma (2006) , who reported that the soot thermal radiation emission at a temperature below 3000 K is red-dominant. Indeed it was not expected in the current study that NVO temperatures could exceed or even reach that high temperature level with the conditions studied. Koopmans *et al* (2003) noted that the estimated temperatures of TDC NVO when significant amount of residuals are trapped could reach approximately 1500K to 1600 K while the reactions are taking place. For a split injection case with injection timing prior to the TDC recompression stroke, it could be inferred that the NVO activities and their successive main autoignition-combustion activities are alike in terms of their similar red-light dominated colours. Furthermore, the recompression stroke activities for this injection strategy are brighter than the autoignition-combustion activities of other studied cases.

The thermal radiation of soot is classified as grey-body radiation Dec *et al* (1988) this is because carboneous solid particles are not perfect block body emitters (Ma 2006). Instead they emit thermal radiation with some offset, lower intensity at given wavelength as compared to black bodies according to Planck's law. It is assumed that soot emits thermal radiation with an intensity factor of about 0.95 of the total black body emission at a temperature range of 273-373K (Wojas 2008). Nevertheless, the pattern of thermal radiation occurring at a wide range of frequencies remains analogous and the highest radiation intensity shifts towards the shorter wavelength as the temperature increases. As this is the case the extracted data from three camera channels can serve as an indication of NVO temperatures. Like the corresponding individual camera channel spectral responsivity, more specifically its maximum matches with its specific, real wavelengths (red 700, green 546.1 and blue 435.8 nm) as seen in Figure 4.8B, there are also crosstalks among these channels, which prevent any certain conclusions to be drawn with the data at hand. This is even more pronounced near the infrared region where the three channels accept the radiation intensity with similar maximum acceptance values. A proper analysis, that could yield qualitative or even quantitative results would require a separation of the light bandwidths (by installing

filters), a tracking of only two or three particular wavelengths such as blue, green or red (Ma 2006; Singh *et al* 2005) light, and an account of the lens transmittance. Then calculated ratios for the obtained signals would then produce an indication of temperature in a qualitative way; or if the calibration was initially conducted it could indicate the temperature in quantitative way. However, this detailed analysis remains beyond the scope of this study; but it may constitute an interesting research area for further investigation.

Because recompression stroke activities of the particular split injection cases studied were attributed to the presence of soot, it is therefore thought that this is further soot combustion during the main autoignition-combustion period which is shown or which is contributing to the atypical yellow-ish colour. As the soot is formed during the negative overlap period it is further present and eventually burned out during the main autoignition-combustion period. Consequently when the main autoignition-combustion activities are initiated the presented soot particles are heated by surface combustion and light emitted due to incandescence of solid carbonaceous particles significantly dominates over the weak radiation of chemiluminescence reactions. As this is the case the light emitted during this kind of combustion appears quite bright and seem to be highly dependent on soot concentration and charge burning temperatures surrounding soot particles as the strength of incandescence is temperature and soot concentration dependent. It should be noted that the autoignition-combustion activities of other injection cases investigated appears as a purely chemiluminescence dominated, even including the split injection scheme with the pilot injection occurring during the TDC recompression stroke. It is thought that soot concentration was too low to significantly affect the main auto-ignition combustion period for this case. Moreover some of this soot formed during the NVO could have been consumed in the reaction with water vapor producing CO and H₂, therefore even lowering this low concentration of formed soot.

The current study's observations are in good agreement with the research conducted by Dec *et al* (1998) in the early days on optical diesel engine combustion. Dec *et al* observed that sooty combustion exhibits a yellow colour, moreover a colour of much higher intensity

than its preceding chemiluminescence. Also their study demonstrated that soot incandescence and its further burnout period contributed to that high luminosity. By quantifying the light emission coming from the diesel combustion process Dec *et al* noted that the chemiluminescence is a few orders of magnitude weaker than it is for sooty combustion. Another interesting investigation performed by Singh *et al* (2005) of the diesel combustion process clearly confirms that sooty combustion is 4-5 orders of magnitude brighter than the preceding chemiluminescence. Furthermore Picket *et al*'s (2009) insightful detailed diesel study pointed out that the sooty combustion due to its high luminescence could easily lead to the saturation of the camera's sensitive area when the light integration period is kept the same as for the preceding chemiluminescence activities. Secondly in accordance with Heywood (Heywood 1988), the premixed stoichiometric or lean flames are of low blue luminosity, whereas the rich mixtures or diffusion flames are characteristics of bright luminosity ranging from an orange to a red colour especially at some zones due to incandescence and burning of carbon particles.

The colour and intensity of sooty combustion reported in the aforementioned studies agree well with the observations laid out in current investigation. This agreement implies that there must be soot production during the recompression period and its further combustion in the main autoignition-combustion period. The light emitted during the NVO period is due to the incandescence of solid carbonaceous particles, while the combustion of soot (incandescence of solid carbonaceous particles being heated by surface combustion) in the main autoignition-combustion period produces a bright yellow-ish luminosity. Furthermore the intensity of main autoignition-combustion activities is much brighter, than the chemiluminescence of any other investigated cases during the corresponding period. This would scale well with observations in referenced studies (Dec *et al* 1998; Singh *et al* 2005; and Picket *et al* 2009) that chemiluminescence is a few order of magnitudes lower than it is for sooty combustion. It is intriguing that Gaydon (1974) observed a bright blue emission from the flames of CO and air/oxygen; and for premixed flames (at very rich mixtures) the faint bluish zone is due to CH. Also for rich mixtures, he noted that any yellow luminosity is

indeed attributed to carbon and “occurs above the reaction zone where C_2 and CH are emitted” (Gaydon 1974). For diffusion flames Gaydon (1974) also noted a blue light zone for the CO-flame spectrum on the oxygen side. Sometimes this was associated with the Schuman-Runge bands of O_2 . With this type of flames C_2 was adjacent to yellow luminous and dark bluish-green zones. The CH in this case was often traveling further towards the oxygen side than diatomic carbon.

A direct correlation the observations made above and any insightful and pioneering optical diagnostics of HCCI recompression stroke injection reported in open literature such as Berntsson *et al* (2007) and Urushihara *et al* (2003) is impeded as the current study was performed at a stoichiometric fuel-air equivalence ratio whereas they operated their engines under lean conditions. One comparison with HCCI work could be made with Hultquist *et al* (1999), with regards to the intensity of the burning solid carbon particles. By visualising the combustion process they observed intense bright spots burning like carbaceous solid particles. By restricting the recorded images to shorter wavelengths, where the thermal radiation intensity is lower for low temperature soot, they did not observe these mystifying spots any longer. Because of this they assumed that these were burning particles derived from lubricating oil. It is also noteworthy that activities under particular engine operating conditions and camera settings Zigler *et al* (2008) suspected the soot formation and burnout process when they obtained a white color for HCCI combustion. However, with the application of various light integration periods to these same conditions they noted that the white colour was an effect of camera saturation rather the existence of soot formation and further burnout. An interesting piece of information for this current study is the fact that the soot produced during HCCI combustion can be oxidised at a lower temperature but also at lower reaction rates than soot from the diesel combustion (Zinola *et al* 2009). Also the significant emission of soot from HCCI combustion, especially under particular engine operating conditions, has been reported in open literature by e.g. Dec *et al* (2003), Price *et al* (2007) and Misztal *et al* 2008 (2008). Various engine operating conditions have been investigated and soot formation was attributed to them, i.e. injection timing Dec *et al* (2003) ,

Misztal *et al* (2009) and strategy Misztal *et al* (2009) , different loads and fuel-air equivalence ratios Dec *et al* (2003) , Price *et al* (2007) and alternatively the influence of intake air temperature Misztal *et al* (2009) .

To gain a further insight into the autoignition-combustion characteristic of investigated injection strategies the relevant data were extracted from images by an application of two image processing techniques. A qualitative analysis, which somewhat quantifies repeatability nature of autoignition occurrence and preferential combustion development patterns with an insight into the preferential locations was performed and relates to the autoignition-combustion areas.

Quantification is accomplished by means of scrutinising the statistical descriptors of normalised image (ensemble image) histogram which provide information about the likelihood of repeatability. Further the combustion growth rates for each individual imaged engine cycle are estimated and shown in relation to the crank-angle. This is done by using a second image processing technique. The computational approaches of by these two image processing techniques were described in chapter 5, sections 5.4.4.1 and 5.4.4.2 of this thesis.

Process, autoignition-combustion occurrence and further development likelihood of repeatability are expressed by statistical descriptors summarised in Tables 8.2-8.5 for each injection case. More specifically these statistical descriptors refer to corresponding ensemble image sequence included in Figures 8.3,8.5,8.7, and 8.9. Because the statistical analysis is found on the image of a normalised histogram of grey levels distribution each individual grey-level was assigned a random variable which numerically corresponded to its value. Hence the terms 'random variable' and 'grey level' will be used interchangeably for the remainder of this section. Also the so called *jet* mapping of Matlab® was used for ensemble images, which indeed assigns a particular colour to each individual grey-level (random variable) of the ensemble image. The lowest value was assigned blue and the highest red, as *jet* colourmap ranges from blue to red.

Some essential similarities in combustion onsets as locations of first autoignition sites are noticeable from Figures 8.3,8.5,8.7, and 8.9 for all the injection strategy cases studied. Principally, this is the area corresponding to the exhaust valves' side of combustion chamber. These activities are illustrated as the places on a given image which have the highest number of random variables at the beginning stage of an ensemble image sequences.

Ensemble Image °CA		Statistical Descriptors						
		<i>Mode (M)</i>	<i>Maximum Probability</i>	<i>Range (R)</i>	<i>Mean (μ_T)</i>	<i>Variance (σ^2)</i>	<i>Skewness (S)</i>	<i>Kurtosis (K)</i>
SPLIT INJECTION 680 and 140°CA	360° CA	1	0.94	0.94	1.06	0.06	3.68	N.D.
	361° CA	1	0.82	0.82	1.18	0.16	1.83	N.D.
	362° CA	1	0.576	0.576	1.48	0.385	1.12	N.D.
	363° CA	2	0.378	0.378	1.99	0.81	0.53	N.D.
	364° CA	3	0.278	0.278	2.61	1.47	-0.02	-1.22
	365° CA	5	0.292	0.292	3.74	3.35	-0.22	-1.06
	366° CA	7	0.156	0.156	6.01	6.33	-0.292	-0.81
	367° CA	12	0.211	0.207	8.83	7.5	-0.6	-0.67
	368° CA	12	0.574	0.573	10.8	3.62	-1.75	2.75
	369° CA	12	0.896	0.8958	11.8	0.8	-6.21	46.8
	370° CA	12	1	1	12	0	0	N.D.

Table 8.2. Statistical descriptors of ensemble images of split injection 680 and 140°CA combustion.

The finding that the combustion onset generally occurs at the hotter exhaust valves is not new and has recently been published by Hultqvist *et al* (1999, 2002) and Aleiferis *et al* (2006). Also port fuel injected HCCI combustion studies conducted in the previous chapter have produced the same indication. Indeed this favourable place for an autoignition to occur can be clarified as temperature inhomogeneities across the combustion chamber surface and artifacts; thus the combustion onset is initiated from the location of the exhaust valves and fundamentally develops towards the side of the intake valves, with different possible patterns. After comparing the autoignition onset of different cases, no particular character was observed for the split injection strategy that yielded atypical autoignition-combustion colour and intensity.

Ensemble Image °CA		Statistical Descriptors						
		<i>Mode (M)</i>	<i>Maximum Probability</i>	<i>Range (R)</i>	<i>Mean (μ_T)</i>	<i>Variance (σ^2)</i>	<i>Skewness (S)</i>	<i>Kurtosis (K)</i>
SPLIT INJECTION 0 and 140°CA	360° CA	1	0.998	0.998	1.0001	0.001	28.4	N.D.
	361° CA	1	0.989	0.989	1.011	0.014	11.2	N.D.
	362° CA	1	0.915	0.915	1.09	0.085	3.23	N.D.
	363° CA	1	0.672	0.672	1.418	0.4402	1.49	1.59
	364° CA	1	0.386	0.386	2.39	1.79	0.47	-0.88
	365° CA	4	0.263	0.263	3.69	2.78	-0.033	-0.63
	366° CA	5	0.279	0.279	5.27	2.67	-0.0698	0.272
	367° CA	6	0.239	0.239	6.57	3.17	0.198	-0.432
	368° CA	10	0.2309	0.2302	7.99	4.004	-0.5715	-0.6107
	369° CA	10	0.3446	0.3439	9.5	2.74	-1.34	2.1
	370° CA	12	0.3422	0.3415	10.7	2.14	-1.95	6.14
	371° CA	12	0.7445	0.7440	11.48	1.39	-3.82	20.6
	372° CA	12	1	1	12	0	0	N.D.

Table 8.3. Statistical descriptors of ensemble images of split injection 0 and 140°CA combustion.

Ensemble Image °CA		Statistical Descriptors						
		<i>Mode (M)</i>	<i>Maximum Probability</i>	<i>Range (R)</i>	<i>Mean (μ_T)</i>	<i>Variance (σ^2)</i>	<i>Skewness (S)</i>	<i>Kurtosis (K)</i>
SPLIT INJECTION 40 and 140°CA	360° CA	1	1	1	1	0	0	N.D.
	361° CA	1	1	1	1	0	0	N.D.
	362° CA	1	1	1	1	0	0	N.D.
	363° CA	1	0.952	0.952	1.05	0.049	4.44	N.D.
	364° CA	1	0.782	0.782	1.243	0.236	1.91	N.D.
	365° CA	1	0.654	0.654	1.52	0.705	1.69	2.38
	366° CA	1	0.382	0.382	2.27	1.71	0.73	-0.583
	367° CA	5	0.175	0.175	4.3	4.02	-0.0106	-0.9862
	368° CA	8	0.256	0.256	6.87	4.02	-1.02	0.832
	369° CA	9	0.371	0.371	8.43	2.9	-1.68	3.15
	370° CA	10	0.463	0.433	9.58	1.64	-1.8	4.94
	371° CA	10	0.41	0.41	10.4	0.95	-0.91	3.8
	372° CA	12	0.509	0.509	11.25	0.88	-1.39	2.68
	373° CA	12	0.783	0.783	11.7	0.41	-2.35	5.9
	374° CA	12	0.934	0.934	11.91	0.158	-5.27	31.6
	375° CA	12	1	1	12	0	0	N.D.

Table 8.4. Statistical descriptors of ensemble images of split injection 40 and 140°CA combustion.

Contrary to this, it was an instance of a split injection strategy with fuel inserted after TDC NVO, which showed a slightly different preference for first identifiable autoignition sites. When contrasting ensemble images from Figure 8.7 with others included in Figures 8.3, 8.5 and 8.9 it is noticeable that the first autoignition sites form almost in the middle of the exhaust valves' side in some cases and for other cases the first identifiable autoignition sites are located at the edges of the accessible part of the combustion chamber. After analysing further the likelihood of repeatability of these first autoignition activities (while assuming that

Ensemble Image °CA		Statistical Descriptors						
		<i>Mode (M)</i>	<i>Maximum Probability</i>	<i>Range (R)</i>	<i>Mean (μ_T)</i>	<i>Variance (σ^2)</i>	<i>Skewness (S)</i>	<i>Kurtosis (K)</i>
SINGLE INJECTION 140°CA	362° CA	1	0.969	0.969	1.03	0.03	5.42	N.D.
	363° CA	1	0.955	0.955	1.05	0.053	4.97	N.D.
	364° CA	1	0.918	0.918	1.07	0.096	3.72	N.D.
	365° CA	1	0.671	0.671	1.42	0.404	1.54	2.13
	366° CA	2	0.517	0.517	1.89	0.612	0.923	1.53
	367° CA	2	0.678	0.678	2.41	0.663	1.79	3.62
	368° CA	2	0.504	0.504	2.78	1.06	1.492	1.92
	369° CA	3	0.387	0.387	3.3	2.14	1.3	0.93
	370° CA	3	0.333	0.333	4.1	3.67	0.9	-0.212
	371° CA	3	0.227	0.227	5.59	5.69	0.34	-0.999
	372° CA	11	0.17	0.17	7.4	7.2	-0.28	-1.04
	373° CA	11	0.283	0.283	8.87	4.99	-0.89	-0.034
	374° CA	11	0.376	0.376	9.8	2.25	-0.95	0.82
	375° CA	11	0.487	0.487	10.4	1.26	-0.68	0.31
	376° CA	11	0.498	0.498	10.6	1.03	-0.563	-0.558
	377° CA	11	0.521	0.521	10.9	0.82	-0.779	0.039
	378° CA	11	0.569	0.569	11.16	0.521	-0.825	1.14
	379° CA	11	0.582	0.582	11.35	0.302	-0.2	0.128
	380° CA	11	0.512	0.512	11.48	0.27	-0.105	N.D.
	381° CA	12	0.654	0.654	11.65	0.24	-0.81	-0.58
	382° CA	12	0.765	0.765	11.76	0.196	-1.59	2.52
	383° CA	12	0.87	0.87	11.87	0.126	-2.77	10.05
	374° CA	12	0.941	0.941	11.94	0.061	-4.31	N.D.
	375° CA	12	1	1	12	0	0	N.D.

Table 8.5. Statistical descriptors of ensemble images of single injection 140°CA combustion.

the first three images in the corresponding sequence are representative), it should be stated that these first sites are barely repeatable since the observed means do not exceed a value of 1.48 for any case investigated.

Also these are not only the indications of low estimated expectance magnitudes which indicate a poor character of process likelihood of repeatability at these initial stages, descriptor indications such as mode values and associated with it maximum probability values, variance or skewness values scrutiny also confirm the trend. Low mode in an order of 1, associated with a high maximum probability of occurrence values not being below 0.5, contributes to the conclusion of a poor likelihood of repeatability. Furthermore low variance values in the order of 0 to 0.385 indicate that data are located close to the observed mean, which in fact is low at this stage. Finally, high (positive) skewness magnitudes imply that the data are biased to the left hand side of the normalised ensemble image histogram. This would clearly indicate that the autoignition-combustion marked areas of the ensemble images at these cycle points are represented by scattered low grey-level pixel intensity values as a result of either an actual mismatch in occurrence of first autotignition sites or as importantly as a result of the difference in their sizes. Also the analysis does not account for variations in combustion onset phasing; and as specified by standard deviations of CA5 and CA10 they occur for investigated cases and reach as high values as 3.2 and 3.4°CA, which in fact contributes to weakening the likelihood of repeatability at this stage.

Further as the combustion progresses there is a progressive elevation of observed mean magnitudes associated with the more uniform distributed data of the normalised histogram as indications of higher variances and lower skewness magnitudes. Preferentially the combustion develops from the initial location towards the intake valves side with different patterns observed for various injection cases studied. Finally as the imaged part of combustion chamber becomes enflamed by each individual cycle image the mean values reach the maximum possible and the distribution becomes right hand biased, tending to be one random variable distribution. Variance values at this late combustion stage are progressively smaller as an effect of the whole combustion chamber being enflamed. This

simple analysis indicated no particular behaviour with regards to autoignition formation for split injection when a pilot injection was introduced prior to the TDC recompression stroke. Also combustion development progresses essentially from the exhaust valves towards the intake valve sides, however with distinct actual patterns for the investigated cases as seen in ensemble image sequences.

The distributions of estimated combustion growth rates on a crank angle basis for studied injection cases are respectively demonstrated in Figures 8.15-8.18. The burned points of 5, 10, 50 and 90% of the corresponding imaged cycles are also plotted in these figures for the correlation of estimated combustion growth rate with the actual combustion process of heat release rates. By carefully comparing the aforementioned figures it can be seen that the maximum values of estimated burned area expansion rates are alike regardless of injection timing or strategy, with no significant variations noticed. They are in the range of 8-8.5 m²/s. Although this is a single injection case, which exhibited lower expansion rates of burned areas. By further analysing the correlation between the data on combustion growth rates and the burned points plotted in Figures 8.15-8.18, another observation could be made: the maximum values of the burned area expansion rate scale with CA50 points for the three cases investigated i.e. split injection strategy II,III and single injection. This is the case of injection timing potentially producing a sooty combustion which exhibits a different pattern of combustion growth rate distribution versus the location of burned points, especially CA10-CA50 window. It is illustrated that maximum values of combustion growth rates occur in the window of burned points referred to as CA10-CA50, thus these activities are halfway between CA10 and CA50 points as correlated to the heat release profiles. Similar distributions of expansion burned areas versus burned points were observed by contrasting the stoichiometric with the lean PFI combustion in the previous chapter.

However, the identified differences in the magnitudes of combustion growth rates between the stoichiometric and lean combustion were attributed to the effects contributing to the observations. The current study rather indicates the different characteristics preceding

sooty combustion in comparison to other cases. More specifically the highest magnitudes of combustion growth rates occurs prior to 50% of consumed charge.

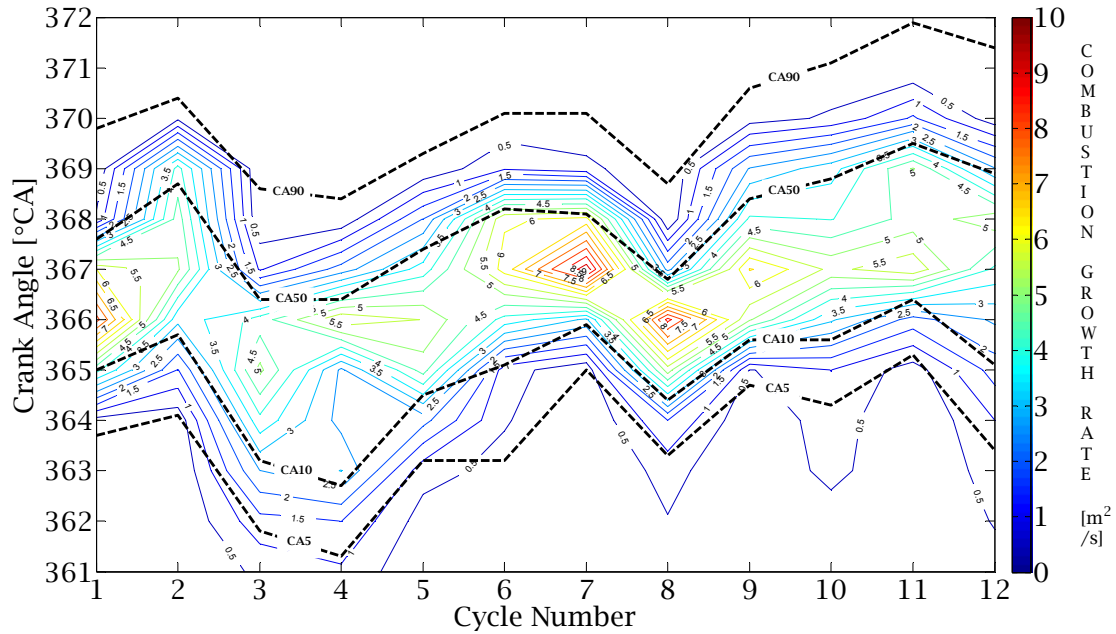


Figure 8.15. Distribution of expansion rates of burned areas in a relation to burned points of CA5, CA10, CA50 and CA90 for an imaged cycles of split gasoline injection with timing of 680/140° CA at $\Phi=1$.

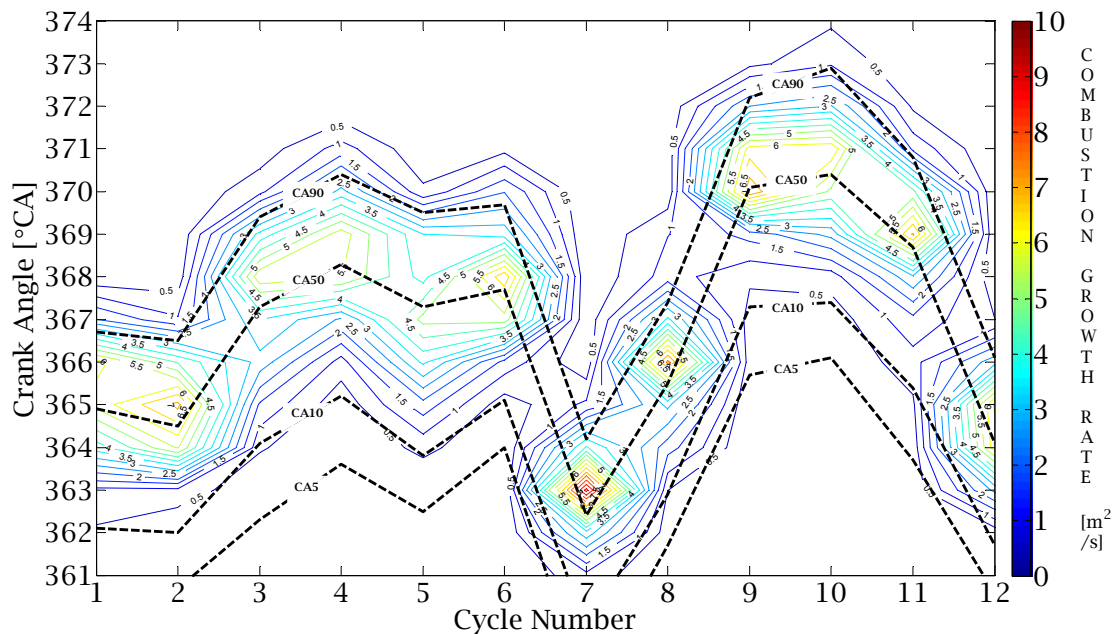


Figure 8.16. Distribution of expansion rates of burned areas in a relation to burned points of CA5, CA10, CA50 and CA90 for an imaged cycles of split gasoline injection with timing of 0/140° CA at $\Phi=1$.

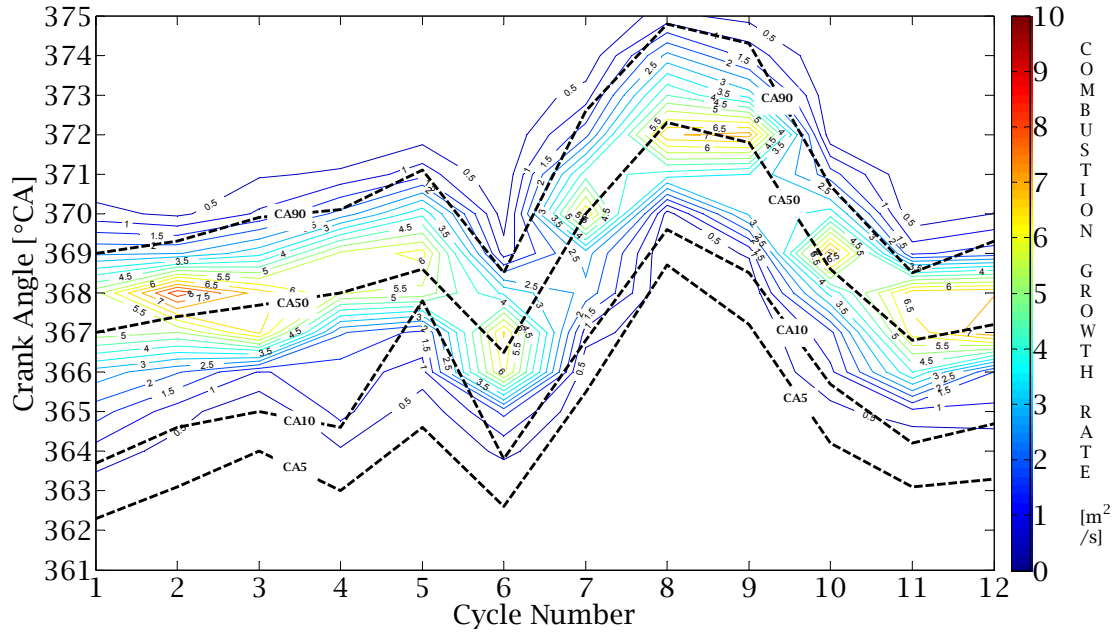


Figure 8.17. Distribution of expansion rates of burned areas in a relation to burned points of CA5, CA10, CA50 and CA90 for an imaged cycles of split gasoline injection with timing of 40/140° CA at $\Phi=1$.

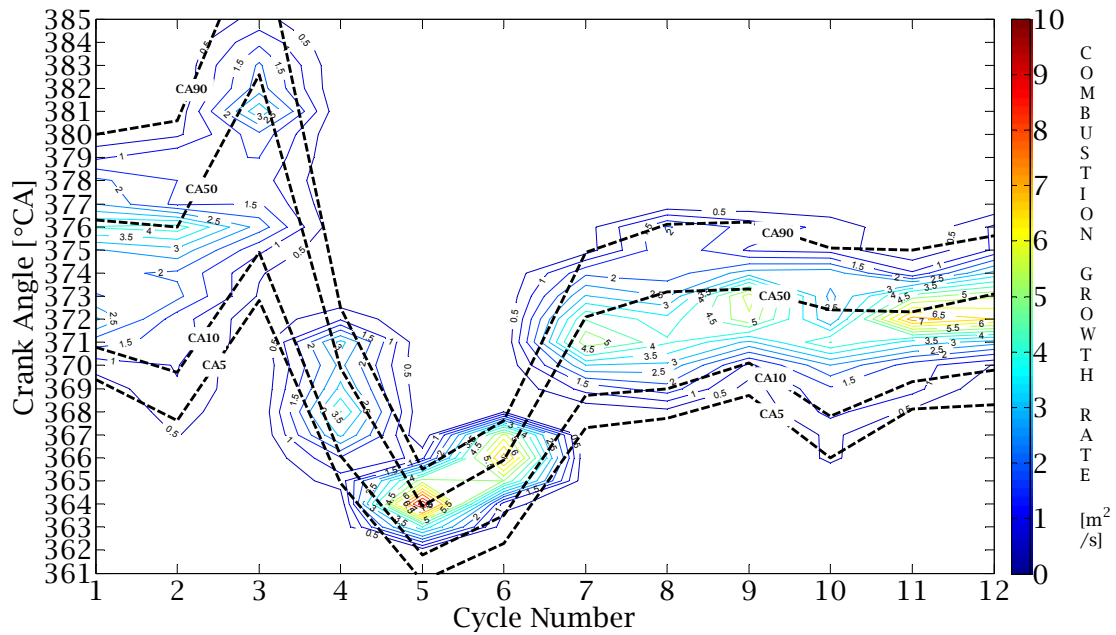


Figure 8.18. Distribution of expansion rates of burned areas in a relation to burned points of CA5, CA10, CA50 and CA90 for an imaged cycles of single gasoline injection with timing of 140° CA at $\Phi=1$.

It should also be noted here that this analysis is a planar one (2-D) with line-of-sight images, and real combustion should be considered as 3-D observations. Current study analysis results, more specifically the highest values of combustion growth rates obtained are in good agreement with the data of stoichiometric PFI combustion conducted in the previous chapter. However, the general expansion of the burned area rates seems to be slightly higher for investigated PFI stoichiometric than for any DI case presented in this study. As the engine operating conditions i.e. speed, intake air temperature, the valve timing event and fuel were the same as the previous chapter this would facilitate the making of the quantifiable comparison.

Under the lean operating conditions ($\Phi \approx 0.25-0.34$) when fuelling an engine with an isooctane/n-heptane blend Hultqvist *et al* (2002) observed estimated combustion growth rates in the order of $3.45 \text{ m}^2/\text{s}$. As the fuel-air ratio was low and studies were performed with different sorts of fuel it could clarify differences regardless of other factors and also constitute a reference point for the current study.

8.4 Analysis of PRF40 HCCI operation with various injection strategies and timings

The study presented in this section shows the influence of a split injection strategy on NVO and main autoignition-combustion activities with a PRF40 fuel blend. As in the previous section's analysis of the split injection strategy with a pilot injection occurring prior to TDC NVO has demonstrated significant discernible activities during the recompression stroke period and as importantly atypical colour and intensity for subsequent main autoignition-combustion, therefore this injection strategy was selected for further investigation in this section. Further, because split injection has shown negligible NVO activities or no primary activities when fuel is introduced into the TDC NVO this injection strategy was also chosen for an investigation in this section. Furthermore this selection was dictated by the fact that the

main autoignition-combustion activities demonstrated a similar character, more specifically colour and intensity in comparison to the other injection strategies studied, for instance excluding one when fuel is injected prior to TDC NVO. Although the same start of injection for both pilot and main pulses of split injection was used as well as the same duration of the pilot injection, the split ratio could have not been retained as for a gasoline study. It is an effect of fuel replacement that a main injection pulse width (as a selected pulse) must be prolonged in order to sustain the stoichiometric fuel-air equivalence ratio. Hence the split ratios estimated as a proportion of main injection to the pilot injection pulse widths were 2.93 and 2.2 for PRF40 and gasoline respectively.

Experimental results, grayscale ensemble-average images of the current study are included in Figure 8.19. Each ensemble-average image was composed of five individual images at a given crank angle degree coming from different cycles. The selected greyscale range provides accommodation for all the grey tones of the most intense images demonstrated, thereby showing the raw image data correctly. The highest value was assigned to the colour white and the weakest, zero luminosity to the colour black. This presentation of the images was done to enhance visibility.

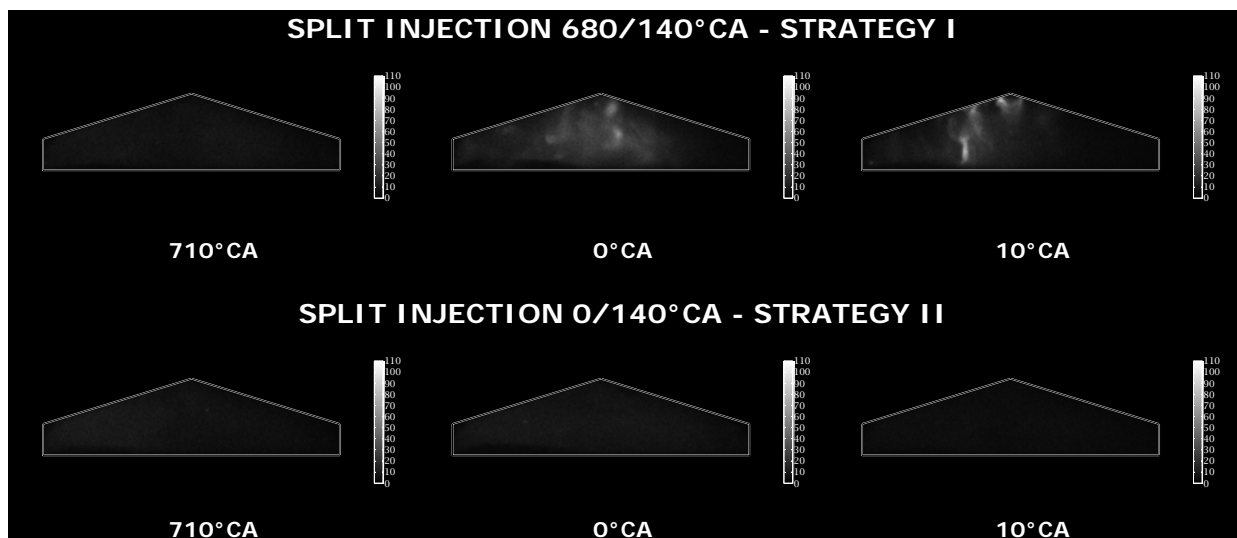


Figure 8.19. Monochromatic ensemble-average images of NVO with different injection timing and strategies. The individual images composing ensemble-average image were taken through the side view using iCCD camera.

The corresponding images of Figure 8.19 show the bright luminous activities of the split injection with a pilot injection occurring prior to TDC NVO. Furthermore, there are no distinct activities of the recompression stroke when fuel is introduced into the TDC NVO. These initial fundamental observations are in agreement with those of the previous section. By further analysing the corresponding images of Figure 8.19 in conjunction with the data about light emission quantification plotted in Figure 8.20 other observations could be made. Firstly, based on the images relating to a split injection strategy one can see that the potential activities, soot zones have a local rather than a global character. This is in fact further emphasised by the indications of mean values and their standard deviations (included as bars in the plot) and as importantly the high differences between maximum and mean values. In fact these indications suggest a non-uniform distribution of light emission within the imaged combustion chamber; which what consequently implies the existence of brighter and weaker light emitting areas. Because of this it is clear that the potential soot clouds appear and are formed locally. Secondly, as the incandescence of solid carbaceous particles starts to dominate by approximately 5°CA before TDC NVO (indeed for the injection scheme with fuel introduced prior to TDC NVO) and remains high for approximately another 25°CA as inferred in accordance with Figure 8.20. The similarities between this current section studies and gasoline investigations can be noted by tracking maximum magnitudes of Figure 8.20.

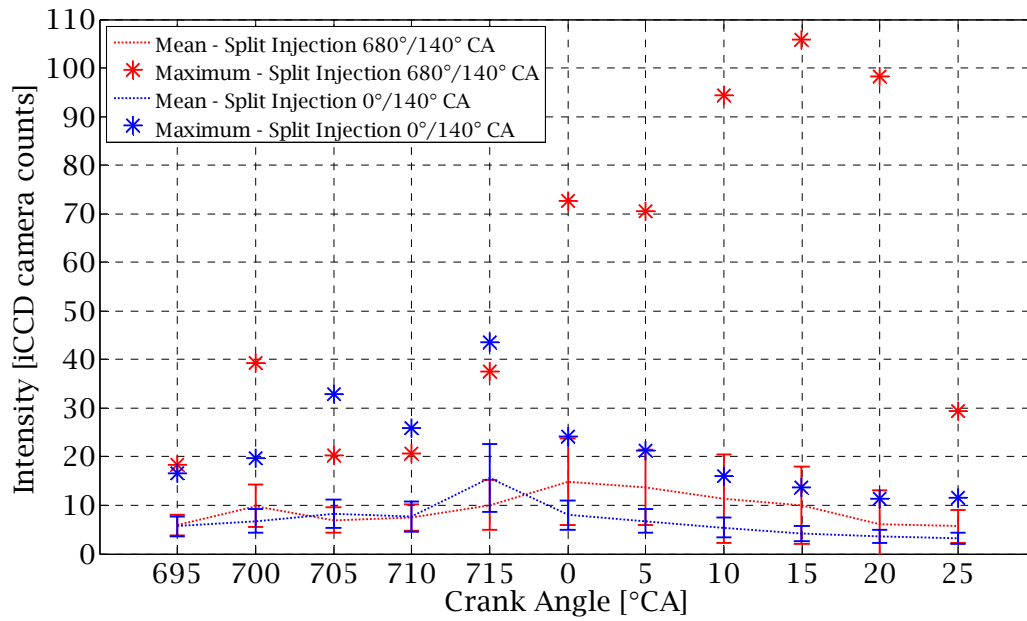


Figure 8.20. Quantification of natural light (radiation) emission intensity during the period of recompression stroke for split injections with pilot pulses at 680°CA and 0°CA.

Finally, when comparing the light emitted during the main combustion process plotted in Figure 8.21 for these two injection cases studied here, it appears that the combustion with potential soot oxidation (an injection strategy with a pilot injection at 680°CA) produced a higher luminosity than the combustion of a split injection strategy with a pilot injection occurring at 0°CA. However, differences or proportions in light emissions do not appear that are significant as in case of the previous section's observations. This is stated contrasting light emission of images combustion activities corresponding to CA10-CA90. This data presentation seems to be reasonable as each image acquired comes from a different cycle and experience variations in combustion onsets between cases. Therefore it is not profitable for the data to be shown and correlated strictly with on the crank angle basis. CA10 was chosen because it is the onset of HTHR phase (Hwang *et al* 2008). The finding that the disproportions between the light emitted during the combustion period are higher for split injections with pilot pulse at 680°CA than with pilot pulse at 0°CA when engine is fuelled with

gasoline rather than with PRF40 is not that surprising, as soot formation is highly fuel type dependent.

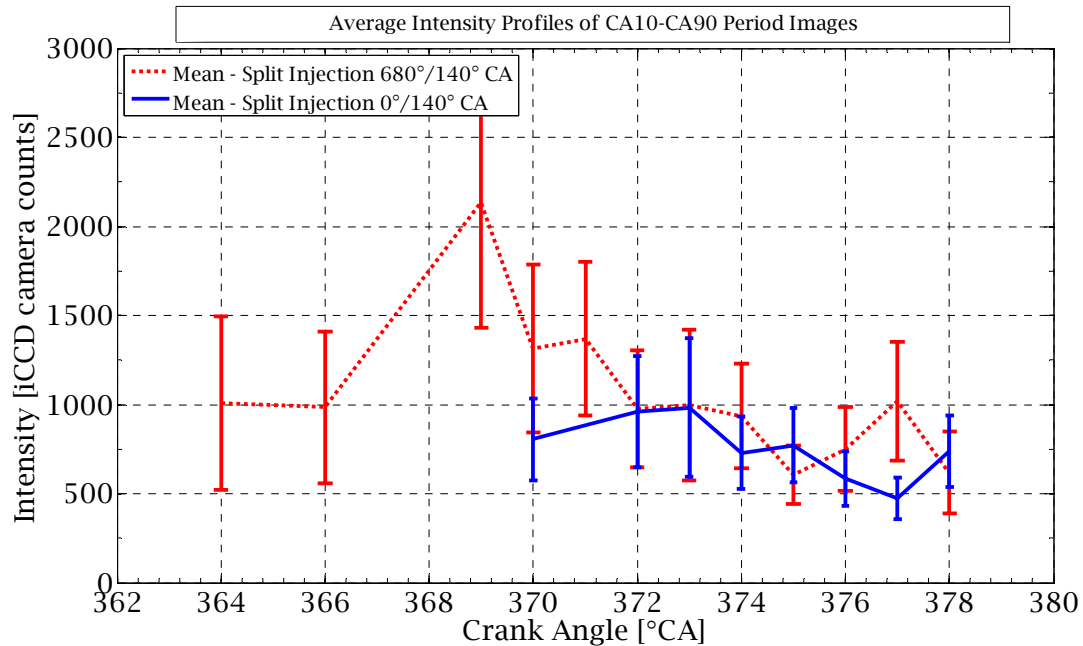


Figure 8.21. Quantification of natural light (radiation) emission intensity during the period of combustion within CA10-CA90 points region for split injections with pilot pulses at 680°CA and 0°CA.

Principally, the propensity of a fuel to soot formation increases with a higher carbon number in molecules; for a diesel fuel the soot formation is the most favourable for molecules with carbon numbers of 12 to 22 (Heywood 1988). Indeed soot formation is more favoured by aromatic hydrocarbons, is dependent on sulphur content (Dec *et al* 1998,2003; Price *et al* 2007; and Bartok *et al* 1991) and also increases with iso-paraffins in contrast to normal paraffins (Gaydon 1974). Because gasoline is a multi-component fuel containing hundreds of numbers of various hydrocarbons, as well as other non organic components a higher propensity to soot formation might be expected than for isooctane/n-heptane blends. In fact this might be responsible for the reduction in soot concentration in the case of PRF40 during the NVO period when gasoline was used with the split injection occurring prior to TDC NVO. As an effect of the reduced soot concentration the differences in quantifiable recorded light emission were lower compared to other injection strategies, for with instance use of PRF40

in contrast to gasoline. Nevertheless, besides the effect of fuel type the different split ratios and imagers might have contributed to these observations. The iCCD with a coupled lens utilised for imaging in the current study has broader spectral responsivities for covering the UV region than the CMOS imager does. As this is the case an additional radiation of UV has potentially been recorded, which might have contributed to the elevation of light intensity for the injection strategies investigated. In turn, this may have given a significant rise in the case of split injection with a pilot injection at 0°CA , and been masked by the soot oxidation in the case of fuel introduced into the TDC NVO. However, this above statement should only be considered as a hypothesis.

8.5 Spectra of NVO of PRF40 HCCI operation with different split injection strategies

Spectroscopic measurements were conducted to further understand the nature of the NVO activities, which are considered here as a potential source for significant changes in the behaviour of the autoignition-combustion process, which has been demonstrated. The recompression stroke spectra were captured in this section for two split injection strategies: one with a pilot injection at 680°CA and the other at 0°CA , fuelling the engine with a PRF40 blend. As the engine operating conditions and fuel are preserved the same as in the previous section, the images of the previous section are a good reference (correlation) for the spectroscopic measurements presented in this current section. Figure 8.22 demonstrates spectra taken at 710 , 0 and 10°CA for a split injection strategy where a fuel is introduced prior to TDC NVO. As start point of 710°CA for spectroscopic measurements was chosen based on the initial insight into the recompression stroke provided by imaging. It is thought that this is a time interval when the soot is formed, as no discernible activities (traces of incandescence) have been identified at this particular crank angle based on the images taken (see Figure 8.19, the image in the first row on the left side).

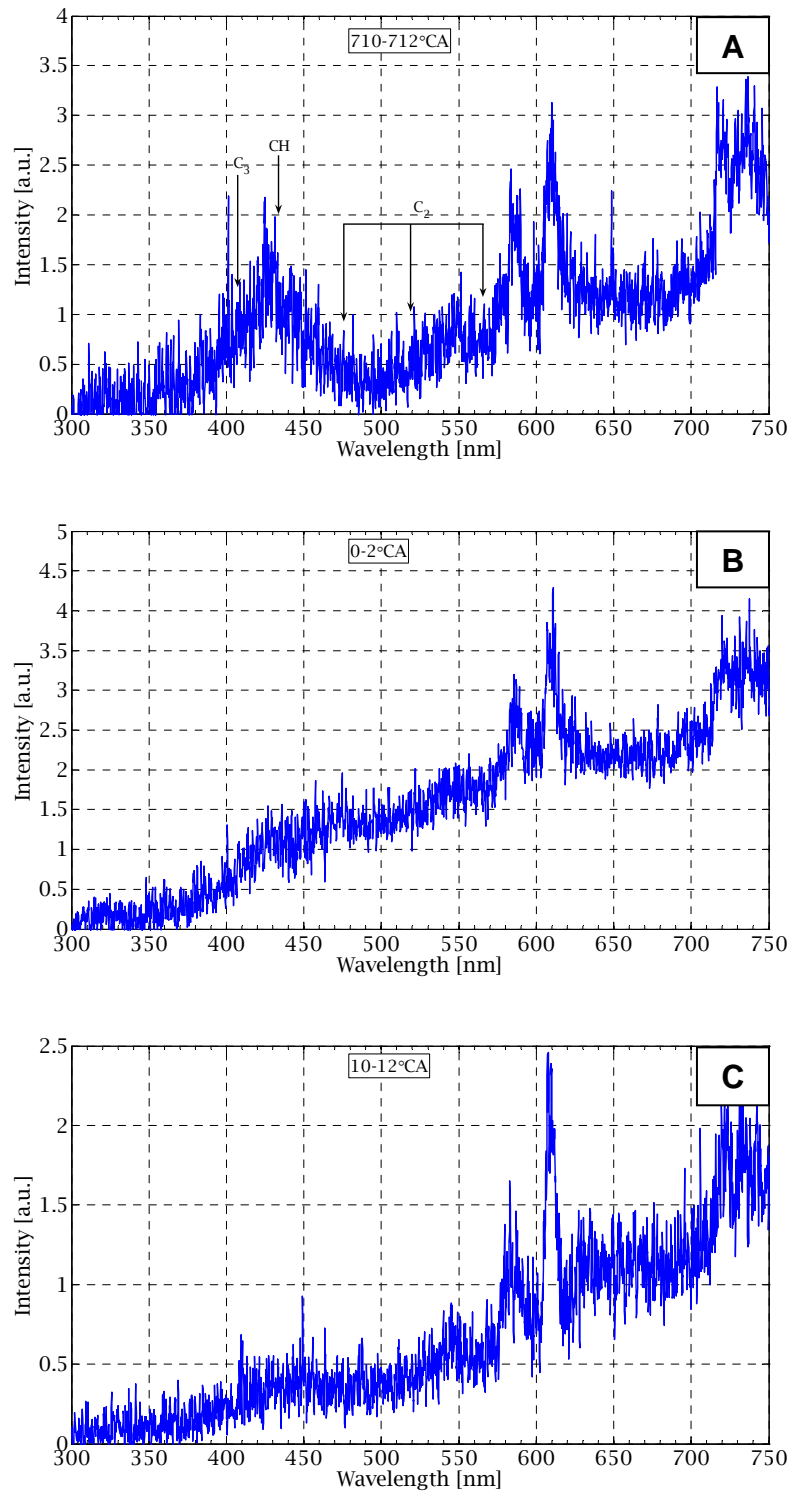
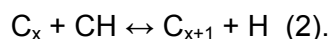
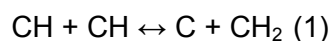


Figure.8.22. Spectra sequences for NVO period with split injection of pilot pulse at 680°CA for PRF40. Spectra sequences demonstrate activities at corresponding crank angles 710-712°CA (A), 0-2°CA (B) and 10-12°CA (C).

Spectra for a split injection strategy introducing fuel into the TDC recompression stroke are shown in Figure 8.23, for two crank angle degrees. This is because no activities were

identified during an NVO period for this injection strategy, which can be inferred from images included in Figure 8.22. Only two crank-angle periods were selected for a spectra acquisition, starting from the amount of fuel injection. As any light emission during the recompression stroke for a particular injection strategy was attributed to an incandescence of solid carbon particles, in this study great attention is paid to the identification of those species such as C_2 , C_3 and CH that contribute to or take part in soot formation. A comparison of the three spectra plotted in Figure 8.23, shows similar shapes (patterns) for the 0 and 10°CA spectra, however with different magnitudes. Furthermore these two spectra are different in shape to the one taken ten crank angles before TDC NVO. Starting from 710°CA spectra, the peak at around 430 nm is clearly observable. Indeed this appears as banded spectra, not pure line spectra. This was identified as a CH, having the strongest emission at 431.5 nm, with other heads degraded to 431.4 and 431.2 nm (Gaydon 1974). Also under some circumstances the CH might be observable as a band at around 390 nm (Gaydon 1974):. Further the triatomic carbon molecule (C_3) could also be identifiable at around 405 nm. C_3 normally appears as diffuse bands at the aforementioned wavelength position (Gaydon 1974). With regard to the currently discussed spectrum, the triatomic carbon molecule is overlaid in banded spectra, so it is difficult to distinguish its bands. Swan bands of the diatomic carbon molecule (C_2) are also pointed out, and C_2 are generally considered as a predecessor of soot formation. Surprisingly the CH emission appears as the most intense of the above identified species. These identified species would be consistent with the process of further soot formation.

Also, it is noteworthy that C_2 and CH are characteristic of an emission occurring below the zone of the yellow sooty luminosity region in rich flames (Gaydon 1974). The presence of CH could contribute to following reactions in accordance with Gaydon (Gaydon 1974):



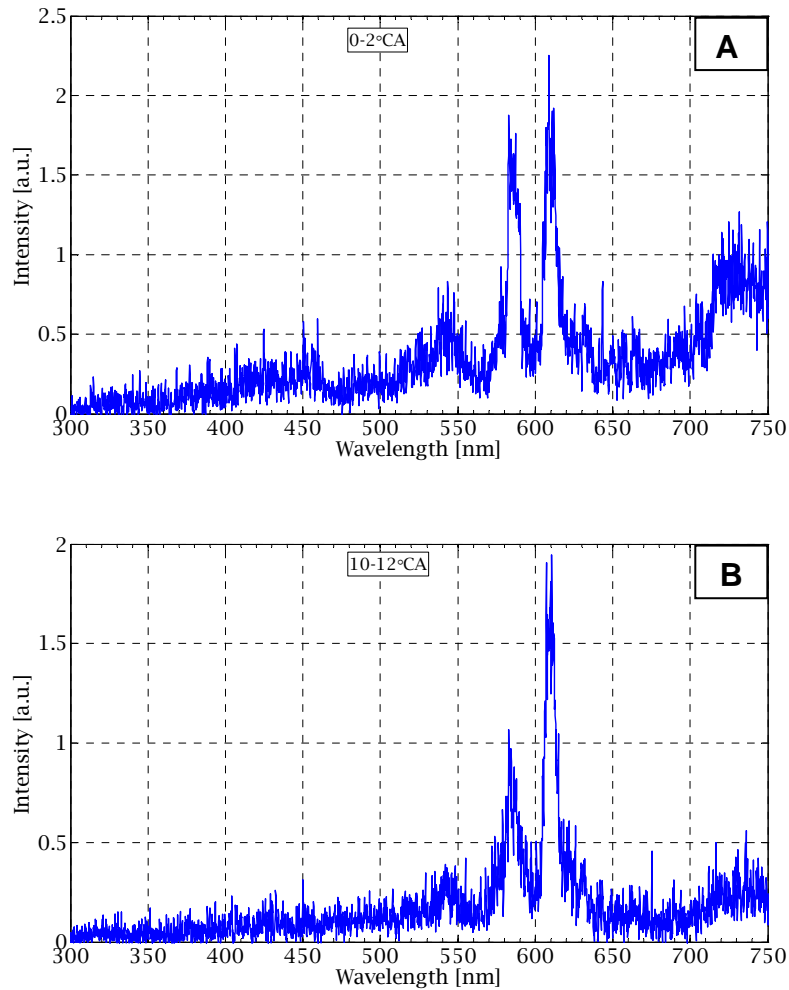
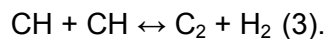


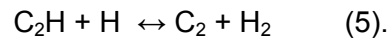
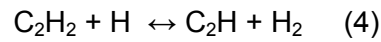
Figure 8.23. Spectra sequences for NVO period with split injection of pilot pulse at 0°C A for PRF40. Spectra sequences demonstrate activities at corresponding crank angles 0-2°C A (A) and 10-12°C A (B).

Nevertheless, it was observed in a flames study, that the concentration of CH was not high enough to be in charge of larger carbon particle formation (Gaydon 1974). Indeed this pathway presents an adequate way for both diatomic and triatomic carbon molecule formation. The other way the CH would contribute to the formation of C_2 and further soot is well described by the reaction:



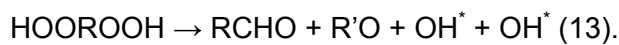
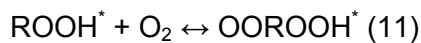
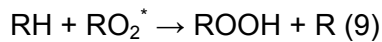
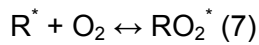
However, it is thought that this is CH, which is formed from the C_2 (Gaydon 1974) rather than the other way around. The other investigation conducted and presented in reference of Gaydon (Gaydon 1974) pointed out that the formation of CH requires oxygen, not just being

the result of the fuel molecule thermal breakdown process. Despite this, the peak of CH is distinguishable in this study. The presence of lines of diatomic and triatomic carbon molecules on the current discussed spectrum, clearly imply the soot formation during the recompression stroke. C₂ and C₃ lines are typical features of spectra of organic flames showing soot formation (Gaydon 1974 and others). The formation of soot, or more specifically soot precursors during the fuel molecule pyrolysis could proceed according to the following reaction as the molecule dehydrogenation:



This would be the case if the thermal fuel molecule break down would be capable of yielding the monatomic hydrogen.

Noteworthy of explanation here is that distinguishable peaks of CH are usually superimpose on Emeleus's cool flame bands (CH₂O), however the engine operating conditions (theoretically no oxygen presence during the recompression stroke) would clearly prevent the low temperature heat release reactions to occur during the NVO, as the initiation of reactions leading to cool flame activities (reactions 6-13), formation of formaldehyde require and oxygen to be presented:



Therefore, despite the potential temperature window conducive for low temperature heat release which might be encountered during the studied NVO, there is no potential for proceeding cool flames as no oxygen is available. Furthermore study of Hwang *et al* [30] indicated that the formaldehyde emission covers the range of 350-540 nm, with the distinctive peak around the 450 nm. Their observations reported apart the aforementioned fact further contradict that the banded spectra around the CH is affected by the emission of formaldehyde and therefore proceeding the cool flame. It is though that the wide banded spectra about the identified CH peak is due to band group of CH starting at 390 and prolonging to 431.4, 431.5 and 431.2 nm. Also the rise could have been given by identified C₃.

The spectra of 0 and 10°CA (Figure 8.22 B and C) are greatly dominated on the continuum. The continuum spans entirely over the spectral region recorded, with different intensities. These continuum spectra, which in fact were caused by thermal radiation emitted by solid materials i.e. solid carbon particles (Dec *et al* 1998, Gaydon 1974, Skoog *et al* 2001) further confirm the presence of soot in the NVO at these particular crank angle periods and as importantly for the injection strategy studied. Different intensities for these 0 and 10°CA spectra, most likely were caused by the influence of a temperature on solid carbon particles influence, as with the increase of the temperature the peak of thermal radiation is shifted towards shorter wavelengths. This might be the case with the higher in-cylinder gas temperatures. Therefore, solid carbon particles (in this case) are essentially expected at TDC NVO. Contrary to the observations currently made, spectra plotted in Figure 8.23 for a split injection strategy when fuel is introduced into TDC NVO, show neither CH, C₂, or C₃ lines when fuel is injected prior to TDC; and nor the continuum spectra is a result of the incandescence of solid carbon particles. It should be clearly said that for both split injection strategies investigated here, spectra constantly show two distinct peaks around the 585 and 610 nm, which have remained unidentified in this study. As the entrapped residuals possess not only stoichiometric combustion products but also other species it is thought that the thermal excitation of the given species could have contributed to this emission.

As a reference to the current study's observations, Dec *et al* (1998) noted a high continuum spectrum for the sooty diesel combustion process, for which the incandescence of the sooty particles dominated. Obviously the intensity of incandescence in their study for a low wavelength spectral region could have been much higher than in our case as a combination of both diesel fuel better propensity to form soot and a higher in-cylinder temperature (near flame temperatures). Similarly they observed that the CH emission was higher than the corresponding C₂ emission. Running engines under lean operating conditions with isooctane and n-heptane or pure isooctane blends with well premixed conditions Hwang *et al* (2008) and Hultqvist *et al* (1989) observed no diatomic carbon band emission on the acquired spectra of the HCCI combustion process. Hultqvist *et al* (2008) *inferred* that their observations were in agreement with the engine emission featuring negligible PM emissions. Hwang *et al* (2008), concluded that the lack of C₂ often, attributed as a soot predecessor, had to do with engine operating conditions studied, which disfavoured its formation.

8.6 Summary

An investigation which characterises the influence of injection strategy and timing on the autoignition-combustion of HCCI as well as the activities of the recompression stroke was carried out. The comprehensive examination of injection strategy covered the split injection and single injection strategies. With a split injection strategy, fuel was injected with different phasing into the negative valve overlap period via a pilot injection pulse and the main injection was set to occur at an introduction stroke. The single injection strategy was set to correspond to the timing of the main injection of the split injection. The study was conducted with the optical engine, which was operated at a stoichiometric fuel-air ratio, a constant engine speed of 1000 rpm and a significant constant negative valve overlap period. Comprehensive studies conducted could be divided into two parts from a fuel standpoint, as initial research was accomplished with standard gasoline and further insights were gained by

using the blend PRF40. Within this study only passive optical techniques were used, imaging and spectroscopy. Hence the comprehensive study involved the application of three diagnostic instruments: the Complementary Metal-Oxide Semiconductor (CMOS) high-speed colour imager, the intensified Charge Couple Device (CCD) and the imaging spectrograph. Furthermore, particular image processing techniques were applied to the obtained data in order to extract relevant information.

A natural light emission of autoignition-combustion activities has been observed different when fuel is introduced prior to the TDC recompression stroke in comparison to the other injection strategies investigated, including the one when fuel is injected at TDC NVO. This particular split injection strategy with pilot injection occurring prior to TDC has shown autoignition-combustion activities dominated by a bright yellowish colour emission, while the other injection strategies studied have depicted a consistent dark bluish colour emission during the same period. Furthermore very bright light emission intensity was identified, which persisted for a long period of time, approximately 25°CA for the NVO activities of the split injection when the pilot injection occurred prior to TDC NVO. The split injection strategy, where fuel is injected at the TDC negative valve overlap has not exhibited the significantly discernible activities of the TDC NVO. Only minor activities were identified.

Spectroscopic measurements conducted of an NVO have shown the continuum spectra during a particular crank angle of the NVO period, when fuel is injected prior to TDC NVO. Also prior to this crank angle some traces of C_2 , C_3 and CH could have been identified by a spectrum. This is because of the spectroscopic results and the aforementioned observations. It is though that this is soot formation during the NVO, and its incandescence, which emitted the recorded light. The soot formation during the NVO could be the product of a thermal breakdown (pyrolysis) of fuel molecules, into hydrogen and carbon. As this happens further autoignition-combustion behaviour, i.e. colour and intensity is due to soot combustion.

The assessment of the autoignition and combustion likelihood of repeatability has not revealed significant differences among the cases and generally yielded the same tendency to repeatability with the similar identified preferential locations for an autoignition to occur.

Expansion growth rate areas were showed similar magnitudes, at least the greater magnitudes.

Chapter 9

Conclusions and Future Work

9.1 Conclusions

Optical and thermal single cylinder engines were established in a Jaguar V8 like configuration. Injection-ignition controlling software was adopted, and further marginally modified for more demanding requirements. The code managing the position of camshafts (the variable valve timing system) was built and combined with electronics to control the camshaft phasing as a closed loop feedback. Then two data acquisition systems were developed and implemented for each engine. All the aforementioned codes for the controls and the data acquisition system have been written (developed) in Labview® graphical programming language.

9.1.1 The development of image processing techniques for an HCCI autoignition-combustion analysis

Three relevant image processing techniques were implemented to study the autoignition-combustion characteristics based on optical data, more specifically to extract the information about autoignition-combustion from the images.

The first technique, which allows the assessment of the likelihood of the probability of the occurrence or development of autoignition and combustion, was entirely devised by the author of this thesis. This procedure was named *Autoignition Occurrence and Combustion Development Pattern Likelihood of Repeatability Technique*. In summary this method is

based on the analysis of pixel intensity distribution (a normalised histogram) of an ensemble image. The ensemble image is made up of a number of single images captured at a certain crank angle degree. These images are in the form of binary images, in which values of 1 are assigned to the autoignition-combustion areas and values of 0 to the non autoignition-combustion areas. Therefore, after adding these single images the ensemble image contains gray level values possibly spanning in range from 0 to the number of individual images taken for an analysis. By applying statistical descriptors (moments) such as expectance, variance, skewness and kurtosis, the mean grey level, the data spread and the shape of the normalised histogram of ensemble image are determined. A correlation between these statistical indicators in relation to the autoignition-combustion areas provides an insight into the tendency of the repeatability process. The limitations of this technique are that it uses time-resolved data and therefore does not account for any crank-angle variations in the combustion onset. Also as this method is based on a statistical analysis of the ensemble image of a normalised histogram, the sizes and shapes of the autoignition-combustion areas are relevant and do matter.

The second method providing insight into combustion behaviour is straightforward procedure that numerically differentiates burned area(s) i.e. the *Expansion Rate of Burned Areas*. Therefore, this quantifiable insight was accomplished by estimating the expansion rate of burned areas. This technique was not totally new, and as stated in section 5.4.4.2, constitutes one of a few steps required to compute speed analysis for a spark ignited combustion process within a comprehensive mean flame front expansion. This method was adopted for the first time in an HCCI combustion analysis by Hultqvist *et al* (2002).

The reacting structures front spreading velocities constitute the third and final image processing method used for the optical data analysis in this thesis. This developed reaction front spreading velocity method was developed to derive burning zone front local velocity magnitudes along the reaction(s) contour(s), and as importantly to get mean velocities. This quantifiable procedure could be seen as a modified version of firstly shown one by Hultqvist

et al (2002), however, with significantly different approaches which allowed local values to be estimated.

It is important to note here that as the methods and the comprehensive image processing analysis were written and conducted in Matlab® language, their computational steps were addressed in relation to general image processing foundations and also to those aspects available and offered by a Matlab® programming environment. This concerns the different image object area and distance calculations available, and has a great impact on the obtained results. This theme was also addressed in great detail in this thesis, in sections 5.4.2 and 5.4.3.

9.1.2 Analysis of the nature of HCCI autoignition and combustion

The characteristics of the autoignition and combustion of an Homogenous Charge Compression Ignition engine were defined and presented under various engine operating conditions using different fuels. To start with, existing literature was reviewed to show the background of the combustion process via autoignition, and the importance of fuel molecule type on the process. This provided an insight into current terminology in HCCI autoignition-combustion process classification.

By selecting a potentially two-step ignition fuel, a blend of PRF40 and running the engine under various engine speeds and trapped residual rates it has been shown how these engine operating variables contribute to an autoignition-process type. To observe the influence of one variable the other was kept constant, thus isolating one from the other. For instance, when the effect of speed was investigated the fraction of trapped residuals was kept constant and vice versa. These investigations showed the suppressive effect on cool flame activities of the two-stage ignition process when engine speed or the rate of trapped residuals increases. As this is the case, the transition from a two- to a one- step ignition process has been identified under particular engine operating conditions either at higher

engine speeds or elevated rates of trapped residuals or as a combination of both. These conditions were determined not favourable for a two-step ignition process to occur.

A physicochemical insight into the one- and two-step ignition process in an optical engine operated in HCCI mode was gained by recording the images and spectra, and by a further analysis of the optical data. Images have shown that the light emission intensity of the two-step ignition process is higher at low temperature heat release than at the one-step ignition process at the corresponding stage. This is apparent as a one-step ignition process might not exhibit light because the air-fuel charge does not traverse this phase. Furthermore, a quantifiable analysis of light emission has shown that the light emission during the LTHR is significantly lower at around 100 magnitudes than the light during the main combustion period (HTHR). Spectra taken for corresponding phases have shown that cool flame activities are dominated by a formaldehyde emission, and the main combustion period by hydroxyl radicals.

Finally, knowing the nature of the process and the influence of engine operating conditions and fuel type based on the experimental work and literature review, experiments were undertaken to gain an understanding of the role of fuel octane rating and octane sensitivity in an HCCI operated engine. This was accomplished by fuelling a thermal engine with two reference fuel blends of different RONs and MONs values. It was found that their RONs and MONs values scale well with the magnitudes of the cool flame activities they exhibit under the engine operating conditions investigated. It is thought that the differences in the magnitudes of the LTHR derive from volumetric differences in the reactive n-heptane, as contributing to the LTHR between these blends. Tests clarifying the effect of octane fuel sensitivity were conducted by using the nonsensitive Primary Reference blend and sensitive Toluene/n-Heptane blends, of the same RONs and different MONs. To examine the potential sensitivity impact, this was performed under different intake air temperatures. The major finding was that at a low intake air temperature (charge temperature) the magnitude of the cool flame activities was nearly the same, however, at an elevated intake temperature their magnitudes were found to be different, the one for a TSF was higher than the one for PRF.

This correlated with the currently well known toluene inhibitor effect; and it seemed that this effect was temperature dependent. As a consequence it is thought that it is an effect of fuel octane sensitivity between these blends.

9.1.3 Analysis of the premixed HCCI based on high-speed imaging

To gain insight into the formation and development of autoignition and combustion in an HCCI premixed operation, high-speed crank-angle resolved images were taken. The study was conducted at stoichiometric as well as lean engine operational conditions. The interpretation of obtained images was based on an application of the three image processing techniques which were introduced in section 5.4.4. Therefore, discussions were concentrated on an analysis of the identification of the first autoignition sites, their likelihood of repeatability, combustion development pattern, expansion rate of burned area(s) and burning structures front spreading velocities.

It was observed that at both air-fuel charge stoichiometries the likelihood of the repeatability of the occurrence at the initial stage is quite poor and therefore it is thought that the first identified autoignition areas have a random occurrence character, considered as a spatial character. Further as combustion developed, the likelihood of repeatability gradually increased as a consequence of a greater combustion chamber area becoming enflamed. Despite the poor global process likelihood of repeatability at the initial stages, the preferential location for an autoignition to occur was identified. This was an area corresponding to the, or being observed as, the space underneath the exhaust valve region.

With the analysis of combustion growth rate, it has been noticed that the expansion rate of burned area(s) at the stoichiometric fuel-air ratio is higher than at the lean engine operating conditions. The estimated maximum values at $\Phi=1$ were approximately $10 \text{ m}^2/\text{s}$ and at $\Phi \approx 0.83$ they were $\approx 7 \text{ m}^2/\text{s}$. A similar observation was made by comparing the combustion growth rates at the initial stages. Finally, different patterns of combustion growth rate

distributions were noted between these two cases for the same heat release rate points windows, specified as CA10-CA50.

The analysis of reacting structures fronts spreading velocities has generated the quantifying insight into the local values along the contours and the mean values at different analysed autoignition and combustion stages. The effect of mixture strength was pronounced at each investigated autoignition or combustion stage investigated. It was found that at the initial stage of combustion the reacting structures spreading front velocities could reach up to 55 with a mean of 16 m/s at $\Phi=1$ and up to 35 with a mean of 14.5 m/s at $\Phi\approx 0.83$. At developed combustion stage, values of the velocities were greater and could reach up to a mean of 31.2 m/s with local values of 110 m/s for $\Phi=1$.

9.1.4 A characterisation of HCCI operation with different direct injection strategies and timings

An analysis of a direct injection Homogeneous Charge Compression Ignition operation under different injection strategies and timings was conducted based on acquired data from passive optical methods. Therefore, experimental investigational study involved high-speed colour imaging, imaging using an intensified camera (monochromatic images) and spectroscopic measurements.

When fuelling an optical engine with a commercial gasoline, and introducing fuel as a split injection strategy with a pilot injection pulse occurring at 40°CA prior to TDC NVO, the yellowish bright light emission of main autoignition-combustion activities has been noted. This was observed as contrary to the other injection strategies investigated, split and single injection strategies for which their main autoignition-combustion activities were consistently shown with a dark bluish light emission. This was even the case for an injection strategy when a pilot injection was introduced at the TDC recompression stroke. Further analysis with regards to NVO activities has shown bright light emission intensity persisting for

approximately 25°CA when some quantity of fuel is injected prior to TDC NVO. No such comparable or discernible activities were noted for a case when fuel was introduced at the TDC recompression stroke. Since the spectra taken at these points (activities) have shown a continuum spectrum with preceding spectrum for which the C₂, C₃ and CH are identifiable it is thought that this is soot formation during the NVO and its incandescence causes the light emission. At stoichiometric engine operating conditions and high temperatures, the soot can be formed as an effect of the pyrolysis of fuel molecules, a thermal breakdown into hydrogen and carbon. Furthermore, it is thought that this yellowish bright light intensity was due to a dominance of soot oxidation at this stage as conditions became favourable. This finding is highly corroborated within the literature review of other HCCI investigations and as importantly in diesel studies about the features of sooty combustion.

Further analysis is concentrated on the application of image processing methods to obtain the information in the interest of the study. It should be said that the assessment of autoignition and combustion likelihood of repeatability has not revealed significant differences among the injection strategies and timings cases investigate. Generally at corresponding stages of autoignition and combustion this analysis has shown a similar value for the likelihood of repeatability. The identified preferential autoignition locations for an occurrence seem to be the same for all the cases investigated. Estimated rates of the expansion of burned areas showed similar magnitudes, at least the greatest magnitudes. In comparison to premixed combustion growth rates, these magnitudes are similar in values; presumably this is because the mixture strength is preserved.

9.2 Suggestions for future work

A clear area for future work seems to concern the further development of current image processing techniques presented here and the elaboration of more advanced new ones.

Then to carry out a further research, which will constitute a continuation of the current work covered in this thesis would be profitable.

In particular, the likelihood of repeatability tracking technique could be modified to a more advanced version as the area of probability provides the opportunity for a great variety of analyse to be conducted. A suggested future version could assess the probability of occurrence in a given combustion chamber area, by dividing the imaged combustion chamber area into smaller subzones with the sizes as small as the potential size of a pixel. It is thought this would give an indication of the likelihood of repeatability with an automatic identification of preferential zones across the combustion chamber. Also more recommendable is a kind of statistical analysis based on a greater number of points (data) available, more specifically on individual images taken into the creation of an ensemble image. This itself in fact would yield more reliable outcomes.

Investigations leading to an understanding of the relevance of current fuel octane number designations and octane fuel sensitivity should involve the usage of higher component number fuels. However, initially and as a continuation of current work octane sensitivity should be further examined for more Toluene Standardisation Fuels and Primary Reference Fuel blends to obtain a comprehensive *spectrum* into the role of the toluene inhibitor effect. This should be conducted also under a wider range of engine operational conditions. The application of simulation is definitely a powerful tool in understanding obtained results and chemical kinetics. This could presumably be performed within Chemkin software as the best choice.

Interesting research seems to be conducted with regard to the in-cylinder temperature estimations under those operating conditions where soot is presented. Therefore the combustion temperatures and even recompression stroke gas temperature could be approximated. Soot formation might be favoured by stimulating the engine operating conditions as a rich air-fuel charge or even as at late injection strategy. Then the application of the pyrometry technique to the thermal radiation emitted by glowing soot particles should constitute a good temperature indicator, in reference to the actual in-cylinder temperature

when first calibrated. Moreover this might show local indications of temperature within the combustion chamber when the thermal radiation emitted is considered locally across the combustion chamber.

Appendix A - Fuel Data

Fuel	ULG 95	PRF40	PRF75.6	PRF80	PRF75.6
Composition Characteristic					
Paraffins (normal+iso) 2,2,4 Trimethylpentane / N-Heptane	48.26 % vol. - / -	100 % vol. 40 / 60 % vol.	100 % vol. 75.6 / 24.4 % vol.	100 % vol. 80 / 20 % vol.	42 % vol. 0 / 42 % vol.
Olefins	16.2 % vol.	0 % vol.	0 % vol.	0 % vol.	0 % vol.
Napthenes	3.66 % vol.	0 % vol.	0 % vol.	0 % vol.	0 % vol.
Aromatics	30.2 % vol.	0 % vol.	0 % vol.	0 % vol.	58 % vol.
Toluene	unknown	0 % vol.	0 % vol.	0 % vol.	58 % vol.
Others	1.68 % vol.	0 % vol.	0 % vol.	0 % vol.	0 % vol.
C Atoms (Equivalent Molecule)	6.37	7.4	7.756	7.8	7
H Atoms (Equivalent Molecule)	11.68	16.8	17.512	17.6	11.36
Anti-knock (Autoignition) Characteristic					
RON (ASTM D 2699)	95.8	40	75.6	80	75.6
MON (ASTM D 2700)	84.9	40	75.6	80	66.9
Fuel Sensitivity (RON-MON)	10.9	0	0	0	8.7
Antiknock Index (RON+MON/2)	90.35	40	75.6	80	71.25
Distillation (Volatility) Characteristic					
Boiling Point	-	98.4°C (C ₇ H ₁₆) 99.3°C (C ₈ H ₁₈)	98.4°C (C ₇ H ₁₆) 99.3°C (C ₈ H ₁₈)	98.4°C (C ₇ H ₁₆) 99.3°C (C ₈ H ₁₈)	98.4°C (C ₇ H ₁₆) 110°C (C ₇ H ₈)
E70 (ISO 3405:88)	36.1 %vol.	-	-	-	-
E100 (ISO 3405:88)	53.5 %vol.	-	-	-	-
E120 (ISO 3405:88)	65.7 % vol.	-	-	-	-
E150 (ISO 3405:88)	86 %vol.	-	-	-	-
E180 (ISO 3405:88)	95.8 %vol.	-	-	-	-
RVP (ASTM323:08)	98.4 hPa	-	-	-	-
Other Properties					
Density @ 15°C	738.7 kg/m ³	685 kg/m ³	687 kg/m ³	687 kg/m ³	790 kg/m ³
Molecular Weight	≈ 110	105.6	110.58	111.2	95.6
Stoichiometric Air-Fuel Ratio	14.6	15.16	15.124	15.12	14.2
LHV	44 MJ/kg	44.46 MJ/kg	44.36 MJ/kg	44.35 MJ/kg	42.26 MJ/kg
HHV	47.3 MJ/kg	47.97 MJ/kg	47.87 MJ/kg	47.86 MJ/kg	44.84 MJ/kg
Enthalpy of Vaporization	305 kJ/kg	305.6 kJ/kg	296.3 kJ/kg	295.2 kJ/kg	372 kJ/kg

Table A-1. Fuel Data (Data taken from Owen and Coley 1995).

Appendix B

Image Thresholding Techniques

The thresholding is a method distinguishing and separating image object(s) from background by specifying predetermined threshold level. The image's pixels are separated into two classes – pixels of object(s) and background based on their intensities value and criterion (threshold) set. Thresholding methods could be classified as following:

1) Global thresholding (single level threshold)

The threshold level is determined for an entire image or region of interest in global thresholding methods. The only one single threshold level is then used to separate the object(s) from the background.

2) Local thresholding

The entire image or region of interest is divided into subimages or subregions and the threshold levels are defined for each individual subimage (subregion). Consequently a number of threshold levels are determined corresponding to number of subregions created. Each subimage is then segmented using a corresponding threshold level.

3) Adaptive thresholding

The threshold level is specified for each individual pixel at any image coordinates (m,n) based on the predetermined neighbourhood size around the analyzed pixel.

4) Global thresholding (multi level thresholding)

A number of threshold ranges are determined for an entire image or region of interest. If the pixel intensities at any coordinates in an image falls into given range the pixel is assigned either an object or background values.

Four thresholding procedures introduced here are global single level thresholding methods. Mathematically this could be described as follows:

Thresholding Greyscale Image

to Greyscale Image

$$\text{if } T \geq M(m,n) \quad M'(m,n) = M(m,n)$$

$$\text{if } T < M(m,n) \quad M'(m,n) = 0$$

to Binary Image

$$\text{if } T \geq M(m,n) \quad M'(m,n) = 1$$

$$\text{if } T < M(m,n) \quad M'(m,n) = 0$$

where:

T - determined and specified threshold level,

$M(m,n)$ - analysed image or region analyzed image region of interest,

$M'(m,n)$ - resultant, thresholded image.

Triangle Algorithm based on Histogram

This method is based on straightforward comparisons of distances, which are measured as perpendicular lines from the line joining the histogram peaks of maximum and the minimum histogram. Preliminary the line linking histogram maximum and minimum is constructed. Then distances for each grey scale level pixel numbers presented in histogram are estimated. The lengthiest distance indicates the threshold value being a grey level value corresponding to one marked by this line.

Otsu Technique

The image thresholding technique developed by Otsu is founded on 1st statistical common moments – means – global and local and uses global and interclass variances - 2nd central statistical moments. This is because the normalised histogram provides a probability of occurrence information for each of the grey-level constituting an image, the first step in Otsu thresholding technique algorithm could be obtained directly from a normalised histogram:

$$p_i = \frac{n_i}{n}; \quad i = 0, 1, 2, \dots, L-1 \quad \text{Eq.1}$$

n_i – number of pixels having given (the same) grey – level in an analyzed image,

n – total number of pixels in an analyzed image,

i – random variable corresponding to gray level,

L – possible number of grey levels i.e. 256.

$$\sum_{i=0}^{L-1} p_i = 1; \quad \text{Eq.2}$$

With data at hand regarding the grey-level probability of occurrence, the measure of the average grey level of a scrutinised image is straightforwardly obtainable from the calculation of a global first common statistical moment – according to Equation 3.

$$\mu_T = \sum_{i=0}^{L-1} i \cdot p_i; \quad \text{Eq.3}$$

At this stage the technique requires the initial threshold value to be defined dividing image pixels into two classes, it could be said that one class is the image pixels subset belong to background and another pertaining an object. The probability of occurrence and the average grey level (local means) determinations for these two classes are worked out using following equations:

$$P_0 = \sum_{i=0}^T p_i; \quad \text{Eq.4}$$

$$P_0 = P_T;$$

$$P_1 = \sum_{i=T+1}^{L-1} p_i; \quad \text{Eq.5}$$

$$P_1 = 1 - P_T;$$

$$\mu_0 P_0 = \sum_{i=0}^T i \cdot p_i; \quad \text{Eq.6}$$

$$\mu_1 P_1 = \sum_{i=T+1}^{L-1} i \cdot p_i; \quad \text{Eq.7}$$

$$\mu_T = \mu_0 P_0 + \mu_1 P_1;$$

As evidently noticed i.e. Equations 6 and 7 the average grey level for an each class forms (are computed as) a local first statistical moment. Subsequently the local variances - σ_0^2 and σ_1^2 , the interclass variance σ_B^2 and the global second statistical moment σ_T^2 are defined. The equations determining them are shown below:

$$\sigma_0^2 P_0 = \sum_{i=0}^T (i - \mu_0)^2 p_i; \quad Eq.8$$

$$\sigma_1^2 P_1 = \sum_{i=T+1}^{L-1} (i - \mu_1)^2 p_i; \quad Eq.9$$

$$\sigma_B^2 = P_0 (\mu_0 - \mu_T)^2 + P_1 (\mu_1 - \mu_T)^2 = P_0 P_1 (\mu_0 - \mu_1)^2 \quad Eq.10$$

$$\sigma_T^2 = \sum_{i=0}^{L-1} (i - \mu_T)^2 p_i \quad Eq.11$$

$$\eta = \frac{\sigma_B^2}{\sigma_T^2} \quad Eq.12$$

From the above stated it is apparent that the probability of occurrence of grey-level constituting an image – Eq. 1, the global mean - Eq. 3 and global variance - Eq. 11 are constant values for a given analysed image. Because this technique is fundamentally based on the determination of the maximum interclass variance value, the equations no 4 to 12 are repeated for a number of time with different initial thresholding values where maximum number of iterations equals to the number of grey levels presented in an analysed image.

The maximum value of σ_B^2 $\arg \max_{0 < T < L-1} \eta(T) = \arg \max_{0 < T < L-1} \sigma_B^2(T)$ over the initial thresholds

investigated defines the threshold value found at this maximum interclass variance.

Gray-level Gradient Technique

An essential approach in defining a threshold value using a grey-level gradient technique is the creation of gradient modules derived from operations performed on a nearest neighbourhood (grey level distribution) within an analyzed pixel for all the pixels in the region of interest. Hence the size of the gradient modules array is identical in its dimension to the

analyzed image or image region of interest spatial resolution. The gradient module value at any location (m,n) is obtained based on arithmetical operations performed on the four neighbours grey level values, two vertical and horizontal elements surrounding analyzed pixel at the location (m,n) of the input image. The gradient module is computed as a:

$$GMofM(m,n) = \max\{|M_m(m,n)|, |M_n(m,n)|\} \quad Eq.13$$

$$M_m(m,n) = M(m+1,n) - M(m-1,n) \quad Eq.14$$

$$M_n(m,n) = M(m,n+1) - M(m,n-1) \quad Eq.15$$

$GMofM(m,n)$ – gradient module of the input image array pixel at (m,n) location,

$M_m(m,n), M_n(m,n)$ – constituents of a gradient module.

Then threshold value is defined via formula:

$$T = \frac{\sum_m \sum_n M(m,n) \cdot GMofM(m,n)}{\sum_m \sum_n GMofM(m,n)} \quad Eq.15$$

Although this method is quite simple, there is one obvious hurdle associated with this technique which needs to be resolved before this technique is implemented to estimate a image threshold value. This regarding grey-level values assignment to the gradient modules which lie on the border of region of interest and determination the elements being a potential neighbourhood. Figure B-1 illustrates various possible pixels locations and their potential 4 (horizontal and vertical) neighbours. Array element (6,6) constitute a *classical* location with four neighbours, the gradient module's constituents can be computed based on the procedure specified above.

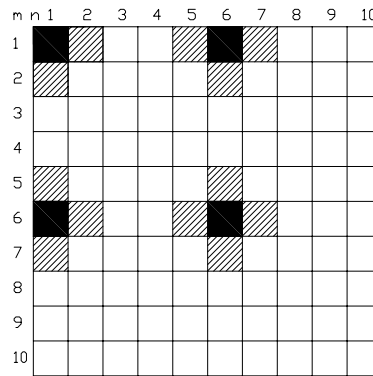


Figure B-1. The array (image) representative illustration with different elements (pixels) locations.

The thing becomes more complicated with border pixels (1,6) and (6,1) surrounded by total number of three vertical and horizontal neighbours. For this case the gradient module was evaluated using the one constituent calculated according to the equation 14 or 15 and another was assigned a grey-level value corresponding to the single neighbour surrounded the pixel in a given coordinate. Apparently is that *corner array's element* e.g. at location (1,1) has got only two neighbours, one in a vertical and one in horizontal direction. The single gradient module's constituent is assigned a grey-level value corresponding to a grey-level value of a single neighbour.

Iterative Technique

The iterative technique utilizes local first common statistical moments. Similarly to the Otsu technique algorithm the image (histogram) is partitioned into two classes by a user specified initial threshold value. Once the initial threshold is specified, local means could be computed according to the equations 6 and 7 with preceding occurrence probability calculation. The new threshold value is determined as an average of these two means:

$$T_k = \frac{\mu_0 + \mu_1}{2}; \quad Eq.16$$

k – ith iteration.

The optimal threshold value is determined while the threshold from the current iteration equals to one derived from the previous iteration $T_k = T_{k-1}$ and because of the image array elements are discrete values each time threshold value obtained from ith iteration is rounded to the nearest integer.

References

- Aleiferis, P.G., Charalambides, A.G., Hardalupas, Y., Taylor, A.M.K.P., Urata, Y. ***Autoignition Initiation and Development of N-Heptane HCCI Combustion Assisted by Inlet Air Heating, Internal EGR or Spark Discharge: An Optical Investigation.*** SAE Technical Paper 2006-01-3273, 2006.
- Amneus, P., Tuner, M., Mauss, F., Collin, R., Nygren, J., Richter, M., Alden, M., Kraft, M., Bhawe, A., Hildingsson, L., Johansson, B.. ***Formaldehyde and Hydroxyl Radicals in an HCCI Engine – Calculations and LIF-Measurements.*** SAE Technical Paper 2007-01-0049, 2007.
- Andor Dictionary*** [Online]. Available from <http://www.andor.com/learning> [Accessed March 2009].
- Andor Products Overview*** [Online]. Available to download from <http://www.andor.com> [Accessed March 2009].
- Andor iStar iCCD DH734I Camera Technical Guide*** [Online]. Available to download from <http://www.andor.com> [Accessed March 2009].
- Aroonsrisopon, T., Sohm, V., Werner, P., Foster, D.E., Morikawa, T., Iida, M.. ***An Investigation Into the Effect of Fuel Composition on HCCI Combustion Characteristics.*** SAE Technical Paper 2002-01-2830, 2002.
- Aroonsrisopon, T., Nitz, D.G., Waldman, J.O., Foster, D.E., Iida, M. ***A Computational Analysis of Direct Fuel Injection During the Negative Valve Overlap Period in an Iso-Octane Fueled HCCI Engine.*** SAE Technical Paper 2007-01-0227, 2007.
- ASTM D 2699
Standard Test Method for Research Octane Number of Spark-Ignition Engine
- ASTM D 2700
Standard Test Method for Motor Octane Number of Spark-Ignition Engine
- Atkins, P., De Paula, J. ***Physical Chemistry.*** Oxford University Press, 2006.
- Bartok, W., Sarofim, A.F. ***Fossil Fuel Combustion – A Source Book.*** John Wiley & Sons, Inc. U.S.A., 1991.

Berntsson, A.W., Denbratt, I. ***Optical Study of HCCI Combustion using NVO and SI Stratified Charge***. SAE Technical Paper 2007-24-0012, 2007.

BNC2090 Rack-Mountable Connector Block Guide [Online]. Available to download from <http://www.ni.com> [Accessed December 2006].

Bradley, D., Morley, C., Walmsley, H.L.. ***Relevance of Research and Motor Octane Numbers to the Prediction of Engine Autoignition***. SAE Technical Paper 2004-01-1970, 2004.

Bunting, B., Fairbridge, C., Mitchell, K., Crawford, R., Gallant, T., Storey, J. ***The Chemistry, Properties, and HCCI Combustion Behaviour of Refinery Streams Derived from Canadian Oil Sands Crude***. SAE Technical Paper 2008-01-2406, 2008.

Cao, L., Zhao, H., Jiang, X. ***Investigation into Controlled Auto-Ignition Combustion in a GDI Engine with Single and Split Fuel Injections***. SAE Technical Paper 2007-01-0211, 2007.

Christensen, M., Johansson, B., Amneus, P., Mauss, F. ***Supercharged Homogenous Charge Compression Ignition***. SAE Technical Paper 980787, 1998.

Dec, J.E., Espey, C. ***Chemiluminescence Imaging of Autoignition in a DI Diesel Engine***. SAE Technical Paper 982685, 1998.

Dec, J.E., Sjoberg, M. ***A Parametric Study of HCCI Combustion – the Sources of Emissions at Low Loads and the Effects of GDI Fuel Injection***. SAE Technical Paper 2003-01-0752, 2003.

Dec, J.E., Sjoberg, M. ***Isolating the Effects of Fuel Chemistry on Combustion Phasing in an HCCI Engine and the Potential of Fuel Stratification for Ignition Control***. SAE Technical Paper 2004-01-0557, 2004.

Dobosz, M. ***Statistical Analysis of Experimental Results***. Exit Publishing, 2004, Warsaw, Poland.

Druck PMP 1400 Pressure Sensor Technical Guide [Online]. Available to download from <http://www.gesensing.com> [Accessed May 2006].

Eping, K., Acevs, S., Bechtold, R., Dec, J. ***The Potential of HCCI Combustion for High Efficiency and Low Emission***. SAE Technical Paper 2002-01-1923, 2002.

Fused Silica – Windows and Lenses Guide. Alkor crystal optics [Online]. Available from <http://www.alkor.net>. [Accessed November 2008].

Garcia-Campana, A.M., Baeyens, W.R.G. ***Chemiluminescence in Analytical Chemistry.*** Marcel Dekker, Inc., New York, NY, U.S.A., 2001.

Gaydon, A.G. ***Spectroscopy of Flames.*** Chapman and Hall, Ltd., London, U.K, 1974.

Gonzalez, R.C., Woods, R.E. ***Digital Image Processing.*** Prentice Hall, 2nd Edition, Upper Saddle River, New Jersey, U.S.A., 2002.

Haireza, S., Sunden, B., Mauss, F. ***Effect of Inhomogeneities in the End Gas Temperature Field on the Autoignition in SI Engines.***
SAE Technical Paper 2000-01-0954, 2000.

He, X., Zigler, B.T., Walton, S.M., Wooldridge, M.S., Atreya, A. ***A rapid compression facility study of OH time histories during iso-octane ignition.*** Combustion and Flame 145 (2006), 552-570.

Herold, R.E., Ghandhi, J.B. ***Data Normalization Schemes for Assessing Mixture Stratification from PLIF Data.***
SAE Technical Paper 2008-01-1070, 2008.

Heywood, J.B. ***Internal Combustion Engine Fundamentals.***
McGraw-Hill Book Co, Singapore, 1988.

Hildingsson, L., Persson, H., Johansson, B., Collin, R., Nygren, J., Richter, M., Alden, M., Hasegawa, R., Yanagihara, H. ***Optical Diagnostics of HCCI and Low-Temperature Diesel Using Simultaneous 2-D PLIF of OH and Formaldehyde.***
SAE Technical Paper 2004-01-2949, 2004.

Hong, S., Wooldridge, M.S., Im, H.G., Assanis, D.N., Pitsch, H.. ***Development and application of a comprehensive soot model for 3D CFD reacting flow studies in a diesel engine.*** Combustion and Flame 143 (2005), 11-26.

Hultqvist, A., Christensen, M., Johansson, B., Franke, A., Richter, M., Alden, M. ***A Study of the Homogeneous Charge Compression Ignition Combustion Process by Chemiluminescence Imaging.*** SAE Technical Paper 1999-01-3680, 1999.

Hultqvist, A., Engdar, U., Johansson, B., Klingmann, J.. ***Reacting Boundary Layers in a***

Homogenous Charge Compression Ignition (HCCI) Engine.

SAE Technical Paper 2001-01-1032, 2001.

Hultqvist, A., Christensen, M., Johansson, B., Richter, M., Nygren, J., Hult, J., Alden, M.

The HCCI Combustion Process in a Single Cycle – Speed Fuel Tracer LIF and Chemiluminescence Imaging. SAE Technical Paper 2002-01-0424, 2002.

Hwang, W., Dec, J.E., Sjöberg, M. ***Spectroscopic and Chemical-Kinetic Analysis of the Phases of HCCI Autoignition and Combustion for Single- and Two-Stage Ignition Fuels.*** Combustion and Flame 154 (2008), 387-409.

Hyvonen, J., Haraldsson, G., Johansson, B. ***Operating Conditions Using Spark Assisted HCCI Combustion During Combustion Mode Transfer to SI in a Multi-Cylinder VCR-HCCI Engine.*** SAE Technical Paper 2005-01-0109, 2005.

Ishibashi, Y., Asai, M. ***Improving the exhaust emissions of two-stroke engines by applying the Activated Radical Combustion.*** SAE Technical Paper 960742, 1996.

Kalghatgi, G. ***Fuel Anti-Knock Quality – Part I. Engine Studies.*** SAE Technical Paper 2001-01-3584, 2001.

Kalghatgi, G. ***Fuel Anti-Knock Quality – Part II. Vehicle Studies – How Relevant is Motor Octane Number (MON) in Modern Engines.*** SAE Technical Paper 2001-01-3585, 2001.

Kalghatgi, G., Risberg, P., Angstrom, H.E. ***A Method of Defining Ignition Quality of Fuels in HCCI Engines.*** SAE Technical Paper 2003-01-1816, 2003.

Kalghatgi, G., Risberg, P., Angstrom, H.E. ***Autoignition Quality of Gasoline-Like Fuels in HCCI Engines.*** SAE Technical Paper 2003-01-3215, 2003.

Kalghatgi, G., Head, R.A. ***The Available and Required Autoignition Quality of Gasoline-Like Fuels in HCCI Engines at High Temperatures.*** SAE Technical Paper 2004-01-1969, 2004.

Kalghatgi, G. ***Autoignition Quality of Practical Fuels and Implications for Fuel Requirements of Future SI and HCCI Engines.*** SAE Technical Paper 2005-01-0239, 2005.

Kawahara, N., Tomita, E., Kagajyo, H. ***Homogenous Charge Compression Ignition***

Combustion with Dimethyl Ether –Spectrum Analysis of Chemiluminescence.

SAE Technical Paper 2003-01-1828, 2003.

Keller, J., Singh G. ***Update on Engine Combustion Research at Sandia National Laboratories.*** SAE Technical Paper 2001-01-2060, 2001.

Kistler® 6051A Pressure Transducer and 5011B Kistler® Charge Amplifier Technical Specifications. www.kistler.com

Koepecek, L., Wintner, E., Lackner, M., Winter, F., Hultqvist, A. ***Laser Stimulated Ignition in a Homogeneous Charge Compression Ignition Engine.***

SAE Technical Paper 2004-01-0937, 2004.

Koopmans, L., Denbratt, I. ***A Four Stroke Camless Engine Operated in Homogenous Charge Compression Ignition Mode with Commercial Gasoline.***

SAE Technical Paper 2001-01-3610, 2001.

Koopmans, L., Backlund, O., Denbratt, I. ***Cycle-to-Cycle Variations: Their Influence on Cycle Resolved Gas Temperature and Unburned Hydrocarbons from a Camless Gasoline Compression Ignition Engine.*** SAE Technical Paper 2002-01-0110, 2002.

Koopmans, L., Ognik, R., Denbratt, I. ***Direct Gasoline Injection in the Negative Valve Overlap of a Homogeneous Charge Compression Ignition Engine.***

SAE Technical Paper 2003-01-1854, 2003.

Koopmans, L., Stromberg, E., Denbratt, I. ***The Influence of PRF and Commercial Fuels with High Octane Number on the Auto-Ignition Timing of an Engine Operated in HCCI Combustion Mode with Negative Valve Overlap.***

SAE Technical Paper 2004-01-1967, 2004.

Koopmans, L., Wallesten, J., Ognik, R., Denbratt, I. ***Location of the First Auto-Ignition Sites for Two HCCI Systems in a Direct Injection Engine.*** SAE Technical Paper 2004-01-0564

Koopmans, L. ***HCCI/CAI Development Towards Increased Operational Window.*** Presentation, Homogeneous Charge Compression Ignition Symposium, Lund 12-14 September 2007.

Krieger, R.B., Borman, G.L. ***The Computation of Apparent Heat Release for Internal Combustion Engines.*** ASME, 1967.

Kuwahara, K., Ando, H., Furutani, M., Ohta, Y. ***Impact of Formaldehyde Addition on Auto-Ignition in Internal Combustion Engines***. JSME Vol.48, No.4, 2005.

Leppard, W.R. ***The Chemical Origin of Fuel Octane Sensitivity***.
SAE Technical Paper 902137, 1990.

Luszcz, P., Xu, H., Wyszynski, M., Tsolakis, A., Frackowiak, M., Wilson, T., Qiao, J. ***An Investigation of a Presence of Uncontrolled Combustion Phenomena in Spark Ignition Single Cylinder Optical Engine***. Journal of KONES, Vol.13, ISSN 1231-4005.

Luszcz, P., Xu, H., Wyszynski, M., Tsolakis, A., Stevens, R., Qiao, J. ***Image Processing Techniques for HCCI Autoignition and Combustion Analysis Using Matlab® and An Insight into Port Fuel Injected HCCI Autoignition and Combustion Process based on High-Speed Imaging***. Combustion and Flame, submitted.

Ma, H., ***Optical Diagnostics and Combustion Analysis in a Gasoline Direct Injection Engine***, Doctoral Thesis, University of Oxford, 2006.

Mahrous, A.F.M., Potrzebowski, A., Wyszynski, M., Xu, H., Tsolkais, A., Luszcz, P. ***A 1D Analysis into the Effect of Variable Valve Timing on HCCI Engine Parameters***.
SAE Technical Paper 2008-01-2459, 2008.

Mahrous, A.F.M., Potrzebowski, A., Wyszynski, M., Xu, H., A.Tsolkais, Luszcz, P. ***A modelling study into the effects of variable valve timing on the gas exchange process and performance of a 4-valve DI homogeneous charge compression ignition (HCCI) engine***. Energy Conversion and Management 50 (2009), 393-398.

Malina, W., Smiatacz, M. ***Digital Image Processing Techniques***. Exit Publishing, 2008, Warsaw, Poland.

Mancaruso, E., Merola, S.S., Vaglieco, B.M. ***Extinction and Chemiluminescence Measurements of HCCI Mode in Diesel Engine Operating with Late Injection***.
SAE Technical Paper 2008-01-0027, 2005.

Matlab Image Processing Toolbox Tutorials and Help. Matlab 7.1 Version, 2005.

Megaritis, A., Yap, D., Wyszynski, M. ***Effect of inlet valve timing and water blending on bioethanol HCCI combustion using forced induction and residual gas trapping***. Fuel 87 (2008), 732-739.

Misztal, J., Xu, H., Wyszynski, M., Price, P., Stone, R., Qiao, J. ***Effect on Injection Timing on Gasoline HCCI Particulate Emission***. Submitted to Engine Research Journal, 2009.

Misztal, J., Xu, H., Wyszynski, M., Price, P., Stone, R., Qiao, J. ***Influence of Inlet Air Temperature on Gasoline HCCI Particulate Emission***. Combustion Science and Technology 181 (2009), 695-709.

Naik, C.V., Pitz, W.J., Westbrook, C.K., Sjöberg, M., Dec, J.E., Orme, J., Curran, H.J., Simmie, J.M. ***Detailed Chemical Kinetic Modeling of Surrogate Fuels for Gasoline and Application to an HCCI Engine***. SAE Technical Paper 2005-01-3741, 2005.

Oriel MS260i™ ¼ m Imaging Spectrograph Brochure. Newport. www.newport.com.

Nikon UV-Nikkor 105 mm f/4.5 Lens - Brochure/Manual [Online]. Available to download from <http://www.nikon.com> [Accessed March 2006].

Nikon 24-85 mm f/2.5 – 4D IF Lens - Brochure/Manual [Online]. Available to download from <http://www.nikon.com> [Accessed March 2006].

Noguchi, M., Tanaka, Y., Tanaka, T., Takeuchi, Y. ***A study on gasoline engine combustion by observation of intermediate reactive products during combustion***. SAE Technical Paper 790840, 1979.

Olofsson, J., Seyfried, H., Richter, M., Alden, M., Vressner, A., Hultqvist, A., Johansson, B., Lombaert, K. ***High-Speed LIF Imaging for Cycle-Resolved Formaldehyde Visualization in HCCI Combustion***. SAE Technical Paper 2005-01-0641, 2005.

Onishi, S., Hong Jo, S., Shoda, K., Do Jo, P., Kato, S. ***Active thermo-atmospheric combustion (ATAC) – a new combustion process for internal combustion engines***. SAE Technical Paper 790501, 1979.

Otsu, N. ***A threshold selection method from gray level histograms***. IEEE Transactions on Man and Cybernetics Systems, Volume 9, Issue 1, January 1979.

Owen, K., Coley, T. ***Automotive Fuels Reference Book***. SAE, Warrendale, Pennsylvania, U.S.A., 1995.

Pajot, O., Maunoury, B., Duverger, T., Mokkadem, K., Lacas, F. ***Optical Investigation of Auto-Ignition Process in a Small DI Diesel Engine***. SAE Technical Paper 2002-01-1162, 2002.

PCI-6602 Card Technical Data [Online]. Available to download from <http://www.ni.com> [Accessed December 2006].

PCI-6023E Card Technical Data [Online]. Available to download from <http://www.ni.com> [Accessed December 2006].

Persson, H., Hildingsson, L., Hultqvist, A., Johansson, B., Ruebel, J. **Investigation of Boundary Layer Behaviour in HCCI Combustion using Chemiluminescence Imaging**. SAE Technical Paper 2005-01-3729, 2005.

Persson, H., Hultqvist, A., Johansson, B., Remon, A. **Investigation of the Early Flame Development in Spark Assisted HCCI Combustion Using High Speed Chemiluminescence Imaging**. SAE Technical Paper 2007-01-0212, 2007.

Phantom v7.1 CMOS Color Camera Technical Guide. www.visionresearch.com
Photonics Spectra. **CCD vs. CMOS: Facts and Fiction**. Laurin Publishing Co.Inc.,
Pittsfield, Massachusetts, U.S.A., January 2001.

Photonik. **Electronic Shuttering for High Speed CMOS Machine Vision Application**.
AT-Fachverlag GmbH Publishing, Fellbach, Germany May 2005.

Pickett, L.M., Kook, S., Williams, T.C. **Visualization of Diesel Spray Penetration, Cool-Flame, Ignition, High-Temperature Combustion, and Soot Formation Using High-Speed Imaging**. SAE Technical Paper 2009-01-0658, 2009.

Price, P., Stone, R., Misztal, J., Xu, H., Wyszynski, M., Wilson, T., Qiao, J. **Particulate Emissions from a Gasoline Homogenous Charge Compression Ignition Engine**. SAE Technical Paper 2007-01-0209, 2007.

Qiao, J., Wyszynski, M., Xu, H., Golunski, S. **Controlled Homogenous Auto-Ignition Supercharged Engine (CHASE)**, CHASE Annual Project Review, 14 December 2005.

Richter, M., Franke, A., Alden, M., Hultqvist, A., Johansson, B. **Optical Diagnostics Applied to Naturally Aspirated Homogenous Charge Compression Ignition Engine**. SAE Technical Paper 1999-01-3649, 1999.

Richter, M., Engstrom, J., Franke, A., Alden, M., Hultqvist, A., Johansson, B. **The Influence of Charge Inhomogeneity on the HCCI Combustion Process**. SAE Technical Paper 2000-01-2868, 2000.

Risberg, P., Kalghatgi, G., Angstrom, H.E. ***Auto-ignition Quality of Gasoline-Like Fuels in HCCI Engines.*** SAE Technical Paper 2003-01-3215, 2003.

Risberg, P., Kalghatgi, G., Angstrom, H.E. ***The Influence of EGR on Auto-ignition Quality of Gasoline-Like Fuels in HCCI Engines.*** SAE Technical Paper 2004-01-2952, 2004.

Risberg, P., Kalghatgi, G., Angstrom, H.E. ***Auto-ignition Quality of Diesel-Like Fuels in HCCI Engines.*** SAE Technical Paper 2005-01-2127, 2005.

Rotary Incremental Shaft Encoders Guide [Online]. Available to download from <http://www.baumerelectric.com> [Accessed December 2006].

Rothamer, D.A., Ghandhi, J.B. ***On the Calibration of Single-Shot Planar Laser Imaging Techniques in Engines.*** SAE Technical Paper 2002-01-0748, 2002.

Sanders, S.T., Kim, T., Ghandhi, J.B. ***Gas Temperature Measurements During Ignition in an HCCI Engine.*** SAE Technical Paper 2003-01-0744, 2003.

Schiessl, R., Dreizler, A., Mass, U. ***Comparison of Different Ways for Image Post-Processing: Detection of Flame Fronts.*** SAE paper 1999-01-3651, 1999.

Schiessl, R., Dreizler, A., Mass, U., Grant, A.J., Ewart, P. ***Double-Pulse PLIF Imaging of Self-Ignition Centres in an SI Engines.*** SAE paper 2001-01-1925, 2001.

Skoog, D.A., West, D.M., Holler, F.J., Crouch, S.R. ***Fundamentals of Analytical Chemistry.*** Eighth Edition, Brooks/Cole, Belmont, CA, U.S.A., 2004.

Shibata, G., Oyama, K., Urushihara, T., Nakano, T. ***The Effect of Fuel Properties on Low and High Temperature Heat Release and Resulting Performance of an HCCI Engine.*** SAE Technical Paper 2004-01-0553, 2004.

Shibata, G., Oyama, K., Urushihara, T., Nakano, T. ***Correlation of Low Temperature Heat Release with Fuel Composition and HCCI Engine Combustion.*** SAE Technical Paper 2005-01-0138, 2005.

Shibata, G., Urushihara, T. ***The Interaction Between Fuel Chemicals and HCCI Combustion Characteristics under Heated Intake Air Conditions.*** SAE Technical Paper 2006-01-0207, 2006.

Shibata, G., Urushihara, T. ***Auto-Ignition Characteristics of Hydrocarbons and Development of HCCI Fuel Index.*** SAE Technical Paper 2007-01-0220, 2007.

Singh, S., Reitz, R.D., Musculus, M.P.B. **2-Colour Thermometry Experiments and High-Speed Imaging of Multi-Mode Diesel Engine**. SAE Technical Paper 2005-01-3842, 2005.

Sjoberg, M., Dec, J.E. **Combined Effects of Fuel-Type and Engine Speed on Intake Temperature Requirements and Completeness of Bulk-Gas Reactions for HCCI Combustion**. SAE Technical Paper 2003-01-3173, 2003.

Sjoberg, M., Dec, J.E. **An Investigation of the Relationship Between Measured Intake Temperature, BDC Temperature, and Combustion Phasing for Premixed and DI HCCI Engines**. SAE Technical Paper 2004-01-1900, 2004.

Sjoberg, M., Dec, J.E. **EGR and Intake Boost for Managing HCCI Low-Temperature Heat Release over Wide Ranges of Engine Speed**. SAE Technical Paper 2007-01-0051, 2007.

Sjoberg, M., Dec, J.E., Hwang, W. **Thermodynamic and Chemical Effects of EGR and its Constituents on HCCI Autoignition**. SAE Technical Paper 2007-01-0207, 2007.

Song, H.H., Edwards, C.F. **Optimization of Recompression Reaction for Low-Load Operation of Residual-Effectuated HCCI**. SAE Technical Paper 2008-01-0016, 2008.

Steinberg, R., Lenz, I., Koehnlein, G., Scheidt, M.E., Saupe, T., Buchinger, W. **A Fully Continuous Variable Cam Timing Concept for Intake and Exhaust Phasing**. SAE Technical Paper 980767, 1998.

Swarts, A., Yates, A., Viljoen, C., Coetzer, R. **Standard Knock Intensity Revisited: Atypical Burn Rate Characteristics Identified in the CRF Octane Rating Engine**. SAE Technical Paper 2004-01-1850, 2004.

Swarts, A., Yates, A., Viljoen, C., Coetzer, R. **A Further Study of Inconsistencies between Autoignition and Knock Intensity in the CRF Octane Rating Engine**. SAE Technical Paper 2005-01-2081, 2005.

Szybist, J.P., Bunting, B.G. **Cetane Number and Engine Speed Effects on Diesel HCCI Performance and Emissions**. SAE Technical Paper 2005-01-3723, 2005.

Szybist, J.P., Boehman, A.L., Haworth, D.C., Koga, H. **Premixed ignition behavior of alternative diesel fuel-relevant compounds in a motored engine experiment**. Combustion and Flame 149 (2007), 112-128.

TORLON®, *Polyamide-imide Design Guide*. Solvay Advanced Polymers [Online]. Available to download from [http:// www. solvayadvancedpolymers.com](http://www.solvayadvancedpolymers.com) [Accessed December 2006].

Urata, T., Awasaka, M., Takanshi, J., Kakinuma, T., Hakoza, T., Umemoto, A. ***A Study of Gasoline-fuelled HCCI Engine Equipped with an Electromagnetic Valve Train.*** SAE Technical Paper 2004-01-1898, 2004.

Urushihara, T., Hiraya, K., Kakuhou, A., Itoh, T. ***Expansion of Operating Region by the Combination of Direct Fuel Injection, Negative Valve Overlap and Internal Fuel Reformation.*** SAE Technical Paper 2003-01-0749, 2003.

Waldman, J., Nitz, D., Aroonsrisopon, T., Foster, D.E., Iida, M. ***Experimental Investigation into the Effects of Direct Fuel Injection During the Negative Valve Overlap Period in an Gasoline Fueled HCCI Engine.*** SAE Technical Paper 2007-01-0219, 2007.

Walton, S.M., He, X., Zigler, B.T., Wooldridge, M.S., Atreya, A. ***An Experimental Investigation of Iso-octane Ignition Phenomena.*** Combustion and Flame 150 (2007), 246-262.

Weinrotter, M., Wintner, E., Iskra, K., Neger, T., Olofsson, J., Seyfried, H., Alden, M., Lackner, M., Winter, F., Vressner, A., Hultqvist, A., Johansson, B. ***Optical Diagnostics of Laser-Induced and Spark Plug-Assisted HCCI Combustion.*** SAE Technical Paper 2005-01-0129, 2005.

Westbrook, C.K. ***Chemical Kinetics of Hydrocarbon Ignition in Practical Combustion Systems.*** Proceeding of the Combustion Institute, Volume 28 p. 1563-1577, 2000.

Wilson, T.S., Xu, H., Richardson, S., Yap, D., Wyszynski, M. ***An Experimental Study of Combustion Initiation and development in an Optical HCCI Engine.*** SAE Technical Paper 2005-01-2129, 2005.

Wilson, T.S., Xu, H., Richardson, S., Yap, D., Wyszynski, M., Megaritis, T. ***Optical Study of Flow and Combustion in HCCI Engine with Negative Valve Overlap.*** Journal of Physics: Conference Series 45 (2006) 94-103.

Wojas, J. ***Thermal Radiation and Its Detection***, WNT Publishing, Warsaw, 2008.

Worldwide Fuel Charter. *Fourth Edition*, September 2006.

Wrobel, Z., Koprowski, R. ***Image Processing Methods Using Matlab.***

Exit Publishing, 2004, Warsaw, Poland.

Yang, J., Kenney, T. ***Robustness and Performance Near the Boundary of HCCI Operating Regime of a Single-Cylinder OKP Engine.***

SAE Technical Paper 2006-01-1082, 2006.

Yates, A., Viljoen, C., Swarts, A. ***Understanding the Relation Between Cetane Number and Combustion Bomb Ignition Delay Measurements.***

SAE Technical Paper 2004-01-2017, 2004.

Yates, A., Swarts, A., Viljoen, C. ***Correlating Auto-Ignition Delays and Knock-Limited Spark-Advance Data for Different Types of Fuel.***

SAE Technical Paper 2005-01-2083, 2005.

Zinola, S., Lavy, J. ***Detailed Particulate Characterization from HCCI Combustion for Future DPF Development.*** SAE Technical Paper 2009-01-1185, 2009.

Zhang, Y., He, B.Q., Xie, H., Zhao, H. ***The Combustion and Emission Characteristics of Ethanol on a Port Fuel Injection HCCI Engine.***

SAE Technical Paper 2006-01-0631, 2006.

Zhao, H., Ladommatos, N. ***Engine Combustion Instrumentation and Diagnostics.***

SAE, Warrendale, Pennsylvania, U.S.A., 2001.

Zhao, F., Asmus, T.W., Assanis, D.N., Dec, J.E., Eng, J.A., Najt, P.M. ***Homogenous Charge Compression (HCCI) Engines: Key Research and Development Issues.***

SAE, Warrendale, Pennsylvania, U.S.A., 2003.

Zhao, H., Peng, Z., Ma, T. ***Investigation of the HCCI/CAI Combustion Process by 2-D PLIF Imaging of Formaldehyde.***

SAE Technical Paper 2004-01-1901, 2004.

Zhao, H., Li, J., Ma, T., Ladommatos, N. ***Performance and Analysis of a 4-Stroke Multi-Cylinder Gasoline Engine with CAI Combustion.***

SAE Technical Paper 2002-01-0420, 2002.

Zigler, B.T., Walton, S.M., Assanis, D., Perez, E., Wooldridge, M.S., Wooldridge, S.T. ***An Imaging Study of Compression Ignition Phenomena of Iso-Octane, Indolene, and Gasoline Fuels in a Single-Cylinder Research Engine.***

Journal of Engineering for Gas Turbines and Power 130 (2008) / 052803-1.